A Qubit insensitive to noise

Nicolas Piot

THÈSE

Pour obtenir le grade de

DOCTEUR DE L'UNIVERSITÉ GRENOBLE ALPES

École doctorale : PHYS - Physique
Spécialité : Nanophysique
Unité de recherche : PHotonique, ELectronique et Ingéniérie QuantiqueS

Un bit quantique isolé du bruit

A Qubit insensitive to noise

Présentée par :

Nicolas PIOT

Direction de thèse :

Xavier JEHL Directeur de recherche, CEA Centre de Grenoble	Directeur de thèse
Romain MAURAND Ingénieur HDR, CEA Centre de Grenoble	Co-directeur de thèse

Rapporteurs :

CHRISTOPHE STAMPFER
Professeur, Universität Aachen
JOHN MORTON
Professeur, University College London

Thèse soutenue publiquement le **18 avril 2023**, devant le jury composé de :

CHRISTOPHE STAMPFER Professeur, Universität Aachen	Rapporteur
JOHN MORTON Professeur, University College London	Rapporteur
ANDREA HOFMANN Professeur assistant, Universität Basel	Examinatrice
FREDERICO MARTINS Ingénieur de recherche, Hitachi Cambridge Laboratory	Examinateur
MAIRBEK CHSHIEV Professeur des Universités, UNIVERSITE GRENOBLE ALPES	Président

Invités :

XAVIER JEHL
Directeur de recherche, CEA CENTRE DE GRENOBLE
ROMAIN MAURAND
Ingénieur HDR, CEA CENTRE DE GRENOBLE

A QUBIT INSENSITIVE TO NOISE

N. PIOT

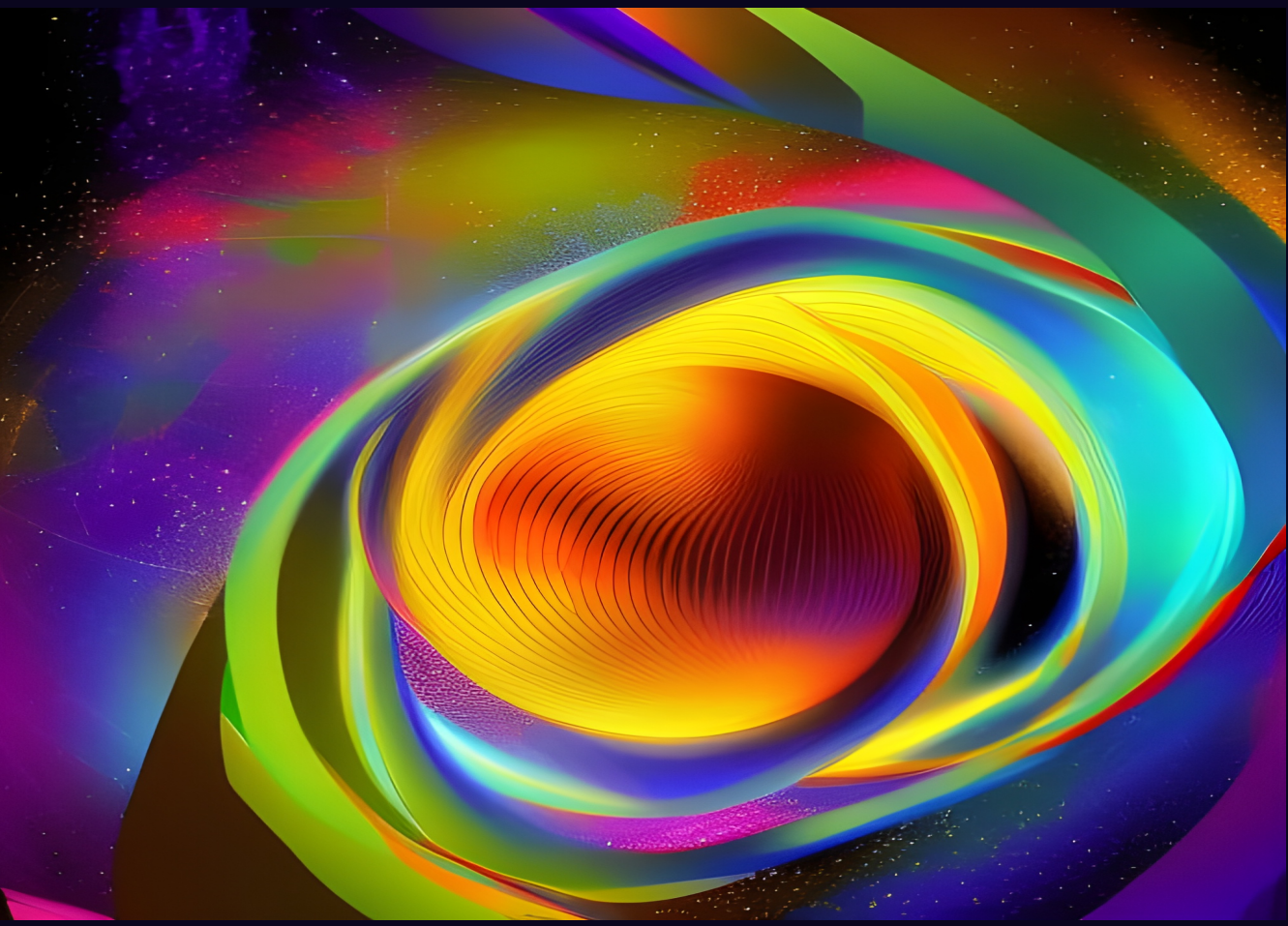

A Qubit insensitive to noise

"Nobody ever figures out what life is all about, and it doesn't matter. Explore the world. Nearly everything is really interesting if you go into it deeply enough."

Richard Feynman

Version Française

Les bits quantiques de spin (qubits de spin) piégés dans des boites quantiques sont apparus comme une plateforme prometteuse pour le traitement de l'information quantique. En particulier, les semi-conducteurs du groupe IV tels que le silicium et le germanium présentent des résultats particulièrement encourageants. Parmi ses nombreuses qualités, le plus grand atout du silicium reste sa compatibilité avec les technologies de fabrication courantes et la possibilité d'éliminer les spins nucléaires parasites via une purification isotopique. En outre, les qubits de spin électronique peuvent tirer parti de la résonance dipolaire de spin médiatisée par un couplage spin-orbite artificiel. Cette technique permet une manipulation particulièrement rapide de l'état de spin d'un électron. Bien que les boites quantiques promettent des densités d'intégration élevées en raison de leur faible empreinte spatiale, la nécessité d'utiliser des modules complémentaires excessivement encombrants pour tirer parti du couplage spin orbite est en réalité un frein dans une perspective d'évolutivité. À l'inverse, les états de trous dans le silicium possèdent un couplage spin-orbite intrinsèque et entièrement modulable, ce qui est un atout substantiel. Dans cette thèse, nous présentons un unique qubit de trou dont le temps de cohérence a été grandement amélioré grâce à une compréhension poussée du couplage spin orbite dans nos dispositifs. Les résultats obtenus prouvent que les trous d'électrons sont des concurrents de taille pour leurs homologues électroniques.

Il est intrinsèquement difficile de mesurer l'état de spin d'une seule particule. Pour se faire, nous avons fait correspondre chaque état de spin à un état de charge qui est lui facilement mesurable. Ce type de mesure rendu possible grâce à la discrimination en énergie des états de spin. Concrètement, nous avons réalisé un capteur intégré à l'échantillon en mettant en résonance un grand îlot de trous d'électron avec leur réservoir. Ce dernier est également connecté un résonateur, qui est en permanence excité par une onde sinusoïdale. La réflexion de cette onde

par le résonateur en fonction de l'état de charge du système constitue un détecteur à la pointe des performances atteignable en laboratoire à ce jour. Un seul trou d'électron a ensuite été isolé à proximité du capteur, afin d'étudier ses propriétés. Le couplage spin-orbite combiné au confinement asymétrique du trou donne lieu à une énergie Zeeman très anisotrope. Par conséquent, nous avons mesuré les facteurs g ainsi que la susceptibilité électrique de spin en fonction de l'orientation du champ magnétique. Toutefois, bien que ce couplage soit une aubaine, il rend paradoxalement les qubits de trou sensibles au bruit électrique environnant. Nous avons démontré que pour une orientation spécifique du champ magnétique, nous étions capables de minimiser le couplage longitudinal, améliorant d'un facteur cinq le temps de cohérence. La technique mentionné ci-dessus offre donc une méthode pour isoler le qubit du bruit, améliorant ainsi ses caractéristiques. Dans un second temps, nous avons également étudié l'origine du bruit affectant la durée de vie du spin. À basse fréquence, le bruit magnétique provenant de l'isotope 29 du silicium restant apparaît comme un candidat très probable, tandis qu'à haute fréquence, la principale source de bruit est dû à des parasites électriques. L'absence de phonons, qui devrait être le principal mécanisme de retournement du spin, reste cependant une question ouverte. Le travail présenté offre une nouvelle brique élémentaire pour le traitement de l'information quantique, réalisée à l'aide d'une technologies CMOS.

English version

Spin quantum bits (qubits) defined in semiconductor quantum dots have emerged as a promising platform for quantum information processing. In particular, group IV semiconductors such as silicon and germanium show encouraging results. Among their numerous qualities, the biggest strength of silicon is its compatibility with mainstream manufacturing technology and the ability to eliminate spurious nuclear spins through isotopic purification. Furthermore, electron spin qubits can take advantage of electron dipole spin resonance enabled via an artificial spin orbit coupling, allowing for fast and full electrical spin manipulation. Although quantum dots promise to enable high-integration densities due to their small footprint, the necessity to use cumbersome add-ons to leverage the spin orbit coupling worsens the scalability prospect. Conversely, hole states in silicon possess an intrinsic and fully tunable spin orbit coupling, key for practical, fast and potentially scalable qubit control. In this thesis, we report a single hole spin with enhanced coherence time in natural silicon, achieved by the understanding and the optimization of the spin orbit coupling.

It is intrinsically hard to measure the spin state of a single particle. Consequently, we mapped the spin onto the charge state via an energy selective readout. To do so, a built-in sensor is created by bringing into resonance a large hole island with a reservoir, which is then connected to a tank circuit. The signal is finally recorded via radio frequency reflectometry, allowing for fast and efficient charge sensing. A single hole was then isolated close to the sensor, to study its properties. The spin-orbit coupling combined with asymmetric confinement of the hole give rise to an anisotropic Zeeman energy. Consequently, we measured the g-factors and the spin susceptibility as a function of magnetic field orientation. Although, full electrical driving of hole spin state is a strength, it also renders the qubits sensitive to surrounding electrical noise. We demonstrated that for specific magnetic field orientation, we were able to minimize the longitudinal coupling, improving by a factor five the coherence time. The above-mentioned tuning offers a method to hide the qubit from the noise, helping to improve its property. We also studied the origin of noise affecting the spin lifetime. At low frequency, magnetic noise from the remaining silicon 29 isotope emerge as a highly probable candidate, while at high frequency the main noise source is electrical. The absence of phonons, which should be the main mechanism for spin flips, however remains an open question. The presented work offers a new tunable basic unit, made with CMOS technologies for quantum information processing.

Acknowledgments

I am extremely grateful to **Xavier JELH**, my PhD director, for his unwavering support and guidance throughout my research journey. Xavier was always willing to lend a helping hand, whether it was with scientific questions or administrative tasks such as paperwork. His dedication to my success was evident in every interaction we had, and his willingness to assist me on any subject was truly appreciated. Towards the end of my thesis work, his exceptional management skills proved invaluable in ensuring that the project was completed on time despite the many unforeseen events that arose. As we say : "No pain, no gain !".

I am honored to acknowledge **Romain Maurand**, my thesis supervisor, for his exceptional contributions to my research work. Romain's remarkable ability to provide relevant pathways to explore and his accurate vision of quantum computing were instrumental in shaping my research direction and ensuring its success. Despite my occasional lack of knowledge and silly questions, Romain challenged me to think critically and pushed me to achieve my best. His no-nonsense approach and occasional shaming responses were tough, but ultimately incredibly helpful in helping me grow as a researcher.

I would like to give a shoutout to my friend and colleague, **Dr. Before** (B^4), who worked closely with me on **SMURF**, our beloved fridge. Boris was an incredible supervisor who always had my back and pushed me to be my best. Although he may not have been the best at coding (at all !!), his intuition and problem-solving abilities were nothing short of amazing. Our countless hours working together on the fridge and discussing physics were always engaging and productive, and his insights and suggestions were instrumental in shaping my research direction. I truly enjoyed our friendly taunts and banter, which always kept the work atmosphere light-hearted and fun. Boris's superior abilities in all aspects of research and science are undeniable, and I am honored to have had the opportunity to work with such a remarkable colleague and friend.

I would like to extend a special thank you to **Yann Michel NIQUET** for his invaluable contributions. Yann Michel provided not only the necessary theoretical support but also a wealth of knowledge and insights through countless hours of discussion. His guidance and feedback were critical to my understanding of the subject. Additionally, I would like to express my gratitude to all the other members of the group, including **Vincent**, **Biel**, **José**, and **Esteban**, for their support and collaboration. Their diverse perspectives and expertise were instrumental in enriching and it was always a pleasure to discuss with all of you.

Silvano I have to thank you so much, but let us face it. Of the two of us, you are the one who sucks at darts. I never dared admit it to you for fear of being

fired from the lab. It was a pleasure to learn from you, you are an inexhaustible source of information.

I would also like to thank **Francois**, you who is the head of this laboratory. You always have good ideas to make the lab day a success, in a good mood. On the other hand, the prerogative to make the darts disappear during the covid is still a painful period for me. I would like to remind you that there is still a price on your head and that you will have to drink a lot of punch to clear your debt.

I would like to express my gratitude to all the support staff who have made it possible for us to work smoothly at the CEA. In particular, I want to thank **Marielle** for her administrative skills and patience in handling the endless paperwork with efficiency, even when I caused unexpected delays. But also a big thank you to **Michel**, without whom the continuous improvement of the fridges with nice mechanical parts would not have been possible. In addition, of course, thank you **Jean-Luc**. I swear I wear my mask correctly every day at home.

This adventure would have been really different without all my PhD colleagues, who are also my friends. Starting from the elders, thank you **Agostino**, **Rami**, **Chotivut**, **Gonzalo**.

Thomas and **Claire**, many thanks for the many hours spent in the lab but also outside. Whether it is climbing, camping, barbecues or game nights, you were always available to have a good time.

Cécile, thank you for being my thesis twin. Although Chinese meat cakes are clearly not on my top list, Chinese fondue is. A big thank you also to **Baptiste** and **Yuzu** who have always welcomed me warmly. I cannot wait to come and visit you in Delft (and finally work there !!).

Thank you **Victor M.** for your joy of living and all the help you can provide to others. Without you, I think I would still be trying to install Python on my computer. It is always a pleasure to chat with you over a cup of hot tea. Thanks also for the board game nights.

Florie, I hope your American adventure lives up to your expectations. I hope to see you soon for a bike ride with **Martin**. Thanks again for introducing me to the Cairnes bakery.

Estelle, thank you for keeping quiet when you were the first to know. I still owe you plenty of chips, because as we all know, without potatoes I'm not sure you'll last a week. Last line for your thesis, I'm crossing my fingers that everything goes better than I did, you deserve it.

'Chef' **Vivi**! It hurts to say it, but congratulations on your success. In any case, you know where to ring if you want a beer; I will always be there for that.

Simon, probably the best of all the Swiss. I have never met anyone who knows so much about physics. Whatever the subject, you know everything and understand everything, it is impressive. Thanks for the board games and raclette evenings at your place.

Nathan, I wish I had spent more time messing with you. Always too busy, you are a great person. Good luck with your thesis, it is almost over.

Thomas H., thank you for participating in all the events I organised. It was always a pleasure to have you with us.

A big thank you to **Axel** and **Victor C.** The two inseparable companions. I still have not managed to find out which one of you is the most stupid. However, that is probably why I adore you both so much. See you next time for a beer, but please stop making me watch sappy movies.

Marion, thank you so much for putting up with me every day. Physics is good but holidays are better. I can't wait for the next destinations, walking, camping, laughing and so much more. And of course, good luck with your thesis, it's almost over.

Good luck to **Nesrine** and **Leo** for their debut in the lab. I hope they will have as good a time as I did.

And of course thank you to all my friends outside the lab. In particular my two loves: **Zozo** and **Papito** without whom life would be very bland. I also want to thank **the crew of Centrale**, the people from **Montpellier**, the friends from **Aix en Provence** and **many others**.

A gigantic thank you to my **family** for the support throughout my schooling. My thesis was only a tiny part of what I was able to achieve thanks to them. I can never thank you enough for everything you have done. I promise I will choose a good retirement home, love!

Ultimately, I would like to thanks the members of the jury, **John MORTON**, **Christoph STAMPFER**, **Andrea HOFMANN**, **Frederico MARTINS**, **Mairbek CHSHIEV** for reviewing this work and attending the defense. Thank you for all of your questions and remarks during the defense.

Contents

Page

List of Figures **13**

List of Tables **15**

1 Introduction **17**
- 1.1 Version Française . . . 18
- 1.2 English version . . . 24
- References . . . 31

2 Theory & mathematical tools **33**
- 2.1 Quantum dots . . . 35
  - 2.1.1 Single quantum dot . . . 35
  - 2.1.2 Double quantum dot . . . 37
- 2.2 One half Spin based qubits (General case) . . . 38
  - 2.2.1 Larmor precession . . . 39
  - 2.2.2 Spin rotation in the Rotating Wave Approximation (RWA) 40
  - 2.2.3 Spin relaxation and dephasing . . . 42
- 2.3 Hole spin qubit in Silicon . . . 44
  - 2.3.1 Simplest valence band description . . . 44
  - 2.3.2 Spin-orbit coupling . . . 45
  - 2.3.3 Zeeman splitting . . . 49
- 2.4 G-matrix formalism . . . 50
  - 2.4.1 Rotation transformation . . . 51
  - 2.4.2 The Zeeman tensor . . . 51
  - 2.4.3 Spin driving mechanisms . . . 52
- 2.5 Noise sources acting on hole spin qubits . . . 56
  - 2.5.1 Hyperfine interaction . . . 56
  - 2.5.2 Electrical noise . . . 58
  - 2.5.3 High frequency : Jonhson Nyquist Noise . . . 62
- 2.6 Power spectral density . . . 64

2.6.1 Fourier transform Definition . . . 64
2.6.2 PSD from Fourier transform . . . 66
2.6.3 PSD from signal autocorrelation . . . 67
2.6.4 Noise color . . . 68
References . . . 74

3 Experimental Setup **75**
3.1 Device Fabrication . . . 77
3.1.1 Active area : The nanowire . . . 78
3.1.2 Shaping a landscape : The Gates . . . 79
3.1.3 Claiming quantum properties : The Spacers . . . 79
3.1.4 tank of electrons : Source and Drain . . . 79
3.1.5 Device . . . 81
3.2 Setup . . . 82
3.2.1 Dry dilution fridge . . . 82
3.2.2 Control lines . . . 83
3.2.3 Readout lines . . . 85
3.2.4 Setup configuration . . . 85
3.3 Radio frequency reflectometry . . . 86
3.3.1 Wave scattering at an impedance mismatch . . . 87
3.3.2 Probing an electrical resonator . . . 88
3.3.3 Dispersive readout configuration . . . 90
3.4 Device screening . . . 90
References . . . 95

4 From device to qubit **97**
4.1 Device . . . 99
4.2 Resonators . . . 101
4.3 Charge sensor . . . 102
4.3.1 Coulomb peaks . . . 102
4.3.2 QD3 & QD4 : Single dot regime . . . 103
4.3.3 Stability diagram of the first hole . . . 105
4.4 Spin readout . . . 106
4.4.1 Energy selective spin readout . . . 107
4.4.2 Rates tuning . . . 107
4.4.3 Three stages protocol . . . 109
4.4.4 Elzerman tail : time average measurement . . . 109
4.4.5 Fast single shot spin measurement . . . 112
4.5 Initialization & Manipulation . . . 114
4.5.1 Two stage protocol . . . 114
4.5.2 Rabi chevrons . . . 114
References . . . 119

5 Single hole spin coherence **121**
5.1 Single hole properties . . . 123
5.1.1 Experimentally measured g factors . . . 123
5.1.2 k-p model for g factors simulations . . . 124
5.2 Longitudinal spin electric susceptibility (LSES) . . . 127
5.2.1 $LSES_{G2}$ . . . 127
5.2.2 $LSES_{G1}$ . . . 129
5.3 Extended phase coherence . . . 131
5.3.1 Hahn-echo spin coherence . . . 131
5.3.2 Hahn-echo amplitude . . . 132
5.3.3 Magnetic sweet spots . . . 133
5.3.4 Charge noise in spin qubit platforms . . . 134
5.4 Inhomogeneous dephasing time . . . 135
5.4.1 Ramsey experiment . . . 135
5.4.2 Dephasing time in the non-ergodic regime . . . 137
5.4.3 Ultra low frequency noise . . . 138
5.5 Quality factors . . . 140
References . . . 145

6 Noise characterization **147**
6.1 Ramsey interference . . . 149
6.1.1 Free induction decay (FID) . . . 149
6.1.2 Ultra low frequency spectrum . . . 151
6.1.3 Ramsey Single Shot (RSS) . . . 152
6.1.4 RSS auto-correlation . . . 154
6.2 Charge Sensing (CS) . . . 155
6.2.1 Coulomb peak sensitivity . . . 155
6.2.2 Hyperfine ? . . . 157
6.3 Carr–Purcell –Meiboom–Gill (CPMG) . . . 158
6.3.1 CPMG filtering function . . . 158
6.3.2 CPMG measurement . . . 159
6.3.3 CPMG spectrum . . . 160
6.4 Spin life time . . . 161
6.4.1 T_1 measurement protocol . . . 161
6.4.2 Γ_1 versus magnetic field amplitude . . . 162
6.4.3 Γ_1 versus magnetic field orientation . . . 163
6.4.4 TSES versus magnetic field orientation . . . 164
6.4.5 Johnson Nyquist . . . 166
References . . . 172

7 Conclusion **173**
7.1 Version Française . . . 174
7.2 English version . . . 176

List of Figures

2.1 **Single quantum dot in gated semiconductor.** 36
2.2 **Double quantum dot.** 37
2.3 **Valence band of silicon crystalline structure without spin orbit coupling.** 45
2.4 **Zoom in silicon bulk schematic band diagram around Γ point.** 48
2.5 **Visualisation of the g tensor modulation.** 54

3.1 **Silicon nanowires : Various 3 dimensional nanowire configuration.** 77
3.2 **Main steps of the FinFET fabrication process.** 80
3.3 **Device description.** 81
3.4 **Dilution refrigerator main parts.** 83
3.5 **Experimental setup.** 86
3.6 **Radio frequency reflectometry.** 89
3.7 **Yield across the full wafer.** 91

4.1 **Device description.** 99
4.2 **Room temperature I-V characteristics** 100
4.3 **Radio frequency reflectometry via homodyne detection.** . . 101
4.4 **Probing coulomb peaks with drain reflectometry.** 103
4.5 **Stability diagrams (G3,G4).** 104
4.6 **Zoom in Stability diagram (G3,G4).** 105
4.7 **Charge sensor response after tuning.** 106
4.8 **Full counting statistics** 108
4.9 **Three stage protocol for spin detection.** 110
4.10 **Elzerman tail.** 111
4.11 **Real sequence.** 112
4.12 **Ultra fast single shot spin readout.** 113
4.13 **Spin manipulation.** 115
4.14 **Electrical spin driving.** 116

5.1 Experimental g factors. . . . 124
5.2 First hole wavefunction in a corner dot state. . . . 125
5.3 Dependence of the g-factors on the electric field 126
5.4 Measurement of $\mathrm{LSES_{G2}}$. . . . 127
5.5 Magnetic field anisotropy of $\mathrm{LSES_{G2}}$. . . . 128
5.6 Measurement of $\mathrm{LSES_{G2}}$. . . . 130
5.7 Perfect spin echo rephasing sequence for a short free evolution time. . . . 131
5.8 Hahn-echo decaying shape. . . . 132
5.9 Echo spin coherence anisotropy. . . . 133
5.10 Ramsey sequence. . . . 135
5.11 Free induction decay (FID). . . . 136
5.12 Spin coherence with correlated low-frequency noise 138
5.13 Probing the low frequency noise spectrum. . . . 139
5.14 Rabi frequencies and quality factors. . . . 141

6.1 Free induction decay over night. . . . 150
6.2 Histogram of the signal $\Delta f(\tau_{\mathrm{lab}})$. . . . 150
6.3 PSDs from free inductive decay measurement. . . . 151
6.4 Simulation of Ramsey oscillations for RSS. . . . 152
6.5 Blip matrix from RSS measurement. . . . 153
6.6 PSDs from Ramsey single shot measurement. . . . 154
6.7 Coulomb peak used as a charge sensor for the qubit. . . . 155
6.8 from charge sensing measurement. . . . 156
6.9 Summary of the different spectra. . . . 157
6.10 CPMG filter function. . . . 159
6.11 CPMG protocol. . . . 160
6.12 PSD from CPMG measurement. . . . 161
6.13 T1 measurement protocol. . . . 162
6.14 Γ_1 versus B field in the x direction. . . . 163
6.15 Γ_1 versus B field orientation. . . . 164
6.16 Rabi frequencies linearity. . . . 165
6.17 Transversal spin electric susceptibility. . . . 166
6.18 Anisotropy comparison. . . . 167
6.19 PSD from T_1 measurement. . . . 168
6.20 PSD over 14 decades in frequency. . . . 168

List of Tables

3.1 Five stages filter important characteristics 84

4.1 Calculated parasitic capacitance 102

5.1 Charge noise in spin qubit platform at high frequency (1 MHz) . . 134

Chapter 1

Introduction

"I think I can safely say that nobody understands quantum mechanics."

Richard Feynman

Contents

1.1 Version Française 18
1.2 English version 24
References 31

1.1 Version Française

Bien que l'expression « ordinateur quantique » semble couler de source tellement elle est employée à tort et à travers par les médias de vulgarisation scientifique, elle est en réalité bien plus complexe. Si l'on décortique l'expression, cette dernière est composée de deux termes qui ne semblent pas avoir de lien évident. D'un côté, l'ordinateur, objet déterministe du quotidien, qui reproduit sans cesse les mêmes actions pour aboutir aux mêmes conclusions. De l'autre, le monde de mieux en mieux connu mais pourtant contre-intuitive de la physique quantique. A cette échelle du monde physique, le comportement des objets possède un caractère aléatoire fondamental. De fait, comment imaginer, par exemple, sauvegarder une information si au moment où vous posez les yeux dessus, celle-ci est totalement modifiée ? Avec l'ordinateur quantique, le rêve de la communauté scientifique serait de dompter l'étrange absurdité de l'univers quantique afin de construire un outil de calcul absolument révolutionnaire. Cette thèse est consacrée à l'étude d'une des solutions techniques envisagée pour concevoir la brique élémentaire de cet ordinateur d'un nouveau genre. Pour bien comprendre les tenants et les aboutissants de ces travaux de recherche, resituons-les dans la perspective de long terme qui est celle de l'histoire humaine des outils de calculs. Fondamentalement, qu'est-ce qu'un ordinateur ? Ce nom générique désigne un dispositif électronique réalisant des opérations de calcul simples et à la chaine aussi appelées algorithmes. Suivant cette première définition simple chacun reconnaitra la myriades d'appareils qui se sont immiscés dans nos vies : l'ordinateur du bureau, bien sûr, mais aussi les ordinateurs embarqués dans nos téléphones, montres, voitures, etc. A tel point qu'il est devenu impossible de citer un domaine d'activité où il n'a pas une place prépondérante. De la communication au transport, en passant par la médecine et même le sport, ce minuscule élément fait tout plus vite que nous, et il faut le reconnaitre, bien mieux que nous. Le domaine de la recherche scientifique, en particulier, a connu une évolution sans précédent à l'aide des différents outils de simulation, de traitement ou de visualisation de données. Etymologiquement, le terme ''ordinateur" fait référence à un adjectif tombé en désuétude qui signifiait 'qui met de l'ordre dans le monde", ce qui n'est finalement pas si éloigné d'une définition générale de l'ordinateur moderne. En somme, l'ordinateur est au cœur de notre monde moderne, aussi indispensable qu'il peut être parfois horripilant. Mais il n'a pas toujours été la petite puce électronique que nous connaissons tous et, comme l'ensemble des objets techniques que nous utilisons quotidiennement, sa forme actuelle est le fruit d'une longue et tumultueuse évolution."

L'ordinateur a tout d'abord été théorisé comme un outil de calcul programmable par Charles Babbage en 1834. Sémantiquement, la programmation définit une action présente qui impacte de manière connue le futur. En d'autres termes, un outil programmable exécute une routine connue, aboutissant à une solution préalablement déterminée. De fait, reproduire un programme conduira théoriquement aux mêmes résultats. L'ordinateur apparait donc comme une aide, capable de

modéliser ou résoudre des problèmes, parfois complexes. Pourtant on trouve dans l'histoire des traces de dispositifs dont le fonctionnement est proche de celui d'un ordinateur mais desquels la programmation est absente. Chaque action de ces calculateurs analogiques est prédéterminée par les lois de la physique. La finalité de ces instruments de mesure est de simuler un autre système physique régi par les mêmes équations. Notez ici l'emploi du mot calculateur qui diffère du terme ordinateur (ce qui n'est pas le cas en anglais), et qui peut être vu comme un ancêtre de ce dernier. De ce point de vue, le plus ancien ordinateur connu serait donc daté de 87 av. JC, sous le nom de Machine d'Anticythère. Ce simulateur non programmable n'est autre qu'un mécanisme à engrenage de bronze permettant de prévoir la date de l'heure des éclipses lunaires et solaires. D'une praticité douteuse au vu des considérations actuelles, et surtout relativement encombrant (ça rappellera peut-être au lecteur, par certains points, l'état d'avancement de l'ordinateur quantique).

Ce sont finalement les recherches d'Alan Turing qui ouvrent la voie, dès 1936, à la création d'un véritable ordinateur programmable. D'ailleurs, l'ordinateur moderne dit ''de Turing" porte au passage toujours son nom. Comme souvent, c'est à la faveur d'une guerre, en l'occurrence la seconde guerre mondiale, que les recherches sur l'ordinateur enregistrèrent un progrès notable. Le décryptage des communications ennemies a poussé les chercheurs à toujours perfectionner leurs moyens d'espionnages et d'analyses. Turing s'est particulièrement illustré en la matière puisqu'il a activement contribué à concevoir la machine Enigma qui a joué un rôle prépondérant dans le conflit en se basant sur une technologie électromécanique (analogique) servant au chiffrement et au déchiffrement de l'information. Mais, en 1947, une véritable révolution technologique ouvre la voie d'une nouvelle ère : John Bardeen, William Shockley, and Walter Brattain, chercheurs des laboratoires Bell, présentent le tout premier transistor. Cet objet en germanium, constitué de trois électrodes contactées à l'or, permet de contrôler facilement le courant le traversant. Il s'imposera rapidement comme la brique élémentaire de ce qui deviendra l'ordinateur numérique. Les premières portes logiques, élément indispensable de l'algèbre booléenne (1854), commencent peu à peu à émerger pour aboutir en 1958 au premier circuit imprimé dont Jack Kilby est l'inventeur. Bien qu'initialement en germanium, les hautes mobilités électroniques ont rapidement été mise de côté au profit des transistors en silicium. Ce dernier est non seulement très abondant mais possède aussi un oxyde natif ($SiO2$) dont les propriétés sont bien supérieures à celui du Germanium. En effet l'oxyde de silicium est un très bon isolant électrique et très simple à faire croitre.

Depuis lors Les transistors ont connu une évolution exponentielle. Cette dynamique avait d'ailleurs été théorisée par l'ingénieur Gordon E. Moore sur la base des observations qu'il avait pu réaliser entre 1959 et 1965. Ce dernier avait alors suggéré une extrapolation, qu'on désigne abusivement sous les termes de loi de Moore, selon laquelle le nombre de transistor par unité de surface double tous les

deux ans. A ce jour, cette loi n'a cessé de se vérifier en dépit des obstacles. Ces améliorations sont le fruit, entre autres, de la réduction de la production de chaleur, d'une meilleure dissipation de cette dernière, des interfaces silicium/SiO2 toujours plus propres, de l'augmentation des fréquences d'horloge et bien d'autre. Bien que certains pessimistes prévoyaient un ralentissement depuis quelques années déjà, la recherche a toujours su se renouveler pour aboutir à des puces électroniques contenant maintenant plus de cinquante milliards de transistors, avec une empreinte moyenne par élément en deçà de 5nm. Toutefois, il existe une limite absolue dont on se rapproche inéluctablement. En effet, la réduction de taille drastique des transistor conduit à un changement de paradigme : l'émergence d'effets quantiques, qui est probablement l'un des plus gros défis à venir. Mais derrière tout inconvénient se cache un avantage. Récemment théorisé (1980), l'ordinateur quantique tend à tirer avantage de la physique quantique pour conduire des simulations, mais cette fois d'un autre ordre. Avant d'aller plus loin dans la description du fonctionnement de ces ordinateurs, faisons une comparaison, nécessairement réductrice, afin de nous figurer en quoi ces ordinateurs créent une rupture dans le portrait historique que nous venons de brosser. Son père fondateur, en la personne de Feynman, décrit l'ordinateur quantique, dans son discours d'ouverture de la première conférence dédié au calcul quantique (1981), comme un simulateur exact de la physique quantique, tâche impossible à réaliser pour un ordinateur classique. Mais plus qu'un simulateur quantique, il est bel et bien possible de créer un ordinateur quantique doté de ses propres algorithmes. Imaginez que vous ne possédiez que l'addition comme outil mathématique, alors l'ordinateur quantique serait quant à lui la multiplication. Vous ne verriez pas le monde de la même façon. Parfois, un problème sera plus simple, parfois plus compliqué. Le changement d'algèbre sous-jacent aux calculs ouvre une toute nouvelle voie de recherche dont les implications sont autant méconnues que potentiellement révolutionnaires. Certains algorithmes quantiques ont d'ailleurs déjà une place prépondérante dans l'avenir de l'ordinateur quantique (Shor), tandis que d'autres font figures d'OVNI tant leur résultat semble aller à l'encontre des postulats de la physique (Grover). La réelle force de l'ordinateur quantique réside probablement dans sa complémentarité avec un ordinateur classique. Tant qu'il existera des problèmes mathématiques non déterministes en temps polynomial (complexité NP), alors les deux facettes de la physique couplées à des algorithmes ingénieux, apporteront des solutions inédites à la résolution de certains types de problème.

Pour bien comprendre ce qui distingue les ordinateurs quantiques de ceux que nous côtoyons au quotidien, intéressons-nous à ce qui constitue la brique élémentaire de ces outils techniques. Le plus petit élément composant un ordinateur quantique n'est autre qu'un bit quantique (Qubit). Contrairement à un transistor classique possédant deux états propres ouvert (1) et fermé (0), un qubit peut, quant à lui, être les deux à la fois. Cette propriété physique appelée ''superposition quantique '' est l'un des deux ingrédients majeurs. Le second étant l'enchevêtrement de plusieurs éléments quantiques, impliquant que toute action

réalisée sur l'un se répercute instantanément sur les autres. Une recette de cuisine somme toute simple sur le papier, mais extrêmement difficile à réaliser dans la réalité. En effet, l'information quantique est par définition extrêmement sensible, ce qui requiert un effort de taille pour réduire l'interaction entre un qubit et le monde extérieur. Malheureusement, tout comme un transistor classique, un qubit a aussi besoin d'être contrôlé, ce qui paradoxalement implique une interaction avec le monde extérieur. Toute la difficulté est donc d'isoler le système des perturbations extérieures indésirables (bruits), tout en conservant la capacité d'interagir avec lui (signal). Le principal défi étant indubitablement de trouver le parfait équilibre entre ces deux contraintes.

Fabriquer cette brique élémentaire n'est toutefois pas suffisant pour réaliser un ordinateur quantique performant. Pour améliorer la fiabilité et la performance de ce dernier, la solution la plus intuitive serait de réduire la probabilité qu'il commette des erreurs. Pour ce faire, la communauté scientifique a défini certaines métriques technologiques tels que le temps de vie de l'information quantique (T_1) ou le temps de cohérence (T_2) pour définir la qualité d'un qubit. Intrinsèquement, cela revient à comprendre puis supprimer les mécanismes non désirés interagissant avec notre système quantique. Ces temps caractéristiques ne sont autres que des limites temporelles réduisant le nombre d'opérations réalisables avant de perdre l'information quantique. Elles sont bien sûr à mettre au regard du temps nécessaire pour manipuler l'information (T_R), si l'on veut quantifier l'efficacité de la machine ($Q = T_2/T_R$). En parallèle, l'ingénierie de portes logiques quantiques de grande qualité (Fidelité excédant $> 99\%$) a pour but de supprimer les erreurs introduites par l'expérimentateur. Bien que l'amélioration des métriques des qubits sont en constante évolution, il existe un second moyen d'optimiser l'efficacité des ordinateurs quantiques. A l'instar de son homologue classique, le code de correction d'erreur permet, durant un calcul, de corriger les erreurs indésirables. De fait, la notion de ''qubit logique" émerge comme un ensemble de ''qubit physique" dont les interactions créent un homologue dont toutes les erreurs sont supprimées. Par conséquence, un très grand nombre d'éléments quantiques sont nécessaire pour atteindre un seuil de tolérance d'erreur pour un processeur quantique, ce qui est, pour le moment, est bien au-delà de nos espérances les plus folles. Toutefois, cette thèse s'inscrit dans la première problématique, c'est-à-dire la réalisation d'un qubit performant, dont les caractéristiques seront étudiées en détail.

Le type de support de l'information quantique (''qubit physique") peut être quasiment infini. Il faut imaginer l'évolution d'une technologie comme un arbre qui croît. A tout instant, de nouvelles branches naissent, se développent puis meurent, renforçant la structure globale de l'ensemble. Beaucoup de ces chemins technologiques conduisent à un une voie sans issue, mais le développement de ces solutions n'est pas pour autant une perte de temps. Parmi les technologies les plus prometteuses pour le moment, on retrouve les supraconducteurs, éléments phares de la discipline tant sur le plan académique qu'industriel. Loin derrière

siègent les technologies à base de photon, et bien sûr les spins sous de nombreuses variantes (boite quantique, atome accepteurs, centre Nv). En particulier, les spins d'électrons et de trous piégés à l'intérieur de boite quantique au sein des structures cristallines de silicium et germanium bénéficient du support de l'industrie des semi-conducteurs. Comparés à d'autres matériaux, leur faible empreinte spatiale, l'abondance des éléments, la pureté des matériaux qui peuvent être débarrassés de leur isotopes possédant des spins délétères, sont les principaux avantages les rendant d'excellents outsiders dans la course à l'ordinateur quantique.

Mais avant d'aborder les bits quantiques de spin, intéressons-nous à leur homologue de charge, apparus plus tôt car plus simple à réaliser. La démonstration technologique en 1986, de la première boite quantique (GaAs) [1] permet d'isoler un nombre fini de charge dans un puit de potentiel se comportant comme un atome artificiel[2]. Ces structures factices sont couramment utilisées pour produire des LEDs, des lasers [3], des émetteurs de photon unique [4], et bien d'autres. Le fait que la charge soit piégée dans une région de l'espace limitée peut être utilisé pour encoder une information quantique, ce qui a conduit à la réalisation de qubits de charge [5, 6]. Toutefois, l'ultra sensibilité au bruit de charge environnant, dans les structures semi-conductrices cristallines, sont pour le moment rédhibitoire [7], même si la réalisation récente d'une surface solide de néon semble prometteuse [8]. En sus de la charge, le spin d'un électron peut aussi servir de support à l'information quantique [9, 10, 11]. Les dispositifs en GaAs ont rapidement été limité par le trop grand nombre de spin nucléaires tandis que les réalisations en silicium purifié, plus prometteuses, [12, 13] nécessitent des lignes de contrôle magnétique qui sont peu évolutives et flexibles. C'est dans ce contexte que les qubits de trou sont apparus en alliant théoriquement le meilleur de ces deux mondes.

L'engouement des qubits de trou dans le silicium comme support de l'information quantique est extrêmement récente. Il provient principalement d'une démonstration de concept en 2016 sur une plateforme quasi-industrielle[14]. Leur plus grande force provient de la propriété intrinsèquement modulable de couplage spin-orbit [15, 16, 17, 18, 19, 20], permettant un contrôle entièrement électrique de l'état de spin. Associé à cela, la démonstration de temps de vie et de cohérence très long font les grands jours de cette technologie. Toutefois, de nombreuses questions restent en suspens, auxquelles nous essayerons d'apporter des prémices de réponse dans cette étude. En particulier, nous aborderons les sujets de la modularité du couplage spin-orbit ainsi que les différentes sources de bruit affectant l'information quantique dans ces dispositifs. De plus, à l'aide de nos résultats, nous établirons le fait qu'il existe un formalisme simplifié, particulièrement efficace, permettant de décrire les qubits de trou dans le silicium ouvrant la voie à de l'ingénierie sur le design géométrique des échantillons.

Pour répondre aux questions précédemment soulevées, ce manuscrit se décompose en sept chapitres. Après une description détaillée de la théorie des sys-

tèmes quantiques a deux niveaux, le **chapitre 2** fait aussi l'état des lieux des trous dans le silicium, en introduisant un formalisme simplifié développé par nos équipes théoriques. Le **chapitre 3** s'articule autour des dispositifs nécessaires pour conduire nos expériences, allant des réfrigérateurs à dilution aux instruments de mesure placé à température ambiante. Par la suite, nous introduisons le travail préliminaire (**chapitre 4**) réalisé sur l'échantillon afin de réaliser une lecture de spin unique, jusqu'alors jamais implémenté dans notre laboratoire. Subséquemment, le **chapitre 5** se concentrent quant à lui sur les mesures des métriques technologiques liées à la performance des bits quantiques ainsi que leur facteur les limitants à basse et haute fréquence. Ce chapitre traite en particulier des temps de cohérence, avec la démonstration de l'existence de point de fonctionnement, précédemment théorisés, limitant le bruit de charge. Enfin, avant de proposer une conclusion (**chapitre 7**) sur l'ensemble des travaux réalisés, le **chapitre 6** explore le spectre de bruit fréquentiel, outil de caractérisation des différentes perturbations affectant le qubit pour en déterminer les sources. Cette étude est conduite sur plus de 14 ordres de grandeur, à l'aide de différentes techniques, parfois innovantes mais surtout particulièrement complémentaires.

Chers lecteurs, gardez toutefois à l'esprit que ce manuscrit n'est qu'un bourgeon, d'une petite branche. Et j'espère, qu'avec la contribution de chacun, un bel arbre émergera de cet ensemble. Retenez que ce bref passage par l'histoire montre que l'ordinateur classique et performant que nous connaissons aujourd'hui est le fruit d'un long processus de murissement. L'ordinateur quantique n'est encore qu'à ses balbutiements et le temps sera son plus précieux allié.

1.2 English version

Although the expression "quantum computer" seems to be so trivial that popular science media use it indiscriminately, it is in fact much more complex. If we dissect the expression, it is composed of two terms that do not seem to have an obvious link. On the one hand, the computer, a deterministic object of everyday life, which constantly reproduces the same actions to reach the same conclusions. On the other, the increasingly understood but unpredictable world of quantum physics. At this infinitely small scale, the behavior of objects has a fundamental randomness. In fact, how can you imagine, for example, saving information if the moment you put your eyes on it, it is completely modified. With the quantum computer, the dream of the scientific community would be to tame the strange absurdity of the quantum universe in order to build a revolutionary calculation tool. This thesis is devoted to the study of one of the technical solutions intended to design the basic unit of this new kind of computer. In order to understand the ins and outs of this research framework, let us put it in a long-term perspective of computing tools.

To get started, what is a computer? This generic name designates an electronic device that performs simple computational operations, also called algorithms. Following this first simple definition, everyone will recognize the myriad of devices that have become part of our lives: the office computer, of course, but also the computers embedded in our phones, watches, cars, etc. They are so ubiquitous that it has become impossible to name a field of activity where it does not have a predominant place. From communication to transportation, through medicine and even sports, this tiny element does everything faster and admittedly better than we do. The field of scientific research, in particular, has undergone an unprecedented evolution with the help of various simulation, data processing and data visualization tools. Etymologically, the French term for computer ("ordinateur ") refers to an adjective that has fallen into disuse, used to mean "that puts order into the world", which is not so far from a general definition of the modern computer. In short, the computer is at the heart of our modern world. But it was not always the little electronic chip we all know and, like all the technical objects we use daily, its current form is the result of a long and tumultuous evolution.

The computer was first theorized as a programmable computing tool by Charles Babbage in 1834. Semantically, programming defines a present action that impacts the future in a known way. In other words, a programmable tool executes a routine, leading to a previously determined solution. In fact, reproducing a program should theoretically lead to the same results. The computer thus appears as an aid, capable of modeling or solving problems, sometimes complex. However, we find in history traces of devices whose functioning is close to a computer but where programming is absent. Each action of these analogical simulators is predetermined by the laws of physics. The purpose of these measuring instruments is to simulate

another physical system governed by the same equations. Note here the use of the word simulator which differs from the term computer, and which can be seen as an ancestor of the latter. From this point of view, the oldest known computer would date from 87 BC, under the name of the Antikythera mechanism. This non-programmable simulator is none other than a bronze gear mechanism allowing to predict the date and time of lunar and solar eclipses. Not very useful you may say, and above all relatively cumbersome (it may remind you of the beginnings of the quantum computer).

It is finally Alan Turing's research that opens the way, in 1936, to the creation of a real programmable computer. Note that modern computers known as "Turing's" still bears his name. As it is often the case, it was during a war, in this case the Second World War, that research on computers made significant progress. The decryption of enemy communications pushed researchers to constantly improve their means of spying and analysis. Turing was particularly famous in this field since he actively contributed to the design of the Enigma machine, which played a major role in the conflict. Based on electromechanical (analog) technology, Enigma was used to encrypt and decrypt information. In 1947, a real technological revolution opened the way to a new era: John Bardeen, William Shockley, and Walter Brattain, researchers at Bell Laboratories, presented the very first solid-state transistor. This germanium object, made up of three gold-contacted electrodes, made it possible to easily control the current flowing through it, and it quickly became the basic building block of what would become the digital computer. The first logic gates, an essential element of Boolean algebra (1854), began to emerge little by little, leading to the first printed circuit in 1958, invented by Jack Kilby. Although initially made of germanium, high mobility electronics were quickly put aside in favor of silicon transistors. The latter is not only very abundant and has a native oxide (SiO2) whose properties are far superior to those of Germanium oxide. Indeed, (SiO2) is a very good electrical insulator and very simple to grow.

Since then, transistors have evolved exponentially. This dynamic was theorized by the engineer Gordon E. Moore based on observations he had made between 1959 and 1965. He suggested an extrapolation, which is abusively called Moore's law, according to which the number of transistors per unit area doubles every two years. To this day, this law has continued to hold true despite the obstacles. These improvements include reduced heat generation, better heat dissipation, cleaner silicon/SiO2 interfaces, higher clock frequencies and more. Although some pessimists have been predicting a slowdown for a few years now, research has always been able to renew itself to achieve electronic chips containing now more than fifty billion transistors, with an average footprint per element below 5nm. However we are inevitably approaching an absolute limit in transistor scaling. Indeed, the drastic size reduction of transistors leads to a paradigm shift: the emergence of quantum effects, which is probably one of the biggest challenges to come. But, behind every

drawback lies an advantage.

Recently theorized (1980),a quantum computer tends to take advantage of quantum physics to conduct simulations, but this time of another kind. Before going further in the description of the functioning of these computers, let us make a comparison, necessarily reductive, in order to imagine how these computers create a break in the history we have just described. Its founding father, Feynman, described it in his opening speech at the first conference dedicated to quantum computing (1981), as an exact simulator of quantum physics, a task that is impossible to achieve for a classical computer. But more than a quantum simulator, it is indeed possible to create a quantum computer with its own algorithms. Imagine that you only have addition as a mathematical tool, then a quantum computer would be the multiplication. You would not see the world in the same way. Sometimes a problem will be simpler, sometimes more complicated. The change in the algebra underlying the calculations opens up new avenues of research, the implications of which are both unknown and potentially revolutionary. Some quantum algorithms already have a prominent place in the future of the quantum computer (Shor), while others are like UFOs as their results seem to go against the postulates of classical physics (Grover). The real strength of the quantum computer probably lies in its complementarity with a classical computer. As long as there will be non-deterministic mathematical problems in polynomial time (NP complexity), the two facets of physics, coupled with ingenious algorithms, will bring new solutions to the resolution of certain types of problems.

In order to distinguishes quantum computers from the ones we use every day, let us look at what constitutes the basic unit of these technical tools. The smallest component of a quantum computer is a quantum bit (Qubit). Unlike a classical transistor with two outcomes, open (1) and closed (0), a qubit can be both at the same time. This physical property called "quantum superposition" is one of the two major ingredients. The second one is the entanglement of several quantum elements, implying that any action performed on one of them has instantaneous repercussions on the others. A simple recipe on paper, but extremely difficult to achieve in reality. Indeed, quantum information is extremely sensitive, which requires a great effort to reduce the interaction between a qubit and the outside world. Unfortunately, just like a classical transistor, a qubit also needs to be controlled, which paradoxically implies an interaction with environment. The difficulty is therefore to isolate the system from unwanted external perturbations (noise), while maintaining the ability to interact with it (control). The main challenge is undoubtedly to find the perfect balance between these two constraints.

However, making a qubit is not enough to make a powerful quantum computer. To improve the reliability and performance, the most intuitive solution would be to reduce the probability of making errors. To do this, the scientific community has defined certain technological metrics such as the lifetime of the quantum in-

formation (T_1) or the coherence time (T_2) which define the quality of a qubit. Intrinsically, this means understanding and removing unwanted mechanisms interacting with our quantum system. These characteristic times are effectively temporal limits reducing the number of operations that can be performed before losing the quantum information. They are of course to be set against the time needed to manipulate the information (T_R), giving a way to quantify the efficiency of the whole machine ($Q = T_2/T_R$). In parallel, the engineering of high quality quantum logic gates (typically with fidelities $> 99\%$) aims at eliminating the errors introduced by the experimenter.

Although qubit metrics is continuously improving, there is a second way to optimize the efficiency of quantum computers. Like its classical counterpart, the error correction code allows, during a calculation, to correct undesirable errors. In fact, the notion of "logical qubit" emerges as a set of "physical qubits" whose interactions create a counterpart where all errors are removed. Consequently, a very large number of quantum elements are necessary to reach an error tolerance threshold for a quantum processor, which is, for the moment, far beyond our wildest expectations. However, this thesis is in line with the first problematic, i.e. the realization of a high-performing qubit, whose characteristics will be studied in detail.

The type of platform for quantum information ("physical qubit") can be almost infinite. One must imagine the evolution of a technology as a growing tree. At any moment, new branches are born, develop and die, reinforcing the global structure of the tree. Many of these technological paths lead to a dead end, but the development of these solutions is not a waste of time. Among the most promising technologies, superconductors are for instance the flagship of the discipline in both academic and industrial terms. Far behind are photon-based and spin-based technologies in many variants (quantum dots, acceptors, NV centers). In particular, electrons and holes spin trapped inside quantum dots within silicon and germanium crystal structures are supported by the semiconductor industry. Compared to other devices, their small spatial footprint, the abundance of elements, the purity of the materials which can be stripped of their isotopes possessing deleterious spins, are the main advantages making them excellent outsiders in the quantum computer race.

But before tackling spin quantum bits, let us look at their charge counterpart, which appeared earlier because they were simpler to implement. The technological demonstration in 1986 of the first quantum dot (GaAs) [1] allowed the isolation of a finite number of charges in a quantum well behaving like an artificial atom. These artificial structures are commonly used to produce LEDs, lasers [3], single photon emitters [4], and many others. The fact that a charge is trapped in a limited region of space can be used to encode quantum information, leading to the realisation of charge qubits [5, 6]. However, the ultra-sensitivity to the surrounding

charge noise in crystalline semiconductor structures is for the moment prohibitive [7], even if the recent realisation of a solid surface of neon seems promising [8]. In addition to the charge, the spin of an electron can also serve as a medium for quantum information [9, 10, 11]. GaAs devices were quickly limited by the large number of nuclear spins while the more promising purified silicon realizations still require magnetic control lines that are not very scalable and flexible. It is in this context that hole spin qubits have emerged, theoretically combining the best of both worlds.

The hype of hole-spin qubits in silicon as a qubit is extremely recent. It mainly comes from a proof-of-concept in 2016 on a near-industrial CMOS platform[14]. Their greatest strength comes from the intrinsically quasi fully tunable spin-orbit coupling, allowing all electrical control of the spin state[15, 16, 17, 18, 19, 20] . Combined with this, the demonstration of very long spin lifetime and coherence time are also promising factors. However, many questions remain unanswered, which we explore in this manuscript. In particular, we will address the tunability of the spin-orbit coupling as well as the different sources of noise affecting the quantum information in these devices. Furthermore, we will establish that there is a simplified formalism, particularly efficient, to describe hole spin qubits in silicon, opening the way to engineering new sample design.

To answer the questions raised above, this manuscript is divided into seven chapters. After a detailed description of the theory of two-level quantum systems, **Chapter 2** also gives an overview of holes in silicon, introducing a simplified formalism developed by our theoretical team. **Chapter 3** focuses on the setup needed to conduct our experiments, including dry dilution refrigerators and room temperature measuring instruments. Then, we introduce (**Chapter 4**) the preliminary work carried out on the sample in order to realize a single shot spin readout, never before implemented in our laboratory. Subsequently, **Chapter 5** focuses on the measurement of technological metrics related to the performance of qubits and their limiting factors at low and high frequencies. This chapter deals in particular with coherence times, with the demonstration of the existence of previously theorized operating sweet spots, which are mitigating charge noise detrimental effect. Finally, before proposing a conclusion (**chapter 7**) on all the work carried out, **chapter 6** explores the frequency noise spectrum, a tool for characterizing the various disturbances affecting the qubit in order to determine their sources. This study is conducted over more than 14 orders of magnitude, using different techniques, sometimes innovative but above all particularly complementary.

However, keep in mind that this manuscript is only a bud, of a small branch. I personally hope, with the contribution of each one, that a beautiful tree will emerge from this research field. Keep in mind that this brief passage through history shows that the classical and powerful computer that we know today is the result of a long process of maturation. The quantum computer is still in its infancy

and time will be its most precious ally.

References

[1] M. A. Reed et al. « Spatial quantization in GaAsAlGaAs multiple quantum dots ». In: *Journal of Vacuum Science & Technology B: Microelectronics Processing and Phenomena* 4.1 (1986), pp. 358–360. DOI: 10.1116/1.583331. eprint: https://avs.scitation.org/doi/pdf/10.1116/1.583331. URL: https://avs.scitation.org/doi/abs/10.1116/1.583331.

[2] R. C. C. Leon et al. « Coherent spin control of s-, p-, d- and f-electrons in a silicon quantum dot ». In: *Nature Communications* 11.1 (Feb. 2020), p. 797. ISSN: 2041-1723. DOI: 10.1038/s41467-019-14053-w. URL: https://doi.org/10.1038/s41467-019-14053-w.

[3] D. L. Huffaker et al. « 1.3 um room-temperature GaAs-based quantum-dot laser ». In: *Applied Physics Letters* 73.18 (1998), pp. 2564–2566. DOI: 10.1063/1.122534. eprint: https://doi.org/10.1063/1.122534. URL: https://doi.org/10.1063/1.122534.

[4] Peter Lodahl, Sahand Mahmoodian, and Søren Stobbe. « Interfacing single photons and single quantum dots with photonic nanostructures ». In: *Rev. Mod. Phys.* 87 (2 May 2015), pp. 347–400. DOI: 10.1103/RevModPhys.87.347. URL: https://link.aps.org/doi/10.1103/RevModPhys.87.347.

[5] J. Gorman, D. G. Hasko, and D. A. Williams. « Charge-Qubit Operation of an Isolated Double Quantum Dot ». In: *Phys. Rev. Lett.* 95 (9 Aug. 2005), p. 090502. DOI: 10.1103/PhysRevLett.95.090502. URL: https://link.aps.org/doi/10.1103/PhysRevLett.95.090502.

[6] Zhan Shi et al. « Coherent quantum oscillations and echo measurements of a Si charge qubit ». In: *Physical Review B* 88.7 (Aug. 2013). DOI: 10.1103/physrevb.88.075416. URL: https://doi.org/10.1103%2Fphysrevb.88.075416.

[7] Anasua Chatterjee et al. « Semiconductor qubits in practice ». In: *Nature Reviews Physics* 3.3 (Mar. 2021), pp. 157–177. ISSN: 2522-5820. DOI: 10.1038/s42254-021-00283-9. URL: https://doi.org/10.1038/s42254-021-00283-9.

[8] Xianjing Zhou et al. « Single electrons on solid neon as a solid-state qubit platform ». In: *Nature* 605.7908 (May 2022), pp. 46–50. ISSN: 1476-4687. DOI: 10.1038/s41586-022-04539-x. URL: https://doi.org/10.1038/s41586-022-04539-x.

[9] F. H. L. Koppens et al. « Driven coherent oscillations of a single electron spin in a quantum dot ». In: *Nature* 442.7104 (2006), pp. 766–771. ISSN: 1476-4687. DOI: 10.1038/nature05065. URL: https://doi.org/10.1038/nature05065.

[10] F. H. L. Koppens, K. C. Nowack, and L. M. K. Vandersypen. « Spin Echo of a Single Electron Spin in a Quantum Dot ». In: *Physical Review Letters* 100 (23 June 2008), p. 236802. DOI: 10.1103/PhysRevLett.100.236802. URL: https://link.aps.org/doi/10.1103/PhysRevLett.100.236802.

[11] Jarryd J. Pla et al. « A single-atom electron spin qubit in silicon ». In: *Nature* 489.7417 (2012), pp. 541–545. ISSN: 1476-4687. DOI: 10.1038/nature11449. URL: https://doi.org/10.1038/nature11449.

[12] R. Zhao et al. « Single-spin qubits in isotopically enriched silicon at low magnetic field ». In: *Nature Communications* 10.1 (2019), p. 5500. ISSN: 2041-1723. DOI: 10.1038/s41467-019-13416-7. URL: https://doi.org/10.1038/s41467-019-13416-7.

[13] Jun Yoneda et al. « A quantum-dot spin qubit with coherence limited by charge noise and fidelity higher than 99.9% ». In: *Nature Nanotechnology* 13.2 (2018), pp. 102–106. ISSN: 1748-3395. DOI: 10.1038/s41565-017-0014-x. URL: https://doi.org/10.1038/s41565-017-0014-x.

[14] R. Maurand et al. « A CMOS silicon spin qubit ». In: *Nature Communications* 7.1 (2016), p. 13575. ISSN: 2041-1723. DOI: 10.1038/ncomms13575. URL: https://doi.org/10.1038/ncomms13575.

[15] Stefano Bosco and Daniel Loss. « Fully Tunable Hyperfine Interactions of Hole Spin Qubits in Si and Ge Quantum Dots ». In: *Physical Review Letters* 127 (19 Nov. 2021), p. 190501. DOI: 10.1103/PhysRevLett.127.190501. URL: https://link.aps.org/doi/10.1103/PhysRevLett.127.190501.

[16] Stefano Bosco and Daniel Loss. *Hole spin qubits in thin curved quantum wells*. 2022. DOI: 10.48550/ARXIV.2204.08212. URL: https://arxiv.org/abs/2204.08212.

[17] Stefano Bosco, Bence Hetényi, and Daniel Loss. « Hole Spin Qubits in Si FinFETs With Fully Tunable Spin-Orbit Coupling and Sweet Spots for Charge Noise ». In: *PRX Quantum* 2 (1 Mar. 2021), p. 010348. DOI: 10.1103/PRXQuantum.2.010348. URL: https://link.aps.org/doi/10.1103/PRXQuantum.2.010348.

[18] Vincent P. Michal, Benjamin Venitucci, and Yann-Michel Niquet. « Longitudinal and transverse electric field manipulation of hole spin-orbit qubits in one-dimensional channels ». In: *Physical Review B* 103 (4 Jan. 2021), p. 045305. DOI: 10.1103/PhysRevB.103.045305. URL: https://link.aps.org/doi/10.1103/PhysRevB.103.045305.

[19] V. P. Michal et al. *Tunable hole spin-photon interaction based on g-matrix modulation*. 2022. DOI: 10.48550/ARXIV.2204.00404. URL: https://arxiv.org/abs/2204.00404.

[20] Benjamin Venitucci and Yann-Michel Niquet. « Simple model for electrical hole spin manipulation in semiconductor quantum dots: Impact of dot material and orientation ». In: *Physical Review B* 99 (11 Mar. 2019), p. 115317. DOI: 10.1103/PhysRevB.99.115317. URL: https://link.aps.org/doi/10.1103/PhysRevB.99.115317.

Chapter 2

Theory & mathematical tools

"It doesn't matter how beautiful your theory is, it doesn't matter how smart you are. If it doesn't agree with experiment, it's wrong."

Richard Feynman

The theory of quantum mechanics emerged following the first experiments whose results were in disagreement with classical mechanics. Between 1880 and 1900, the ultraviolet catastrophe cannot be explained by any classical theory and pushed physicists to change their vision of the world. This is why, at the end of the century, Max Planck proposed the idea that any atomic system radiating energy can be divided into discrete "energy elements" (Nobel Prize 1918). This quantification of energy, very quickly demonstrated experimentally by Einstein (which also earned him a Nobel Prize in 1921), laid the first brick of quantum physics. The notion of wave-particle duality then led Erwin Schrödinger to write one of the most famous equations and probably one of the most used theoretically: the Schrödinger equation. However, classical computers are very quickly outdated for the resolution of this equation as soon as several elements interact with each other, leading to many simplifications of the problem. In this chapter, we first discuss the way to isolate a hole spin in silicon, one of the proposals as a basic element for a qubit. The second section summarizes the physics of a two-level system, such as an electron spin. Then, we introduce the interaction of holes with electromagnetic fields, inside a silicon crystal structure. In particular, the strong spin-orbit coupling is a relativistic interaction that both complicates the problem and gives the hole qubit a major advantage. The next section focuses on the g-matrix formalism which simplifies the previous problem to a more easily simulated two-level system (Pseudo-spin). Then, we sum up the two main noise contributions which degrade the qubit properties. Finally, the last section of this chapter proposes some useful

mathematical tools to understand the results of this thesis.

Contents

2.1 Quantum dots . . . 35
2.1.1 Single quantum dot . . . 35
2.1.2 Double quantum dot . . . 37
2.2 One half Spin based qubits (General case) . . . 38
2.2.1 Larmor precession . . . 39
2.2.2 Spin rotation in the Rotating Wave Approximation (RWA) . . . 40
2.2.3 Spin relaxation and dephasing . . . 42
2.3 Hole spin qubit in Silicon . . . 44
2.3.1 Simplest valence band description . . . 44
2.3.2 Spin-orbit coupling . . . 45
2.3.3 Zeeman splitting . . . 49
2.4 G-matrix formalism . . . 50
2.4.1 Rotation transformation . . . 51
2.4.2 The Zeeman tensor . . . 51
2.4.3 Spin driving mechanisms . . . 52
2.5 Noise sources acting on hole spin qubits . . . 56
2.5.1 Hyperfine interaction . . . 56
2.5.2 Electrical noise . . . 58
2.5.3 High frequency : Jonhson Nyquist Noise . . . 62
2.6 Power spectral density . . . 64
2.6.1 Fourier transform Definition . . . 64
2.6.2 PSD from Fourier transform . . . 66
2.6.3 PSD from signal autocorrelation . . . 67
2.6.4 Noise color . . . 68
References . . . 74

2.1 Quantum dots

A quantum dot (QD) is an artificial 0-dimension structure which confines charges (positive : holes or negative : electrons) within a small volume (few nanometers in size). Spatial confinement enables the discretization of energy levels in the QD, necessary ingredient for a precise control over the charge occupation. QD filling is possible via charge exchange with nearby reservoirs. The exchange rate is mainly controlled by tunnel barriers height and width. Experimentally, the QD can be capacitively coupled to gate electrodes, which aim at modifying its local electrostatic environment. In case of holes, applying a negative voltage on the gate would increase the charge population inside the dot. Because QDs is a general concepts, it has been implemented in various physical structure, namely two-dimensional electron gas (GaAs [1], SiGe [2] hetero-structures), nanocrystals, single molecule, nanowires [3].

Today, QDs stand for an elementary building block in the scope of spin-based quantum information. As a matter of fact, when filled with a few charges, QDs may be operated as spin qubit. Understanding spin physics, especially in terms of holes, is therefore one of the topmost subject in order to possibly engineer quantum computers.

2.1.1 Single quantum dot

We consider a single quantum dot connected to two reservoirs on both sides (source and drain) and electrostatically controlled by a plunger gate, as depicted in Fig. 2.1-a. The population in the QD is stable depending on two major effects. On the one hand, the Coulomb repulsion that quantifies the force between charged particles bring close together. In other words, adding a charge in the system is energetically unfavorable. This extra-energy is called charging energy and is denoted Ec. In particular, if thermal fluctuations are smaller than the charging energy $k_bT << E_c$, then tunneling between the reservoir and the dot is forbidden : the QD population remains unchanged. For low enough temperatures, the system is therefore in a Coulomb blockade configuration. On the other hand, the confinement in all spatial directions leads to additional quantum effects that increase when the dot size decreases. The energy level spacing is bigger and adding a charge is even more difficult (orbital energy : E_{orb}), thus favoring stability in the number of charge. The pattern for the discrete levels of energy in QDs reassembles in many ways as artificial atoms [4, 5, 6].

We introduce the electrochemical potential $\mu(N)$ as the difference of two consecutive energy levels in the dot ($\mu(N) = U(N) - U(N-1)$). Here N denotes the QD number of charges. Consequently, the energy to add the N^{th} charge into the dot is $E_{add}(N) = E_C + \Delta E$, stemming from the sum of charging energy and additional energy spacing. In the constant interaction model, the charging energy

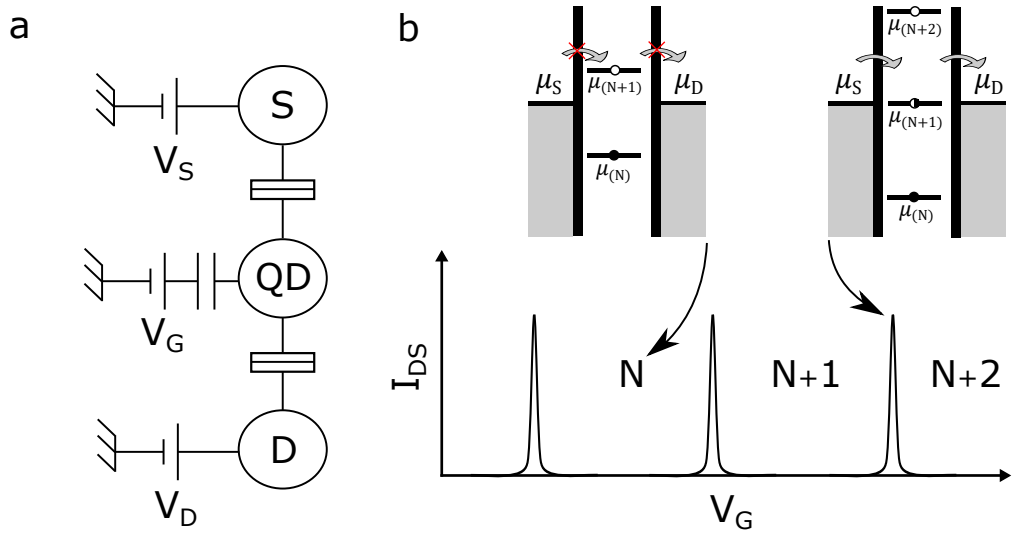

Figure 2.1 – **Single quantum dot in gated semiconductor. (a)** Electrical schematic circuit of a single quantum dot connected to source and drain and capacitively coupled to a plunger gate (V_G). **(b)** Current through the quantum dot measured as a function of the voltage applied on the gate. First schematic shows the QD in a Coulomb blockade regime, the number of charge is stable and no current flows because the chemical potential level is misaligned with the reservoir levels. In the second schematic, the chemical potential of the QD stands the bias windows ($\mu_S - \mu_D$). Consequently, charges go one by one through the QD, resulting in a measurable current.

stands for a purely electrostatic contribution as $E_c = e^2/C$, with $C = \sum_i C_i$, the sum of all capacitances connected to the dot. The term ΔE takes into account confinement, spin contribution, valley for electrons etc... Note that, by definition, the chemical ladder is linearly depending on the gate voltage whereas the energy has a quadratic dependence [7]. Consequently, tuning the gate voltage on the dot displaced the μ-ladder as a whole, while keeping the energy spacing constant.

Fig 2.1 resumes the single QD behavior. The coulomb blockade regime appears, at low temperature when the chemical potential ladder is misaligned with the Bias windows (top left schematic). Conversely, charges can flow through the dot under the alignment condition. In the case of a single reservoir connected to a QD, a resonant phenomenon emerges as the charge goes back and forth from the dot to the reservoir. Additionally, be aware that Fig 2.1-b (bottom) depicts a perfect metallic QD. In case of semiconductors SQD, the height and width of the picks are greatly modulated by the shape of the tunnel barrier.

2.1.2 Double quantum dot

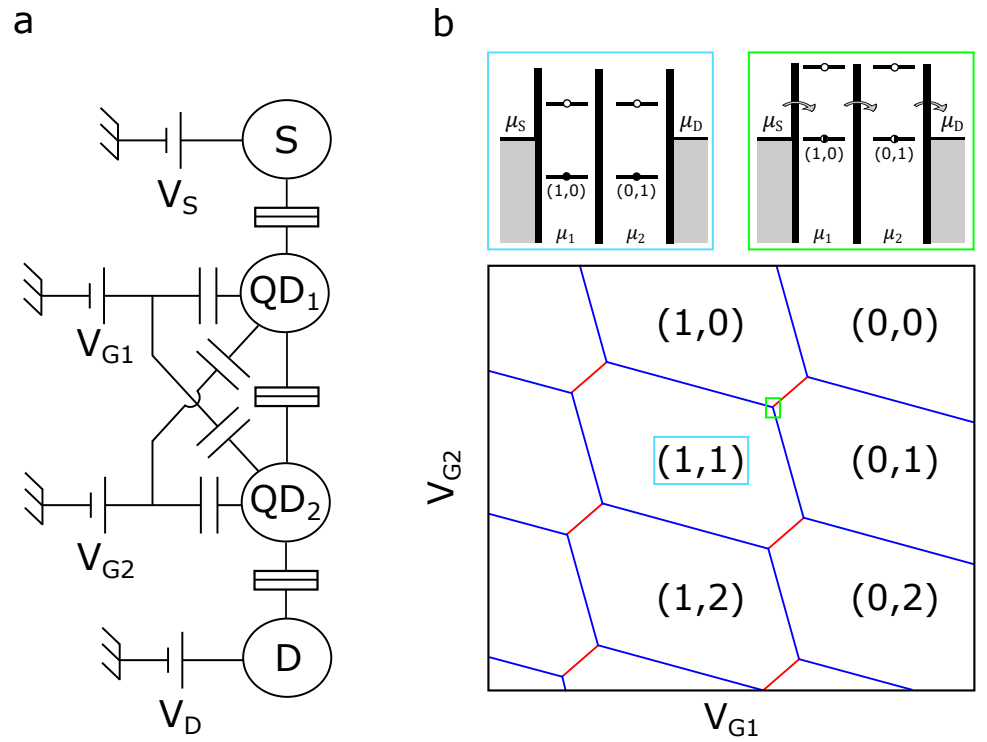

Figure 2.2 – **Double quantum dot. (a)** Electrical schematic circuit of mutual coupled double quantum dot connected to source and drain. **(b)** Honey comb pattern for a perfect DQD. Numbering indicates number of holes trapped in each QD. Blue region represents both dot in a Coulomb blockade regime with a single hole in each dot. Green region is a triple point where current flows through the device.

Adding a second QD in series with the first one complicates the global picture, especially due to the mutual coupling between the two dots. Indeed, when QDs are capacitively coupled, the addition of a charge inside one of the QD slightly changes the electrostatic energy of the other QD. In addition, gates also have a non-zero cross-talk, which may be almost perfectly compensated afterwards thanks to virtual gates [8, 9, 10]). Fig. 4.5-a presents the equivalent electrical circuit with two coupled quantum dots in series connected on both sides to source and drain. Each quantum dot can be in equilibrium with its given number of charge (N_1 for QD1 and N_2 for QD2). The stability diagram presented in Fig. 4.5-b maps the number of holes in each QD in the twofold subspace (V_{G1}, V_{G2}). Lines with a negative slope (blue) represent a resonant behavior between a QD with a reservoir (almost horizontal lines are related to QD1, whereas vertical lines are related to QD2), highlighting the addition of a charge. Conversely, the line with a positive

slope (red), which appear only in the case of a coupled QDQ, embody resonant events occurring between the two dots. In this case, a charge flows from one dot to the other, meaning that their electrochemical potentials are aligned. This peculiar pattern for DQD is the so-called honeycomb pattern.

At the particular point where three lines meet (triple-point, green schematic in Fig. 4.5), three charge configurations is available, sign that all chemical potentials in the device are aligned. Consequently, transport through the double dot is enabled. Setting a voltage difference between the two reservoirs (creating a so-called bias window) would expand these triple-points into triangular-shaped regions [7] (sup inf S2/S3 of ref.[3]), in which Pauli spin blockade principle can be applied to perform parity readout [11, 12]. In the particular case where both quantum dots become too big, charge wave functions expand until having a certain overlap, thus resulting in a merging of the two dots. The system finally boils down to the previous case of a unique quantum dot, controlled by two different voltage gates with the same impact. Then, the honeycomb pattern becomes a grid of 45° lines with negative slope.

2.2 One half Spin based qubits (General case)

A quantum bit (qubit) represents a fundamental two-level system used as the basic unit for quantum processors. Nowadays, a wide range of physical implementations for qubit exists, among which superconducting platforms are acknowledged as the most developed and appealing ones. In 1998, Loss and DiVincenzo [13] first suggested an implementation of a universal set of quantum bit gates using the spin states of electrons (holes) trapped in QDs. As a matter of fact, the spin of an electron (fermion) can only take two distinct values (± 1/2), setting it as a theoretically perfect two-level system. The latter increases fidelity by avoiding leaking to other nearby quantum states.

$$i\hbar\frac{\partial}{\partial t}\left|\psi(t)\right\rangle = \hat{\mathcal{H}}\left|\psi(t)\right\rangle \tag{2.1}$$

The evolution of a quantum-mechanical system is governed by the Schrödinger equation (eq. 2.1), where $|\psi\rangle$ describes its wave function and $\hat{\mathcal{H}}$ represents the Hamiltonian which is an operator corresponding to the total energy of that system. If we respectively consider a $+1/2$ (-1/2) spin denoted as up-state $|\uparrow\rangle$ (down-state $|\downarrow\rangle$), the spin wavefunction may be written as the following (omitting a global phase factor):

$$|\psi(t)\rangle = \cos(\theta/2)\,|\downarrow\rangle + \sin(\theta/2)e^{i\phi}\,|\uparrow\rangle \tag{2.2}$$

One would recognize that the spin state can be mapped on a spherical coordinate system where θ and ϕ respectively represents the polar and azimuthal angles. The total radius is always equal to 1 (renormalization of the probability amplitude). The geometrical representation is the so-called Bloch sphere, named after the physicist Felix Bloch. Note that the poles are stationary states (energy eigenvectors). Moreover, points on the surface of the sphere correspond to the pure states of the system, whereas the interior points correspond to mixed states. One tricky additional point is that the sphere does not catch entirely the physic of the system. Indeed, applying a 2π pulse on a spin should on the Bloch sphere bring the system back into its initial position. Practically, it adds a global phase of π (Dirac's belt trick for spin 1/2 particle).

2.2.1 Larmor precession

A particle with a spin possesses a non zero magnetic moment, and thus transfer of energy with surrounding magnetic field occurs. Considering a uniform magnetic field B_0, along the $\vec{z}$ axis, the Hamiltonian describing the system may be written as:

$$\mathcal{H}_0 = \omega_L \mathcal{S}_z = \begin{bmatrix} \hbar\omega_L/2 & 0 \\ 0 & -\hbar\omega_L/2 \end{bmatrix} \tag{2.3}$$

Here $\mathcal{S} = \hbar/2\boldsymbol{\sigma}$ represents the Pauli matrices, and $E_z = \hbar\omega_L = hf_L = g\mu_B B_0$ is the Zeeman energy. Since the Hamiltonian is independent of time, solving the Schrödinger equation (2.1) means searching for the stationary states of the system. Concretely, we look for the eigenvectors of the Hamiltonian denoted as $\{|\uparrow\rangle, |\downarrow\rangle\}$ [I] :

$$\begin{cases} \mathcal{H}_0\,|\uparrow\rangle = +\dfrac{hf_L}{2}\,|\uparrow\rangle \\ \mathcal{H}_0\,|\downarrow\rangle = -\dfrac{hf_L}{2}\,|\downarrow\rangle \end{cases} \tag{2.4}$$

A static magnetic field therefore lifts the spin degeneracy by the Zeeman energy (difference in eigenvalues equal to E_z). In addition, if we now consider the

I. $\{|\uparrow\rangle, |\downarrow\rangle\}$ form an orthonormal basis of S_z and S^2, such that $\langle\uparrow \mid \downarrow\rangle = 0$ and $\langle\uparrow \mid \uparrow\rangle = \langle\downarrow \mid \downarrow\rangle = 1$, where $\langle\cdot\rangle$ represents the scalar product.

time-dependence of the states, prepared in any initial condition (eq. 2.2), the system evolution is (solving eq. 2.1) :

$$|\psi(t)\rangle = \cos(\theta/2)e^{-\frac{iE_z t}{\hbar}}|\downarrow\rangle + \sin(\theta/2)e^{i\phi}|\uparrow\rangle \tag{2.5}$$

Consequently, static magnetic field does not change the initial admixture of states, but the system picks a relative phase over time. Concretely, the spin rotates about the $\vec{z}$ axis at the Larmor frequency f_L, proportional to the magnetic field amplitude B_0.

2.2.2 Spin rotation in the Rotating Wave Approximation (RWA)

Adding a small, oscillating perturbation (at angular frequency ω_d), perpendicular to the static magnetic field, in the form of $\boldsymbol{B}_\perp(t) = \boldsymbol{B}_\perp \cos(\omega_d t + \phi)$ (the term $\boldsymbol{B}_\perp$ refers to a magnetic field purely orthogonal to $\boldsymbol{B}_0$) can change the spin state over time. The wave function of the system may be written, in a general case, as :

$$|\psi(t)\rangle = a_\uparrow(t)|\uparrow\rangle + a_\downarrow(t)|\downarrow\rangle \tag{2.6}$$

In addition, the new Hamiltonian of the system is then :

$$\hat{\mathcal{H}}(t) = \mathcal{H}_0 + \hat{\mathcal{H}}_{pert}(t) = \frac{g\mu_B}{\hbar}\mathcal{S}\cdot[\mathbf{B}_0 + \mathbf{B}_\perp(t)] \tag{2.7}$$

We define $\hbar\omega_{R_0} = g\mu_B|B_{pert}|$ in order to develop the previous equation and we obtain [II] :

$$\hat{\mathcal{H}}(t) = \omega_L\mathcal{S}_z + \omega_{R_0}[\cos(\omega_d t)\mathcal{S}_x + \sin(\omega_d t)\mathcal{S}_y] \tag{2.8}$$

Corresponding in the $\{|\uparrow\rangle,|\downarrow\rangle\}$ basis to the Hamiltonian :

II. Here we intentionally suppressed the phase ϕ, which correspond to a rotation of $(\mathcal{S}_x,\mathcal{S}_y)$.

$$\hat{\mathcal{H}}(t) = \frac{\hbar}{2}\begin{bmatrix} \omega_L & \omega_{R_0} e^{-i\omega_d t} \\ \omega_{R_0} e^{+i\omega_d t} & -\omega_L \end{bmatrix} \tag{2.9}$$

Using the Schrödinger equation (2.1), we obtain two coupled equations :

$$\begin{cases} i\dfrac{d}{dt}a_\uparrow(t) = +\dfrac{\omega_L}{2}\, a_\uparrow(t) + \dfrac{\omega_{R_0}}{2} e^{-i\omega_d t}\, a_\downarrow(t) \\ i\dfrac{d}{dt}a_\downarrow(t) = -\dfrac{\omega_L}{2}\, a_\downarrow(t) + \dfrac{\omega_{R_0}}{2} e^{+i\omega_d t}\, a_\uparrow(t) \end{cases} \tag{2.10}$$

Eq. 2.10 is a system of equations linear with time. The trick to solve them is to perform a variable change in the form of [14] :

$$\begin{cases} b_+(t) = e^{+i\omega_d t/2}\, a_\uparrow(t) \\ b_-(t) = e^{-i\omega_d t/2}\, a_\downarrow(t) \end{cases} \tag{2.11}$$

In particular, in the new basis, which correspond to the rotating frame, the Hamiltonian of the system is :

$$\hat{\mathcal{H}} = \frac{\hbar}{2}\begin{bmatrix} \omega_L - \omega_d & \omega_{R_0} \\ \omega_{R_0} & -(\omega_L - \omega_d) \end{bmatrix} \tag{2.12}$$

The new Hamiltonian is now time-independent (conservative system). Consequently, solving Schrödinger equation is much simpler. Note that the previous transformation is in fact $|\tilde{\psi}(t)\rangle = R(t)\,|\psi(t)\rangle$ where $R(t) = e^{i\omega_d t S_z/\hbar}$ is a unitary operator, corresponding to a change of basis and describing a rotation about the $\vec{z}$ axis, at the speed ω_d. After resolution of eq. 2.12, the probability to measure $|\uparrow\rangle$ is given by the Rabi formula [III]:

$$P_\uparrow(t) = \frac{\omega_{R_0}^2}{\omega_{R_0}^2 + \delta\omega^2} \sin^2\left(\sqrt{(\delta\omega)^2 + (\omega_{R_0})^2}\,\frac{t}{2}\right) \tag{2.13}$$

III. To recover the Rabi formula, one should solve the Schrödinger equation to access $|\psi(t)\rangle$ and then calculate $P_\uparrow(t) = |\langle\uparrow|\psi(t)\rangle|^2$

The generalized Rabi frequency (ω_R) of the system is then :

$$\omega_R = \sqrt{(\delta\omega)^2 + (\omega_{R_0})^2} \tag{2.14}$$

Where $\delta\omega = \omega_L - \omega_d$ is the detuning from the Larmor frequency. In the rotating frame, spin flips occur about an effective magnetic field $\mathbf{B}_{eff} = \frac{\hbar}{g\mu_B}(\delta\omega\ \vec{\boldsymbol{z}} - \omega_{R_0}\ \vec{\boldsymbol{x}})$. In particular, at the resonance $\omega_L = \omega_d$, the spin is perfectly flipped at a frequency ($f_R = \omega_{R_0}/2\pi$) proportional to the perturbation. In the lab frame, the spin spirals down over the Bloch sphere with a composite rotation.

Importantly, we only considered a transverse perturbation for the spin driving. If the driving is not perfect, the excitation term can be rewritten as $\mathbf{B}_1(t) = B_{\parallel}(t) \cdot \vec{\boldsymbol{z}} + B_{\perp}(t)\vec{\boldsymbol{x}}$, where $B_{\parallel}(t)$ accounts for small perturbations in the Larmor frequency. In the RWA approximation, the fast oscillating term is discarded as a second order perturbation, thus not changing the Rabi frequency of the system. In case anyone would still like to calculate the corrections, just follow Ref [15] (Supplementary information S2).

2.2.3 Spin relaxation and dephasing

Any two-level quantum system is undoubtedly interacting with its surrounding environment. Thus, coupling with noise disturb the qubit's quantum state in an uncontrolled manner that leads to loss of information. The latter is described in its easiest form by the Maxwell-Bloch equations and leads to exponential decay of the spin state (T_1) and of the phase (T_2). The density matrix for a half spin is ([16] Appendix A):

$$\rho = \begin{bmatrix} \rho_{\uparrow\uparrow} & \rho_{\uparrow\downarrow} \\ \rho_{\downarrow\uparrow} & \rho_{\downarrow\downarrow} \end{bmatrix} = \frac{1}{2}\begin{bmatrix} 1+s_z & s_x - is_y \\ s_x + is_y & 1-s_z \end{bmatrix} = \frac{1}{2}(1 + \mathbf{s}\cdot\boldsymbol{\sigma}) \tag{2.15}$$

Where $\rho = |\psi(t)\rangle\langle\psi(t)|$ gives a simple vision of the statistical mixture of states and $\boldsymbol{s}$ is the spin polarization. The density matrix exhibits particular properties such as hermiticity ($^t\rho = \rho$) and unitary trace ($Tr(\rho) = 1$).

Using an alternative parameterization, the Bloch equations read :

$$\frac{d}{dt}\rho_{\uparrow\uparrow} = -\Gamma_\uparrow \rho_{\uparrow\uparrow} + \Gamma_\downarrow \rho_{\downarrow\downarrow} = -(\Gamma_\uparrow + \Gamma_\downarrow)\rho_{\uparrow\uparrow} + \Gamma_\downarrow \tag{2.16}$$

Where $\Gamma_\uparrow$ is the transition rate from the ground state to the excited stated and $\Gamma_\downarrow$ the transition rate from the excited state to the ground stated. It yields to $1/T_1 = \Gamma_1 = \Gamma_\uparrow + \Gamma_\downarrow$ known as the Fermi's golden rule. Similarly, on the off diagonal term we find :

$$\frac{d}{dt}\rho_{\uparrow\downarrow} = -\left(\frac{\Gamma_\uparrow + \Gamma_\downarrow}{2} + \Gamma_\phi\right)\rho_{\uparrow\downarrow} = -\Gamma_2\,\rho_{\uparrow\downarrow} \tag{2.17}$$

Here Γ_ϕ represents the pure dephasing rate. If the latter is totally canceled like in the case of well designed super conducting qubits [17], then the spin life time automatically sets the upper limit for the decoherence so that $T_2 = 1/\Gamma_2 = 2\,T_1$.

The spin decays incoherently given two parameters in the original Bloch work :

— The longitudinal relaxation time T_1, correlated to the loss of information on the spin state due to the exchange of energy with the environment.

— The transversal relaxation time T_2, linked to the loss of information on the phase.

Any longitudinal noise coupled to the qubit introduces a random component $\delta\phi(t)$ to the qubit phase such as $\phi(t) = 2\pi f_L t + \delta\phi(t)$. After free evolution over time of the accumulated random phase, the random component reads at first order in the noise [18, 19] :

$$\delta\phi(t) = 2\pi \int_0^t dt'\,\delta f_L(t') \tag{2.18}$$

The pure dephasing is characterized by the decay of the off-diagonal element of the spin density matrix in the rotating frame [19] :

$$\langle\tilde{\rho}_{\downarrow\uparrow}\rangle(t) = \tilde{\rho}_{\downarrow\uparrow}(0)\langle e^{i\delta\phi(t)}\rangle = \tilde{\rho}_{\downarrow\uparrow}(0)e^{-\frac{1}{2}\langle\delta\phi^2(t)\rangle}\,, \tag{2.19}$$

Where $\langle\cdot\rangle$ denotes an ensemble average (over the random processes). Considering a Gaussian noise, it yields

$$\langle \delta\phi^2(t) \rangle = 4\pi^2 \int_{-\infty}^{+\infty} dt' \int_{-\infty}^{+\infty} dt'' \, \langle \delta f_L(t') \delta f_L(t'') \rangle \tag{2.20}$$

2.3 Hole spin qubit in Silicon

Hole spin trapped in silicon or germanium quantum dots exhibits a rich physics with notable properties. In the electronic bulk structure of those two materials, the valence band possesses, at the Γ point, four degenerate states with an angular momentum $J = 3/2$, constituting two sub-bands (upper-band : Heavy-Hole $J_z = 3/2$ (HH) and lower-band : Light-Hole $J_z = 1/2$ (LH)). These two bands are separated by the energy spin-orbital splitting (Δ_0) from the twofold $J = 1/2$ degenerated state. The latter sub-band, refereed as the split off band is energetically far away ($\Delta_0^{Si} = 44\,\text{meV}$, $\Delta_0^{Ge} = 300\,\text{meV}$) compared to the LH-HH level spacing, and thus is accounted for small correction, or even neglected, in many models . The states in the topmost valence band are properly described by the Luttinger-Kohn Hamiltonian [20]. In particular, the property of SOC is of great interest because it allows for very fast full electrical spin driving [3, 21, 22, 23]. This section aims at giving a very general description of bands in silicon devices. Then, focusing on the LH and HH manifold, we lift the spin degeneracy applying a static magnetic field to create a spin qubit.

2.3.1 Simplest valence band description

The electronic band structure allows to describe the energy states of electrons and holes in silicon. In particular, the valence bands (holes) have an energy minimum at the Γ point, a key point for the accumulation of the first charges in a QD. Considering bulk material with no spin orbit coupling, valence band in silicon possesses three bands that are 6 times degenerated at the Γ point. Note that for a given finite k, bands are not degenerated anymore, except along very specific axis of symmetry. The Hamiltonian describing these three bands (paraboloids approximation around Γ point) is of the form:

$$\hat{\mathcal{H}}_{3\boldsymbol{k}\cdot\boldsymbol{p}}(k) = \begin{bmatrix} Lk_x^2 + M(k_y^2 + k_z^2) & Nk_xk_y & Nk_yk_z \\ Nk_xk_y & Lk_y^2 + M(k_z^2 + k_x^2) & Nk_zk_x \\ Nk_yk_z & Nk_zk_x & Lk_z^2 + M(k_x^2 + k_y^2) \end{bmatrix}$$

Where :

$$L = -5.641\frac{\hbar^2}{2m_0} \tag{2.21}$$

$$M = -3.607\frac{\hbar^2}{2m_0} \tag{2.22}$$

$$N = -8.676\frac{\hbar^2}{2m_0} \tag{2.23}$$

Here m_0 represents the rest mass of the particles and (L, M, N) corrections due to interaction with the host material. Indeed, the curvature of the energy (i.e. the second derivative) is proportional a term denoted as $m^* = m_0/f(M, N, L)$, defining an effective mass for the holes, which may be experimentally measured. The Hamiltonian (eq. 2.21) allows for drawing the band structure, for a given direction as depicted in Fig. 2.3. The latter plots for two highly symmetric directions (L -> Γ -> X) the band structure in bulk silicon with no SOC interaction.[IV] The blue curve corresponds to two degenerated bands while the red curve is a single band.

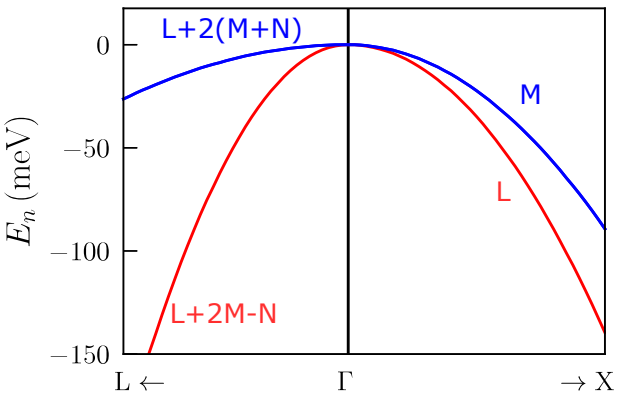

Figure 2.3 – **Valence band of silicon crystalline structure without spin orbit coupling.** Along, highly symmetrical direction, blue curve is 2 time degenerated, while red is a single band. Note that all bands are degenerated at the Γ point. Figure has been taken and modified from [24].

2.3.2 Spin-orbit coupling

Maxwell equations provide a classical description of electric and magnetic fields generated by charges, currents and time variation of those same fields. Especially, dynamical charges nearby a magnetic dipole induce a force able to rotate it. Similarly, in quantum mechanics, a spin in motion inside a potential give raise to a

IV. Here -> X represents $\vec{k} = (\alpha, 0, 0)$, while L -> is $\vec{k} = (\alpha, \alpha, \alpha)$.

relativistic interaction, the so-called spin orbit coupling (SOC). A key example of this phenomenon is the shift in an electron's atomic energy levels. The so-called Zeeman splitting is due to electromagnetic interaction between the electron's magnetic dipole motion and the electrostatic field of the positively charged nucleus. In its more general form, the SOC Hamiltonian is :

$$\hat{\mathcal{H}}_{SO} = \lambda(r)\,\mathbf{L}\cdot\mathbf{S} = \lambda(r)(L_xS_x + L_yS_y + L_zS_z) \tag{2.24}$$

At first order, we deduce that SOC is negligible for electrons. Indeed, the conduction band is mostly constitute of s-type orbitals ($L = 0$), thus canceling SOC. Whereas, in the case of holes, the valence band is essentially made of p-type orbitals ($L = 1$), making them particularly sensitive to SOC. The main difference arises from the reduction of symmetry between both orbital types. In a more general case, SOC is enhanced by symmetry breaking, often refereed as inversion asymmetry. Two main contributions exist in solid state physic namely bulk inversion asymmetry (BIA) or structural inversion asymmetry (SIA).

First contribution (BIA) arises in crystal bulk lacking inversion symmetry. It is particularly true in the zincblende structure of GaAs containing two types of atoms. The local electric fields are leading to a contribution, known as the Dresselhaus effect (DSOC). Note that DSOC is generally stronger for heavier elements. In case of silicon, the cubic crystal system is highly symmetric, removing the DSOC. Nonetheless, asymmetric confining potentials (confinement, gate potential, strain) also generate a spin-orbit contribution. It originates from the band mixing, thus creating a nonzero average electric field. This contribution, namely Rashba spin orbit coupling (RSOC), is dominant in silicon and germanium devices. The SOC of Rashba type is given by the Hamiltonian:

$$\mathcal{H}_R = \alpha\,[\mathbf{E}\times\mathbf{p}]\cdot\boldsymbol{\sigma} \tag{2.25}$$

With α a number that is material specific and also depends on the confining potential. Consequently, for a given device, α is particularly hard to access and equation eq. 2.24 would be preferred for numerical resolution. For silicon bulk material, the RSOC gives an excellent approximation, and calculation of the 6 bands $k-p$ model Hamiltonian can be found in ref [24]. The main message is that the SOC (around the Γ point, k=0) repeal the twofold degenerated split-off band $J = 1/2$ by the amount of energy $-2\Delta_{So}/3$ and the HH/LH bands by $+\Delta_{So}/3$. Thus, the gap between those bands is equal to Δ_{So}, which is material dependent (depending on Bloch states). In case of silicon, the energy gap is considered big

enough (strong SOC) to simply remove the contribution of the SO band[V]. Consequently, the new 4 band $k-p$ Luttinger-Kohn Hamiltonian describes the new bands mixing in the form of:

$$\hat{\mathcal{H}}_{LK} = \begin{bmatrix} P+Q & L & M & O \\ L^* & P-Q & 0 & M \\ M^* & 0 & P-Q & -L \\ 0 & M^* & -L^* & P+Q \end{bmatrix} \tag{2.26}$$

where

$$P = -\frac{\hbar^2}{2m_0}\gamma_1 k^2 \tag{2.27}$$

$$Q = \frac{\hbar^2}{2m_0}\gamma_s(2k_z^2 - k_x^2 - k_y^2) \tag{2.28}$$

$$L = \frac{\hbar^2}{2m_0}2\sqrt{3}\gamma_s k_- k_z \tag{2.29}$$

$$M = \frac{\hbar^2}{2m_0}\sqrt{3}\gamma_s k_-^2 \tag{2.30}$$

With $k_\pm = k_x \pm ik_y$ and $k^2 = k_x^2 + k_y^2 + k_z^2$. The LK Hamiltonian ($\hat{\mathcal{H}}_{LK}$) is described here in the reduced subspace (LH,HH), defined by the eigenstates of $J_z : |3/2\rangle, |1/2\rangle, |-1/2\rangle, |-3/2\rangle$. The off diagonal terms (M,L) lead to mixing between the pure states at finite k.

V. Contribution of the SO band can also be theoretically treated as a small perturbation in the HH/LH manifold. The same principle is used to explain EDSR with electrons which should, in theory will not be possible.

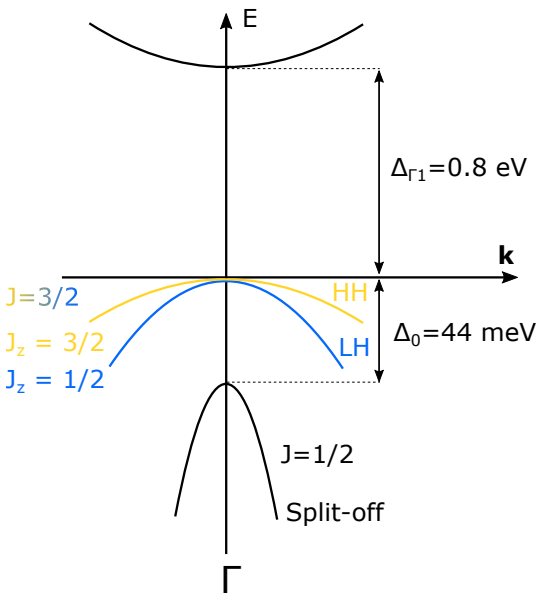

Figure 2.4 – **Zoom in silicon bulk schematic band diagram around Γ point.** The ground state in silicon bulk, at finite **k**, is mostly p-type orbitals ($L = 1$) from the LH and HH bands. The split-off band is located 44 meV below the top edge of the valence band.

Adding a strong 1D quantum confinement lift the fourfold degeneracy by pulling away the LH band from the HH band. This phenomenon is particularly true for planar germanium heterostructures [25] and hutwires [26, 27] where the first hole exhibits an almost pure HH state along the out of plane quantization axis. [VI] In the case of a nanowire with two similar confinement directions [28, 29], the admixture of both bands is much more pronounced and may even result in a strong LH state. On top of hard wall structural boundaries, smoother electrical confinement defined by local gates also impacts the admixture. It mostly confines the quantum dot laterally (then mixes HH/LH states) but also breaks the symmetries by pinching the wave function against a wall. The subtle contribution of those two elements creates a fully tunable artificial atom [30, 31, 32, 33], leveraging a "hole" new playground for qubit design. Solving the SOC interaction in those peculiar configurations is of particular difficulty, forcing theorists to propose model simplifications that do not necessarily correspond to experimental realities. Note that this work only deals about hole spin-orbit qubits in one-dimensional channels, which can be modeled by a long rectangle (z»(x, y)). The theory dealing about these devices can be found in Refs [21, 29, 33, 34, 35].

VI. Note that the in plane mass of the HH state ($m_{\parallel}^{HH}$) is paradoxically remarkably light, hence often confusing.

2.3.3 Zeeman splitting

Adding a magnetic field breaks the time inversion symmetry [36] and thus lift the spin degeneracy (Kramers degeneracy theorem). The corresponding Hamiltonian is :

$$\hat{\mathcal{H}}_Z = -2k\mu_B \boldsymbol{B} \cdot J - 2q\mu_B \boldsymbol{B} \cdot J^3 \tag{2.31}$$

Where $\boldsymbol{J} = (J_x, J_y, J_z) = \boldsymbol{L} + \boldsymbol{S}$ is a set of matrices and $J_{x,y,z}$ the total angular momentum (in the subspace $j = 3/2$). (k,q) are Luttinger parameters depending on the material (in silicon k =??). The Hamiltonian takes both into account the contribution of a pure Zeeman splitting ($\mathbf{B} \cdot \mathbf{S}$), and corrections due to the electromagnetic potential vector ($\mathbf{B} \cdot \mathbf{L}$). From now on, the second term in the Hamiltonian will be neglected.

Heavy-Hole (HH)

Considering a pure heavy hole (subspace $|3/2, \pm 3/2\rangle$), eq. 2.31 reduces to :

$$\hat{\mathcal{H}}_Z = -3k\mu_B B_z \sigma_z \tag{2.32}$$

Previous equation can be rewritten, in a proper basis, as $\hat{\mathcal{H}}_Z = \frac{\mu_B}{2} {}^t\boldsymbol{\sigma} \cdot \hat{g}_d \cdot \boldsymbol{B}$, where ${}^t\boldsymbol{\sigma} = (\sigma_x, \sigma_y, \sigma_z)$ are the Pauli matrices and $\hat{g}_d = (0, 0, 6k)$ is a diagonal matrix representing the measurable g-factors in the main magnetic axis direction. HH are only responsive to magnetic field along the quantization axis. Consequently, magnetic spin manipulation (ESR) on pure HH is impossible since the particle is insensitive to transverse magnetic field.

Light-hole (LH)

In the same manner, the Hamiltonian for pure light hole is :

$$\hat{\mathcal{H}}_Z = -k\mu_B(2B_x\sigma_x + 2B_y\sigma_y + B_z\sigma_z) \tag{2.33}$$

Which, once again can be written as $\hat{\mathcal{H}}_Z = \frac{\mu_B}{2} {}^t\boldsymbol{\sigma} \cdot \hat{g}_d \cdot \boldsymbol{B}$, where $\hat{g}_d = (4k, 4k, 2k)$. The g-factors anisotropy for LH is less pronounced than for HH.

Conclusion

Because HH and LH states have very different behavior in a magnetic field, then, characterization of the Zeeman splitting as a function of the magnetic field orientation is a powerful experimental tool to understand the pure states mixing.

2.4 G-matrix formalism

Theoretically [21, 33, 29] and experimentally [28, 37, 38, 39, 40] works confirmed that a strong SOC in the valence band (Silicon, Germanium) yields to very anisotropic Zeeman energy as a function of the magnetic field orientation. In this section, we introduce the G-matrix formalism which aim at describing in a simple way the behavior of spin qubits in the linear-response regime (as a function of B field and voltage excitation). The formalism summarises the previous sections, partially hiding the inherent physic for the benefit of a general overview. We take advantage of this to mathematically define important concepts such as the spin susceptibility.

Neglecting the hyperfine interaction, the Hamiltonian of a single hole spin qubit trapped in a QD can be expressed via an effective g-matrix ($\tilde{g}(V)$). The purpose is to mimic a two-level Hamiltonian, and thus be able to use the formalism described in section. 2.2. We define a Kramers doublet pseudo-spin $\{|\Uparrow\rangle,|\Downarrow\rangle\}$), which correspond to the two lowest energy eigenstates of the total Hamiltonian. In this subspace, the system is described by :

$$\hat{\mathcal{H}} = \hat{\mathcal{H}}_{LK} + \hat{\mathcal{H}}_{SO} + \hat{\mathcal{H}}_{Z} + V_{conf} = \frac{\mu_B}{2}\, {}^t\boldsymbol{\sigma} \cdot \tilde{g}(V) \cdot \mathbf{B} \tag{2.34}$$

Where $\tilde{g}(V)$ is the g-matrix (real 3×3 matrix with 9 independent parameters) [22, 34]. Importantly, eq. 2.34 only takes into account the linear effect of the magnetic field. V_{conf} describe the confinement, specific to the device geometry, around a given working point. We also define the Larmor pseudo vector along the unit vector $\boldsymbol{n}$:

$$\boldsymbol{\omega}_L = \frac{\mu_B}{\hbar}\tilde{g}(V) \cdot \mathbf{B} = \omega_L\, \boldsymbol{n} \tag{2.35}$$

Note that because $\tilde{g}(V)$ is a matrix, the Larmor vector is not anymore along the magnetic field axis, differing with electron spin physic. This property is disturbing because the Bloch sphere representation is now totally dissociated from the spacial space. In other word, the z-direction in the Bloch sphere (spin up in

the double Kramer pair) does not correspond to the $\vec{z}$ magnetic axis.

2.4.1 Rotation transformation

By construction, there is always a Kramer basis so that $\tilde{g}(V)$ is diagonal ($\tilde{g}_d$). We introduce $\hat{U}$ and $\hat{W}$ as a rotation matrix (${}^tR = R$) [VII], so that $\tilde{g}(V) = \hat{U}\cdot\tilde{g}_d\cdot{}^t\hat{W}$. From eq. 2.34 it yields :

$$\mathcal{H} = \frac{\mu_B}{2}\,{}^t({}^t\hat{U}\cdot\boldsymbol{\sigma})\cdot\tilde{g}(V)\cdot({}^t\hat{W}\cdot\mathbf{B}) \tag{2.36}$$

Consequently, $({}^t\hat{W}\cdot\mathbf{B})$ rotates the magnetic field main axis into three orthonormal magnetic axes denoted as $\boldsymbol{X}$, $\boldsymbol{Y}$ and $\boldsymbol{Z}$. Similarly, $({}^t({}^t\hat{U}\cdot\boldsymbol{\sigma}))$ set three new spin matrices, or, equivalently, three new orthogonal quantization axes for the pseudo-spin of the Kramers doublet. Choosing correctly the basis [22] yields to :

$$\mathcal{H} = \frac{\mu_B}{2}(g_{\boldsymbol{X}}B_{\boldsymbol{X}}\sigma_{\boldsymbol{X}} + g_{\boldsymbol{Y}}B_{\boldsymbol{Y}}\sigma_{\boldsymbol{Y}} + g_{\boldsymbol{Z}}B_{\boldsymbol{Z}}\sigma_{\boldsymbol{Z}}) \tag{2.37}$$

2.4.2 The Zeeman tensor

According to eq. 2.34, the Zeeman splitting ΔE between the eigenstates of $\mathcal{H}$ is :

$$\Delta E = \mu_B|\tilde{g}\cdot\boldsymbol{B}| = \mu_B\sqrt{{}^t\boldsymbol{B}\cdot{}^t\tilde{g}\cdot\tilde{g}\cdot\boldsymbol{B}} = \mu_B\sqrt{{}^t\boldsymbol{B}\cdot\tilde{G}\cdot\boldsymbol{B}} \tag{2.38}$$

$\tilde{G} = {}^t\tilde{g}\cdot\tilde{g}$, which is obviously symmetrical by construction (6 independent parameters), is refereed as the symmetric Zeeman tensor. In terms of experimentation, $\tilde{G}$ is measurable for any magnetic field orientation. Even more, the symmetric Zeeman tensor is reconstructable given only 6 measures to fix the independent parameters. Indeed, these 6 elements can be broken down into two categories. On the one hand the diagonal terms, representing the Zeeman splitting in the main magnetic field directions. On the other hand, the remaining 3 parameters can be seen as the angle of rotation of the main B field directions with respect to the crystallographic axes. Note that $\tilde{G}$ only depends on the choice of

VII. In this manuscript we arbitrary chose the matrices so that $\det(R)$=1 which set their uniqueness.

a frame for the magnetic field. Importantly, measuring the Zeeman splitting does not give access to $\tilde{g}$, since the Kramers doublet choice is important.

Eq. 2.37 shows that eigenvalues of $\tilde{G}$ are $(g^2_{\boldsymbol{X}},g^2_{\boldsymbol{Y}},g^2_{\boldsymbol{Z}})$, with corresponding eigenvectors $(\boldsymbol{X},\boldsymbol{Y},\boldsymbol{Z})$. Consequently, the characterization of the Zeeman splitting gives the anisotropic principal absolute value of g-factors associated with the main magnetic axis.

2.4.3 Spin driving mechanisms

In this subsection, we derive the Rabi formula to highlight different driving mechanism. During the drive, microwaves are applied to a nearby gate, thus modulating the parameter V. For small oscillations of the voltage around a working point V_0, we can rewrite eq. 2.34 with a first order Taylor series:

$$\mathcal{H} = \frac{\mu_B}{2} {}^t\boldsymbol{\sigma} \cdot \tilde{g}(V) \cdot \mathbf{B} = \frac{\mu_B}{2} {}^t\boldsymbol{\sigma} \cdot [\tilde{g}(V_0) + \frac{\partial \tilde{g}}{\partial V}(V_0)\, \delta V] \cdot \mathbf{B} \tag{2.39}$$

We introduce $\tilde{g}'$ the derivative of $\tilde{g}$ with respect to the parameter V. We also define both quantities :

$$\beta_{\parallel} = (\frac{\partial g}{\partial V}(V_0) \cdot \boldsymbol{b}) \cdot \boldsymbol{n}) \tag{2.40}$$

.

$$\beta_{\perp} = |(\frac{\partial g}{\partial V}(V_0) \cdot \boldsymbol{b}) \wedge \boldsymbol{n}| \tag{2.41}$$

.

Were $\boldsymbol{b} = \boldsymbol{B}/||\boldsymbol{B}||$ and $\boldsymbol{n} = \tilde{g}(V) \cdot \boldsymbol{B}/||\tilde{g}(V) \cdot \boldsymbol{B}||$ is the re-normalized Larmor vector. $\beta_{\parallel}$ and $\beta_{\perp}$ are respectively the spin sensitivity in the longitudinal and transverse direction. Injecting into eq. 2.39, it yields :

$$\mathcal{H} = \frac{\hbar}{2}\left[(\omega_L + \frac{\mu_B B}{2\hbar}\beta_{\parallel}\delta V)\sigma_{\parallel} + \frac{\mu_B B}{2\hbar}\beta_{\perp}\delta V \sigma_{\perp}\right] \tag{2.42}$$

Where $\sigma_{\parallel}$ (resp. $\sigma_{\perp}$) denotes the longitudinal (resp. transversal) spin components. If the drive is in the form of $\delta V = V_d \cos(\omega_d t + \phi))$, we may go into the rotating frame where the oscillating term at the driving frequency along the Larmor frequency may be neglected ($\beta_{\parallel}\delta V$). The Hamiltonian finally writes:

$$\mathcal{H} = \frac{\hbar}{2}\left[(\omega_L - \omega_d)\sigma_{\parallel} + \frac{\mu_B B}{2\hbar}\beta_{\perp} V_d \sigma_{\perp}\right] \tag{2.43}$$

Following eq. 2.14, the Rabi frequency at the resonance $\omega_L = \omega_d$, is proportional to ω_{R0} :

$$\omega_{R_0} = \frac{\mu_B B}{2\hbar}\beta_{\perp} V_d = \frac{\mu_B B V_d}{2|g|\hbar}[\tilde{g}(V_0)\cdot \boldsymbol{b}] \times [\frac{\partial \tilde{g}}{\partial V}(V_0)\cdot \boldsymbol{b}] \tag{2.44}$$

Note that the Rabi frequency is proportional to the amplitude of the drive V_{ac} and the magnetic field B. Moreover, the driving process of the spin is entirely captured in the g-matrix formalism by the derivative of the g-matrix with respect to the parameter V. For the same reason that $\tilde{g}$ is not experimentally accessible, we show that it is the same for $\tilde{g}'$. Nonetheless, given a clever decomposition, we can exhibit two different driving mechanisms. Mathematically expressing $\tilde{g}'$ yields to :

$$\tilde{g}' = ({}^t\hat{U})' \cdot \tilde{g_d} \cdot \hat{W} + {}^t\hat{U} \cdot \tilde{g_d}' \cdot \hat{W} + {}^t\hat{U} \cdot \tilde{g_d} \cdot \hat{W}' \tag{2.45}$$

Three terms appear in the driving process each of them due to a physical process :

— ${}^t\hat{U}' \cdot \tilde{g_d} \cdot \hat{W}$ correspond to a change in the Kramer basis during the drive. Note that in this case, the Zeeman energy of the system is kept constant leading to a driving term refereed as Izo-Zeeman.

— ${}^t\hat{U} \cdot \tilde{g_d}' \cdot \hat{W}$ correspond to change in the main g-factors, which may arise from the modification of the confining potential. An example is when the wave function is pinched against a hard wall potential such as the edge of the canal or a static defect in the crystal.

— ${}^t\hat{U} \cdot \tilde{g_d}' \cdot \hat{W}'$ correspond to a change in the main magnetic axis. The g-factor peanut shape is this time rotated by the drive. The process is mainly due to inhomogeneous strain field.

Importantly, the first contribution does not the Zeeman energy of the system. It corresponds mostly to a displacement of the wave function as a whole, while keeping all other variables constant. It happens mostly when the wave-function is translated along the nanowire, when the environment seen by the hole is exactly

the same.

The last two terms in eq. 2.46 are measurable experimentally as a variation of the Larmor frequency while varying the confinement potential V. Fig. 2.5 shows a visual representation of both phenomena. For the sake of simplicity, we only plotted g in a plane. On one hand, only the main g-factors are changed (Fig. 2.5-a), resulting in a deformation of the peanut shape (main g-factor modulation). On the other hand, the main magnetic axis rotates, conserving the peanut shape during the process (magnetic axis modulation).

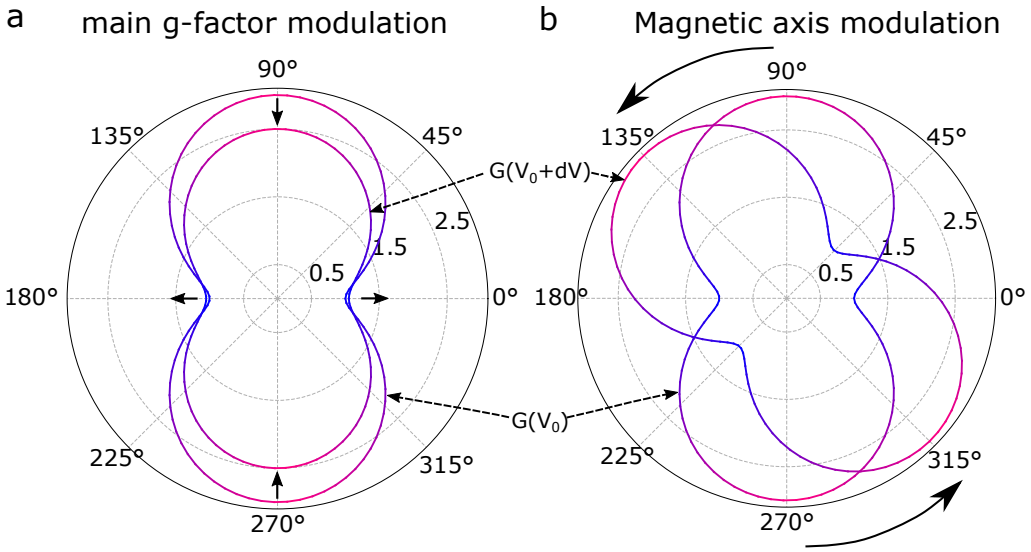

Figure 2.5 – **Visualisation of the g tensor modulation.** **(a)** Main g-factor modulation : $({}^t\hat{U} \cdot \tilde{g_d}' \cdot \hat{W})$, the magnetic are conserved and the peanut shaped is not rotated during the process. The phenomenon exhibits a sweet spot (qubit resonance frequency has a vanishing derivative), only if the peanut shape is contracted in one direction and elongated on the other. **(b)** Magnetic axis modulation : $({}^t\hat{U} \cdot \tilde{g_d}' \cdot \hat{W})$. The peanut shape rotates during the drive.

G' matrix

We introduce the derivative of $\hat{G}$, which is experimentally measurable as the displacement of the Larmor frequency with respect to parameter V , so that :

$$\hat{G}'(V_0) = \frac{\hat{G}(V_0) - \hat{G}(V_0 + \delta V)}{\delta V} = {}^t\tilde{g} \cdot \tilde{g}' + {}^t\tilde{g}' \cdot \tilde{g} \tag{2.46}$$

We then express ${}^t\tilde{g}\cdot\tilde{g}'$ as a sum of a symmetric (S) and anti-symmetric matrices (A) [VIII].

$$ {}^t\tilde{g}\cdot\tilde{g}' = A + S \tag{2.47}$$

In particular, thanks to $\tilde{g}$ properties, we have :

$$ {}^t({}^t\tilde{g}\cdot\tilde{g}') = {}^t\,\tilde{g}'\cdot\tilde{g} = A - S \tag{2.48}$$

Izo-Zeeman driving (IZ)

It emerges from eqs. 2.46, 2.47 and 2.48 that $\hat{G}' = 0$ if ${}^t\tilde{g}\cdot\tilde{g}'$ is anti-symmetric. In other words, even if $\hat{G}' = 0$, there is room for spin driving. The latter mechanism is called Izo-Zeeman driving, because no change of the Zeeman energy is induced during the process. We then define :

$$ \tilde{g}'_{IZ} = ({}^t\tilde{g})^{-1}\cdot A \tag{2.49}$$

g-tensor modulation resonance (g-TMR)

Similarly to the previous description, we define the g-TMR contribution to the symmetrical part. It is also related to $\hat{G}'$ so that :

$$ \tilde{g}'_{TMR} = ({}^t\tilde{g})^{-1}\cdot S = ({}^t\tilde{g})^{-1}\cdot\frac{\hat{G}'}{2} \tag{2.50}$$

Full driving

From eqs. 2.47, 2.49 and 2.50, we obtain :

VIII. The decomposition is mathematically always possible, since subspace S and A represents a base for 3×3 matrices).

$$\tilde{g}'(V_0) = \tilde{g}'_{TMR}(V_0) + \tilde{g}'_{IZ}(V_0) \tag{2.51}$$

Injecting in eq. 2.44, working in the basis in order to diagonalize $\tilde{g}$, we finally obtain :

$$\omega_{R_0} = \frac{\mu_B B V_d}{2|g|\hbar}[\tilde{g}(V_0) \cdot \boldsymbol{b}] \times [(\tilde{g}'_{TMR} + \tilde{g}'_{IZ}) \cdot \boldsymbol{b}] \tag{2.52}$$

Finally, eq. 2.52 enables to find the IZ contribution. Indeed, measuring the g-factors and the Rabi frequency for different magnetic field angles lets only the IZ as a free parameter in the fit (See [22] for more details). Note that the IZ should bring only a small contribution in driving process [35], even when driving with lateral gates. In fact, impurities in the channel tend to strengthen the g-TMR contribution.

Conclusion

As a conclusion, g-TMR is experimentally measurable by accessing the matrix $\hat{G}'$. Nonetheless, IZ contribution can only be recovered from the Rabi frequency map as a function of the magnetic field [22]. Importantly the effect of one contribution may run counter to the effect of the second, even canceling spin rotation, in the worst case.

2.5 Noise sources acting on hole spin qubits

In this section we focus on the main sources of noise acting on the qubit, which can be divided into two categories. On the one hand the electrical noise acting through the SOC and on the other hand the interaction with the surrounding nuclear spins whose contribution produces a slowly varying magnetic field.

2.5.1 Hyperfine interaction

The interaction between a spin qubit trapped in a QD and the isotopes nuclear spins of the host material (nuclear Overhauser effect) is known as the hyperfine interaction. The slow variations of the surrounding nuclear spins locally change the magnetic field perceived by the qubit, thereby changing the Zeeman energy of the system. Consequently, hyperfine interaction leads to a reduction in the coherence time (T_2), and must be either reduced or even totally suppressed (nuclear spin purification).

In the case of electrons, the predominant term is known as the hyperfine contact interaction [7], due to an overlap of the wave function of the electron and the nuclear spins. In this setting, hyperfine contact interaction has an isotropic response in a magnetic field. In the case of holes, the valence band is essentially composed of p-type orbitals. Specifically, the hole wave function cancels at the atomic nucleus sites, thus destroying the contact interaction. However, a second term originating from the dipole-dipole interaction takes over, which can be just as important as the electron one in silicon and germanium [41]. In this configuration, the interaction becomes strongly anisotropic [42] with the magnetic orientation. Moreover, the anisotropy may disappears in the case of a pure HH to which a magnetic field transverse to the quantization axis is applied[30], reaching a form of Ising interaction [43]. Consequently, the hyperfine interaction is theoretically fully tunable, with working point which may even coincide with electrical sweet spot [30]. In the general case, the hyperfine interactions between the hole and the N nuclei spins are described by the following Hamiltonian [30, 44] :

$$\hat{\mathcal{H}}_h = \frac{A}{2n_0} \sum_{n=1}^{N} \delta(\mathbf{r} - \mathbf{R}_n) \otimes \mathbf{J} \cdot \mathbf{I}_n \,, \tag{2.53}$$

Where A is the hyperfine coupling constant, n_0 is the density of nuclei in the crystal, $\mathbf{I}_n$ is the spin operator of nuclei n at position $\mathbf{R}_n$, and $\mathbf{J}$ is the angular momentum operator acting on the $J = 3/2$ Bloch functions of the heavy and light holes (whereas the $\delta(\mathbf{r} - \mathbf{R}_n)$ acts on the envelopes). We discard here the small contributions from the split-off $J = 1/2$ components as well as the small $\propto J_x^3$, J_y^3, J_z^3 corrections arising from the cubic symmetry of the crystal [44].

Let $|\uparrow\rangle$ and $|\downarrow\rangle$ be the pseudo-spin states of the dot at a given magnetic field, and $|\psi_{\text{nucl}}\rangle$ be the nuclear configuration. The first-order correction to the Larmor energy $\varepsilon_L = hf_L$ is [IX]:

$$\delta\varepsilon_L = \frac{A}{2n_0} \sum_{n=1}^{N} \langle\psi_{\text{nucl}}| \mathbf{I}_n |\psi_{\text{nucl}}\rangle \cdot \big(\langle\uparrow| \delta(\mathbf{r}-\mathbf{R}_n)\otimes\mathbf{J} |\uparrow\rangle - \langle\downarrow| \delta(\mathbf{r}-\mathbf{R}_n)\otimes\mathbf{J} |\downarrow\rangle \big) \tag{2.54}$$

We next average over the nuclei configurations assuming uncorrelated and unpolarized nuclear spins with Gaussian-distributed quasi-static fluctuations [45]. The variance of $\delta\varepsilon_L$ is then:

IX. All the calculations in this subsection have been conducted by Romain MAURAND.

$$\left\langle \delta\varepsilon_L^2 \right\rangle = \frac{A^2}{4n_0^2} \sum_{n=1}^{N} \left\langle I_x^2 \right\rangle \delta J_x^2(\mathbf{R}_n) + \left\langle I_y^2 \right\rangle \delta J_y^2(\mathbf{R}_n) + \left\langle I_z^2 \right\rangle \delta J_z^2(\mathbf{R}_n) \,, \tag{2.55}$$

where, for $\alpha \in \{x, y, z\}$:

$$\delta J_\alpha(\mathbf{R}_n) = \langle\uparrow| \, \delta(\mathbf{r} - \mathbf{R}_n) \otimes J_\alpha \, |\uparrow\rangle - \langle\downarrow| \, \delta(\mathbf{r} - \mathbf{R}_n) \otimes J_\alpha \, |\downarrow\rangle \;, \tag{2.56}$$

and $\left\langle I_x^2 \right\rangle = \left\langle I_y^2 \right\rangle = \left\langle I_z^2 \right\rangle = I(I+1)/3$. Taking a second average over nuclei spin distributions, and assuming slowly varying envelope functions, we reach:

$$\left\langle\left\langle \delta\varepsilon_L^2 \right\rangle\right\rangle = \frac{A^2}{12n_0} I(I+1)\nu \left(\overline{\delta J_x^2} + \overline{\delta J_y^2} + \overline{\delta J_z^2} \right) \;, \tag{2.57}$$

where ν is the fraction of nuclei carrying a spin, and:

$$\overline{\delta J_\alpha^2} = \int d^3\mathbf{R} \, \delta J_\alpha^2 \left(\mathbf{R} \right) \;. \tag{2.58}$$

Finally, the rate of inhomogeneous dephasing due to hyperfine interactions is [46, 47]:

$$\Gamma_2^* = \frac{1}{T_2^*} = \frac{\sqrt{\left\langle\left\langle \delta\varepsilon_L^2 \right\rangle\right\rangle}}{\sqrt{2}\hbar} = \frac{|A|}{2\hbar} \sqrt{\frac{\nu I(I+1)}{6n_0}} \left(\overline{\delta J_x^2} + \overline{\delta J_y^2} + \overline{\delta J_z^2} \right)^{1/2} \;. \tag{2.59}$$

2.5.2 Electrical noise

Spin qubits are sensitive to decoherence due to surrounding environment degrees of freedom. The latter appear as noise on the main parameters of the qubit in the Hamiltonian : the g-factor. Modifications of the g-factor results in a change of the Zeeman energy (E_z : longitudinal noise). Rewriting eq. 2.39 and projecting

the Pauli matrices $\boldsymbol{\sigma}$ on the spin precession vector $\boldsymbol{n}$ into component longitudinal ($\parallel$) and transversal ($\perp$), we obtain :

$$\mathcal{H}_{noise} = \frac{\mu_B}{2}(B_\parallel \sigma_\parallel + B_\perp \sigma_\perp) \cdot \delta V(t) \tag{2.60}$$

$B_\parallel$ expresses the decoherence in terms of energy fluctuations due to external noise sources (T_2), where as $B_\perp$ is related to spin relaxation (T_1). We also define for each noise source in the system its symmetrized (s) spectral power density with respect to a variable α such as :

$$S_{s,\alpha}(\omega) = \frac{S_\alpha(\omega) + S_\alpha(-\omega)}{2} \tag{2.61}$$

.

Pure dephasing from different pulse sequences

We introduce the Longitudinal spin electric susceptibility (LSES) [X] with respect to gate G_i as :

$$LSES_{G_i} = D_{G_i} = \frac{\mu_B B}{h}\beta_\parallel = \frac{\partial f_L}{\partial V_{G_i}} \tag{2.62}$$

Which is proportional to the magnetic field amplitude. Under the assumptions that the noise on the different gates are independent, and that their respective auto-correlation functions are homogeneous in time, we reach in the frequency domain:

$$\langle \delta\phi^2(t) \rangle = 4\pi^2 \int_{-\infty}^{+\infty} df \sum_i D_{\mathrm{G}i}^2 S_{\mathrm{G}i}(f) \left|\tilde{\eta}_t(f)\right|^2 , \tag{2.63}$$

Where $S_{\mathrm{G}n}(f) = \int_{-\infty}^{+\infty} dt\, e^{-2i\pi ft} \langle \delta V_{\mathrm{G}n}(t) \delta V_{\mathrm{G}n}(0) \rangle$ is the Fourier transform of the auto-correlation function of the noise on gate Gn (the symmetrical power spectrum according to the Wiener-Khinchin theorem), and $\tilde{\eta}_t(f) = \int_{-\infty}^{+\infty} dt\, e^{-2i\pi ft}\, \eta_t(t)$ is the filter function of the pulse sequence $\eta_t(t')$. Eq. (2.63) can also be formalized using the filter function concept [19, 48, 49]. We analyze below the different pulse sequences relevant for the manuscript experiments.

X. For equation visibility, we rename the $LSES_{G_i}$ as D_{G_i} which is not ideal for the reader to follow.

Free induction decay

Free induction decay (or FID) is the observable signal generated by non-equilibrium nuclear spin polarization precessing about the magnetic field. This non-equilibrium may be created by applying a pulse of radio-frequency close to the Larmor frequency of the qubit. This phenomenon is also refereed as Ramsey fringes [50].

To calculate the pure dephasing from electrical noise, we define the filter function for the Ramsey sequence :

$$\left|\tilde{\eta}_t^{\mathrm{R}}(f)\right|^2 = \left(\frac{\sin(\pi f t)}{\pi f}\right)^2 \tag{2.64}$$

Therefore, $\left|\tilde{\eta}_t^{\mathrm{R}}(f)\right|^2/t^2$ is close to unity up to $|f| \sim 1/t \sim 1/T_2^*$, so that free induction decay is sensitive to noise in this whole range of frequencies. For low-frequency noise spectra of the form $S_{\mathrm{G}i}(f) = S_{\mathrm{G}i}^{\mathrm{lf}}\, f_0/\max(|f|, f_l)$ together with a (soft) high-frequency cutoff f_h, we get in the regime $2\pi f_l \ll 2\pi f_h \ll 1/t$:

$$\exp\left(-\frac{1}{2}\langle\delta\phi_R(t)^2\rangle\right) \approx \exp\left[-4\pi^2 t^2 \ln\left(\frac{f_h}{f_l}\right) f_0 \sum_i D_{\mathrm{G}i}^2\, S_{\mathrm{G}i}^{\mathrm{lf}}\right] \equiv \exp\left[-\left(\frac{t}{T_2^*}\right)^2\right] \tag{2.65}$$

with [18]:

$$\frac{1}{T_2^*} \approx 2\pi\sqrt{\ln\left(\frac{f_h}{f_l}\right) f_0 \sum_i D_{\mathrm{G}i}^2\, S_{\mathrm{G}i}^{\mathrm{lf}}} \tag{2.66}$$

The averaged T_2^* decreases with increasing $t_{\mathrm{meas}} \sim 1/(2\pi f_{\mathrm{l}})$ as the experiment probes smaller and smaller noise frequencies. We can also estimate the contribution of higher frequency noises with spectra $S_{\mathrm{G}i}(f) = S_{\mathrm{G}i}^{\mathrm{hf}}\sqrt{f_0/f}$. The Ramsey oscillations then decay as $\exp(-\frac{1}{2}\langle\delta\phi_R(t)^2\rangle) = \exp(-(t/T_{2,\mathrm{hf}}^*)^{3/2})$, where we define:

$$\frac{1}{T_{2,\mathrm{hf}}^*} = \left(\frac{16\pi^2}{3} f_0^{1/2} \sum_i D_{\mathrm{G}i}^2\, S_{\mathrm{G}i}^{\mathrm{hf}}\right)^{2/3} \approx 14\left(f_0^{1/2} \sum_i D_{\mathrm{G}i}^2\, S_{\mathrm{G}i}^{\mathrm{hf}}\right)^{2/3} \tag{2.67}$$

The low-frequency and high-frequency contributions to the decay of the Ramsey signal cross over at time $t_* = T_2^*(T_2^*/T_{2,\mathrm{hf}}^*)^3 \ll T_2^*$ when $T_2^* \ll T_{2,\mathrm{hf}}^*$, and the decay is dominated by the low-frequency noise when $t \gg t_*$.

Hahn Echo sequence

In magnetic resonance, a spin echo or Hahn echo is the refocusing of spin polarization via a pulse of resonant electromagnetic radiation. In this manuscript, the refocusing event is a π pulse about x or y axis.

For the Hahn echo sequence, the filter function is :

$$\left|\tilde{\eta}_t^{\mathrm{E}}(f)\right|^2 = \frac{\sin^4(\pi f t/2)}{(\pi f/2)^2} \tag{2.68}$$

Therefore, the integrand in Eq. (2.63) is small at frequencies $|f| \ll 1/t$ and the integral is dominated by the region around $f_* = 2/(\pi t)$ (with extent $\sim f_*$). f_* is of the order of $10-100\,\mathrm{kHz}$ for Hahn-echo sequences with total length $t = 10-100\,\mu\mathrm{s}$. If in this range of frequencies the noise spectra are of the form $S_{\mathrm{G}i}(f) = S_{\mathrm{G}i}^{\mathrm{hf}}(f_0/f)^\alpha$ ($0 < \alpha \leq 2$ typically), then:

$$\exp\left(-\frac{1}{2}\langle\delta\phi_E(t)^2\rangle\right) = \exp\left(-C_\alpha(2\pi t)^{\alpha+1} f_0^\alpha \sum_i D_{\mathrm{G}i}^2\, S_{\mathrm{G}i}^{\mathrm{hf}}\right) \equiv \exp\left[-\left(\frac{t}{T_2^{\mathrm{E}}}\right)^{\alpha+1}\right] \tag{2.69}$$

where $C_\alpha = 2\sin(\frac{\alpha\pi}{2})(2^{1-\alpha}-1)\Gamma(-1-\alpha)$, with Γ the Gamma function [51], and:

$$\frac{1}{T_2^{\mathrm{E}}} = 2\pi\left(C_\alpha f_0^\alpha \sum_i D_{\mathrm{G}i}^2\, S_{\mathrm{G}i}^{\mathrm{hf}}\right)^{\frac{1}{\alpha+1}} \tag{2.70}$$

In the particular case $\alpha = 0.5$ (see main text), $C_{0.5} = \frac{4\sqrt{2\pi}}{3}(2^{1/2}-1) \approx 1.38$, so that:

$$\frac{1}{T_2^{\mathrm{E}}} \approx 7.8 \left(f_0^{1/2} \sum_i D_{\mathrm{G}i}^2 \, S_{\mathrm{G}i}^{\mathrm{hf}} \right)^{2/3} \tag{2.71}$$

The Hahn echo T_2^{E} and Ramsey $T_{2,\mathrm{hf}}^*$ [Eq. (2.67)] are thus proportional.

Carr–Purcell–Meiboom–Gill (CPMG) sequence

CPMG is a sequence using several refocusing pulse to extend even more the coherence time of the spin qubit. In this sense, Hahn echo experiment may be seen as a CPMG_1, because of its single π pulse.

For the more general CPMG sequence [48, 52] with noise spectra $S_{\mathrm{G}i}^{\mathrm{hf}}(f_0/f)^\alpha$ over extent $\sim 1/t$ around the frequency $f_{N_\pi} = N_\pi/(2t) \sim N_\pi/(2T_2^{\mathrm{CPMG}})$, we get the scaling

$$\langle \delta\phi^2(t) \rangle \sim t^{\alpha+1} N_\pi^{-\alpha} f_0^\alpha \sum_i D_{\mathrm{G}i}^2 \, S_{\mathrm{G}i}^{\mathrm{hf}} \tag{2.72}$$

so that $\langle \delta\phi^2(t) \rangle \sim (t/T_2^{\mathrm{CPMG}})^{\alpha+1}$, with:

$$T_2^{\mathrm{CPMG}} \sim N_\pi^\gamma f_0^{-\gamma} \left(\sum_i D_{\mathrm{G}i}^2 \, S_{\mathrm{G}i}^{\mathrm{hf}} \right)^{-\frac{1}{\alpha+1}} \tag{2.73}$$

and $\gamma = \alpha/(\alpha+1)$, in agreement with Ref. [52].

2.5.3 High frequency : Jonhson Nyquist Noise

Johnson–Nyquist noise is equilibrium noise when the system is in thermodynamic equilibrium, and thus $< I >= 0$. It originates from the thermal fluctuations of the micro-states of the system; for non-interacting electrons, this is simply due to the equilibrium statistical fluctuations in the occupation number of single-electron eigenstates (which can carry current). Obviously, such fluctuations (and corresponding noise) vanishes in the zero-temperature limit.

At high frequency, noise on the qubit mainly lead to spin relaxation. At the Larmor frequency, we express the transition rate due to Jonhson Nyquist Noise (from [18]) :

$$\Gamma_{\downarrow} = \frac{1}{4}(\frac{\mu_B B}{\hbar} B_{\perp})^2 \cdot S_V^{JN}(+\omega_L) \tag{2.74}$$

$$\Gamma_{\uparrow} = \frac{1}{4}(\frac{\mu_B B}{\hbar} B_{\perp})^2 \cdot S_V^{JN}(-\omega_L) \tag{2.75}$$

where :

$$S_V^{JN}(\omega_L) = 2\hbar\omega_L R \cdot \left(1 + n_B\left(\frac{\hbar\omega_L}{k_B T}\right)\right) \tag{2.76}$$

k_B is the Boltzman constant, R the equivalent resistor emitting the noise and T its temperature. We also define the Bose–Einstein statistics function $n_B(x) = 1/(e^x - 1)$.

The relaxation rate is finally obtain with :

$$\Gamma_1 = \Gamma_{\uparrow} + \Gamma_{\downarrow} \tag{2.77}$$

Combining eq. 2.76 and eq. 2.77 yields to :

$$\begin{aligned}\Gamma_1 &= \frac{R\hbar\omega_L}{2} \cdot (\frac{\mu_B B}{\hbar} B_{\perp})^2 \cdot \left[n_B\left(\frac{\hbar\omega_L}{k_B T}\right) - n_B\left(-\frac{\hbar\omega_L}{k_B T}\right)\right] \\ &= \frac{R\hbar\omega_L}{2} \cdot (\frac{\mu_B B}{\hbar} B_{\perp})^2 \left[\coth\left(\frac{\hbar\omega_L}{2k_B T}\right)\right]\end{aligned} \tag{2.78}$$

and the symmetric power spectral density is given by :

$$S_{s,V}^{JN}(\omega) = 2\hbar\omega R \cdot \left[\coth\left(\frac{\hbar\omega}{2k_B T}\right)\right] \tag{2.79}$$

Similarly to eq. 2.62, we define the transversal spin electric susceptibility with respect to a given gate such that :

$$\mathrm{TSES_{Gi}} = \frac{\partial \mathrm{f_r}}{\partial \mathrm{V_{G_i}}} = \frac{\mu_\mathrm{B} \mathrm{B}}{2\mathrm{h}} \beta_\perp \tag{2.80}$$

If we suppose only one gate (G_i) contributes to the spin relaxation, Eq 2.78 and 2.79 finally yields :

$$S^{JN}_{s,V}(\omega) = \frac{\Gamma_1}{|TSES_{\mathrm{G_i}}|^2} \tag{2.81}$$

2.6 Power spectral density

To characterize whatever noise source mathematics tools are available. It can be described either by its amplitude distribution (mostly Gaussian with a standard deviation σ) in time domain signal or its power spectral density (PSD) in frequency domain. Note that two identical PSD may arise from different amplitude distribution. Moreover, those two figure of merit only give an int on the mechanism responsible for the noise. Indeed, since there is no bijection from mechanism to mensurable response, experimenter often need to guess the origin of the noise. In particular, hyperfine interaction and dynamical charge noise are tricky to distinguish in spin qubit physics and particularly complicated experiences have to be conducted to catch signature of those phenomenon.

The power spectral density $S_x(f)$ (PSD) of a time series x(t) describes the power distribution in the frequency domain of the components composing that signal. The statistical average of a certain signal as analyzed in terms of its frequency content, is called its spectrum. The spectrum of a physical process x(t) contains essential information about the nature of x. Each experiences gives information on narrow frequency window depending on the sampling rate f_s and the total duration of the measurement τ_{tot}. In this section we describe how to reconstruct the PSD using Fourier transform.

2.6.1 Fourier transform Definition

Mathematically, we define the Fourier transform as follow :

$$\mathcal{F}(g) : f \to \hat{g}(f) = \int_{-\infty}^{+\infty} g(t) e^{-2i\pi ft} dt \tag{2.82}$$

Where $\hat{g}$ is the Fourier transform of the function g, f the frequency and t the time-domain variable. Using a standard "Backward" definition, the inverse Fourier transform is defined by :

$$\mathcal{F}^{-1}(\hat{g})(t) = g(t) = \int_{-\infty}^{+\infty} \hat{g}(f) e^{+2i\pi ft} df \tag{2.83}$$

In fact, we never have access to a function when performing measures in physics. We do record evaluations of the function g at regularly spaced interval in time domain $\in [t_0, .., t_{N-1}]$. We define $\Delta t = t_1 - t_0$ the inverse of the sampling rate. As a consequence, we evaluate the function $\hat{g}$ using a fast Fourier transform (FFT) algorithm which computes the discrete Fourier transform (DFT) of a sequence $[g(t_0), .., g(t_N)] = [g(0), .., g((N-1)\Delta t)]$. The DFT is defined by the formula :

$$X_f = \sum_{n=0}^{N-1} g(n\Delta_t) e^{-2i\pi fn/N} \tag{2.84}$$

and the Fourier transform may be expressed as :

$$\hat{g}(f) = \Delta t \sum_{n=-\infty}^{+\infty} g(n) e^{-2i\pi fn\Delta t} \tag{2.85}$$

Consequently, $X_f * \Delta t \approx \hat{g}(f)$ is a reasonable evaluation of the Fourier transform at the frequency f. The bigger is N the number of point recorded in a data set, the better is the evaluations of $\hat{g}$. The negative side is that all All known $\mathcal{FFT}$ algorithms require $O(N \log N)$ operations. The best way to improve code speed is to calculate the $\mathcal{FFT}$ on a sample size equal to a power 2 so that $N_{tot} = 2^N$.

As an experimenter, an easy think to keep in mind when analyzing frequency domain signal is :

$$\forall f \; : \; \mathcal{F} = \mathcal{FFT} \cdot \Delta t \tag{2.86}$$

2.6.2 PSD from Fourier transform

The average power $\mathcal{P}$ of a signal g(t) is defined by :

$$\mathcal{P} = \lim_{T \to \infty} \frac{1}{T} \int_{-\infty}^{+\infty} |g(t)|^2 dt \tag{2.87}$$

The Parseval's theorem gives an alternative definition for the energy which links it to the Fourier transform $\hat{g}$:

$$\mathcal{P} = \lim_{T \to \infty} \frac{1}{T} \int_{-\infty}^{+\infty} |\hat{g}(f)|^2 df \tag{2.88}$$

From eq. 2.88, the integrand $|\hat{g}(f)|^2$ can be interpreted as a power spectral density function. It directly yields to :

$$S_g(f) = \lim_{T \to \infty} \frac{1}{T} |\hat{g}(f)|^2 \tag{2.89}$$

For frequencies positive and negative in units of $unit(g)^2/Hz$. Since we are dealing with discrete signal, we finally obtain as experimenters :

$$S_g(f) = \frac{\Delta t^2 \cdot |\mathcal{FFT}(g(t))|^2}{T_{\text{tot}}} = \frac{\Delta t \cdot |\mathcal{FFT}(g(t))|^2}{N} \tag{2.90}$$

Equivalent to a "two sided" definition. In a classical definition, the PSD is a symmetric function. We can define the "one sided" PSD $J_g(f) = S_g(-f) + S_g(f) = 2 \cdot S_g(f)$.

2.6.3 PSD from signal autocorrelation

We define the autocorrelation of a continuous stochastic process g as :

$$r_{gg}(\tau) = \boldsymbol{E}[\bar{g}(t)g(t-\tau)] \tag{2.91}$$

The Wiener–Khinchin theorem states that if the auto-correlation of g $r_{gg}(\tau)$ exist for every τ and if we suppose the power spectral density absolutely continuous (always true in physics), then we may define the PSD so that :

$$r_{gg} = \int_{-\infty}^{+\infty} S_g(f)e^{2\pi\tau f}df = \mathcal{F}^{-1}(S_g(f)) \tag{2.92}$$

Finally, applying the fourrier transform to eq. 2.92 yields :

$$S_g(f) = \int_{-\infty}^{+\infty} r_{gg}(t)e^{-2\pi\tau f}dt = \mathcal{F}(r_{gg}(t)) \tag{2.93}$$

The Fourier transform of the auto-correlation for a continuous process g is exactly equal to the PSD. The results is also true for the discrete-time case. In particular, as experimenters we keep the in mind the formula :

$$S_g(f) = \Delta t \cdot \mathcal{FFT}(r_{gg}(t)) \tag{2.94}$$

Filtering and autocorrelation

We define the frequency response of a given filter as $H(f)$, given by the Fourrier transform of its impulse response $h(t)$. Then, the output of the filter $(y(t))$ is :

$$y(t) = \int_{-\infty}^{+\infty} x(u)h(t-u)du \tag{2.95}$$

Where $x(t)$ is the input signal. Then the auto-correlation (r_{yy}) of $y(t)$ is given by :

$$r_{yy}(f) = (2\pi)^2 * H(f) * r_{xx}(f) \tag{2.96}$$

In the particular case where the filter is just a numerical average over N consecutive values, then the filter is :

$$y(t) = \frac{1}{N} \sum_{l=0}^{N-1} x(t + l * T_E) \tag{2.97}$$

And the associated filtered function is :

$$H(f) = \frac{1}{n} \sum_{l=0}^{N-1} e^{-2i\pi f l T_e} = \frac{1}{n} \frac{\sin(\pi f N T_e)}{\sin(\pi f T_e)} e^{-2i\pi f (N-1) T_e} \tag{2.98}$$

Consequently to eq 2.98, averaging numerically a signal and taking its PSD is not equivalent to take the PSD of the bare signal. A correction due to the filtering should be taken into account.

2.6.4 Noise color

We define different colors for the noise given the power spectral density.

— $S_g(f) = f_0$: White noise. Associated to classical thermal noise to shot noise. The latter one emerges from electron not flowing as a smooth fluidlike while thermal noise represents voltage fluctuations even if no current flows through the device. For white noise, each hertz of frequency contains the same noise power and the PSD is absolutely flat.

— $S_g(f) = f_0/f$: Pink noise. Often associated to numerous two level system oscillating at their own frequency. It manly characterizes electrical charge noise and hyperfine interaction in spin qubit device.

— $S_g(f) = (f_0/f)^2$: Red noise. Typical of Brownian motion. In our devices it may come from hyperfine interaction at very low frequency or after a cut-off frequency for the last charge two level system.

Conclusion

In this chapter, we have given tangible mathematical support to some interactions between a hole qubit and the surrounding medium. In particular, the biggest advantage of holes lies in the strong spin-orbit coupling that mixes the different valence bands, thus allowing a full electrical control of the pseudo-spin state. It is also noted that the direction of the applied electric field when manipulating the spin state is of great importance as different mechanisms come into play (g-tmr, IZ-zeeman). However, this coupling to the electric field inevitably leads to a sensitivity to the surrounding charge noise in addition to the naturally present hyperfine interaction. These two contributions can considerably reduce the performance of hole qubits and justify the characterisation of noise in a device as well as the search for operating sweet spots that minimise noise impact.

References

[1] J. M. Elzerman et al. « Single-shot read-out of an individual electron spin in a quantum dot ». In: *Nature* 430.6998 (2004), pp. 431–435. ISSN: 1476-4687. DOI: 10.1038/nature02693. URL: https://doi.org/10.1038/nature02693.

[2] N. W. Hendrickx et al. « A single-hole spin qubit ». In: *Nature Communications* 11.1 (2020). ISSN: 20411723. DOI: 10.1038/s41467-020-17211-7. arXiv: 1912.10426. URL: http://dx.doi.org/10.1038/s41467-020-17211-7.

[3] R. Maurand et al. « A CMOS silicon spin qubit ». In: *Nature Communications* 7.1 (2016), p. 13575. ISSN: 2041-1723. DOI: 10.1038/ncomms13575. URL: https://doi.org/10.1038/ncomms13575.

[4] L P Kouwenhoven, D G Austing, and S Tarucha. « Few-electron quantum dots ». In: *Reports on Progress in Physics* 64.6 (May 2001), pp. 701–736. DOI: 10.1088/0034-4885/64/6/201. URL: https://doi.org/10.1088/0034-4885/64/6/201.

[5] C. H. Yang et al. « Orbital and valley state spectra of a few-electron silicon quantum dot ». In: *Phys. Rev. B* 86 (11 Sept. 2012), p. 115319. DOI: 10.1103/PhysRevB.86.115319. URL: https://link.aps.org/doi/10.1103/PhysRevB.86.115319.

[6] R. C. C. Leon et al. « Coherent spin control of s-, p-, d- and f-electrons in a silicon quantum dot ». In: *Nature Communications* 11.1 (Feb. 2020), p. 797. ISSN: 2041-1723. DOI: 10.1038/s41467-019-14053-w. URL: https://doi.org/10.1038/s41467-019-14053-w.

[7] R. Hanson et al. « Spins in few-electron quantum dots ». In: *Reviews of Modern Physics* 79 (4 Oct. 2007), pp. 1217–1265. DOI: 10.1103/RevModPhys.79.1217. URL: https://link.aps.org/doi/10.1103/RevModPhys.79.1217.

[8] A. R. Mills et al. « Computer-automated tuning procedures for semiconductor quantum dot arrays ». In: *Applied Physics Letters* 115.11 (Sept. 2019), p. 113501. DOI: 10.1063/1.5121444. URL: https://doi.org/10.1063%2F1.5121444.

[9] H. Moon et al. « Machine learning enables completely automatic tuning of a quantum device faster than human experts ». In: *Nature Communications* 11.1 (Aug. 2020), p. 4161. ISSN: 2041-1723. DOI: 10.1038/s41467-020-17835-9. URL: https://doi.org/10.1038/s41467-020-17835-9.

[10] T.-K. Hsiao et al. « Efficient Orthogonal Control of Tunnel Couplings in a Quantum Dot Array ». In: *Phys. Rev. Applied* 13 (5 May 2020), p. 054018. DOI: 10.1103/PhysRevApplied.13.054018. URL: https://link.aps.org/doi/10.1103/PhysRevApplied.13.054018.

[11] A. C. Johnson et al. « Singlet-triplet spin blockade and charge sensing in a few-electron double quantum dot ». In: *Phys. Rev. B* 72 (16 Oct. 2005), p. 165308. DOI: 10.1103/PhysRevB.72.165308. URL: https://link.aps.org/doi/10.1103/PhysRevB.72.165308.

[12] K. C. Nowack et al. « Coherent Control of a Single Electron Spin with Electric Fields ». In: *Science* 318.5855 (2007), pp. 1430–1433. ISSN: 0036-8075. DOI: 10.1126/science.1148092. eprint: https://science.sciencemag.org/content/318/5855/1430.full.pdf. URL: https://science.sciencemag.org/content/318/5855/1430.

[13] Daniel Loss and David P. DiVincenzo. « Quantum computation with quantum dots ». In: *Physical Review A* 57 (1 Jan. 1998), pp. 120–126. DOI: 10.1103/PhysRevA.57.120. URL: https://link.aps.org/doi/10.1103/PhysRevA.57.120.

[14] F. Laloe C. Cohen-tannoudji B. Diu. « Mecanique quantique Vol1 ». In: *Rev. Mod. Phys.* 1 (3 1997), p. 500. DOI: 10.1103/RevModPhys.53.497.

[15] Stefano Bosco and Daniel Loss. *Hole spin qubits in thin curved quantum wells*. 2022. DOI: 10.48550/ARXIV.2204.08212. URL: https://arxiv.org/abs/2204.08212.

[16] Peter Stano and Daniel Loss. *Review of performance metrics of spin qubits in gated semiconducting nanostructures*. 2021. arXiv: 2107.06485 [cond-mat.mes-hall].

[17] Jonas Bylander et al. « Noise spectroscopy through dynamical decoupling with a superconducting flux qubit ». In: *Nature Physics* 7.7 (July 2011), pp. 565–570. ISSN: 1745-2481. DOI: 10.1038/nphys1994. URL: https://doi.org/10.1038/nphys1994.

[18] G. Ithier et al. « Decoherence in a superconducting quantum bit circuit ». In: *Physical Review B* 72.13 (Oct. 2005), p. 134519. DOI: 10.1103/physrevb.72.134519.

[19] E. Paladino et al. « $1/f$ noise: Implications for solid-state quantum information ». In: *Reviews of Modern Physics* 86.2 (Apr. 2014), pp. 361–418. DOI: 10.1103/revmodphys.86.361.

[20] J. M. Luttinger and W. Kohn. « Motion of Electrons and Holes in Perturbed Periodic Fields ». In: *Phys. Rev.* 97 (4 Feb. 1955), pp. 869–883. DOI: 10.1103/PhysRev.97.869. URL: https://link.aps.org/doi/10.1103/PhysRev.97.869.

[21] Benjamin Venitucci et al. « Electrical manipulation of semiconductor spin qubits within the g-matrix formalism ». In: *Physical Review B* 98.15 (Oct. 2018), p. 155319. DOI: 10.1103/physrevb.98.155319. URL: https://journals.aps.org/prb/abstract/10.1103/PhysRevB.98.155319.

[22] Alessandro Crippa et al. « Electrical Spin Driving by g-Matrix Modulation in Spin-Orbit Qubits ». In: *Physical Review Letters* 120.13 (Mar. 2018), p. 137702. DOI: 10.1103/physrevlett.120.137702.

[23] N. W. Hendrickx et al. « Fast two-qubit logic with holes in germanium ». In: *Nature* 577.7791 (2020), pp. 487–491. ISSN: 1476-4687. DOI: 10.1038/s41586-019-1919-3. URL: https://doi.org/10.1038/s41586-019-1919-3.

[24] BENJAMIN VENITUCCI. « Modeling of the electrical manipulation of hole spin qubits in silicon ». Thèse. 2020.

[25] N. W. Hendrickx et al. « A single-hole spin qubit ». In: *Nature Communications* 11.1 (July 2020), p. 3478. ISSN: 2041-1723. DOI: 10.1038/s41467-020-17211-7. URL: https://doi.org/10.1038/s41467-020-17211-7.

[26] Hannes Watzinger et al. « Heavy-Hole States in Germanium Hut Wires ». In: *Nano Letters* 16.11 (Nov. 2016), pp. 6879–6885. ISSN: 1530-6984. DOI: 10.1021/acs.nanolett.6b02715. URL: https://doi.org/10.1021/acs.nanolett.6b02715.

[27] Hannes Watzinger et al. « A germanium hole spin qubit ». In: *Nature Communications* 9.1 (2018), p. 3902. ISSN: 2041-1723. DOI: 10.1038/s41467-018-06418-4. URL: https://doi.org/10.1038/s41467-018-06418-4.

[28] S. D. Liles et al. « Electrical control of the g tensor of the first hole in a silicon MOS quantum dot ». In: *Phys. Rev. B* 104 (23 Dec. 2021), p. 235303. DOI: 10.1103/PhysRevB.104.235303. URL: https://link.aps.org/doi/10.1103/PhysRevB.104.235303.

[29] Vincent P. Michal, Benjamin Venitucci, and Yann-Michel Niquet. « Longitudinal and transverse electric field manipulation of hole spin-orbit qubits in one-dimensional channels ». In: *Physical Review B* 103 (4 Jan. 2021), p. 045305. DOI: 10.1103/PhysRevB.103.045305. URL: https://link.aps.org/doi/10.1103/PhysRevB.103.045305.

[30] Stefano Bosco and Daniel Loss. « Fully Tunable Hyperfine Interactions of Hole Spin Qubits in Si and Ge Quantum Dots ». In: *Physical Review Letters* 127 (19 Nov. 2021), p. 190501. DOI: 10.1103/PhysRevLett.127.190501. URL: https://link.aps.org/doi/10.1103/PhysRevLett.127.190501.

[31] Stefano Bosco et al. *Fully tunable longitudinal spin-photon interactions in Si and Ge quantum dots*. 2022. DOI: 10.48550/ARXIV.2203.17163. URL: https://arxiv.org/abs/2203.17163.

[32] Stefano Bosco, Bence Hetényi, and Daniel Loss. « Hole Spin Qubits in Si FinFETs With Fully Tunable Spin-Orbit Coupling and Sweet Spots for Charge Noise ». In: *PRX Quantum* 2 (1 Mar. 2021), p. 010348. DOI: 10.1103/PRXQuantum.2.010348. URL: https://link.aps.org/doi/10.1103/PRXQuantum.2.010348.

[33] Benjamin Venitucci and Yann-Michel Niquet. « Simple model for electrical hole spin manipulation in semiconductor quantum dots: Impact of dot material and orientation ». In: *Physical Review B* 99 (11 Mar. 2019), p. 115317. DOI: 10.1103/PhysRevB.99.115317. URL: https://link.aps.org/doi/10.1103/PhysRevB.99.115317.

[34] V. P. Michal et al. *Tunable hole spin-photon interaction based on g-matrix modulation*. 2022. DOI: 10.48550/ARXIV.2204.00404. URL: https://arxiv.org/abs/2204.00404.

[35] Biel Martinez and Yann-Michel Niquet. *Variability of electron and hole spin qubits due to interface roughness and charge traps*. 2021. arXiv: 2107.10902 [cond-mat.mes-hall].

[36] H. W. van Kesteren et al. « Fine structure of excitons in type-II GaAs/AlAs quantum wells ». In: *Phys. Rev. B* 41 (8 Mar. 1990), pp. 5283–5292. DOI: 10.1103/PhysRevB.41.5283. URL: https://link.aps.org/doi/10.1103/PhysRevB.41.5283.

[37] Y. Kato et al. « Gigahertz Electron Spin Manipulation Using Voltage-Controlled g-Tensor Modulation ». In: *Science* 299.5610 (2003), pp. 1201–1204. DOI: 10.1126/science.1080880.

[38] N. Ares et al. « Nature of Tunable Hole g Factors in Quantum Dots ». In: *Physical Review Letters* 110 (4 Jan. 2013), p. 046602. DOI: 10.1103/PhysRevLett.110.046602. URL: https://link.aps.org/doi/10.1103/PhysRevLett.110.046602.

[39] Matthias Brauns et al. « Electric-field dependent g-factor anisotropy in Ge-Si core-shell nanowire quantum dots ». In: *Phys. Rev. B* 93 (12 Mar. 2016), p. 121408. DOI: 10.1103/PhysRevB.93.121408. URL: https://link.aps.org/doi/10.1103/PhysRevB.93.121408.

[40] N. Piot et al. *A single hole spin with enhanced coherence in natural silicon*. 2022. arXiv: 2201.08637 [cond-mat.mes-hall].

[41] Pericles Philippopoulos, Stefano Chesi, and W. A. Coish. « First-principles hyperfine tensors for electrons and holes in GaAs and silicon ». In: *Phys. Rev. B* 101 (11 Mar. 2020), p. 115302. DOI: 10.1103/PhysRevB.101.115302. URL: https://link.aps.org/doi/10.1103/PhysRevB.101.115302.

[42] Alexander V. Khaetskii, Daniel Loss, and Leonid Glazman. « Electron Spin Decoherence in Quantum Dots due to Interaction with Nuclei ». In: *Phys. Rev. Lett.* 88 (18 Apr. 2002), p. 186802. DOI: 10.1103/PhysRevLett.88.186802. URL: https://link.aps.org/doi/10.1103/PhysRevLett.88.186802.

[43] Jan Fischer et al. « Spin decoherence of a heavy hole coupled to nuclear spins in a quantum dot ». In: *Phys. Rev. B* 78 (15 Oct. 2008), p. 155329. DOI: 10.1103/PhysRevB.78.155329. URL: https://link.aps.org/doi/10.1103/PhysRevB.78.155329.

[44] Paweł Machnikowski, Krzysztof Gawarecki, and Łukasz Cywi ński. « Hyperfine interaction for holes in quantum dots: $k \cdot p$ model ». In: *Physical Review B* 100 (8 Aug. 2019), p. 085305. DOI: 10.1103/PhysRevB.100.085305. URL: https://link.aps.org/doi/10.1103/PhysRevB.100.085305.

[45] I. A. Merkulov, Al. L. Efros, and M. Rosen. « Electron spin relaxation by nuclei in semiconductor quantum dots ». In: *Physical Review B* 65 (20 Apr. 2002), p. 205309. DOI: 10.1103/PhysRevB.65.205309. URL: https://link.aps.org/doi/10.1103/PhysRevB.65.205309.

[46] Jan Fischer et al. « Spin decoherence of a heavy hole coupled to nuclear spins in a quantum dot ». In: *Physical Review B* 78 (15 Oct. 2008), p. 155329. DOI: 10.1103/PhysRevB.78.155329. URL: https://link.aps.org/doi/10.1103/PhysRevB.78.155329.

[47] C. Testelin et al. « Hole–spin dephasing time associated with hyperfine interaction in quantum dots ». In: *Physical Review B* 79 (19 May 2009), p. 195440. DOI: 10.1103/PhysRevB.79.195440. URL: https://link.aps.org/doi/10.1103/PhysRevB.79.195440.

[48] Łukasz Cywi ński et al. « How to enhance dephasing time in superconducting qubits ». In: *Physical Review B* 77 (17 May 2008), p. 174509. DOI: 10.1103/PhysRevB.77.174509. URL: https://link.aps.org/doi/10.1103/PhysRevB.77.174509.

[49] M J Biercuk, A C Doherty, and H Uys. « Dynamical decoupling sequence construction as a filter-design problem ». In: *Journal of Physics B: Atomic, Molecular and Optical Physics* 44.15 (July 2011), p. 154002. DOI: 10.1088/0953-4075/44/15/154002. URL: https://doi.org/10.1088/0953-4075/44/15/154002.

[50] Norman F. Ramsey. « A Molecular Beam Resonance Method with Separated Oscillating Fields ». In: *Phys. Rev.* 78 (6 June 1950), pp. 695–699. DOI: 10.1103/PhysRev.78.695. URL: https://link.aps.org/doi/10.1103/PhysRev.78.695.

[51] Frank W. Olver et al. *NIST Handbook of Mathematical Functions*. 1st. USA: Cambridge University Press, 2010. ISBN: 0521140633.

[52] J. Medford et al. « Scaling of Dynamical Decoupling for Spin Qubits ». In: *Physical Review Letters* 108 (8 Feb. 2012), p. 086802. DOI: 10.1103/PhysRevLett.108.086802. URL: https://link.aps.org/doi/10.1103/PhysRevLett.108.086802.

Chapter 3

Experimental Setup

3

"While I am describing to you how Nature works, you won't understand why Nature works that way. But you see, nobody understands that."

Richard Feynman

This chapter illustrates the upstream work necessary to perform measurement of hole spin qubits for quantum processors. The first section is devoted to the device fabrication and special adjustment added to standard CMOS industrial process. Next, the second section gives a complete description of the dry dilution fridge and all the electrical lines used both for charge/spin manipulation and readout. The chapter then continues with theoretical consideration about electrical matching of quantum devices in order to perform high resolution single-shot detection of a spin. The conclusion summarizes all the previous sections and focuses on the main sample presented in this manuscript.

Contents

3.1 Device Fabrication 77
3.1.1 Active area : The nanowire 78
3.1.2 Shaping a landscape : The Gates 79
3.1.3 Claiming quantum properties : The Spacers 79
3.1.4 tank of electrons : Source and Drain 79
3.1.5 Device 81
3.2 Setup 82
3.2.1 Dry dilution fridge 82
3.2.2 Control lines 83
3.2.3 Readout lines 85
3.2.4 Setup configuration 85

3.3 Radio frequency reflectometry 86
3.3.1 Wave scattering at an impedance mismatch 87
3.3.2 Probing an electrical resonator 88
3.3.3 Dispersive readout configuration 90
3.4 Device screening 90
References 95

3.1 Device Fabrication

Spin qubit in silicon take advantage of the well-established complementary metal-oxide-semiconductor (CMOS) technology, widespread for all kind of integrated circuit (micro-processors, micro-controllers, memory cells) in electronic devices [1]. The CMOS technology is partly used to produce metal–oxide–semiconductor field-effect transistor (MOSFET), one among many transistor architecture. The latter is defined by a metallic gate, isolated from a silicon channel by an oxide insulator (or a high-k dielectric) with high capacitance and clean interfaces. Thus, the gate can capacitively tune the electrostatic landscape to allow/disable the charge flow through the channel. Note that the complementary term stands for doping process, so that the charge flow is either electrons (N-doped) or holes (P-doped). Originally, CMOS inverter were designed for their lower power consumption and low generated heat in micro-processors [2].

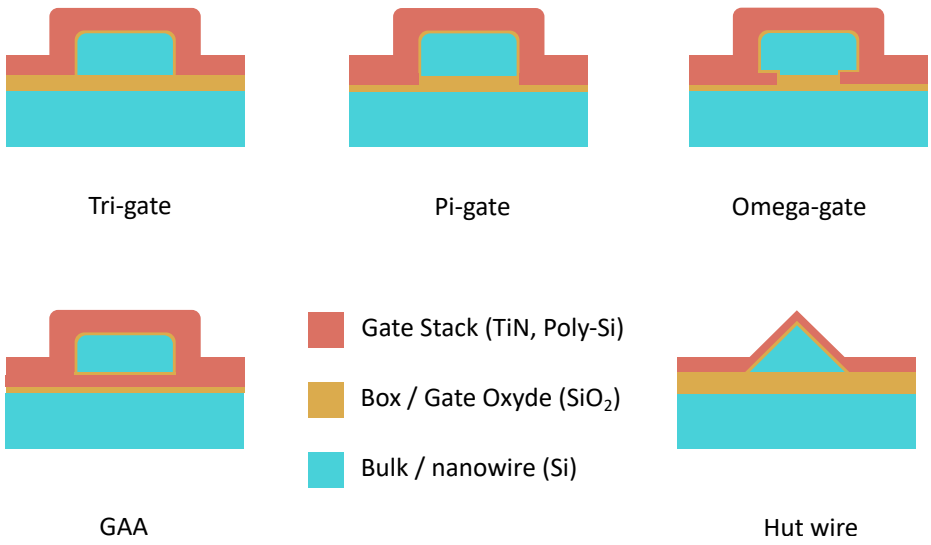

Figure 3.1 – **Silicon nanowires : Various 3 dimensional nanowire configuration.** Top row shows gate partially surrounding the nanowire. Fourth schematic is a gather all around gate (GAA) where the nanowire is totally wrapped inside a gate. Finally, the hut wire has a triangular shape configuration resulting in a strong accumulation in the apex.

The constant race for transistor miniaturization continuously pushes forward the necessity for new technologies. In particular, silicon on insulator (SOI) was one among the several manufacturing strategies [3] developed by industrial. The introduction of a buried oxide (BOX) sandwiched on one side by an intrinsic silicon bulk and on the other side by a high quality crystallized silicon layer creates

a new type of substrate. The SOI technology drastically reduces current leakage to the substrate, the parasitic capacitance within the device and helps for high-performance radio frequency reflectometry for spin readout [4, 5, 6, 7, 8].

The main technological change for nodes 14, 10 and 7 nm, is essentially due to the fin field-effect transistor (FinFET), a special type of multi-gate MOSFET. For the first time, the usual planar silicon CMOS technology is more and more abandoned in favor of 3D geometries where gate is partially (Tri/Pi/Omega gates : See Fig. 3.1) or totally surrounding (GAA) the silicon channel. Note that in case the device is used to form a quantum dot, the shape of the gate strongly influence the electron/hole wave function position thus its intrinsic properties [9, 10].

Even if transistor technology is extremely mature, the biggest bottleneck is the necessity to adjust conventional process to build an efficient quantum device [11, 12]. From now on, we should restrict our attention only on the fabrication process of the device under investigation (Fig. 4.1) [I]. A special attention will be given on unconventional steps differing from mainstream transistors.

3.1.1 Active area : The nanowire

The sample fabrication process begins on a 300 mm SOI wafer [13]. At the bottom, intrinsic bulk silicon with a thickness of 775 μm acts as a support. On top of it, a 145 nm thick layer of silicon dioxide (BOX) is thermally grown. The oxide is an excellent dielectric, which isolate the future nanowire from the bulk. In other words, it acts as a hard wall boundary for confinement. Finally, the last sheet is a thin film (around 100 nm) of extremely good feature crystalline silicon.

The first step for nanowire designing is to etch the uppermost silicon layer. Plasma oxidation quickly followed by the suppression of the formed oxide layer with hydrogen fluoride (HF) reduces the film thickness (down to 17 nm). Thereafter, patterning by deep ultra-violet (DUV) lithography outline the final shape of the nanowire (length and width). The latter is always designed so that the channel is align with the [110] direction. An optional intermediate step may be added to further reduce the dimension : the trimming process. Indeed, for DUV, $\lambda_{DUV} = 193$ nm, and resolution is limited to $\lambda_{DUV}/3$, resulting in patterning around 70 nm. Trimming is a partial etching of the resist which drastically shrink dimension of the pattern down to a few tens of nanometer. The main drawback is an alteration of the shape, in particular the corners which become rounder. Moreover, the pitch stay unchanged and thus trimming do not increase transistor density. Finally, plasma etching removes the bare silicon not protected by the resist and stops slightly below the BOX interface (up to 20 nm). Thus, wires are isolated from one another (mesa isolation technique). The full process is described in Refs [14, 15].

I. All devices are made by the LETI, a semi-industrial foundry, on 300mm SOI wafers.

3.1.2 Shaping a landscape : The Gates

Gates are the key ingredient for spin qubits trapped in quantum dots. Shape and position are of utmost importance both for the wave function design but also for spin manipulation process in case of holes. Their creation follows a bunch of classical steps in order to partially wrap the nanowire. First, a thin layer (few nm) of silicon oxide is thermally grown (thus consuming silicon at a ratio of 1:3) on top of the nanowire which acts as an insulator to avoid gate leaks. The two layers being very similar, it results in a clean interface with density of positively charged traps values typically around $\sigma_{\text{trap}} = 5 \times 10^{10}$ cm^{-2}. Note that bottom interface with the BOX is cleaner with higher mobility [16] than the top one. Finally the metal stack is composed of an atomic layer deposition of TiN (6 nm) and heavily doped poly-silicon (50 nm). E-beam patterning may replace DUV to reduce the device pitch. Nonetheless, it also greatly increase the time needed to produce a batch and tarnish the scaling up perspective in the long term.

At few kelvin, the substrate is insulating but, with the help of an optic fiber, shining light may create a bottom gate[17] to displace, vertically, the position of the 1D hole gas. Note that the use of light also changes the parasitic capacitance and highly degrades radio frequency signal for readout. A second row of gates which aim at controlling the tunnel can also be implemented [15]. For the time being, the unavailability of these industrially produced control gates is a significant barrier to the realization of complex quantum logic gates. In this sense, their development is not only necessary but urgent.

3.1.3 Claiming quantum properties : The Spacers

The lateral size of these protective side walls is the main modification from classical electronics in order to dive into the quantum world. Originally, the spacers had two main goals : first create a tunnel barrier in between quantum dots but also protect the channel from ion implantation (creating undesired dark spot) . Their dimension exponentially influence the transparency of the tunnel barrier, which is one of the most critical parameters for spin qubits trapped in QDs. Spacers width can vary from 7 nm to 70 nm and are made in Si_3N_4 with a very high charge trap density $\rho_{\text{trap}} = 5 \times 10^{17}$ cm^{-3} [11]. Considering that only charges in the first tenth nanometers truly disturb the wave function localization, it finally corresponds to a density of trap $\sigma_{\text{trap}} = 5 \times 10^{11}$, one order of magnitude higher than the Si/SiO_2 interface. Thus, in order to increase qubits reproducibility and reduce surrounding charge noise, change in spacer material is of paramount importance.

3.1.4 tank of electrons : Source and Drain

Originally, source and drain were added with a second epitaxy in order to increase the area. Then, the reservoirs were two times implanted with a low dose (LDD) and then a high dose (HDD), to create a smooth gradient of the doping

profile to reduce serial resistance, parasitic capacitances and hot-electrons injections. For the doping, Phosphorus or arsenic are used for NMOS, while boron is used for PMOS. Finally A spike annealing activate the impurities.

The device under investigation in this manuscript comes from a batch on which a new technique was employed : in situ doping. The borons atoms were directly part of the gas used for the chemical vapor deposition (CVD) of the reservoirs. Finally, To further improve the contact resistance and in order to avoid Schottky junctions, the surface of the contacts is metalized. The metal is an alloy formed by the reaction at high temperature of a deposited metal with the silicon (Here we use a $NiPt$ alloy, resulting in $NiPtSi$.).

Fig. 3.2 summarizes the main step described above in the case of a device with two gates in series.

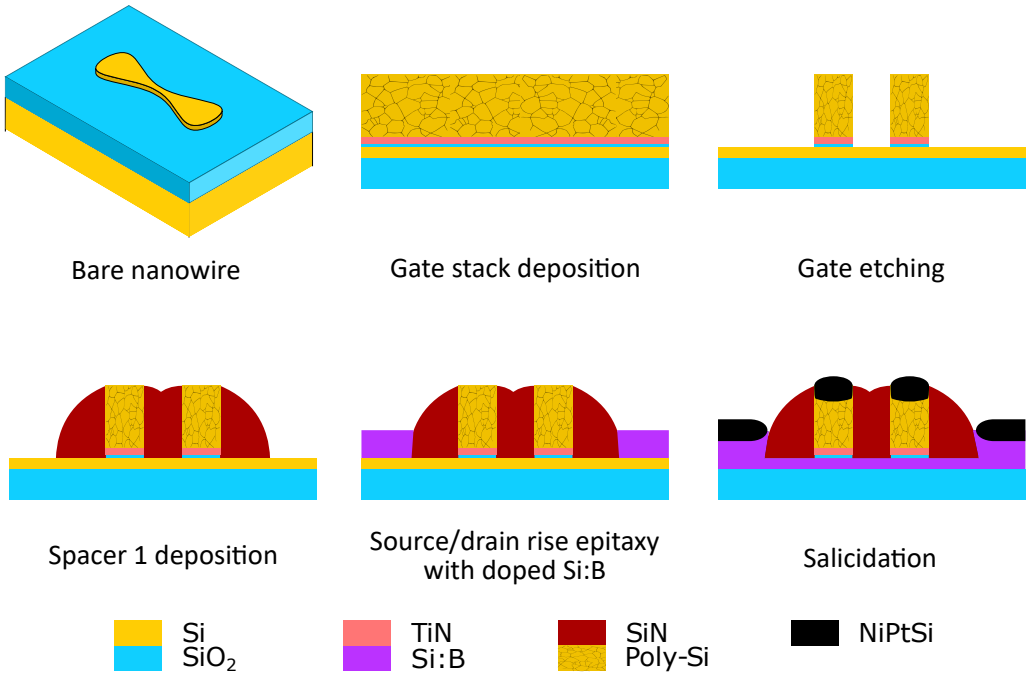

Figure 3.2 – **Main steps of the FinFET fabrication process.** Adapted and re-colorized from [18]

3.1.5 Device

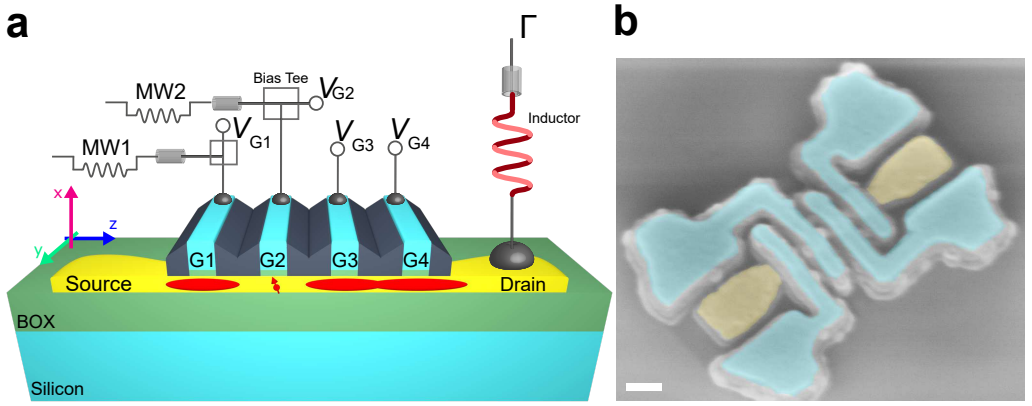

Figure 3.3 – **Device description. (a)** Simplified 3-dimensional representation of a silicon (yellow)-on-insulator (green) nanowire device with four overlapping gates (light blue) labelled G1, G2, G3 and G4. The channel is connected on both side to p-doped (Boron) source and drain acting as reservoir for the device. Gate G2 defines a quantum dot (QD2) hosting a single hole. G3 and G4 define a hole island used as reservoir and sensor for hole spin readout; G1 defines a hole island screening QD2 from dopant disorder and fluctuations in the source. Using bias-tees, both static voltages (V_{G1}, V_{G2}) and time-dependent, high-frequency voltages (MW1, MW2) can be applied to G1 and G2, respectively. The drain contact is connected to an off-chip, surface-mount inductor to enable rf reflectometry readout. The coordinate system used for the magnetic field is shown on the left side (in the crystal frame, $x = [001]$, $y = [1\bar{1}0]$ and $z = [110]$). Each axis is given a different color, which is used throughout the manuscript to indicate the magnetic field orientation. **(b)** Colorized scanning electron micrograph showing a tilted view of a device similar to the measured one. Image taken just after the etching of the spacer layers. Scale bar: 100 nm

The device is a four-gate in series silicon-on-insulator nanowire without isotopic purification (See Fig. 4.1). The undoped [110]-oriented silicon nanowire channel is 17 nm thick and 100 nm wide. It is connected to wider boron-doped source and drain pads used as reservoirs of holes. The four wrapping gates (G1, G2, G3 and G4) are 40 nm long and they are spaced by 40 nm, corresponding to a 80 nm pitch. All gates have on both side spacers approximately 25 nm long, which fill the full inter-gate spacing. The gate stack consists of a 6 nm thick SiO_2 dielectric layer followed by a metallic bilayer with 6 nm of TiN and 50 nm of heavily doped poly-silicon.

3.2 Setup

The Zeeman energy level spacing of a single hole spin qubit in semiconductor materials is of the order of a few µeV (tens of GHz range). As a consequence, to perform energy selective readout, the electronic temperature of the leads requires $T_e << g\mu_B B/k_B$ corresponding to sub kelvin temperatures. Only dilution fridge are currently able to reach few mK with a high enough cooling power. However, it is also not possible to completely isolate the qubit from the external environment since the spin must be manipulated and read out. These actions come at a notable price : noise on the system (electrical and mechanical). Thus, careful design of control and readout lines is imperative to disturb as little as possible quantum states.

3.2.1 Dry dilution fridge

Dilution refrigerators are the only way to produce continuous cooling power at only a few mk. If we consider a dry refrigerator, two cooling systems act in concert (Pulse tube (upper) & dilution (lower)). The cooling power of the dilution is provided a mixture of two isotopes of helium helium-3 and helium-4. When cooled to approximately below 870 mK, the helium mixture (mixing chamber) undergoes spontaneous phase separation to form a helium-3-rich phase (the concentrated phase) and a helium-3-poor phase (the dilute phase 6.6%). These two phases are in equilibrium and separated by a phase boundary. The trick then lies in pumping the helium-3 into the dilute phase. Pumping forces the helium 3 to move from the concentrated phase to the dilute phase, which is an endothermic process that reduces the temperature of the mixing chamber. The pumped helium 3 is then evaporated and extracted from the refrigerator (pumping chamber) through heat exchangers before being reinjected, after being purified (cold traps), in liquid form into the mixing (condensing line & impedence) chamber to complete the cycle.

Before launching the dilution, 3-He must undergo a preliminary step : condensing. Therefore, helium is pre-cooled to 3.5 K via a Pulse Tube (PT) cryocooler. PT is filled with 4-he which undergoes thermodynamic cycles at pressures varying from 10 to 30 bar. It cools down with a high cooling power the 50 K and the 4 K plates to initiate dilution and then make the condensing line continuously working. Nonetheless, because of moving parts and high pressure gas flowing, vibrations in the fridge are non negligible and must be weakened.

The refrigerator is also equipped with a three-axis vector superconducting magnet for spin measurement. The main solenoid magnet produces a magnetic field up to 6 T in the z direction, while both transverse Helmholtz coils ramp up to 1 T in the x and y directions. However, one of the axis was broken during the experiment giving no access to measurement in the xy plane. As a consequence, each rotation of the sample implies a warm up and a physical manipulation to

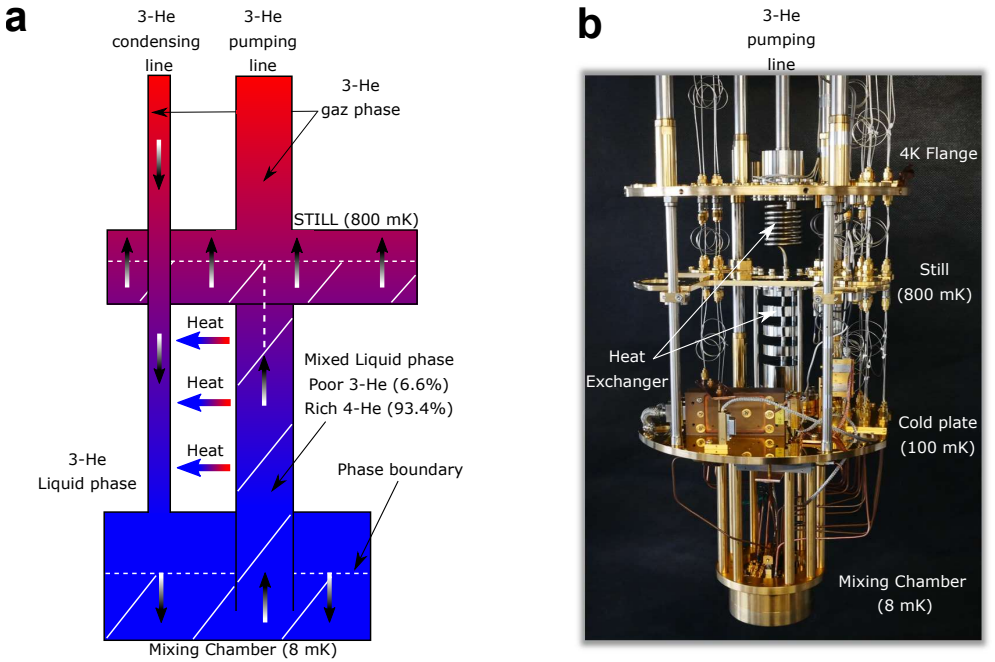

Figure 3.4 – **Dilution refrigerator main parts. (a)** Schematic representation of a dilution refrigerator. The cold plate, valve handling system and nitrogen trap out of the fridge have been removed for clarity sake. **(b)** Picture of the fridge corresponding to the schematic (a).

rotate the sample by 90°.

3.2.2 Control lines

Holes spin qubits exhibits a strong spin orbit coupling (SOC), allowing for fast and full electrical spin manipulation. As a consequence, the cryostat must be equipped with direct current (DC) lines for charge trapping and high frequency (HF) lines for charge and spin control. Both set of lines need thermalization and filtering to improve qubits quality.

DC lines

DC lines are the basic nod of action to modulate the electrostatic landscape of a semiconductor quantum dots. High resolution (21 bits) and stability voltage sources enable confining charges for ages, a basic requirement for applications such as spin qubits or single electron pumps.

The fridge is delivered with 48 low frequency lines. These lines are decom-

posed into 2 shielded looms, containing each one 12 twisted pair with a high thermal resistance in order to avoid thermal bridges between the plates. Given Johnson-Nyquist noise (thermal noise), a resistor in a short circuit dissipates a noise power of $P = 4k_BTR\Delta f$ where k_B is Boltzmann's constant, R the resistor value, T the electronic temperature and Δf the bandwidth. The generated noise can be transmitted through out the circuit whereas hole spin qubits are highly sensitive to electrical noise. Thus, filtering is a critically important consideration.

To attenuates those fluctuations, lines have to be both thermally anchored at each stage (reducing T) and filtered in frequency (reducing Δf). The first point is perfectly realized by BlueFors. To meet the second objective, we added a homemade five stage low pass filter (2 simple RC filters followed by 3 Π- filters) at the mixing chamber rejecting all high frequency components. Note the use of five filters when theoretically one should be sufficient. Indeed, any low-pass filter behaves in reality like a band-pass filter, making it almost useless for filtering high frequencies (f»fc). A short summary is given in Table. 3.1. Moreover, the lines are also filtered at the PCB level by a last RC filter, with a cut-off frequency $f_c = 8\,\text{kHz}$ ($R_{PCB} = 2\,\text{kOhm}$ / $C_{PCB} = 10\,\text{nF}$). On top of the cryostat, the DC gate voltages are generated by a Itest high stability voltage sources (BE2142).

Type	Value/ref	f_c : Cut-off 3 dBm
RC	$R_1 = 1.2\,\text{kOhm}$ / $C_1 = 1\,\text{nF}$	133 kHz
RC	$R_2 = 500\,\text{Ohm}$ / $C_2 = 2.2\,\text{nF}$	145 kHz
Π	LFCN-80	145 MHz
Π	LFCN-1450	1.9 GHz
Π	LFCN-5000	5.6 GHz

Table 3.1 – Five stages filter important characteristics

HF lines

Qubit operation also requires fast manipulations at higher frequencies from MHz (charge : pulsing/readout) to several GHz (spin : MW burst). The fridge is initially equipped with only height coaxial lines (up to 20 GHz) from the top to the puck. Each coaxial line is divided in two sections with different materials. From Room temperature down to the MXC, CuproNickel cables (SCuNi) with a diameter of 0.86 mm avoid thermal bridge in between the stages while conducting electrons. From the MXC to the puck, cooper cables are used in order to both conduct and thermalize well. With HF coaxial line, no frequency domain filtering may be used to cancel noise at the device level. Therefore, reduce the power of a signal without without appreciably distorting its waveform is the only way to reduce the noise. But, the loss are dissipated at the stage where the attenuation

is located, thus inducing a heat load, that may warm up the fridge. Consequently, attenuators are distributed among the stages according to Fig. 3.5 in order to optimize the thermal budget. In addition to the available lines, we also designed a cable tree with ten more coaxial lines, for a total of eighteen available.

In term of signals, sinusoidal microwaves are supplied by a vector IQ signal generator (R&S SMW200A). The IQ amplitude are independently controlled by two channels of an arbitrary waveform generator (AWG) Tektronix AWG5200. Other channels of the AWG are used to generate the different pulse schemes for readout.

Bias T

To apply both DC and HF on a single gate, we combine both signal at the PCB level via a bias tee. It is simply a three-port network acting as a diplexer. The lf (low frequency) port sets the bias while the hf (high-frequency) port passes the radio-frequency signals but blocks the biasing levels. In our case, we made it only with a resistor ($R_{BT} = 1\,\text{Mohm}$) and a capacitor ($C_{BT} = 10\,\text{nF}$) corresponding to a cut-off frequency $f_c^{BT} = 16\,\text{Hz}$ ($60ms$). In almost all experiments, readout time is set around a few hundred of micro-second. In this case, there is no need to introduce a first order high pass correction on the signal (decay over time of a square is less than 0.5%).

3.2.3 Readout lines

To perform radio frequency reflectometry, a special readout circuit was implemented both in the fridge and on the PCB. Before being reflected by the sample, the microwave signal goes down through a very attenuated coaxial line ($-90\,\text{dB}$ see Fig. 3.5 : line RF-Readout (down)) including a directional coupler. The line finally connects to the sample after being filtered by a band-pass filter made by a low pass-filter ($f_c^{LP} = 200\,\text{MHz}$) and a high pass-filter ($f_c^{HP} = 600\,\text{MHz}$). After reflexion, the signal travels, up to the 4K flange, through a superconducting cable in NbTiN. The signal is then amplified by a low noise amplifier (equivalent noise temperature 1.6K) with a 32 dB gain. Outside the fridge, two additional amplifiers (13 dB and 19 dB), interposed by a $-3\,\text{dB}$ attenuator to avoid local oscillations, amplify once again the signal for a total of 61 dB.

3.2.4 Setup configuration

Fig. 3.5 summarizes all the lines and their components used in the experiments described inside this manuscript.

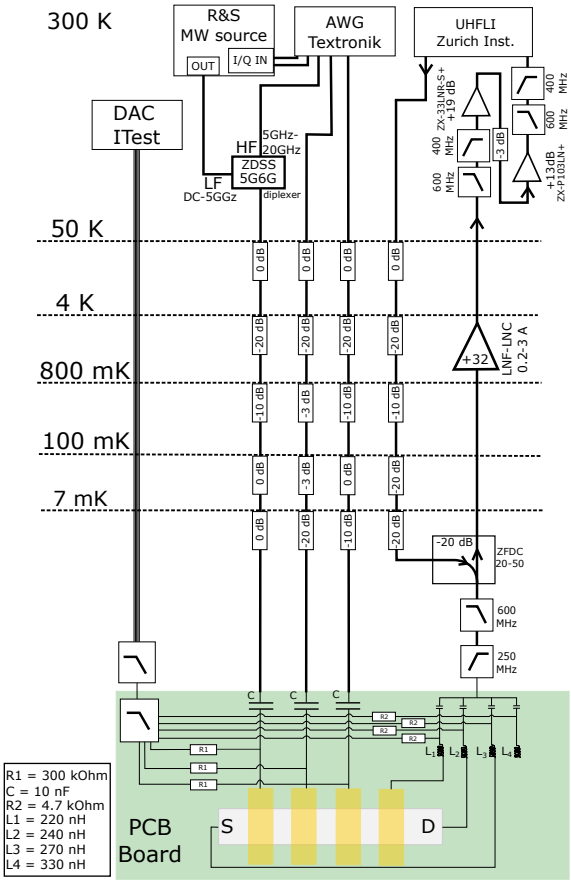

Figure 3.5 – **Experimental setup.** Dilution fridge with all electrical connections to the sample.

3.3 Radio frequency reflectometry

Almost all phenomena in quantum devices evolve over time so that time-average measurement is not efficient enough by itself. Moreover, the measurement problem impose to measure only some definite states meaning that experiences must be repeated a great number of time to reconstruct the superposition state. Thus, the necessity for ultra fast single shot readout to measure such transient effect is a requirement for efficient quantum computing. In that context, radio-frequency reflectometry shows great promises to determine the spin of a particle trapped in quantum dots using spin to charge conversion. Nonetheless, latter technique will probably be a temporary bridge before demonstrating proper non quantum demolition measurement of a spin via a coupled superconducting resonator [19, 20, 21, 22].

3.3.1 Wave scattering at an impedance mismatch

When achieving frequencies above a hundred MHz, wavelength of traveling wave is of the order of one meter. In other terms, the quasistatic approximation does not hold anymore and signal propagation must be taken into account. Coaxial cables are popular transmission lines used to carry high frequency signals. They behave as microwaves wave-guide, whose extremity elements (shord,open, load) greatly influence signal' reflective properties. Next, we describe the behavior of a signal traveling in a coaxial line to understand how radio frequency reflectometry setup can make a good charge sensor.

Coaxial cables may be modeled by lumped-elements representing the capacitance (resp inductance) (L_l, C_l) per unit length to represent a transmission-line. Analyzing the voltage $(V(x,t))$ an current $(I(x,t))$ at each node, the telegraph equations give as solution [23] :

$$V(x,t) = V_+(x - \frac{t}{v}) + V_-(x + \frac{t}{v}) \tag{3.1}$$

$$I(x,t) = \frac{1}{Z_0}[V_+(x - \frac{t}{v}) - V_-(x + \frac{t}{v})] \tag{3.2}$$

where $\pm$ stands for the direction of propagation along x axis and $v = 1/\sqrt{L_l C_l}$ is the phase speed inside the transmission line. Moreover, the ratio between the signal current and the signal voltage is given by the characteristic impedance :

$$Z_0 = \sqrt{\frac{L_l}{C_l}} \tag{3.3}$$

If the coaxial cable is connected to any element not properly matched $(Z_{load}(\omega) \neq Z_0)$, part of the signal must reflected back to satisfy boundary conditions.

$$\frac{V(x,\omega)}{I(x,\omega)} = Z_{load} \tag{3.4}$$

Defining as $x = 0$ the position of the connected element, we obtain the reflection coefficient for a given angular frequency :

$$\Gamma(\omega) = \frac{V_-(0,\omega)}{V_+(0,\omega} = \frac{Z_{load}(\omega) - Z_0}{Z_{load}(\omega) + Z_0} \tag{3.5}$$

By convention, in the microwave industry, all components are matched so that $Z_0 = 50\,\text{ohm}$. The sensitivity to a purely resistive load ($\partial|\Gamma|/\partial Z_{load}$) is maximum when $Z_{load} << Z_0$ and quickly drops to zero when $Z_{load} >> Z_0$. Thus, analysing the reflected (transmitted) signal provides information about the load at the end of the line.

3.3.2 Probing an electrical resonator

The charge sensor, is in our case a gate or reservoir embedded as a resistive element in a matching network at the end of a transmission line including a resonator. Among many model, the simplest one to describe the system is a RLC resonator. The equivalent circuit is depicted in Fig. 3.6-a.

$$Z_{load} = R + j(\omega L - \frac{1}{\omega C}) \tag{3.6}$$

where $j = \sqrt{-1}$. The circuit forms an harmonic oscillator, where the energy is bouncing back and forth from the capacitor to the inductor while being slowly dissipated by the resistor. Γ is a complex quantity and we need a two dimensional subspace to characterize it such as $(Re(\Gamma), Im(\Gamma))$ or $(|\Gamma|, \varphi = arctan(Im(\Gamma)/Re(\Gamma))$. Conventionally, in spin qubit community, amplitude and phase are used to described the response of a resonator. The reflection spectrum exhibits a resonance at the frequency f_r given by :

$$f_r = \frac{1}{2\pi\sqrt{LC}} \tag{3.7}$$

At the resonance frequency, the signal experiences a huge deep, extremely sensitive to local change of (L,C) see Fig. 3.6-b. Note also that the resistance change the depth of the peak and may also be monitored by reflectometry. Consequently, LC resonators match the characteristic impedance of a transmission line and translate the change of sample capacitance to a change of the reflection coefficient Γ. The change of capacitance of the load is of two types :

➥ Pure capacitive shift (static) due to a charge jumping to another site.

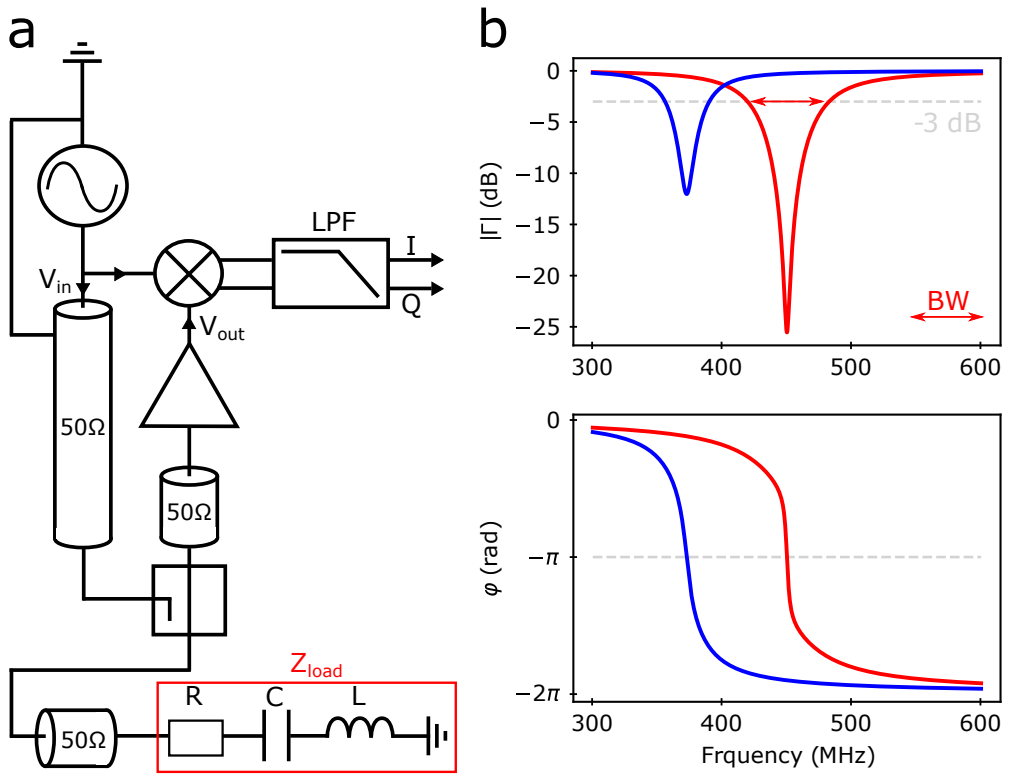

Figure 3.6 – **Radio frequency reflectometry.** **(a)** Setup used for rf-reflectometry connected to a load. **(b)** Reflected signal (Amplitude & phase) probed by homodyne detection when the carrier tone is swept. A change in R modifies the deep of the resonance while a change in C shift the resonance frequency. Both phenomenon can be measured by probing the cavity at a fix frequency.

➙ A dynamic term embedded in the parasitic capacitance C_{par}. The term comprises on the one hand a change in the quantum capacitance due to resonance of a charge with a reservoir or another QD. The quantum capacitance is a correction due to the excess of the kinetic energy compared to the electrostatic energy needed to add a fermion in the dot (reversible) [5, 24, 25]. On the other hand the quantum tunneling capacitance (irreversible).

Finally, comparing amplitude and phase of emitted and reflected allows to make a charge detector. The process can be either performed via homodyne detection (need low frequency compare to digitization) or heterodyne detection when probing high frequency resonators[II]. For more details follow ref [23, 26] for theory and ref [6, 24, 27, 28] for experiments.

II. The homodyne detection is preferred if realizable because it avoids mixers calibrations over time. In this sense, the UHF lock-in amplifier used in this thesis is a powerful instrument.

We also define the bandwidth (Δ_f) of the resonator in term of a Band-stop filter i.e frequencies where half-power is reflected ($|\Gamma|(\Delta_f) < -3\,\mathrm{dB}$) (see Fig. 3.6-b). The bandwidth represents two times the Nyquist rate $\tau_{sampling} = 1/(2 \cdot \Delta f)$ (give by the sampling theorem), where the sampling rate is the time needed to evaluate a change in Z_{laod} parameters. The smaller is the bandwidth, the more sensitive is the system, but as a counterpart, it can only detect slow events.

3.3.3 Dispersive readout configuration

Similar to charge detection methods recently applied to SOI nanowire devices [29, 30], we accumulate a large hole island under the gates G3 and G4, as sketched in Fig. 4.1-a. The island acts both as a charge reservoir and electrometer for the quantum dot Q2 located under G2. However, unlike the above-mentioned earlier implementations, the electrometer is sensed by rf dispersive reflectometry on a tank LC resonator connected to the drain rather than to a gate electrode. Single-shot readout of this hole spin is performed by means of a spin-to-charge conversion technique [31] based on the real-time detection of spin-selective tunneling to the reservoir, a widely used method often referred to as "Elzerman readout".
To this aim, a commercial surface-mount inductor ($L = 240\,\mathrm{nH}$) is wire bonded to the drain pad. This configuration involves a parasitic capacitance to ground $C_p = 0.54\,\mathrm{pF}$, leading to resonance frequency $f = 449.81\,\mathrm{MHz}$. The high value of the loaded quality factor $Q \approx 10^3$ enables fast, high-fidelity charge sensing. The resonator characteristic frequency experiences a shift at each Coulomb resonance of the hole island, *i.e.* when the electrochemical potential of the island lines up with the drain Fermi energy. This leads to a dispersive shift in the phase φ_d of the reflected radio-frequency signal, which is measured through homodyne detection.

3.4 Device screening

Although, a single copy of the device has been studied at cryogenic temperature, numerous nominally identical samples were extensively characterized at room temperature. 90% of the 4 gates devices (i.e around 125 devices) with 80 nm pitch are functional across the full 300 mm wafer. The devices are defined as functional according to 3 criteria :

- With any gate Gi closed ($V_{\mathrm{G}i} = +0.2$ V) and the other gates Gj open ($V_{\mathrm{G}j} = -2$ V, $j \neq i$), the source-drain current I_{D} must be lower than 10^{-11} A at source-drain bias $V_{\mathrm{DS}} = 50$ mV.
- With all gates open ($V_{\mathrm{G}i} = -2$ V), I_{D} must be greater than 10^{-7} A at $V_{\mathrm{DS}} = 50$ mV.
- The gate leakage current $I_{\mathrm{G}i}$ must be lower than 10^{-11} A .

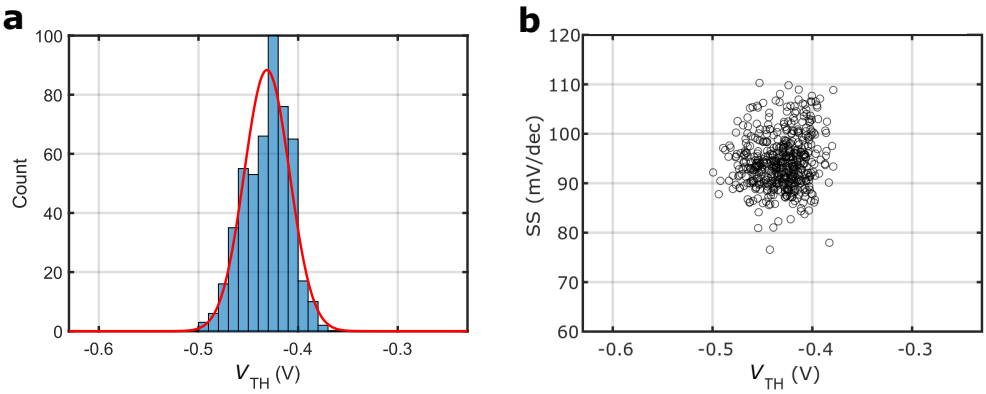

Figure 3.7 – **Yield across the full wafer. (a)** Distribution of the room temperature threshold voltages V_{TH} of all gates of the devices similar to the one measured in this paper (four 40 nm long gates separated by 40 nm, on top of a 17 nm thick and 100 nm wide channel, with a 6 nm thick SiO_2 gate oxide). All 3 other gates are biased at -2 V. The red curve is a gaussian fit. V_{TH} is defined as the gate voltage where the derivative of the transconductance $\partial g_m/\partial V_G$ is maximum. **(b)** Distribution of sub-threshold slope SS versus V_{TH} for all gates of all functional devices.

Figure 3.7-a collects the room temperature threshold voltages V_{TH} measured [III] for each gate of each functional device (with -2 V applied on the 3 other gates). Figure 3.7b displays the sub-threshold slope (SS) versus the threshold voltage V_{TH} of each gate. The distribution of threshold voltages is very peaked around $V_{TH} = -0.43$ V (standard deviation: 22 mV), which testifies the good uniformity of the devices at the wafer scale. As a comparison, the recent Ref. [32] reports a standard deviation of up to 145 mV for the first gate layer. The uniformity of the devices in the wafer is further supported by the consistency of the sub-threshold slopes.

As compared to Ref. [33], the fabrication process has been improved through several major changes, that are for instance described in Ref. [15] (except for the exchange gates, that are not included in the present wafer).

- ✏ The source and drain are now doped *in situ* (during the overgrowth of the contacts). They were previously doped by ion implantation, which resulted in the spurious implantation of dopants near the dots.
- ✏ The source/drain junctions have been engineered to optimize the coupling with the reservoirs, including changes in the spacer design and thermal annealing step.

III. Measures have been performed by the LETI team.

- ✏ The high-k dielectric gate stacks (1.9 nm of $HfSiO_2$ on top of a thin interfacial SiO_2 layer) have been abandoned in favor of a pure silicon oxide solution. High-k dielectrics such HfO_2 are indeed known to give rise to remote Coulomb scattering, which can be very detrimental in the few holes regime [34].
- ✏ The silicon channel is thicker (17 nm) than in Ref. [33] (10 nm), and therefore the devices are more resilient to disorder [34].

Conclusion

Following the different sections of this chapter, we have first understood the fabrication of samples in order to trap a single charge in a QD. Then, the sample was isolated from the external environment by placing it at very low temperature in a cryostat while being electrically connected for charge and spin manipulations. Finally, the description of radio frequency reflectometry allows the detection of both static and dynamic charges close to the sensor. All of these ingredients together make it possible to start experiments to investigate for a spin to charge conversion, in order to build a spin qubit.

References

[1] S.M. Sze. *Semiconductor Devices: Physics and Technology*. John Wiley & Sons Singapore Pte. Limited, 2012. ISBN: 9780470873670. URL: https://books.google.fr/books?id=gmmscQAACAAJ.

[2] J.P. Colinge and E. Demoulin. « A high density CMOS inverter with stacked transistors ». In: *IEEE Electron Device Letters* 2.10 (1981), pp. 250–251. DOI: 10.1109/EDL.1981.25421.

[3] T. Stanley. « Revenue potential from SOI production ». In: *1992 IEEE International SOI Conference*. 1992, pp. 166–167. DOI: 10.1109/SOI.1992.664842.

[4] Alessandro Crippa et al. « Level Spectrum and Charge Relaxation in a Silicon Double Quantum Dot Probed by Dual-Gate Reflectometry ». In: *Nano Letters* 17.2 (Jan. 2017), pp. 1001–1006. DOI: 10.1021/acs.nanolett.6b04354.

[5] A. Crippa et al. « Gate-reflectometry dispersive readout and coherent control of a spin qubit in silicon ». In: *Nature Communications* 10.1 (2019), p. 2776. ISSN: 2041-1723. DOI: 10.1038/s41467-019-10848-z. URL: https://doi.org/10.1038/s41467-019-10848-z.

[6] L. Hutin et al. « Gate reflectometry for probing charge and spin states in linear Si MOS split-gate arrays ». In: *2019 IEEE International Electron Devices Meeting (IEDM)*. 2019, pp. 37.7.1–37.7.4. DOI: 10.1109/IEDM19573.2019.8993580.

[7] Matias Urdampilleta et al. « Gate-based high fidelity spin readout in a CMOS device ». In: *Nature Nanotechnology* 14.8 (2019), pp. 737–741. ISSN: 1748-3395. DOI: 10.1038/s41565-019-0443-9. URL: https://doi.org/10.1038/s41565-019-0443-9.

[8] Virginia N. Ciriano-Tejel et al. « Spin Readout of a CMOS Quantum Dot by Gate Reflectometry and Spin-Dependent Tunneling ». In: *PRX Quantum* 2 (1 Mar. 2021), p. 010353. DOI: 10.1103/PRXQuantum.2.010353. URL: https://link.aps.org/doi/10.1103/PRXQuantum.2.010353.

[9] Stefano Bosco, Bence Hetényi, and Daniel Loss. « Hole Spin Qubits in Si FinFETs With Fully Tunable Spin-Orbit Coupling and Sweet Spots for Charge Noise ». In: *PRX Quantum* 2 (1 Mar. 2021), p. 010348. DOI: 10.1103/PRXQuantum.2.010348. URL: https://link.aps.org/doi/10.1103/PRXQuantum.2.010348.

[10] Stefano Bosco and Daniel Loss. « Fully Tunable Hyperfine Interactions of Hole Spin Qubits in Si and Ge Quantum Dots ». In: *Physical Review Letters* 127 (19 Nov. 2021), p. 190501. DOI: 10.1103/PhysRevLett.127.190501. URL: https://link.aps.org/doi/10.1103/PhysRevLett.127.190501.

[11] M. Vinet et al. « Material and integration challenges for large scale Si quantum computing ». In: *2021 IEEE International Electron Devices Meeting (IEDM)*. 2021, pp. 14.2.1–14.2.4. DOI: 10.1109/IEDM19574.2021.9720708.

[12] M. F. Gonzalez-Zalba et al. « Scaling silicon-based quantum computing using CMOS technology ». In: *Nature Electronics* 4.12 (Dec. 2021), pp. 872–884. ISSN: 2520-1131. DOI: 10.1038/s41928-021-00681-y. URL: https://doi.org/10.1038/s41928-021-00681-y.

[13] Michel Bruel. « Process for the production of thin semiconductor material films ». 1994. URL: https://patents.google.com/patent/US5374564A/en.

[14] B. Bertrand et al. « Development of spin quantum bits in SOI CMOS technology ». In: *2018 IEEE 18th International Conference on Nanotechnology (IEEE-NANO)*. 2018, pp. 1–3. DOI: 10.1109/NANO.2018.8626273.

[15] T. Bedecarrats et al. « A new FDSOI spin qubit platform with 40 nm effective control pitch ». In: *IEDM* (2021). DOI: 10.1109/IEDM19574.2021.9720497. URL: https://ieeexplore.ieee.org/document/9720497.

[16] H. Bohuslavskyi et al. « 28nm Fully-depleted SOI technology: Cryogenic control electronics for quantum computing ». In: (2017), pp. 143–144. DOI: 10.23919/SNW.2017.8242338.

[17] B. Roche et al. « A tunable, dual mode field-effect or single electron transistor ». In: *Applied Physics Letters* 100.3 (2012), p. 032107. DOI: 10.1063/1.3678042. eprint: https://doi.org/10.1063/1.3678042. URL: https://doi.org/10.1063/1.3678042.

[18] Andrea Corna. « Single Spin control and readout in silicon coupled quantum dots ». Thèse. 2017.

[19] V. P. Michal et al. *Tunable hole spin-photon interaction based on g-matrix modulation*. 2022. DOI: 10.48550/ARXIV.2204.00404. URL: https://arxiv.org/abs/2204.00404.

[20] Stefano Bosco et al. *Fully tunable longitudinal spin-photon interactions in Si and Ge quantum dots*. 2022. DOI: 10.48550/ARXIV.2203.17163. URL: https://arxiv.org/abs/2203.17163.

[21] Patrick Harvey-Collard et al. « Coherent Spin-Spin Coupling Mediated by Virtual Microwave Photons ». In: *Phys. Rev. X* 12 (2 May 2022), p. 021026. DOI: 10.1103/PhysRevX.12.021026. URL: https://link.aps.org/doi/10.1103/PhysRevX.12.021026.

[22] Cecile X. Yu et al. *Strong coupling between a photon and a hole spin in silicon*. 2022. DOI: 10.48550/ARXIV.2206.14082. URL: https://arxiv.org/abs/2206.14082.

[23] Florian Vigneau et al. *Probing quantum devices with radio-frequency reflectometry*. 2022. arXiv: 2202.10516 [cond-mat.mes-hall].

[24] Anderson West et al. « Gate-based single-shot readout of spins in silicon ». In: *Nature Nanotechnology* 14.5 (2019), pp. 437–441. ISSN: 1748-3395. DOI: 10.1038/s41565-019-0400-7. URL: https://doi.org/10.1038/s41565-019-0400-7.

[25] Rami Ezzouch et al. « Dispersively Probed Microwave Spectroscopy of a Silicon Hole Double Quantum Dot ». In: *Physical Review Applied* 16.3 (Sept. 2021). ISSN: 2331-7019. DOI: 10.1103/physrevapplied.16.034031. URL: http://dx.doi.org/10.1103/PhysRevApplied.16.034031.

[26] R. Mizuta et al. « Quantum and tunneling capacitance in charge and spin qubits ». In: *Phys. Rev. B* 95 (4 Jan. 2017), p. 045414. DOI: 10.1103/PhysRevB.95.045414. URL: https://link.aps.org/doi/10.1103/PhysRevB.95.045414.

[27] J. I. Colless et al. « Dispersive Readout of a Few-Electron Double Quantum Dot with Fast rf Gate Sensors ». In: *Phys. Rev. Lett.* 110 (4 Jan. 2013), p. 046805. DOI: 10.1103/PhysRevLett.110.046805. URL: https://link.aps.org/doi/10.1103/PhysRevLett.110.046805.

[28] M. F. Gonzalez-Zalba et al. « Probing the limits of gate-based charge sensing ». In: *Nature Communications* 6.1 (Jan. 2015), p. 6084. ISSN: 2041-1723. DOI: 10.1038/ncomms7084. URL: https://doi.org/10.1038/ncomms7084.

[29] Fabio Ansaloni et al. « Single-electron operations in a foundry-fabricated array of quantum dots ». In: *Nature Communications* 11.1 (2020), pp. 1–7. ISSN: 20411723. DOI: 10.1038/s41467-020-20280-3. URL: http://dx.doi.org/10.1038/s41467-020-20280-3.

[30] Emmanuel Chanrion et al. « Charge detection in an array of CMOS quantum dots ». In: *Physical Review Applied* 14.2 (2020), p. 1. ISSN: 23317019. DOI: 10.1103/PhysRevApplied.14.024066. arXiv: 2004.01009. URL: https://doi.org/10.1103/PhysRevApplied.14.024066.

[31] J. M. Elzerman et al. « Single-shot read-out of an individual electron spin in a quantum dot ». In: *Nature* 430.6998 (2004), pp. 431–435. ISSN: 1476-4687. DOI: 10.1038/nature02693. URL: https://doi.org/10.1038/nature02693.

[32] A. M. J. Zwerver et al. « Qubits made by advanced semiconductor manufacturing ». In: *Nature Electronics* 5.3 (Mar. 2022), pp. 184–190. ISSN: 2520-1131. DOI: 10.1038/s41928-022-00727-9. URL: https://doi.org/10.1038/s41928-022-00727-9.

[33] R. Maurand et al. « A CMOS silicon spin qubit ». In: *Nature Communications* 7.1 (2016), p. 13575. ISSN: 2041-1723. DOI: 10.1038/ncomms13575. URL: https://doi.org/10.1038/ncomms13575.

[34] Biel Martinez and Yann-Michel Niquet. *Variability of electron and hole spin qubits due to interface roughness and charge traps*. 2021. arXiv: 2107.10902 [cond-mat.mes-hall].

Chapter 4

From device to qubit

"I learned very early the difference between knowing the name of something and knowing something."

Richard Feynman

In the global race to build a usable and efficient quantum computer, hole spin qubits appear like the ugly duckling. The lack of awareness of hole properties coupled to a huge development gap compare to mature technologies such as superconducting qubit, partially explaining that the field remains confined to fundamental physics. As with all spin qubits, one of the most challenging steps is the development of an efficient charge sensor. Consequently, developing state of the art spin readout protocols would be a first step to lend credibility to the technology. The subsequent chapter illustrates how to build a single shot sensor in a silicon four gates pump nanowire, for a single hole spin qubit. The first section presents the device and all surrounding connections, while the second section focuses solely on one component : the resonator, corresponding to an inductor galvanically connected to the drain. Next, the following parts are dedicated to adjustment of the charge sensor and to the detection of the spin tail via spin to charge conversion, a feature described for the very first time by Elzerman. Finally, the last section shows single hole spin manipulation up to several MHz.

Contents

4.1 Device 99
4.2 Resonators 101
4.3 Charge sensor 102
4.3.1 Coulomb peaks 102
4.3.2 QD3 & QD4 : Single dot regime 103
4.3.3 Stability diagram of the first hole 105

4.4 Spin readout 106
4.4.1 Energy selective spin readout 107
4.4.2 Rates tuning 107
4.4.3 Three stages protocol 109
4.4.4 Elzerman tail : time average measurement 109
4.4.5 Fast single shot spin measurement 112
4.5 Initialization & Manipulation 114
4.5.1 Two stage protocol 114
4.5.2 Rabi chevrons 114
References 119

4.1 Device

In this manuscript, a single transistor was fully characterized at based temperature. Hence, "the device" and its synonyms will always refer to a CMOS four gate in series (pump device) as sketched in the schematic below (Fig. 4.1-a).

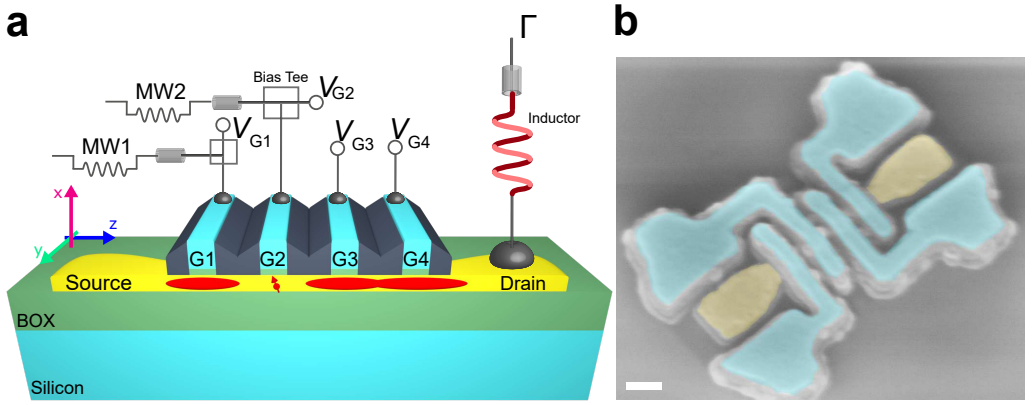

Figure 4.1 – **Device description.** **(a)** Simplified 3-dimensional representation of a longitudinal cut along the channel. Silicon (yellow)-on-insulator (green) nanowire device with four overlapping gates (light blue) labeled G1, G2, G3 and G4. The channel is connected on both side to p-doped (Boron) source and drain acting as reservoirs. G2 defines a quantum dot (QD2) hosting a single hole. G3 and G4 define a hole island used as reservoir and a charge sensor for hole spin readout; G1 accumulates a hole island screening QD2 from dopant disorder and fluctuations in the source. Using bias-tees, both static voltages (V_{G1}, V_{G2}) and time-dependent, high-frequency voltages (MW1, MW2) can be applied to G1 and G2, respectively. The drain contact is connected to an off-chip, surface-mount inductor to enable radio frequency reflectometry readout. The coordinate system used for the magnetic field is shown on the left side (in the crystal frame, $x = [001]$, $y = [1\bar{1}0]$ and $z = [110]$). Each axis is given a different color, which is used throughout the manuscript to indicate the magnetic field orientation. **(b)** Colorized scanning electron micrograph showing a tilted view of a device similar to the measured one. Image taken just after the etching of the spacer layers. Scale bar: 100 nm

The device is a four-gate in series silicon-on-insulator nanowire without isotopic purification. The undoped [110]-oriented silicon nanowire channel is 17 nm thick and 100 nm wide. It is connected to wider boron-doped source and drain pads used as reservoirs of holes. The four wrapping gates (G1, G2, G3 and G4) are 40 nm long and they are spaced by 40 nm, corresponding to a 80 nm pitch. All gates have on both sides spacers, which fill the full inter-gate spacing. The gate

stack consists of a 6 nm thick SiO_2 dielectric layer followed by a metallic bilayer with 6 nm of TiN and 50 nm of heavily doped poly-silicon.

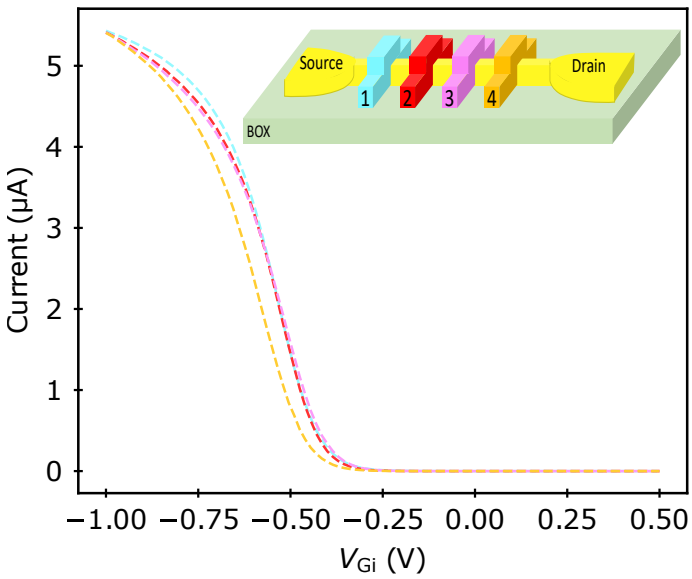

Figure 4.2 – **Room temperature I-V characteristics**. Upon sweeping I-V_{Gi}, other gates are set to −1 V and V_{ds} = 10 mV. Except for G4, I-V curves are extremely similar. This uniformity for 4 gates devices, is excellent at any position on the wafer.

We connected DC lines to source, drain and all four gates to control the electrostatic landscape of the device. I-V characteristics at room temperature are displayed in Fig. 4.2 and show an excellent uniformity thanks to semiconductor industrial processes. The yield of the 4-gate devices across the full 300 mm wafer reaches 90%. At low temperature, applying a negative voltage on a gate creates a QD, which can be filled with a precise number of holes [1, 2]. To perform charge and spin manipulation, semi-rigid coaxial lines are routed to G1 and G2 using on-PCB bias tees. Finally, three commercial surface-mount inductors (220 nH, 270 nH and 240 nH) are soldered on board and bounded respectively to G4, source and drain. Note that only the inductor connected to the drain is displayed on Fig. 4.1.

Similar to charge detection methods recently applied to SOI nanowire devices [3, 4], we accumulate a large hole island under the gates G3 and G4. The island acts both as a charge reservoir and electrometer for the quantum dot QD2 located under G2. However, unlike the above-mentioned implementations, the electrometer is sensed by rf dispersive reflectometry on a tank LC resonator connected to the drain rather than to a gate electrode. Single-shot readout of this single hole spin is performed by means of a spin-to-charge conversion technique based on the real-time averaged time traces acquired via homodyne detection of spin-selective tunneling to the reservoir, a widely used method often referred to as "Elzerman readout"[5].

4.2 Resonators

The commercial inductor (from Coilcraft) soldered on the board acts as an LC tank resonator when performing radio frequency reflectometry, thanks to the parasitic capacitance to the ground [6, 7]. Fig. 4.3-a shows the typical reflected signal frequency response, at based temperature, using homodyne detection when the device is turned off. Three resonances respectively at 434.4 MHz, 449.98 MHz and 489.68 MHz exhibit a clear drop in phase (See tab. 4.1). The spectroscopy also reveals a background with slow variations of the amplitude. Those standing waves originate from the poor matching of the 4 K amplifier, and substantially distorts the lineshape of LC resonances in amplitude. Conversely, phase signal is pretty robust to the distortion. Note that, we post treated the phase signal by removing the electronic delay of the measurement set-up stemming from long cables[8]. For clarity's sake, we also unwrapped the phase.

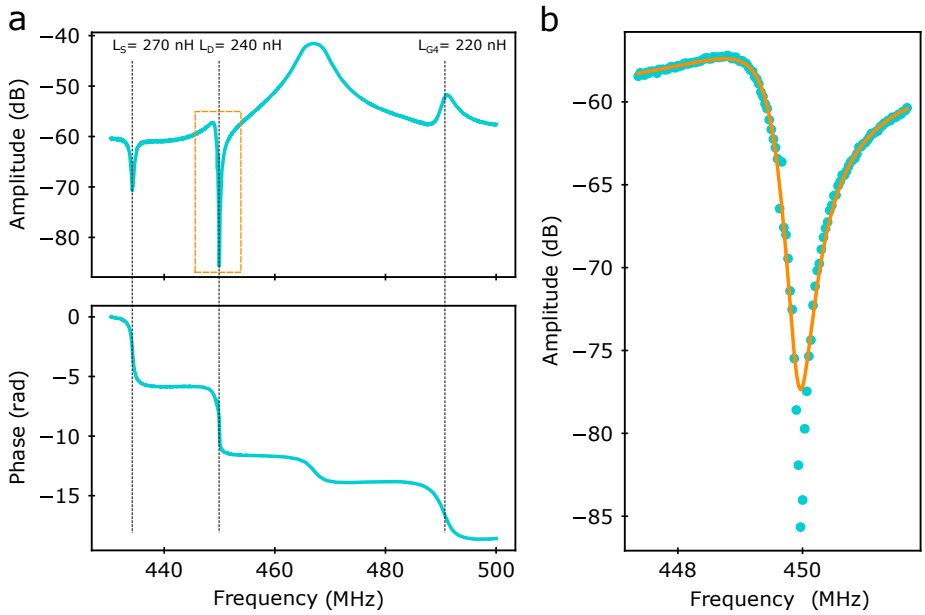

Figure 4.3 – **Radio frequency reflectometry via homodyne detection. (a)** Typical spectrum (amplitude and phase) of the reflected signal with three resonances indicated by the black dashed lines. Phase is post treated by removing the electronic delay and phase shift of the measurement setup. The corresponding values for the commercial inductors are given for each resonance. **(b)** Zoom in (a) corresponding to the orange rectangle. Blue silk points represent data while the orange curve is a fit with a Fano function because of the huge asymmetry induced by standing waves.

Fig. 4.3-b is a zoom on the resonance we used for the built-in charge sensor.

The orange curve is a fit with a Fano function[I] (eq : 4.1) to take into account the asymmetry induced by the standing waves. Even with this process, and given the low number of points for this measurement, the shape is hard to obtain, and the deep is not properly caught. Nonetheless, we extract a bandwitth (BW) approximately equal to 1 MHz corresponding to a quality factor around 500 ($Q \approx 500$).

$$F(E) = B + A \cdot \frac{1 - (q * \Gamma/2 + (f - f_{res}))^2}{(\Gamma/2)^2 + (f - f_{res})^2} \tag{4.1}$$

Where f_{res} is the resonance frequency, Γ describes the line width of the resonant energy and q the Fano parameter responsible for asymmetry.

Lastly, using an equivalent RLC in series model, we calculate the corresponding parasitic capacitance for each galvanic connection and report it in table 4.1. Thanks to FD-SOI fabrication process, the value of the parasitic capacitance (C_p) is rather constant, regardless the gate (or reservoir) the inductor is connected to. This consideration is supported by other measurement on similar devices from the same batch which are not shown here.

Type	L (nH)	f_0 (MHz)	C_p (fF)
Source	270	434.4	497
Drain	240	449.98	521
G4	220	489.68	480

Table 4.1 – Calculated parasitic capacitance

4.3 Charge sensor

Measuring the spin state of a single hole is not an easy thing. The trick is to map a discrete charge state on a given spin state. Consequently, this section focuses on the first step of the process : built an efficient charge sensor, in order to count the number of charges located below G2.

4.3.1 Coulomb peaks

First, we decided to measure charge exchange between QD4 and the drain. To do so, we probe the resonator connected to the drain with a carrier tone at the frequency of 449.98 MHz (close to the resonance). Note that source, drain and all the

I. Here the fano function is used only to described the asymmetry of the curve and not the physic behind.

gates except G4 are grounded. When sweeping V_{G4}, the total capacitance of the device connected to the resonator changes due to the tunneling capacitance (from adiabatic charge motion [9]). Consequently, the resonance frequency is shifted each time the drain enters in resonance with QD4 (as sketched in the inset of Fig. 4.4). Given the non metallic behavior of QD4, the phase of the reflected signal as a function of the V_{G4} shows dips with various amplitude and spacing.

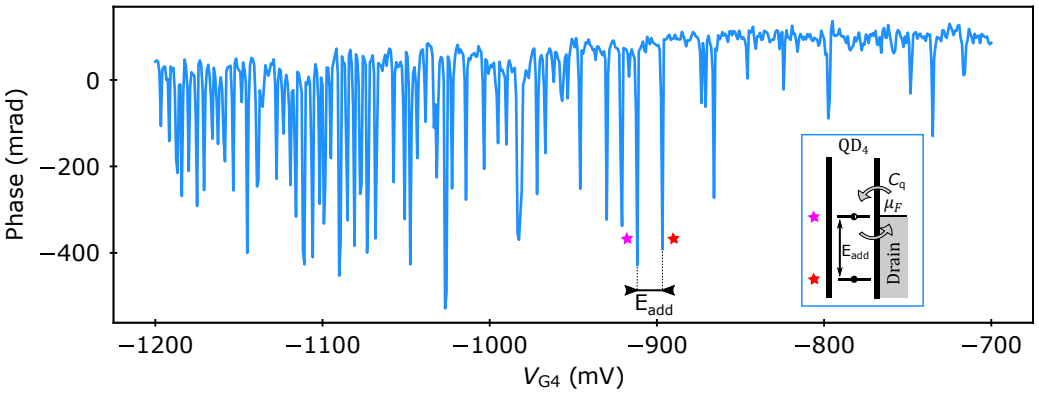

Figure 4.4 – **Probing coulomb peaks with drain reflectometry.** Main panel : Coulomb peaks of QD4 sensed with drain reflectometry. Inset : schematic showing an orbital level (pink star) of QD4 in resonance with the drain, inducing a tunneling capacitance change.

4

Furthermore, there is a change in the tunneling capacitance only if the charge exchange rate is comparable or higher than the resonance frequency [9]. Thus, it is unlikely to detect the first charge event occurring in QD4 (too slow in our devices). Similarly, when the charge exchange rate is too high, the signal also disappear. In any case, we adjust the detector to maximize peaks' amplitude which corresponds to the range $V_{G4} \in [-1.2\,\mathrm{V}, -1\,\mathrm{V}]$. We will now use the high sensitivity of those coulomb peaks to measure a change in the number of charges below G2.

Here it is important to understand that it is the association of a resonator connected to the drain in resonance with QD4 that will subsequently form a charge sensor for QD2. Indeed, when a charge enters in QD2, the energy level of QD4 is capacitively shifted, thus bringing the system out of resonance.

4.3.2 QD3 & QD4 : Single dot regime

In the current configuration where QD3 is empty, the charge sensor has a poor sensitivity to QD2 charge state due to the long distance ($\approx 200\,\mathrm{nm}$ from G2 to G4). Consequently, we decided to merge QD3 and QD4 to form a bigger dot (See

theory 2.1.2).

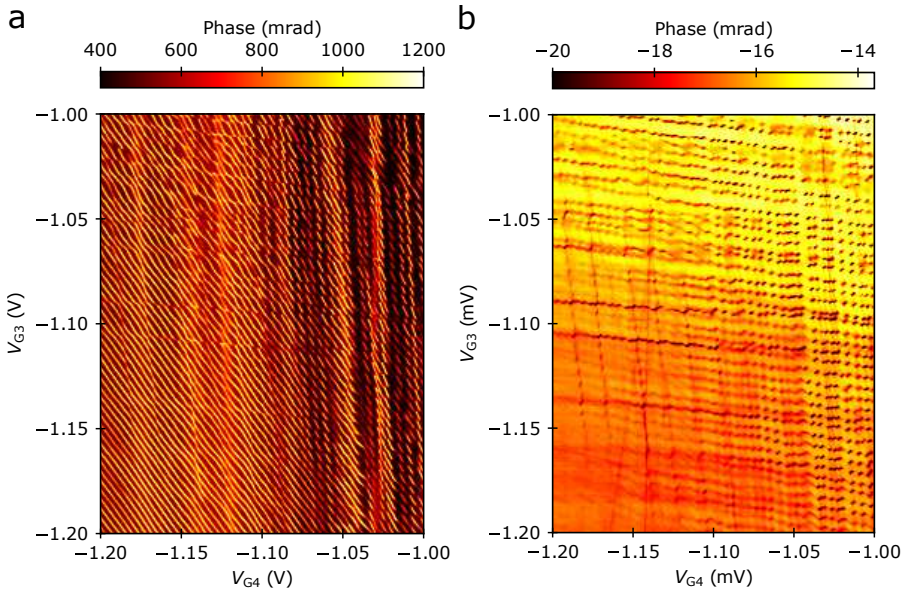

Figure 4.5 – **Stability diagrams (G3,G4).** Left and right panel point out stability diagram of the same (V_{G3}, V_{G4}) subspace. **(a)** is recorded via drain reflectometry while **(b)** shows gate reflectometry (inductor connected to G4).

Fig. 4.5 presents two stability diagrams (V_{G3},V_{G4}) acquired with two different reflectometry techniques. On the left panel, drain reflectometry is sensitive to resonances between QD4 and the drain, represented by discontinuous and almost vertical yellow lines (visible on the right side of the figure. See also Fig. 4.6-a). Those discontinuities highlight charging events occurring in QD3 [II]. On the right panel, gate reflectometry gives a signal when electrochemical potential level of QD3 and QD4 are resonant. The lines tilted at 45 ° are interdots (see also Fig. 4.6-b). The complementarity between these two maps allows to reconstruct the unequivocal honeycomb pattern of the double quantum dot system connected to a single reservoir.

For better visibility, Fig. 4.6 presents zooms in the stability diagram on different dot regimes [2]. On the one hand, Fig. 4.6-a&b points to a coupled double dot regime. Nonetheless, for all experiments in this manuscript, we decided to extend the hole island in order to form a huge quantum dot below G3 & G4, which is clearly achieved in Fig. 4.6-c&d.

II. Note that at this point we have built a nice charge sensor for QD3. Nonetheless, we wanted to isolate the qubit below G2. Thus, the need to merge QD3 and QD4.

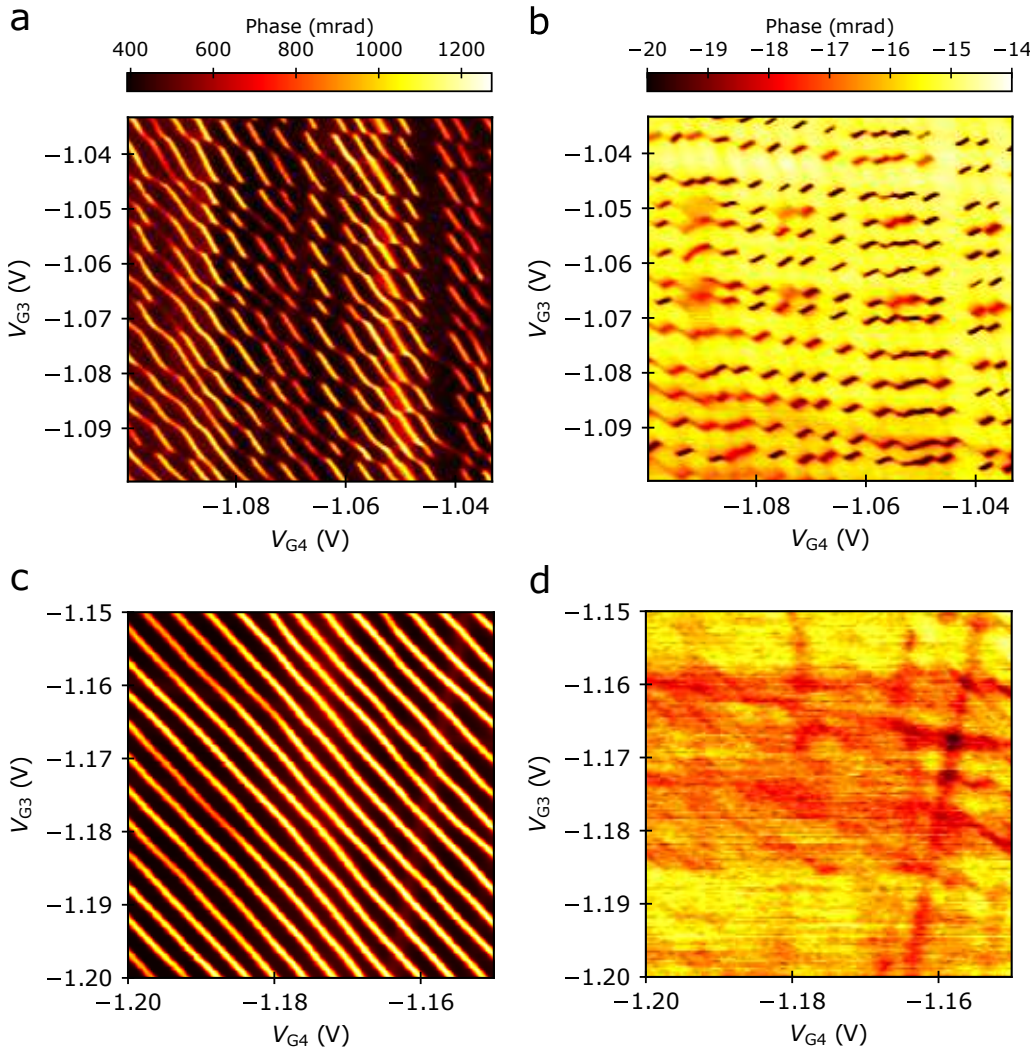

Figure 4.6 – **Zoom in Stability diagram (G3,G4). (a)** & **(b)** exhibits zoom in the double quantum dot region. The horizontal line cuts, visible on (a), prove that we made a sensor for charges located below G3. **(c)** & **(d)** zoom in the single dot regime. Almost no signal appears via gate reflectometry.

4.3.3 Stability diagram of the first hole

Now that we merged QD3 and QD4, we can start counting the number of charges trapped below G2. Fig. 4.7 displays the stability diagram of the device as a function of V_{G2} and V_{G3} . The almost vertical grey dashed lines outline the charging events in QD2, detected as discontinuities in the Coulomb peak stripes of the sensor dot. The lever-arm parameter of gate G2 is $\alpha_{(G2\rightarrow QD2)} \approx 0.37\,\mathrm{eV/V}$, as

inferred from temperature-dependence measurements [10]. To do so, we scanned several coulomb peaks and look at their change of shape with an increase in temperature. Comparatively, the lever-arm parameter of gate G1 with respect to the first hole under G2 is $\alpha_{(G1 \to QD2)} \approx 0.03\,\mathrm{eV/V}$. The charging energy, measured as the splitting between the first two charges is $U = 22$ meV.

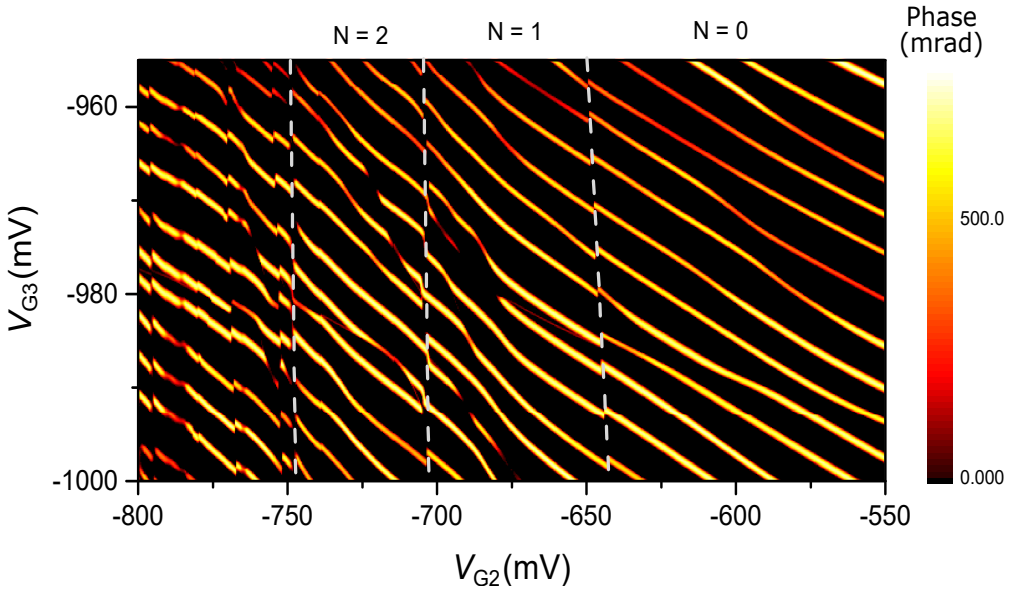

Figure 4.7 – **Charge sensor response after tuning.** Stability diagram as a function of V_{G2} and V_{G3}. Vertical dashed lines are guides to the eyes to pinpoint to charging event occurring below G2. The exact number (N) of charge in the dot is displayed on top of the figure.

4.4 Spin readout

In the previous section, we showed how to create an in-built charge sensor, composed of a resonator connected to a reservoir and a sensor dot. But, the ultimate goal is to measure the spin state of the first hole previously isolated in QD2. Given the tiny magnetic moment of a single hole spin, it is extremely difficult to measure it directly, thus requiring ingenious tricks to map the spin state to the charge state of a particle.

Among solutions addressing the single shot spin detection problem, we use a spin to charge conversion with an energy selective tunneling process often refereed as "Elzerman readout" [5].

This section is dedicated to the several steps to realize the detector used in our experiments. First, we focus on the tunnel rate adjustments and on the sequences applied on G2. Then we look for what we call a spin tail, corresponding to an averaged response of the detector, over a large number of repetitions. If this tail grows proportionally with the magnetic field amplitude, this constitutes a strong proof that we measured correctly the spin state. Finally, we will demonstrate that the readout can even be single shot.

4.4.1 Energy selective spin readout

Applying a magnetic field lifts the spin degeneracy and split the two states according to the Zeeman splitting $E_z = g\mu_b B$. Here $\mu_b = 57.88\,\mu\text{eV.T}^{-1}$ represents the Bohr Magneton. By adjusting the Fermi level of the reservoir so that it is positioned between the two spin energy level, it is then possible discriminate the spin state. Indeed, in this configuration, a spin up ($|\uparrow\rangle$) can escape from the dot and be quickly replaced by a spin down. Conversely, a spin down ($|\downarrow\rangle$) is trapped in the dot. The fact that the charge escapes modifies the detector signal and makes it possible to reconstruct the spin state initially present in the dot. Note, however, that this technique destroys the information originally stored.

This readout relies on a real-time detection of spin-tunneling events to the reservoir. If the charge escapes too fast, the detector may not seen the event. Conversly, if the rate is too slow, the spin may decay before leaving the dot. Consequently, the technique requires a demanding range of rates [11] not only for working but also for optimization [12]. Additionally, the higher is the magnetic field, the bigger is the spin splitting, facilitating the implementation of such a protocol.

4.4.2 Rates tuning

In many devices configuration, a second layer of gates (namely the trench gates) is deposited, in a staggered arrangement with the accumulating gates [13, 14, 15, 16]. This second layer of gate allows for fine rate tuning and such a control knob may either increase the spin readout fidelity or the spin two-qubit gate fidelity [17, 18]. But, in our device, the lack of these trench gates is, at first sight, a deadly end to do Elzerman readout. Here we demonstrate that, the filling and the local shape of the hole island below G3/G4 has a strong impact on the tunnel rates in our system.

Full counting statistics

Thanks to the previously optimized charge sensor, it is now possible to measure the first charge occupying QD2. The phase of the reflected signal can take two distinct values depending on whether QD2 is empty ($|0\rangle$: red) or full ($|1\rangle$: orange). If the chemical potential of QD2 is resonant with that of its reservoir, then the

charge trapped in QD2 can flow in and out, allowing to record the time trace presented in Fig. 4.8-a. The analysis of these time-averaged traces, known as the full counting statistic [19, 20], allows the measurement of the percentage occupancy of the dot (population) as well as the average charge lifetime (inversely proportional to the tunnel rate). Upon sweeping the virtual gate $V_{\mathrm{G2,c}}$, the detuning between chemical potential of the dot and the reservoir changes, thus modifying ratio and duration of the pulses.

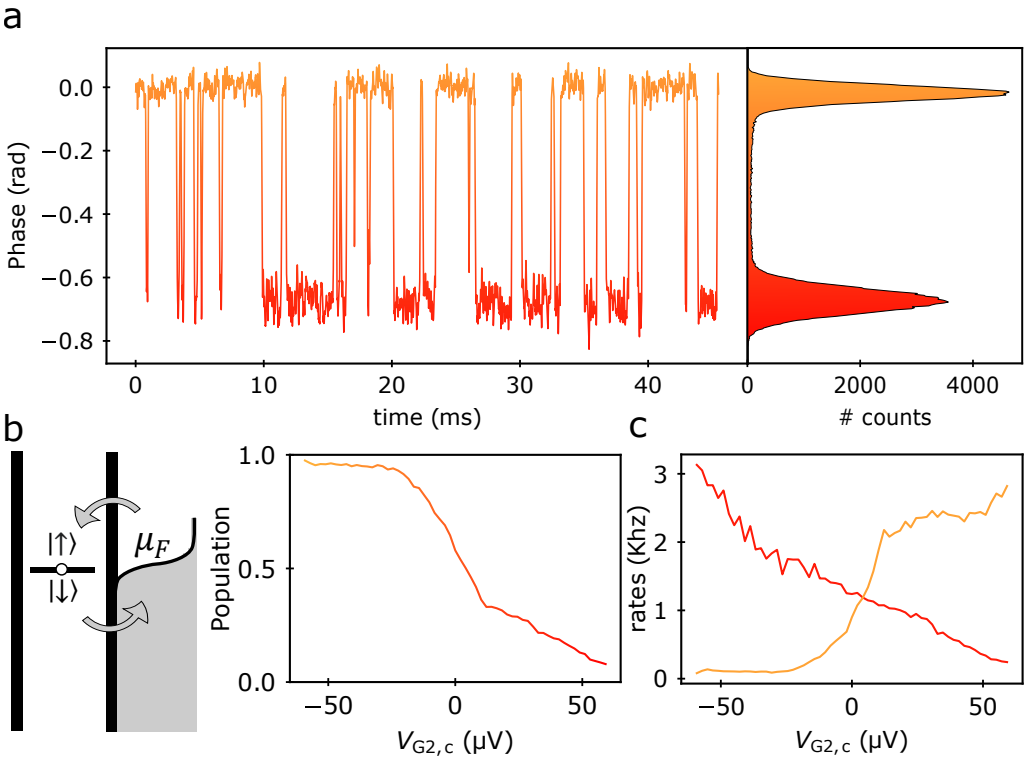

Figure 4.8 – **Full counting statistics (a)** Time-averaged traces of the charge detector with $\tau_c = 6\,\mu$s. Two states are visible in the histogram corresponding to the dot occupied (orange) and emptied (red). **(b)** Schematic shows a two fold degerated state in resonance with a drain. The average population plotted as a function of the virtual gate $V_{\mathrm{G2,c}}$ should in theory have the shape of a Fermi function. **(c)** Γ_{in} : red and Γ_{out} : orange versus G2 virtual gate. Note that we did not observed the expected saturation so that $\Gamma_{in} = 2 \cdot \Gamma_{out}$ for a twofold degenerated energy system.

We define the population as the normalized probability to find the charge trapped in QD2 as plotted in Fig. 4.8-b. The data points should in theory be described by a Fermi function (f(ϵ)) with ϵ the energy detuning. In our setup,

we often obtained asymmetric populations, probably due to residual 50 Hz noise. Finally, we also extracted the number and the time between two successive tunneling events as a function of $V_{\mathrm{G2,c}}$. We calculated Γ_{out} (Γ_{in}) as the inverse of the averaged lifetime for holes out (in) the dot as showed in Fig. 4.8-c. Note that this analysis is valid for an exponential distribution of waiting time with uncorrelated tunneling events. But, for a more precise analyze, one can fit one can fit the lifetime's histogram with a Poissonian distribution ($P_{in}(t) = e^{-t\,\Gamma_{out}}$) so as to account for tunneling events from a QD to a single reservoir [21].

Reproducing this method for each break in Coulomb peaks along the first gray dashed line in Fig. 4.7, permits to find a transition with the desired rates. As stated, the lifetime should be greater than $\tau_c = 6\,\mu$s and lower than the spin life time. The latter being unknown so far, the best way to detect a trace of spin is by setting the tunnel rate in the range [20 kHz, 100 kHz].

4.4.3 Three stages protocol

The major bottleneck with energy selective readout comes from the narrow voltage operating window to detect the spin. According to the Zeeman splitting $E_z = g\mu_b B$ where $\mu_b = 57.88\,\mu\mathrm{eV.T}^{-1}$ is the Bohr Magneton. Consequently, at 1 T, given $\alpha_{(G2\to QD2)}$, we roughly look for bias window as little as 200 μV when scanning V_{G2}.

In order to detect the readout bias window (corresponding to the spin tail[III]), we implemented a three stages sequence (see Fig. 4.9) denoted as (E,L,M). First QD2 is emptied by pulsing far above the Fermi level of the reservoir (E : empty [light yellow]). Then, a hole with a random spin is loaded inside QD2 when the chemical potential of the dot is brought below μ_F (L : load [dark red]). The last stage is set so that $V_{\mathrm{G2,M}} \in [V_{\mathrm{G2,L}}, V_{\mathrm{G2,E}}]$ (M : measure). The total sequence typically last 300 μs, thus setting the global time for the readout process. The loading and emptying are fast if highly detune from the reservoir chemical potential (a few microseconds) whereas the measurement (M) stage has to be long and highly depends on tunnel rates.

4.4.4 Elzerman tail : time average measurement

For each sequence, we record a time-averaged measurement with the lowest integration time possible in order not to lose fast tunneling events. We typically repeat 1000 times the sequence at a given $V_{\mathrm{G2,M}}$ to increase the probability to distinguish the Elzerman tail. The latter appears at the beginning of the readout stage as an average of orange (a charge left the dot) and red signal (no charge left the dot) (See Fig. 4.8). Importantly, signal may be very faint if tunnel rates are out of range. We finally vary $V_{\mathrm{G2,M}}$ over a few hundreds of micro-volts, so we

III. Note that we equivalently use the term "Elzerman tail", in reference to its inventor

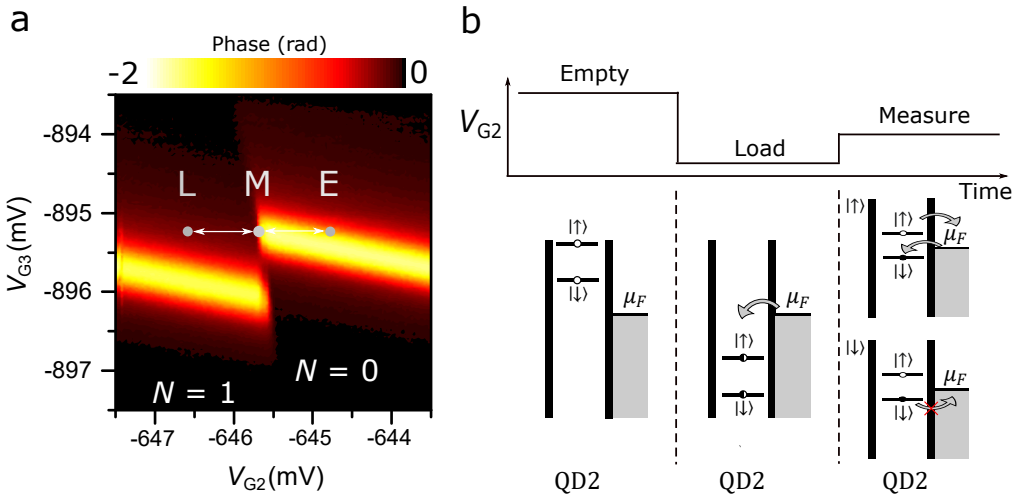

Figure 4.9 – **Three stage protocol for spin detection. (a)** Zoom on the stability diagram close to the working point used in next chapters. The points labeled L (Load), M (Measure) and E (Empty) are the three stages of the pulse sequence applied to V_{G2} for spin readout. **(b)** (Top) Schematic of the three stages pulse sequence applied to V_{G2}. (Bottom) Schematic energy diagrams at the different stages of the pulse sequence. μ_F is the chemical potential of the charge sensor playing the role of reservoir. A random spin is charged during the load stage. At the measure stage, if the loaded spin is up, the hole is able to tunnel out and is replaced by a spin down. On the opposite, if the loaded spin is down, tunneling in or out is impossible. Finally, the dot is discharged during the empty stage.

eventually obtain Fig. 4.10. Time duration of each stage are indicated on the top schematic with the same time scale as the color plot. We pinpoint four different configurations for the stage M, depicted with colored circles so that :

- ↬ Yellow circle : both spin states can escape the dot. At the beginning of the stage, a reddish[IV] line appears inversely proportional to Γ_{out}.
- ↬ Orange circle : Spin down level enters in resonance with the detector. Charges continuously transit back and forth in the dot producing the reddish signal.
- ↬ Red circle : Elzerman tail. V_{G2} range desired in order to perform spin single shot readout. Note the triangular shape of the tail, revealing a change in the tunnel rate with respect to the plunge depth. In principle, the triangle should be the other way around.

IV. The reddish color is given by the extremes of the colorscale. In the end it is a mix in between the dark red (QD filled) and the light yellow (QD emptied). The phenomenon is due to the stochastic tunneling process.

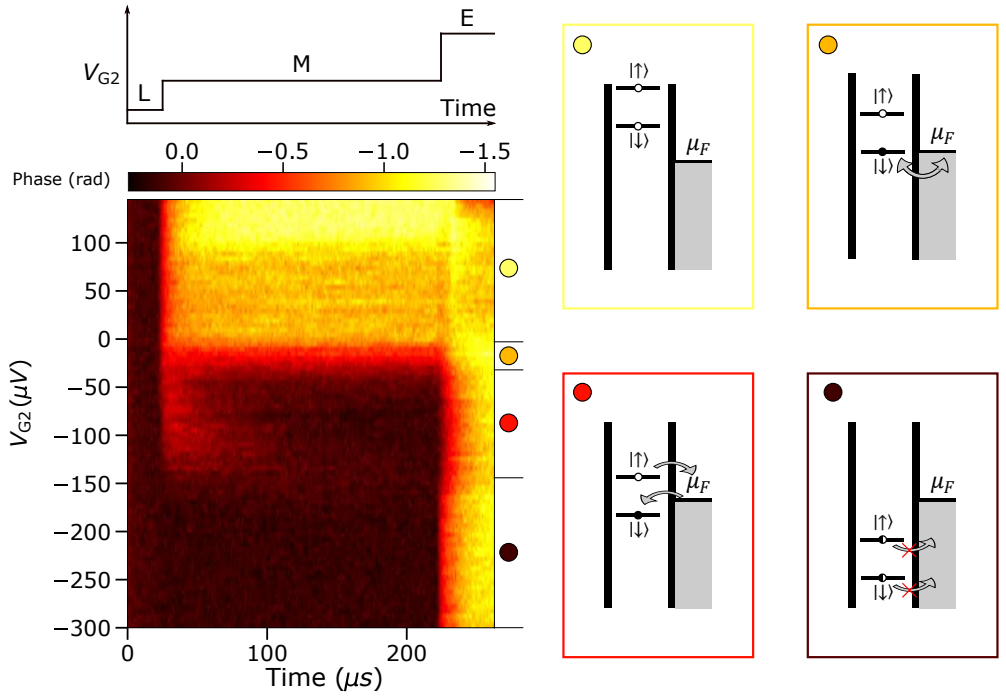

Figure 4.10 – **Elzerman tail.** (left top) Schematic of the pulse sequence applied on V_{G2}. (left Bottom) Spin tail as a function of the measurement pulse stage (M) and time. Each line correspond to the mean phase value over 1000 time-averaged traces with an integration time $\tau_c = 6\,\mu$s. (Right) Schematic energy diagram representing events occurring during the measure stage.

↬ Dark red circle : Both spin states are trapped in QD2. Signal is the same than the loading phase (dark red)

Note that in reality we used a five stage sequence on account of the bias tees which filter DC components. Indeed, the sequence previously presented in Fig. 4.10 has a non zero bias level. Consequently, sweeping $V_{G2,M}$ is also changing $V_{G2,L}$ and $V_{G2,E}$ bias level. To avoid this discrepancy, we added a fourth stage (BR : Bias removing stage) so that the total bias level of a single sequence is zero. Finally, because the fourth pulse is adding a charge in QD2, a fifth step is needed to quickly removes it before starting the sequence again. One may also do the same process with only four stages if correctly designed (L,M,BR,E).

Coarse tuning

To be completely transparent, the tunnel rate calibration presented above was not satisfying for spin detection. In a systematic search, we consequently made

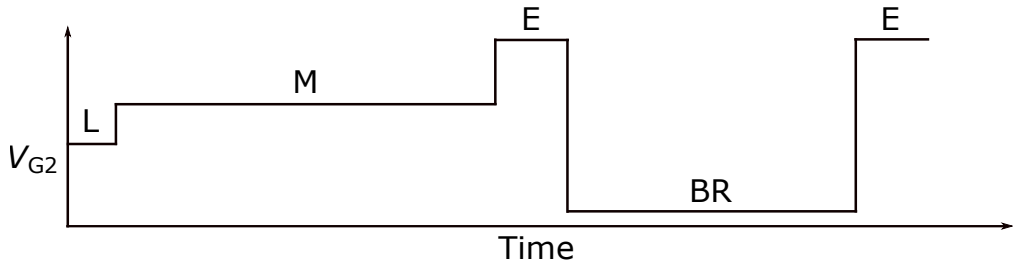

Figure 4.11 – **Real sequence.** Non optimized sequence with a mean value equal to zero used to search the spin tail.

an automatic script to look for the Elzerman tail at each possible transition and kept only the ones with the best results.

Fine tuning

After the program ended, we selected a transition with rates around 100 kHz (like in Fig. 4.10). We discovered that we could access a fine tuning by applying a small bias (δ) around a working point (V_3, V_4) such as $V_{G4} = V_4 + \delta$ and compensating such that $V_{G3} = V_3 - \delta$. Theoretically, in a single dot regime, the system should remain unchanged[V]. Nonetheless, in the device, we probably displace laterally the dot, leveraging changes in the tunnel rates. This method allows to reach rates from 50 kHz to 200 kHz.

4.4.5 Fast single shot spin measurement

We now draw our attention to the last step in order to perform single shot measurement. Using a spin-charge mapping, the underlying issue to measure the spin state is knowing if a single charge escapes or not the dot. To do so, tunneling events are detected by thresholding the phase of the reflectometry signal during the measurement stage. Importantly, the integration time τ_c needed for the time average measurement involves a trade-off. On the one hand, low τ_c massively decreases the SNR and data analyzing automatically results in errors for spin detection. On the other hand, high τ_c suffers a greater risk to miss events occurring quicker than the integration time resulting once again in measurement errors [12]. For a first approximation, we estimate the charge fidelity as a function of the integration time, as :

$$F_c = \frac{F_0 + F_1}{2} \tag{4.2}$$

V. See Fig. 4.7-c with yellow diagonal lines tilted at 45°. The process described above correspond to a displacement in the stability diagram along one of those lines.

Here F_0 (resp. F_1) represents the probability of $|0\rangle$ ($|1\rangle$) not causing (causing) a "blip" in the charge sensor response. Each fidelity is calculated as the percentage area of the Gaussian curve under (resp. above) the voltage threshold. The total charge fidelity is plotted in Fig. 4.12 where we estimate 99 % with an integration time of 5 μs. For now on in this manuscript, and unless it is clearly stated, we fix $\tau_c = 6\,\mu$s for the fastest detector possible without causing errors.

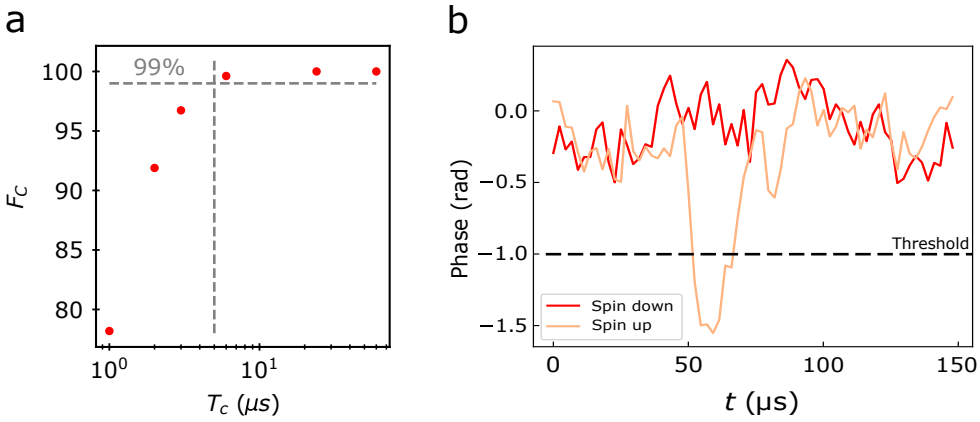

Figure 4.12 – **Ultra fast single shot spin readout. (a)** Charge fidelity as a function of integration time (τ_c). We estimate a fidelity above 99 % for $\tau = 5$ us. **(b)** : Typical time-averaged traces with $\tau_c = 6$ us. A clear "blip", crossing the threshold (black dashed line) is visible on the orange curve which is, a posteriori, assimilated to a spin up state.

We align at stage (M) the center of the Zeeman splitting in QD2 with the chemical potential of the sensor (Red circle position in Fig. 4.10). In this configuration, typical recorded time traces are shown in Fig. 4.12. To discriminate spin states, we employ a simple thresholding protocol (black dashed line) meaning that if a single point is below the given value, the result is considered as a spin down (orange curve).

As a conclusion, this section was dedicated to the realization and the tuning of an ultra fast single shot spin sensor via "Elzerman" readout. The detector exhibits state-of-the-art performances leveraging the possibility to study in detail the first hole spin trapped below G2.

4.5 Initialization & Manipulation

Energy selective readout protocol is definitely a destructive procedure. Demolition of the superposition quantum state due to wave function collapsing is a thing, but in our case we even remove the hole itself. In this section, we use a faster procedure than the three stage sequence which takes advantage of readout hole removal. Then, we demonstrate Rabi oscillations last crucial step to create a qubit.

4.5.1 Two stage protocol

At the end of the measurement stage, the spin state in QD2 is must be a spin down state ($|\downarrow\rangle$). As a consequence, energy selective readout also works as an initialization process if the empty stage (E) is removed. Therefore, we toggle to a two stage sequence (M,C) where M stands for measure (and also acts as an initialization) and C for Control [VI]. In this configuration, if no spin flip are induced, we shall only record spin down time traces (Fig. 4.12 red curve). But, as soon as we hit the hole electric dipole spin resonance (EDSR) [22, 23, 24], blips should appear.

During the C-stage, we burst microwaves during 5 μs on G1 and sweep the microwave frequency in order to drive coherent spin rotations. When hitting the electrical hole spin resonance, signals drastically change. Fig. 4.13-a shows a typical averaged EDSR signal at $B_z = 0.905\,\mathrm{T}$, when repeating each sequence 1000 times. For counting statistics, we define $P_\uparrow$ as the number of recorded spin up states over the total number of sequences. Fig. 4.13-b displays modulation of $P_\uparrow$ as a function of the drive frequency, which may be fit by the Rabi formula (See Theory 2.2.2).

4.5.2 Rabi chevrons

Ultimately, Rabi chevron is the last milestone to achieve a single qubit. According to the Rabi formula, the Rabi frequency (f_{Rabi}) should evolve linearly with the amplitude of the perturbation.

To study our system, we apply the manipulation scheme sketched in Fig. 4.13-a while varying τ_{burst} up to 5 μs. Fig. 4.14-a shows a chevron pattern acquired with $f_L = 17\,\mathrm{GHz}$ and $P_{MW1} = 5\,\mathrm{dBm}$. The lowest flopping frequency at the axial symmetry line (the frequency may also be extracted with a Fourier transform) is equal to the Rabi frequency f_{Rabi}. Sitting at $\Delta f = 0$, we recorded Rabi oscillations for P_{MW1} from 0 to 15 dBm (Fig. 4.14-b). We finally extract a clear linear dependence (Fig. 4.14-c&d) with spin rotation up to ~ 3 MHz while bursting both on G1 and G2. We report relatively slow driving frequency for spin holes which exhibits ultra fast driving frequency (up to hundred MHz [25, 26]). However, we speculate that the Rabi frequency is only limited by the available microwave amplitude and the line attenuation, since we do not observe any saturation with increasing power. After conversion of the microwave power into gate voltage amplitude, we find that the driving efficiency is much larger on gate G2 ($f_{\mathrm{Rabi}} = 7.6$ MHz/mV) than on

VI. The new Control stage (C) corresponds to the previous Loading stage (L)

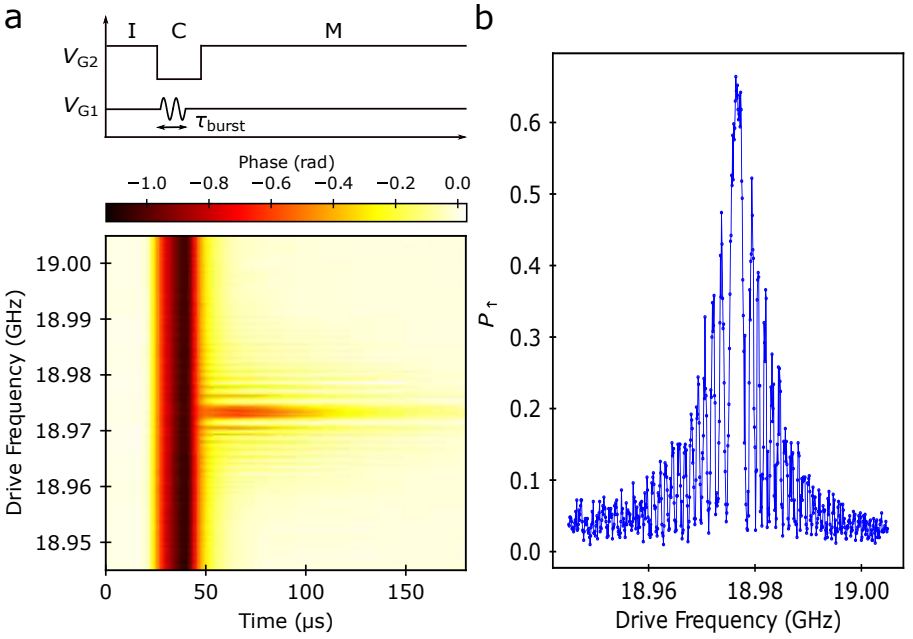

Figure 4.13 – **Spin manipulation.** **(a)** Mean phase value of 1000 realizations of time-averaged traces versus the microwave drive frequency. The continuously running sequence is displayed in the top schematic. The appearance of signal during the measurement stage is due to coherent spin flip via EDSR. **(b)** Post treatment time traces of (a) gives the $P_\uparrow$, which fit the Rabi formula, for a magnetic field oriented along **z**.

gate G1 ($f_{\mathrm{Rabi}} = 1.2$ MHz/mV), which suggests that the spin could be rotated much faster by reducing the attenuation on the G2 line.

Conclusion

To conclude on this chapter, we demonstrated for the first time fast single shot readout of the first hole spin in a silicon nanowire made with CMOS industrial process via drain radio frequency reflectometry. The sensor dot made by the merging of QD3 and QD4, gives access to enough parameters to tune the sensor. Then, we performed energy selective readout at high magnetic field by searching for a spin tail at various localization in the device. Finally, we performed spin rotations by pulsing microwaves to the surrounding gates G1 and G2. The Rabi frequency shows a linear dependence with microwave amplitude up to 3 MHz, limited by the power applied to the device. Next chapter will be dedicated to the single hole spin properties and simulations to describe it.

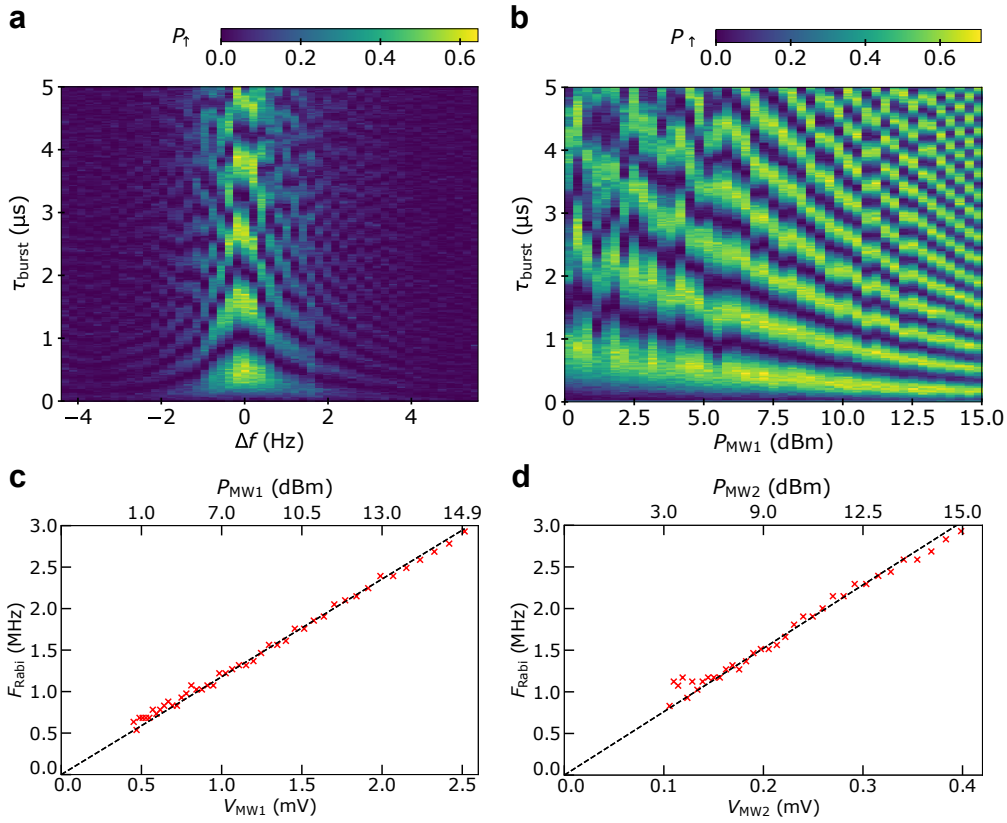

Figure 4.14 – **Electrical spin driving. (a)** Rabi chevron pattern recorded with the same pulse sequence as in Fig. 4.13-a . $P_\uparrow$ is plotted versus MW1 detuning from spin resonance ($\Delta f = f_{MW1} - f_L$) and MW1 burst duration τ_{burst}. The Larmor frequency is $f_L = 17\,GHz$ and the MW1 power on top of the fridge is $P_{MW1} = 5\,dBm$. **(b)** $P_\uparrow$ versus P_{MW1} and τ_{burst} for $\Delta f = 0$. **(c)** Rabi frequency extracted from (b) versus on chip MW1 amplitude V_{MW1} (symbols) assuming 30 dB attenuation from attenuators and 30 dB loss from cables at low temperature. The top axis is the power P_{MW1} delivered on top of the fridge. The dashed line is a linear fit with slope $f_{Rabi} = 1.2\,MHz/mV$, which evidences the absence of saturation at least up to 3 MHz. **(d)** Same as (c) but driving the spin using G2. The attenuation is larger on this line (46 dBm), so that the Rabi oscillations are actually 6 times faster on G2 (slope $f_{Rabi} = 7.6\,MHz/mV$) than on G1.

References

[1] L P Kouwenhoven, D G Austing, and S Tarucha. « Few-electron quantum dots ». In: *Reports on Progress in Physics* 64.6 (May 2001), pp. 701–736. DOI: 10.1088/0034-4885/64/6/201. URL: https://doi.org/10.1088/0034-4885/64/6/201.

[2] R. Hanson et al. « Spins in few-electron quantum dots ». In: *Reviews of Modern Physics* 79 (4 Oct. 2007), pp. 1217–1265. DOI: 10.1103/RevModPhys.79.1217. URL: https://link.aps.org/doi/10.1103/RevModPhys.79.1217.

[3] Emmanuel Chanrion et al. « Charge detection in an array of CMOS quantum dots ». In: *Physical Review Applied* 14.2 (2020), p. 1. ISSN: 23317019. DOI: 10.1103/PhysRevApplied.14.024066. arXiv: 2004.01009. URL: https://doi.org/10.1103/PhysRevApplied.14.024066.

[4] Fabio Ansaloni et al. « Single-electron operations in a foundry-fabricated array of quantum dots ». In: *Nature Communications* 11.1 (2020), pp. 1–7. ISSN: 20411723. DOI: 10.1038/s41467-020-20280-3. URL: http://dx.doi.org/10.1038/s41467-020-20280-3.

[5] J. M. Elzerman et al. « Single-shot read-out of an individual electron spin in a quantum dot ». In: *Nature* 430.6998 (2004), pp. 431–435. ISSN: 1476-4687. DOI: 10.1038/nature02693. URL: https://doi.org/10.1038/nature02693.

[6] Florian Vigneau et al. *Probing quantum devices with radio-frequency reflectometry*. 2022. arXiv: 2202.10516 [cond-mat.mes-hall].

[7] M. G. House et al. « Radio frequency measurements of tunnel couplings and singletâ€“triplet spin states in Si:P quantum dots ». In: *Nature Communications* 6.1 (Nov. 2015), p. 8848. ISSN: 2041-1723. DOI: 10.1038/ncomms9848. URL: https://doi.org/10.1038/ncomms9848.

[8] Cé cile Xinqing Yu et al. « Magnetic field resilient high kinetic inductance superconducting niobium nitride coplanar waveguide resonators ». In: *Applied Physics Letters* 118.5 (Feb. 2021), p. 054001. DOI: 10.1063/5.0039945. URL: https://doi.org/10.1063%2F5.0039945.

[9] R. Mizuta et al. « Quantum and tunneling capacitance in charge and spin qubits ». In: *Phys. Rev. B* 95 (4 Jan. 2017), p. 045414. DOI: 10.1103/PhysRevB.95.045414. URL: https://link.aps.org/doi/10.1103/PhysRevB.95.045414.

[10] M. F. Gonzalez-Zalba et al. « Probing the limits of gate-based charge sensing ». In: *Nature Communications* 6.1 (Jan. 2015), p. 6084. ISSN: 2041-1723. DOI: 10.1038/ncomms7084. URL: https://doi.org/10.1038/ncomms7084.

[11] Andrea Morello et al. « Single-shot readout of an electron spin in silicon ». In: *Nature* 467.7316 (2010), pp. 687–691. ISSN: 1476-4687. DOI: 10.1038/nature09392. URL: https://doi.org/10.1038/nature09392.

[12] D Keith et al. « Benchmarking high fidelity single-shot readout of semiconductor qubits ». In: *New Journal of Physics* 21.6 (June 2019), p. 063011. DOI: 10.1088/1367-2630/ab242c. URL: https://doi.org/10.1088/1367-2630/ab242c.

[13] Nico W. Hendrickx et al. « A four-qubit germanium quantum processor ». In: *Nature* 591.7851 (Mar. 2021), pp. 580–585. ISSN: 1476-4687. DOI: 10.1038/s41586-021-03332-6. URL: https://doi.org/10.1038/s41586-021-03332-6.

[14] Stephan G. J. Philips et al. *Universal control of a six-qubit quantum processor in silicon*. 2022. DOI: 10.48550/ARXIV.2202.09252. URL: https://arxiv.org/abs/2202.09252.

[15] Jun Yoneda et al. « A quantum-dot spin qubit with coherence limited by charge noise and fidelity higher than 99.9% ». In: *Nature Nanotechnology* 13.2 (2018), pp. 102–106. ISSN: 1748-3395. DOI: 10.1038/s41565-017-0014-x. URL: https://doi.org/10.1038/s41565-017-0014-x.

[16] Will Gilbert et al. *On-demand electrical control of spin qubits*. 2022. arXiv: 2201.06679 [cond-mat.mes-hall].

[17] Adam R. Mills et al. « Two-qubit silicon quantum processor with operation fidelity exceeding 99% ». In: *Science Advances* 8.14 (2022), eabn5130. DOI: 10.1126/sciadv.abn5130. eprint: https://www.science.org/doi/pdf/10.1126/sciadv.abn5130. URL: https://www.science.org/doi/abs/10.1126/sciadv.abn5130.

[18] N. W. Hendrickx et al. « Fast two-qubit logic with holes in germanium ». In: *Nature* 577.7791 (2020), pp. 487–491. ISSN: 1476-4687. DOI: 10.1038/s41586-019-1919-3. URL: https://doi.org/10.1038/s41586-019-1919-3.

[19] L. M. K. Vandersypen et al. « Real-time detection of single-electron tunneling using a quantum point contact ». In: *Applied Physics Letters* 85.19 (2004), pp. 4394–4396. DOI: 10.1063/1.1815041. eprint: https://aip.scitation.org/doi/pdf/10.1063/1.1815041. URL: https://aip.scitation.org/doi/abs/10.1063/1.1815041.

[20] R. Schleser et al. « Time-resolved detection of individual electrons in a quantum dot ». In: *Applied Physics Letters* 85.11 (2004), pp. 2005–2007. DOI: 10.1063/1.1784875. eprint: https://doi.org/10.1063/1.1784875. URL: https://doi.org/10.1063/1.1784875.

[21] S. Gustavsson et al. « Counting Statistics of Single Electron Transport in a Quantum Dot ». In: *Phys. Rev. Lett.* 96 (7 Feb. 2006), p. 076605. DOI: 10.1103/PhysRevLett.96.076605. URL: https://link.aps.org/doi/10.1103/PhysRevLett.96.076605.

[22] K. C. Nowack et al. « Coherent Control of a Single Electron Spin with Electric Fields ». In: *Science* 318.5855 (2007), pp. 1430–1433. ISSN: 0036-8075. DOI: 10.1126/science.1148092. eprint: https://science.sciencemag.org/content/318/5855/1430.full.pdf. URL: https://science.sciencemag.org/content/318/5855/1430.

[23] R. Maurand et al. « A CMOS silicon spin qubit ». In: *Nature Communications* 7.1 (2016), p. 13575. ISSN: 2041-1723. DOI: 10.1038/ncomms13575. URL: https://doi.org/10.1038/ncomms13575.

[24] Hannes Watzinger et al. « A germanium hole spin qubit ». In: *Nature Communications* 9.1 (2018), p. 3902. ISSN: 2041-1723. DOI: 10.1038/s41467-018-06418-4. URL: https://doi.org/10.1038/s41467-018-06418-4.

[25] Florian N. M. Froning et al. « Ultrafast hole spin qubit with gate-tunable spin–orbit switch functionality ». In: *Nature Nanotechnology* 16.3 (Mar. 2021), pp. 308–312. ISSN: 1748-3395. DOI: 10.1038/s41565-020-00828-6. URL: https://doi.org/10.1038/s41565-020-00828-6.

[26] Leon C. Camenzind et al. « A hole spin qubit in a fin field-effect transistor above 4 kelvin ». In: *Nature Electronics* 5.3 (Mar. 2022), pp. 178–183. ISSN: 2520-1131. DOI: 10.1038/s41928-022-00722-0. URL: https://doi.org/10.1038/s41928-022-00722-0.

Chapter 5

Single hole spin coherence

"It is not unscientific to make a guess, although many people who are not in science think it is."

Richard Feynman

Semiconductor spin qubits based on spin-orbit states are responsive to electric field excitation, allowing for practical, fast and potentially scalable qubit control. Spin-electric susceptibility, however, renders these qubits generally vulnerable to electrical noise, which limits their coherence time. In this chapter, we report on the longitudinal electric response of a spin-orbit qubit consisting of a single hole electrostatically confined in a natural silicon metal-oxide-semiconductor device. In the first section, we describe the hole g-matrix, image of the valence bands mixing in silicon devices. Then, we study the derivative of the hole g-tensor with respect to different gate voltages. At specific orientations, we reveal the existence of operation sweet spots, where the impact of charge noise is highly reduced, while preserving an efficient electric-dipole spin control. We correspondingly observe an extension of the Hahn-echo coherence time up to 88 μs, exceeding by an order of magnitude the best values reported for hole-spin qubits, and approaching the state-of-the-art for electron spin qubits with synthetic spin-orbit coupling in isotopically-purified silicon. Finally, in the last section, we report qubit's quality factor as a metric to prove the completeness of the demonstrated sweet spot. This finding largely enhances the prospects of silicon-based hole spin qubits for scalable quantum information processing.

Contents

5.1 Single hole properties 123
5.1.1 Experimentally measured g factors 123
5.1.2 k-p model for g factors simulations 124

5.2 Longitudinal spin electric susceptibility (LSES) 127
5.2.1 $LSES_{G2}$ 127
5.2.2 $LSES_{G1}$ 129
5.3 Extended phase coherence 131
5.3.1 Hahn-echo spin coherence 131
5.3.2 Hahn-echo amplitude 132
5.3.3 Magnetic sweet spots 133
5.3.4 Charge noise in spin qubit platforms 134
5.4 Inhomogeneous dephasing time 135
5.4.1 Ramsey experiment 135
5.4.2 Dephasing time in the non-ergodic regime 137
5.4.3 Ultra low frequency noise 138
5.5 Quality factors 140
References 145

5.1 Single hole properties

In order to do a composite drawing of the particle trapped below G2, we focus, in a first step, in its interaction with its close environment. One way of doing this is to measure the resonance frequency of the qubit as a function of different parameters, in this case the orientation of the magnetic field. The previous chapter shows that we manage to read the spin state of a single hole in a few micro seconds and that we are able to induce coherent oscillations. In fact, reproducing this experiment for different magnetic field directions allows to measure the effective g-factor and thus to compare it with the theoretically expected results in our sample configuration.

5.1.1 Experimentally measured g factors

The strong 2D (Lx<Ly«Lz) readily seen in Fig. 4.1-a favors HH-LH mixing [1, 2]. This mixing is expected to manifest in the anisotropy of the hole g-tensor, which bears information on the relative weight of HH and LH components [3, 4, 5]. To verify this, we measure the hole spin resonance frequency f_L while varying the orientation of the magnetic field $\vec{B}$ in both xz and yz planes. The effective g-factor values are plotted in Fig. 5.1 as a function of the magnetic field angles θ_{zx} and θ_{zy}, respectively. These maps highlight the strong anisotropy of the Zeeman splitting, with a maximal g-value of 2.7 close to the y axis (in-plane, perpendicular to the nanowire) and a minimal g-value of 1.4 close the z axis (in-plane, along the nanowire).

The non trivial peanut shape obtain in Fig. 5.1 is recognizable as the inverse of an ellipse. Considering a constant qubit frequency f_L, for an in-plane magnetic field (xy plane for example), g-matrix can be diagonalized with eigenvalues gx,gy. Varying the magnetic field amplitude and orientation at fixed f_L leads to $(g_x B_x)^2 + (g_y B_y)^2$ that remains constant. It results in an ellipse for $||B||$ in a polar plot. Because $||g||$ scales inversely to $||B||$, we finally obtain a peanut shape for the g factors plotted in Fig. 5.1.

Calculated g-factors are also plotted in the same figure as colored solid lines. The agreement with the experimental data is, for the first time, outstanding. Here, theoretical data were calculated given the device geometry and gate voltage applied on the system via a 6 band k-p model. Importantly, the main magnetic axis for the g-factors are tilted, especially in Fig. 5.1-b where the angle is almost equal to 25°. This discrepancy may be due to a misalignment of the sample with respect to the PCB (less likely), or strain as explain later on. In any case, we manually force the rotation of the calculated g-matrix main axis, as an adjustable parameter for the fit. Next subsection details the simulations and the conclusions.

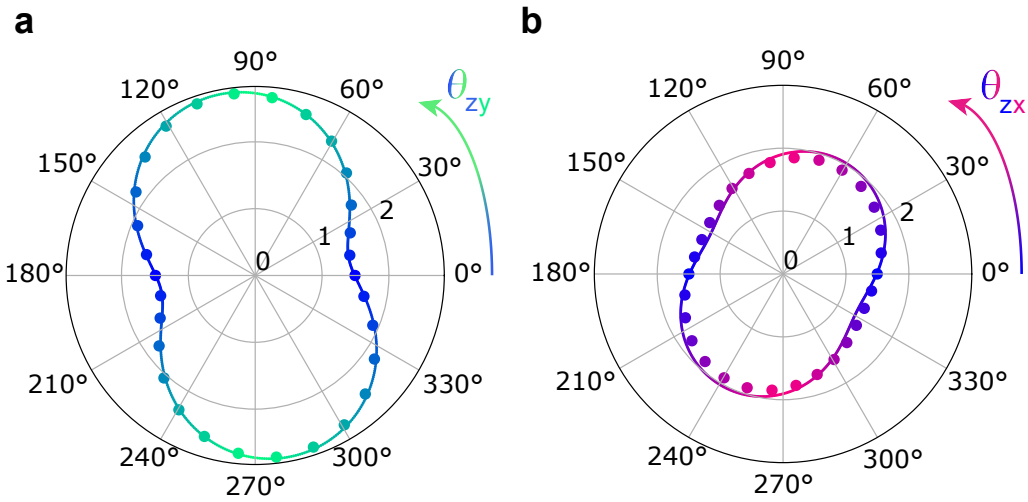

Figure 5.1 – **Experimental g factors. (a)** Measured (dots) and simulated (solid line) hole g-factor as a function of the in-plane magnetic field angle θ_{zy}. $\theta_{zy} = 90°$ corresponds to a magnetic field applied along the y axis. **(b)** Same as (a) in the xz plane. $\theta_{zx} = 90°$ corresponds to a magnetic field applied along the x axis.

5.1.2 k-p model for g factors simulations

For the calculations, we[I] first model the device as a [110]-oriented rectangular nanowire channel with width $W = 100$ nm and height $H = 17$ nm lying on a 145 nm thick buried oxide (BOX). Four 40 nm long and 50 nm tall front gates, separated by 40 nm long Si_3N_4 spacers, are laid across the channel. The potential landscape $V(\mathbf{r})$ in the device is first computed with a finite volumes Poisson solver [6]. Screening by the holes accumulated in the source, drain and below the gates G1, G3, and G4 is accounted for in the Thomas-Fermi approximation. The wave functions in the potential $V_{\mathrm{QD}}(\mathbf{r})$ are finally calculated with a finite differences 6 bands $\mathbf{k}\cdot\mathbf{p}$ model [6]. In this device geometry, the first holes primarily accumulate in the upper corners of the Si nanowire [7]. Fig. 5.2 displays the expected single hole wave function in QD2.

I. Simulation were performed by Y.M Niquet et al. The use of we refers to all contributors of the paper.

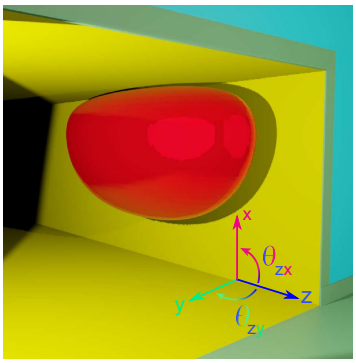

Figure 5.2 – **First hole wavefunction in a corner dot state.** Artistic view of the calculated wave function of the first hole accumulated under G2, enclosing 90% of the density probablity.

If the device were "planar" (germanium heterostructures), the hole would be confined at the top (001) facet of the channel by the quasi-vertical electric field of gate G2 (Fig. 5.3-b (top)). It would, therefore, show the fingerprints of an almost pure (001) heavy-hole, with a large $g_x \simeq -6\kappa + 2\gamma_h \simeq 4.84$, and much smaller g_y and g_z characteristic of the weak heavy-hole/light-hole mixing induced by the lateral confinement ($\gamma_h = 1.16$ being a correction that describes the heavy-hole/light-hole mixing by the magnetic vector potential) [2].

In our nanowire, non-planar geometry is due to gates covering three facets of the nanowire. Consequently, there is a significant in-plane electric field component pushing the hole against the lateral $\{1\bar{1}0\}$ facets. Given the width of the device, the hole is very responsive to the lateral electric field, and gets readily squeezed near one of the top corners of the channel, in a dot with comparable vertical and lateral extensions (Fig. 5.3-b (bottom)). The enhancement of lateral with respect to vertical confinement admixes a light-hole envelope into the hole wave function, which results in a decrease of g_x ($\partial g_x/\partial V_{\mathrm{G2}} > 0$) and an increase of g_y and g_z ($\partial g_z/\partial V_{\mathrm{G2}} < 0$, see Fig. 5.3-a) [8, 2]. The mixing is particularly strong here because the structural vertical confinement is weak ($H = 17$ nm) so that the heavy-hole/light-hole gap is small. The g-factors (especially g_x and g_y) tend to saturate rapidly with increasingly negative V_{G2} as the heavily squeezed hole hardly responds any more to the vertical and lateral electric fields ($|\partial g_x/\partial V_{\mathrm{G2}}| \ll |\partial g_z/\partial V_{\mathrm{G2}}|$).

To sum up, from the numerical simulations, we conclude that the measured g-factors anisotropy results from a strong electrical confinement against the side facet of the channel (along $\vec{y}$) due to the wrapping configuration of the gate. This effect prevails over the mostly structural vertical confinement (along $\vec{x}$). The experimental g-factors and the small misalignment between the principal axes of

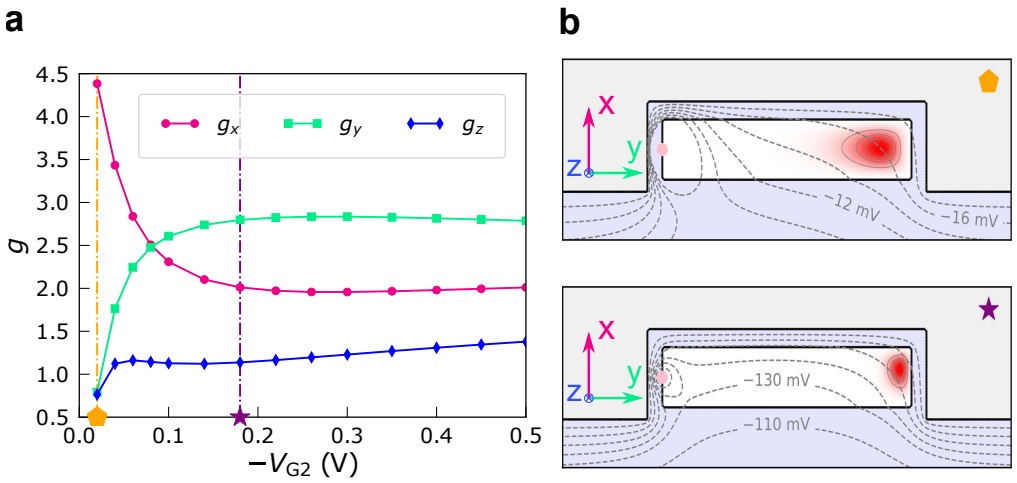

Figure 5.3 – **Dependence of the g-factors on the electric field** in a simpler setup with no hole gases below G1,G3 and G4. **(a)** g-factors g_x, g_y, and g_z as a function of the difference of potential $-V_{G2}$ between gates G2 and gates G1 and G3 (both grounded). The larger $-V_{G2}$, the stronger the vertical and lateral electric fields. **(b)** Maps of the squared wave functions (red) in the cross section of the channel below gate G2, at the biases marked with an orange pentagon and a purple star in (a). The channel is colored in white, the gate G2 in gray and SiO_2 in blue. The dashed gray lines are isopotential lines of $V_{QD}(\mathbf{r})$, spaced by 2 mV in (top) and by 10 mV in (bottom). The isodensity surface of the wave function in (bottom) that encloses 85% of the hole charge is represented in Fig. 5.2.

the g-tensor and the device symmetry axes are best reproduced by introducing a moderate amount of charge disorder in combination with small ($\sim 0.1\%$) shear strains in the silicon channel. The latter likely originate from device processing and thermal contraction at the measurement temperature [9].

Conclusion

Given that the g-factor anisotropy is intimately related to the HH/LH mixing, which is partially controlled by the electrostatic confinement potential, the Larmor frequency is expected to be gate-voltage dependent, and thus sensitive to surrounding charge noise. In this scope, next section focuses on modifications of the Zeeman energy induced by electrical field change.

5.2 Longitudinal spin electric susceptibility (LSES)

The downside of all-electrical spin control is that the required spin-orbit coupling exposes the qubit to charge noise, leading to a reduced hole spin coherence. Recent theoretical works[10, 11, 12], however, have shown that, for properly chosen structural geometries and magnetic field orientations, careful tuning of the electrostatic confinement can bring the hole qubit to an optimal operation point. In this configuration, the effects of charge noise vanish to first order while enabling efficient electric-dipole spin resonance. Thus, we measure the longitudinal spin-electric susceptibility (LSES) with respect to the voltages applied to the lateral gate G1 and to the accumulation gate G2, which we define as $\mathrm{LSES}_{\mathrm{G1}} = \dfrac{\partial f_L}{\partial V_{\mathrm{G1}}}$ and $\mathrm{LSES}_{\mathrm{G2}} = \dfrac{\partial f_L}{\partial V_{\mathrm{G2}}}$, respectively. In essence, $\mathrm{LSES}_{\mathrm{G1}}$ and $\mathrm{LSES}_{\mathrm{G2}}$ characterize the response of the Larmor frequency to the electric-field components parallel (z) and perpendicular (x, y) to the channel direction, respectively.

5.2.1 $\mathrm{LSES}_{\mathrm{G2}}$

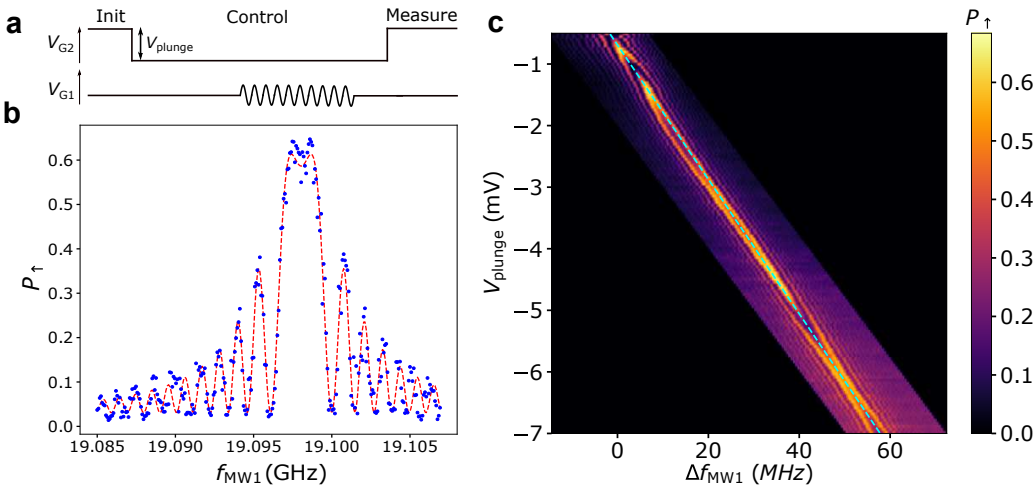

Figure 5.4 – **Measurement of $\mathrm{LSES}_{\mathrm{G2}}$.** **(a)** Schematic representation of the pulse sequence used to monitor spin resonance. We burst on MW1 for 5 μs and average $P_\uparrow$ over 200 such sequences. **(b)** Average $P_\uparrow$ (Blue dots) versus MW1 burst frequency at $V_{\mathrm{plunge}} = -1$ mV. This plot is in essence a line cut of a Rabi chevron at $t_{\mathrm{burst}} = 5\,\mu$s. The red dashed line is a fit used to extract the Larmor frequency. **(c)** Tracking of f_L as a function of V_{plunge}. The dashed blue line is a linear fit whose slope is equal to $\mathrm{LSES}_{\mathrm{G2}}$.

To probe the response to G2, we directly measure the spin resonance frequency f_L at different V_{G2}. Concretely, we apply a two stages sequence (Initialisation/Measure and Control) on MW2 while bursting for 5 μs on MW1 to drive

coherent spin rotations (see Fig. 5.4-a). We record the oscillations of $P_\uparrow$ (averaged over 200 pulse sequences) as a function of the MW1 burst frequency f_{MW1} (Fig. 5.4-b), and fit with a Rabi chevron model to eq. 5.1 to extract the Larmor frequency f_L.

$$P_\uparrow(t) = \frac{f_R^2}{f_R^2 + \Delta_f^2} \cdot sin(2\pi\sqrt{f_R^2 + \Delta_f^2}\frac{t}{2}) \tag{5.1}$$

Where $\Delta_f = f_{MW1} - f_L$ is the frequency detuning and f_R the Rabi frequency. We repeat the experiment for different values of V_{plunge}, and obtain the map of Fig. 5.4-c, where $\mathrm{LSES_{G2}} = \partial f_L / \partial V_{\mathrm{plunge}}$ is the slope of the dashed blue line, here equal to $-10\,\mathrm{MHz/mV}$. Note that the Rabi frequency also depends on V_{plunge} (visible as change of the chevron shape), which may not only be explained by a change in the transmission power through the fast line. The analysis of this phenomenon is nonetheless beyond the scope of this manuscript.

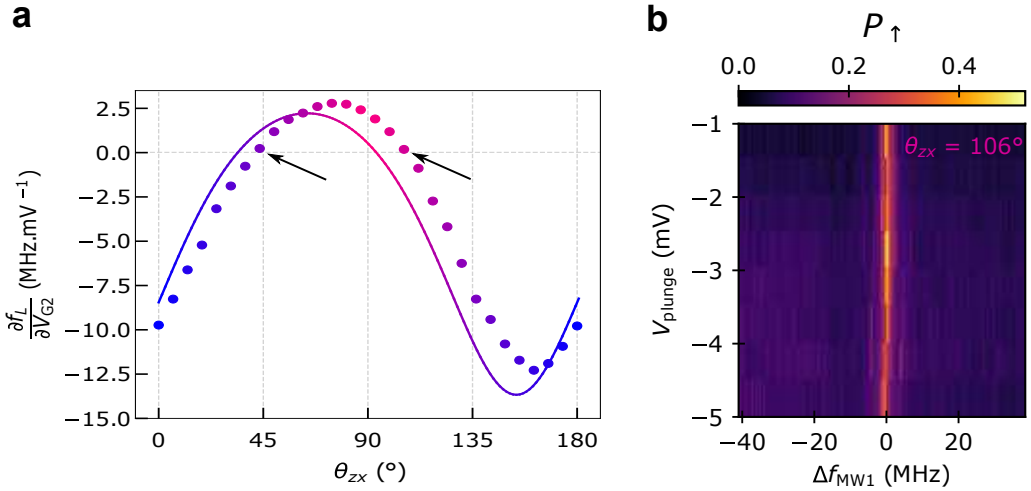

Figure 5.5 – **Magnetic field anisotropy of $\mathrm{LSES_{G2}}$. (a)** Spin-electric susceptibility with respect to V_{G2} ($\mathrm{LSES_{G2}}$) as a function of magnetic field angle θ_{zx} (symbols), at constant Larmor frequency ($f_L = 19\,\mathrm{GHz}$). The LSES vanishes at $\theta_{zx} = 41°$ and 106°, as indicated by the two arrows. The solid line corresponds to the numerically calculated $\mathrm{LSES_{G2}}$. **(b)** $\mathrm{LSES_{G2}}$ at $\theta_{zx} = 106°$ where f_L is robust to any voltage fluctuation on G2.

We then repeat this experiment for different field angles and evaluate the angular dependence of $\mathrm{LSES_{G2}}$. The resulting susceptibility is plotted as a function of the magnetic field angle θ_{zx} in Fig. 5.5-a. The observed angular dependence

(dots) is, once again, in good agreement with the theoretical expectations (plain line). Noticeably, $\mathrm{LSES_{G2}}$ is positive along $\vec{x}$ and negative along $\vec{z}$. Indeed, when increasing V_{G2}, the hole wave function extends proportionally more in the yz plane than in the vertical x direction, which increases g_x and decreases g_y and g_z. As a result of the sign change, $\mathrm{LSES_{G2}}$ vanishes at two magnetic field orientations in the xz plane (marked by arrows in Fig. 5.5-a). A zero in the $\mathrm{LSES_{G2}}$ is visible in Fig. 5.5-b where any voltage fluctuation on G2 does not change the Larmor frequency. More generally, those two sweet-spots cancel all electric-field fluctuations perpendicular to the silicon channel.

Although we found clear sweet spots for electrical perturbations perpendicular to the nanowire, the hole wavefunction is still able to fluctuate along the channel. To further characterize the spin hole response to electrical field modifications, we need to emulate a change in electrical field (along $\vec{z}$) using G1.

5.2.2 $\mathrm{LSES_{G1}}$

To probe the response to G1, we introduce a pulse on V_{G1} in a Hahn-echo sequence [13, 14] [II] as outlined in the schematic in Fig. 5.6-b. This defines a phase gate (see Fig. 5.6-a) robust to low frequency noise, where the parameter φ is controlled by the amplitude δV_{G1} and duration τ_{Z} of the pulse. During the pulse, the system acquires a phase proportional to φ, which is then mapped on the spin state. The principle is very close to Ramsey interference commonly used.

Fig. 5.6-b displays the coherent oscillations recorded as a function of τ_{Z} for three different pulse amplitudes. The frequency of these oscillations is expected to increase linearly with δV_{G1}, with a slope $\mathrm{LSES_{G1}} = \frac{\partial f_L}{\partial V_{\mathrm{G1}}}$. This is shown in Fig. 5.6-c for different magnetic field orientations. $\mathrm{LSES_{G1}}$, plotted in Fig. 5.6-d as a function of θ_{zx}, ranges from $-0.5\,\mathrm{MHz/mV}$ to $-0.1\,\mathrm{MHz/mV}$. Its magnitude is much smaller than $\mathrm{LSES_{G2}}$ because G1 is farther from QD2 than G2 and its field effect is partly screened by the hole gas beneath.

The numerically calculated $\mathrm{LSES_{G1}}$ (solid line) reproduces reasonably well the order of magnitude but not the angular dependence of the measured $\mathrm{LSES_{G1}}$. This discrepancy stems to inaccuracies in the description of the hole gases near QD2 as well as to unaccounted charge disorder and strains. We also notice that $\mathrm{LSES_{G1}}$ never vanishes and that the minimum of $|\mathrm{LSES_{G1}}|$ ($\theta_{zx} = 90\,^\circ$ happens to be almost at the same θ_{zx} as a zero of $\mathrm{LSES_{G2}}$ ($\theta_{zx} = 106\,^\circ$ displayed in Fig. 5.5-b).

II. Hahn-echo sequence is entirely detailed in the next section 5.3.1. We make the choice not to describe in detail Hahn-echo sequence in this section since phase gate may be realized with various gate sequences.

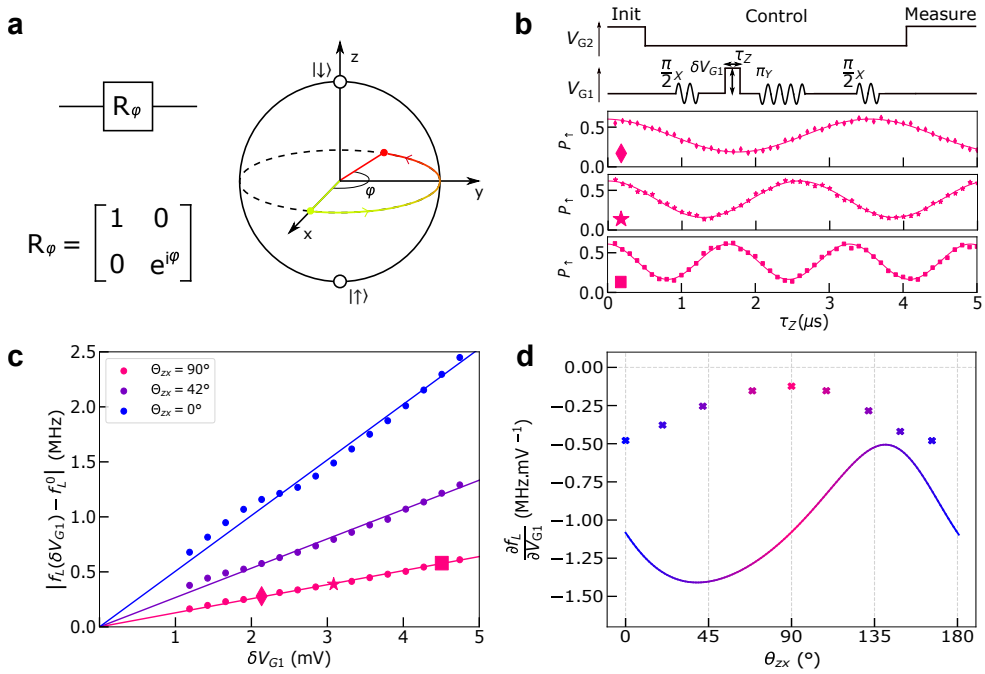

Figure 5.6 – **Measurement of** $\mathrm{LSES_{G2}}$**. (a)** Representation of a phase shift gate (φ). Superposition state remains unchanged while the qubit acquires a phase φ after applying this gate. On a block sphere, the phase shift gate is equivalent to a circular arc with an angle of φ parallel to the equator. **(b)** (top) Pulse sequence used to measure $\mathrm{LSES_{G1}}$: a voltage pulse of amplitude δV_{G1} and duration τ_{Z} is applied to G1 during the first free evolution time of a Hahn-echo sequence. (bottom) Spin-up fraction $P_\uparrow$ as a function of τ_{Z} for $\delta V_{\mathrm{G1}} = 2.16\,\mathrm{mV}$ (diamonds), $3.12\,\mathrm{mV}$ (stars) and $4.80\,\mathrm{mV}$ (squares), at $\theta_{zx} = 90°$. The oscillation frequency varies with δV_{G1}. **(c)** δV_{G1} dependence of the frequency shift extracted from the Hahn-echo measurements at $\theta_{zx} = 0°$, 42° and 90°. Symbols in the latter data set correspond to the $P_\uparrow$ oscillations shown in (b). The solid lines are linear fits to the experimental data whose slope directly yields $|\mathrm{LSES_{G1}}|$. **(d)** Measured (symbols) and calculated (solid line) $\mathrm{LSES_{G1}}$ as a function of θ_{zx}, at constant $f_L = 17\,\mathrm{GHz}$. The negative sign of $\mathrm{LSES_{G1}}$ is inferred from the shift of f_L under a change in V_{G1}.

Conclusion

In order to briefly summarize, data in this section pinpoint to a small range of angles ($\theta_{zx} \in [90\,°, 106\,°]$) where the hole spin could be almost insensitive to electric-field fluctuations. Assuming that the spin coherence is limited by surrounding charge noise, coherence time enhancement lay therefore be observed for proper magnetic field orientations.

5.3 Extended phase coherence

We now draw our attention to the extended hole spin coherence time often refereed as "Hahn-echo coherence time" (T_2^E). After defining the sequence, we focus on the magnetic field angular dependence of T_2^E and investigate its correlation with the longitudinal spin-electric susceptibility [15].

5.3.1 Hahn-echo spin coherence

To get rid of low frequency noise sources, we measure the coherence time [16] using a conventional Hahn-echo protocol [17]. The entire sequence and the corresponding spin state on the Bloch sphere are displayed in Fig. 5.7. The spin is initially forced in the ground state $|\downarrow\rangle$. Then, the qubit is deeply pushed in a Coulomb blockade configuration where we perform electrical spin manipulation. First, we create a superposition state on the equatorial plane of the Bloch sphere via a $\pi_y/2$ pulse. In this configuration, the qubit rotates at the Larmor frequency and accumulates a phase proportional to Δ_f during a time $\tau_{wait}/2$. Because of longitudinal noise, the Larmor frequency change from one sequence cycle to the next, resulting in phase noise on the Bloch sphere. Hence, Hahn-echo refocusing pulse (π_x) tends to suppress slow change in the qubit's energy. After a second free evolution time $\tau_{wait}/2$, the phase state of the qubit is finally projected on the spin state by a last pulse ($\pi_y/2$), before being measured.

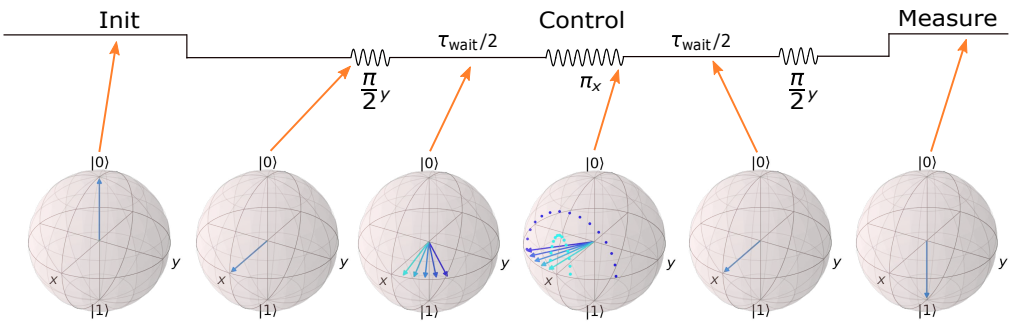

Figure 5.7 – **Perfect spin echo rephasing sequence for a short free evolution time.** After preparing the qubit in a ground state, the spin is brought to the equatorial plane via a $\pi_y/2$ pulse. First free evolution time let all spins evolve at their own speed, before being refocused by the echo π_x pulse. Finally, the relative phase state is projected on the spin state via a last $\pi_y/2$ before measurement.

5.3.2 Hahn-echo amplitude

In order to measure T_2^E, we slightly changed the last pulse in Fig. 5.7 to record the Hahn-echo decay shape [13, 14] as a function of the free evolution time (see Fig. 5.8-a). The sequence is composed of a $\pi_x/2$ (set to 50 ns with 20 dBm), then a π_y rotation and finally a $\pi_\phi/2$ pulse, each separated by a time delay $\tau_{\text{wait}}/2$. We define the angle ϕ of the last pulse so that $\phi = 0$ correspond to $\pi_x/2$ while $\phi = \pi/2$ refers to a $\pi_y/2$ pulse [III]. For each τ_{wait}, we extract the averaged amplitude of the $P_\uparrow$ oscillation obtained by varying the phase ϕ of the last $\pi/2$ pulse (see Fig. 5.8-a bottom), and normalize it to the $P_\uparrow$ oscillation amplitude in the zero-delay limit.

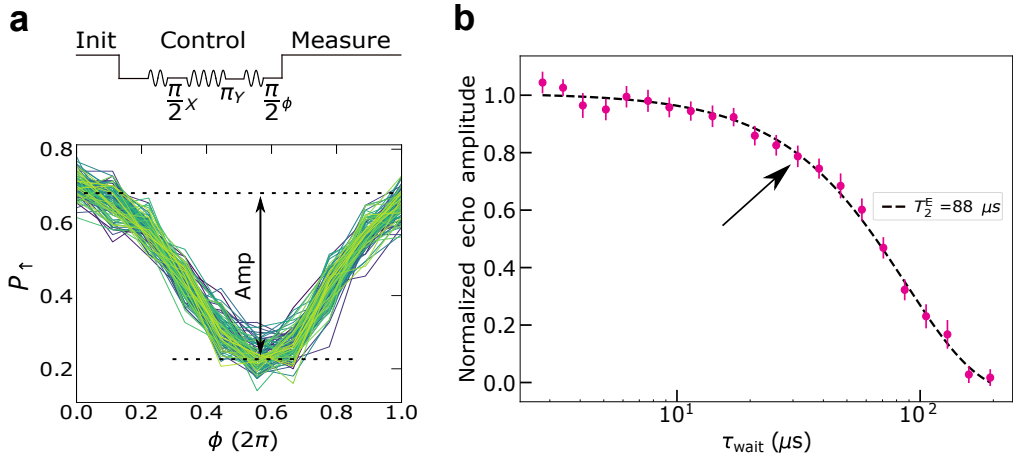

Figure 5.8 – **Hahn-echo decaying shape. (a)** $P_\uparrow(\tau_{\text{wait}} = 31.4\,\mu\text{s})$ *vs* the phase ϕ of the last $\pi/2$ pulse for 100 repetitions. Each of the N curves is fitted with a cosine of amplitude $\text{Amp}_{(\text{n})}$. The mean amplitude value is shown on the graphic. The top inset sketches the pulse sequence. **(b)** Normalized Hahn-echo amplitude *vs* free evolution time τ_{wait} at $f_L = 17\,\text{GHz}$ and $\theta_{zx} = 99°$. The resulting echo amplitudes from (a) is re-normalized and reported in the plot by a black arrow. The dashed curve is a fit to $\exp(-(\tau_{\text{wait}}/T_2^E)^\beta)$ with $\beta = 1.5 \pm 0.1$.

A representative Hahn-echo plot is shown in Fig. 5.8-b. We fit the echo amplitude to an exponential decay $\exp(-(\tau_{\text{wait}}/T_2^{\text{E}})^\beta)$, where the exponent β is left as a free parameter. The best fit is obtained for $\beta = 1.5 \pm 0.1$, which implies a high frequency noise with a characteristic spectrum $S(f) = S_{\text{hf}}(f_0/f)^\alpha$, where $f_0 = 1\,\text{Hz}$ is a reference frequency and $\alpha = \beta - 1 \approx 0.5$ (we note that the same α value was reported for hole spin qubits in germanium [18]). A more detailed study is available in the next chapter.

III. $\tan\phi = A_y/A_x$, where $A_i \in [0, 1]$ represents the amplitude modulation applied on MW I/Q outputs.

5.3.3 Magnetic sweet spots

To explore the angular dependence of T_2^{E} in the xz plane, we measure the decay of the Hahn-echo amplitude for different values of θ_{zx}. The results, shown in Fig. 5.9, reveal a strong anisotropy, with T_2^{E} ranging from 15 μs to 88 μs. Strikingly, the spin coherence time peaks at $\theta_{zx} = 99°$, an angle between the minimum of $|\mathrm{LSES_{G1}}|$ and a zero of $\mathrm{LSES_{G2}}$, highlighting a correlation with the correspondingly suppressed electrical noise. The extended coherence time is much longer than previously reported for hole spin qubits in both silicon and germanium [19].

The observed angular dependence of T_2^{E} can be understood by assuming that the electrical noise is the sum of uncorrelated voltage fluctuations on the different gates Gi with respective spectral densities $S_{\mathrm{G}i}(f) = S_{\mathrm{G}i}^{\mathrm{hf}}(f_0/f)^{0.5}$. Given the Hahn-Echo noise filter function, the decoherence rate can then be expressed as (See theory 2.2.3):

$$\frac{1}{T_2^{\mathrm{E}}} \approx 7.8 f_0^{1/3} \left(\sum_i \left(\frac{\partial f_L}{\partial V_{\mathrm{G}i}} \right)^2 S_{\mathrm{G}i}^{\mathrm{hf}} \right)^{2/3} . \tag{5.2}$$

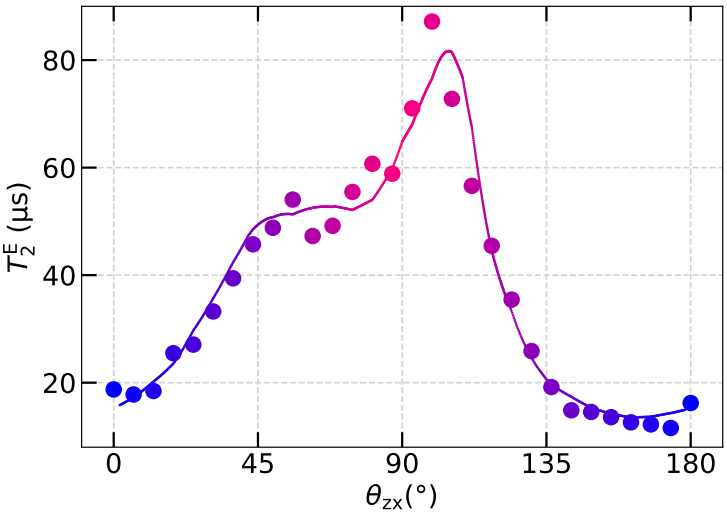

Figure 5.9 – **Echo spin coherence anisotropy**. Measured T_2^{E} vs magnetic field angle θ_{zx} (symbols). The solid line is a fit to Eq. (5.2), using the experimental $\mathrm{LSES_{G1}}$ and $\mathrm{LSES_{G2}}$ from Figs. 5.5 and 5.6

Using the longitudinal spin-electric susceptibilities from Figs. 5.5 and 5.6 and leaving the weights $S_{\mathrm{G}i}^{\mathrm{hf}}$ as adjustable parameters, we achieve a remarkable agreement with the experimental T_2^{E} (see colored solid line in Fig. 5.9). This strongly supports the hypothesis that the Hahn-echo coherence time is limited by electrical noise. As already argued before, $\mathrm{LSES_{G1}}$ and $\mathrm{LSES_{G2}}$ indeed quantify the susceptibility of the hole spin to electric field fluctuations parallel and perpendicular to the channel, respectively. The best fit in Fig. 5.9 is obtained with $S_{\mathrm{G1}}^{\mathrm{hf}} = (1.7\,\mu\mathrm{V}/\sqrt{\mathrm{Hz}})^2$ and $S_{\mathrm{G2}}^{\mathrm{hf}} = (66\,n\mathrm{V}/\sqrt{\mathrm{Hz}})^2$.

5.3.4 Charge noise in spin qubit platforms

The values for the spectral density obtain by the fit in the previous subsection are referring to equivalent voltage fluctuations on respective gate. In fact, the fluctuations may be produced by two level system closer to the qubit and not screened by the hole gas below G1.Converting the spectral density, using lever arm of both gates, we express it as chemical potential fluctuation. It results in $S^{\mathrm{hf}}_{\mu,\mathrm{G1}} = (13\,n\mathrm{eV}/\sqrt{\mathrm{Hz}})^2$ and $S^{\mathrm{hf}}_{\mu,\mathrm{G2}} = (17\,n\mathrm{eV}/\sqrt{\mathrm{Hz}})^2$ where directions have similar impact on the qubit in terms of energy. It suggests that electrical noise in the device is more or less isotropic.

Platform	Doping	Structure	Qubit	α	$S^{hf}_{\mu}(1\,\mathrm{MHz})$	ref
Ge/SiGe	Holes	2D	LD	0.7	$10^{-17}\,eV^2/\mathrm{Hz}$	[20]
^{28}Si/SiGe	Electrons	2D	LD	1	$10^{-18}\,eV^2/\mathrm{Hz}$	[13]
Si/SiGe	Electrons	2D	ST	1	$10^{-18}\,eV^2/\mathrm{Hz}$	[21]
Si	Holes	1D	LD	0.5	$10^{-20}\,eV^2/\mathrm{Hz}$	[22]
^{28}Si/SiGe	Electrons	2D	LD	1	$10^{-21}\,eV^2/\mathrm{Hz}$	[23]
GaAs	Electrons	2D	ST	0.7	$10^{-22}\,eV^2/\mathrm{Hz}$	[24]
GaAs	Electrons	2D	ST	0.7	$10^{-22}\,eV^2/\mathrm{Hz}$	[25]

Table 5.1 – Charge noise in spin qubit platform at high frequency (1 MHz)

We now draw our attention to the high frequency noise in platforms hosting spin qubits. We use as a figure of merit, the chemical potential spectral density at 1 MHz ($S^{hf}_{\mu}(1\,\mathrm{MHz})$), extracted from Hahn-echo measurement, in order to compare different structures and materials with various lever arms. We also report the high frequency noise spectra exponent (α) which may differ from the classical 1/f noise at low frequency by defining $S^{hf}_{\mu}(f) = (f/f_0)^{\alpha}$. Data in the literature are gathered in Table.5.1.

We remark that GaAs remains by far the best platform with minimal charge noise at high frequency. Even the lowest results published on silicon and germanium platforms struggle to go beyond the limit $S^{hf}_{\mu}(1\,\mathrm{MHz}) = 10^{-20}\,\mathrm{eV}^2/\mathrm{Hz}$ despite extra clean interfaces in crystalline heterostructure. Note that best charge noise level were obtain with $\alpha < 0.8$ but no real explanation describes this change of color in the power spectral density.

Conclusion

In conclusion, we correlated the longitudinal electrical spin susceptibility with the extended coherence time for the first hole in a silicon MOSFET device. The results suggest that spin coherence at high frequency is limited by charge noise. The orientation of the electrical contribution is properly caught by G1 and G2, but, it does not imply that the noise originate from these gates. We also measured noise level comparable to state of the art figures in both silicon or germanium spin qubit platforms. Nonetheless, to extend even further the spin coherence, there is work to be done to obtain charge noise level comparable to GaAs.

5.4 Inhomogeneous dephasing time

Specifications of the conditions under which the superposition state decay is acquired conducts to many coherence time definitions. Among them, T_2^*, also called the inhomogeneous dephasing time, is recorded using a Ramsey experiment. The latter is the main published figure of merit to assess qubits' quality. Ramsey experiment over time is also used to perform spectroscopy of the noise impacting the qubit in the low frequency domain (from µHz to hundred of Hz).

5.4.1 Ramsey experiment

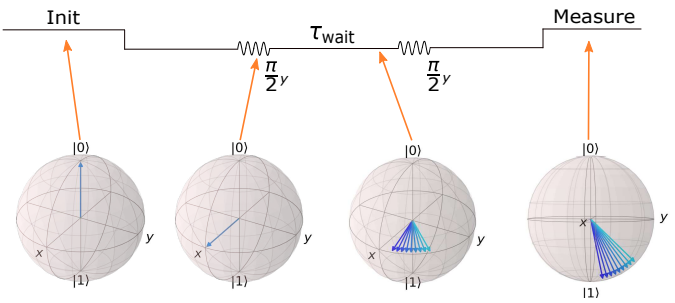

Figure 5.10 – **Ramsey sequence**. A first $\pi_y/2$ pulse creates a superposition state in the Bloch sphere's equatorial plane. Then, the second $\pi_y/2$ pulse projects the phase acquired during the free evolution time τ_{wait} on the spin state.

The Ramsey experiment begins with a qubit initialized in the ground state. A first pulse $\pi_y/2$ creates a superposition state, polarizing the spin in the equatorial plane of the Bloch sphere. After a given time τ_{wait} during which the qubit acquires a phase proportional to the Larmor detuning. Finally, the phase is projected on the spin state via a second $\pi_y/2$. The full sequence is resumed in Fig. 5.10. As a consequence, the recorded spin states oscillates at the frequency $\Delta f = f_{\mathrm{MW1}} - f_L$, often called Ramsey oscillations or fringes. Conversely to Hahn-

echo protocol, the dephasing induced by low frequency noise is not suppressed due to the absence of the refocusing π pulse (see last Bloch sphere in Fig. 5.10). The inhomogeneous dephasing time is obtained by fitting the Ramsey oscillations to $f(t) = A\cos(2\pi\Delta f \cdot t)e^{(-t/T_2^*)^2}$ corresponding to a cosine with a Gaussian decay envelope.

Figure 5.11-a displays $P_\uparrow$ for a series of identical Ramsey sequences recorded on an overall time frame of one hour, with each sequence lasting approximately 5.5 s [24, 14]. The next step is to average $P_\uparrow(\tau_{\text{wait}})$ on a subset of consecutive sequences measured within a total time t_{meas}. This way, an averaged Ramsey oscillation is obtained for each t_{meas}, whose amplitude is fitted to a Gaussian-decay function yielding $T_2^*(t_{\text{meas}})$. Representative Ramsey data sets and corresponding fits are shown in Fig. 5.11-b for three values of t_{meas}. The inhomogeneous dephasing time decreases with increasing t_{meas} due to the contribution of noise components with lower and lower frequency.

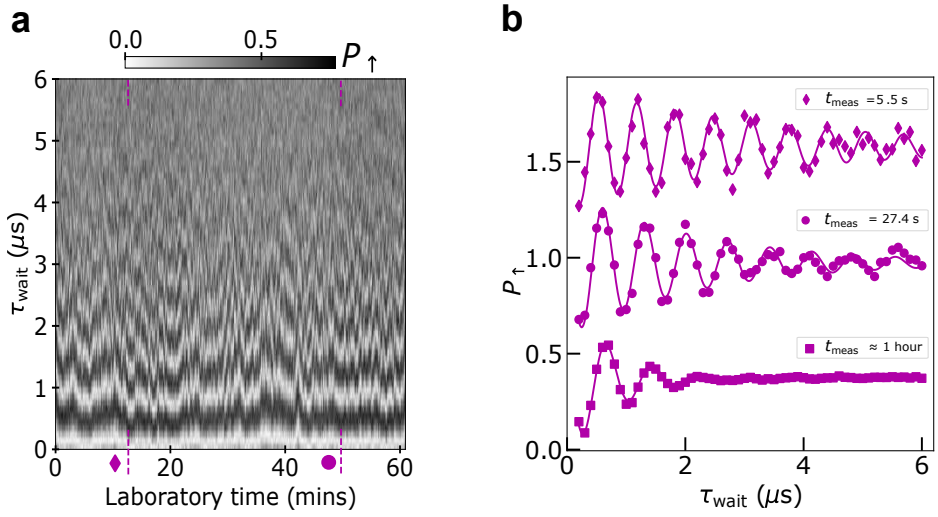

Figure 5.11 – **Free induction decay (FID). (a)** Collection of 600 Ramsey oscillations as a function of τ_{wait}, the free evolution time between two $\pi_x/2$ pulses, at $\theta_{zx} = 118°$. The applied microwave frequency is detuned by ~ 700 kHz from the Larmor frequency. Each Ramsey oscillation is measured in ≈ 5.5 s. The locations of the representatives traces shown in (b) are indicated by a diamond and a dot. **(b)** Selected averages of Ramsey oscillations taken over different measurement times: $t_{\text{meas}} = 5.5$ s corresponding to a single trace (diamonds); $t_{\text{meas}} = 27.5$ s, corresponding to 5 consecutive traces (circles); $t_{\text{meas}} \approx 1$ hour, corresponding to the full set of 600 traces (squares). The solid lines are fits to Gaussian decaying oscillations. Note that the decay time T_2^* depends on the chosen subset of consecutive traces (except for $t_{\text{meas}} \approx 1$ hour).

5.4.2 Dephasing time in the non-ergodic regime

In fact, the hole spin resonance frequency fluctuates over time due to noise during the experiment. If τ_{wait} is much smaller than the total acquisition time (always fulfilled during a Ramsey experiment), the frequency shift during the acquisition of a single point is negligeable. Note that we define a round as a single Ramsey sequence in Fig. 5.10. From initialization to measurement, a round lasts 185 μs. Collecting one Ramsey oscillations (n=1) takes a much longer time denoted as t_{meas}. Indeed we repeat each round 500 times and each oscillations contains 60 elements. Consequently, the duration for a single Ramsey oscillation is approximately 5.5 s. If we suppose Gaussian distribution for the frequency span, then the shape function may be written as :

$$f(t) = \frac{1}{N}\sum_{n=1}^{N} A\cos(2\pi\Delta f_{(r,n)}t) \tag{5.3}$$

Where $\Delta f_{(r,n)}$ is the frequency detuning during the acquisition of a point during round (r) and collection (n). It follows that the parameters of the Gaussian decay envelope $f(t) = A\cos(2\pi\Delta f \cdot t)e^{(-t/T_2^*)^2}$ are given such as :

$$\Delta f = \frac{1}{N}\sum_{n=1}^{N} \Delta f_{(r,n)} \tag{5.4}$$

$$T_2^* = \frac{1}{\sqrt{2}\cdot\pi\cdot\sigma_{\Delta f_{(r,n)}}} \approx \frac{0.225}{\sigma_{\Delta f_{(r,n)}}} \tag{5.5}$$

Hence, those parameters highly depend on the set "N" of consecutive traces (collection) chosen for the averaging. Especially, if the total time (t_{meas}) for the set is lower than the low-frequency noise correlation time τ (non ergodic regime), T_2^* becomes a stochastic variable that can be described by a statistical distribution.

For $N \leq 5$, we can fit the histograms of T_2^* with a Gamma distribution as in Ref. [26] (see Fig. 5.12-a):

$$f(T_2^*; \overline{T}_2^*, k) = \frac{k^k}{\overline{T}_2^{*k}\,\Gamma(k)} T_2^{*k-1} e^{-kT_2^*/\overline{T}_2^*} \tag{5.6}$$

where Γ is the Euler gamma function, $\overline{T}_2^*$ is the mean and k describes the shape (skewness) of the distribution.

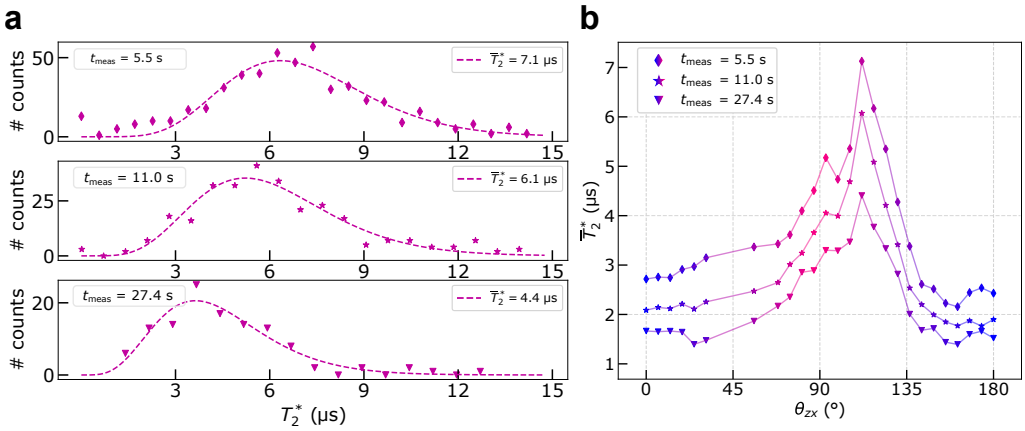

Figure 5.12 – **Spin coherence with correlated low-frequency noise (a)** T_2^* histograms for $t_{\mathrm{meas}} = 5.5\,\mathrm{s}$ ($N = 1$, diamonds), $11\,\mathrm{s}$ ($N = 2$, circles) and $27.4\,\mathrm{s}$ ($N = 5$, squares) at $\theta_{zx} = 111°$. The histograms are fitted with a Gamma distribution (dashed lines). **(b)** $\overline{T}_2^*$ extracted from the fits in (a) as a function of the magnetic field orientation θ_{zx}.

The extracted $\overline{T}_2^*$ is more robust to the presence of T_2^* data points far away from the mean, which are more frequent for small N's. Moreover, for small N, the process is equivalent to a high pass filter, getting rid of very low frequency noise. In Fig 5.12-b, we plot the fitted $\overline{T}_2^*$ as a function of the magnetic field orientation for $N = 1, 2, 5$. The data exhibit a clear peak at $\theta_{zx} = 111°$, close to (but not exactly at) the sweet spot of T_2^{E} (Fig. 5.9).

5.4.3 Ultra low frequency noise

For $N > 5$, the data set (Fig.5.11-a) does not contain enough samples (less than 100) to extract the probability distribution parameters with high enough accuracy. In that case, we simply estimate $\overline{T}_2^*$ as the sample average of T_2^*. We point out that the distribution of T_2^*'s shall narrow when approaching the ergodic regime ($t_{\mathrm{meas}} \gg \tau$).

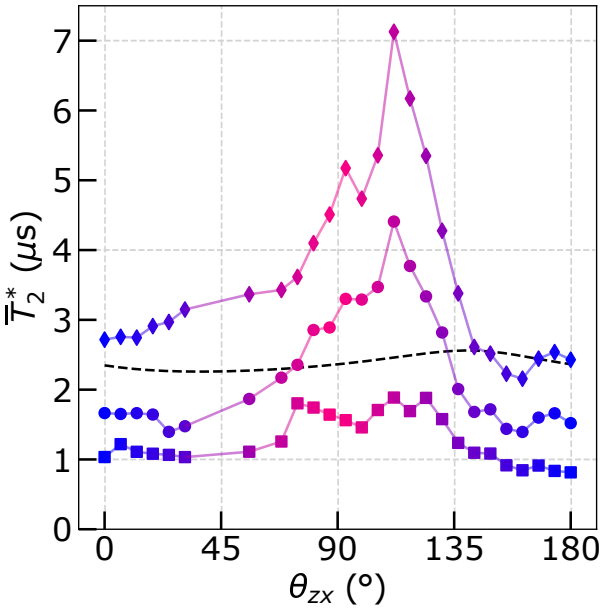

Figure 5.13 – **Probing the low frequency noise spectrum.** Mean $\overline{T}_2^*$ for different t_{meas} as a function of the magnetic field angle θ_{zx}. Symbols are the same as Fig. 5.11 : $t_{\text{meas}} = 5.5\,\text{s}$ corresponding to a single trace (diamonds); $t_{\text{meas}} = 27.5\,\text{s}$, corresponding to 5 consecutive traces (circles); $t_{\text{meas}} \approx 1\,\text{hour}$, corresponding to the full set of 600 traces (squares). The solid lines are guides to the eye. The dashed black line is the calculated dephasing time due to hyperfine interactions.

Fig. 5.13 reports $\overline{T}_2^*$ as a function of the magnetic field orientation for different data set (N=1,2,500). The overall anisotropy of the Hahn-echo decay time reduces at large t_{meas} starting from $t_{\text{meas}} > 50\,\text{s}$. Moreover, assuming that the qubit experiences only a single noise source which spectrum has the same behavior over a wide range of frequency would imply that the Hahn echo T_2^{E} and Ramsey $T_{2,\text{hf}}^*$ are proportional (See theory 2.5.2). Therefore, one would expect $T_{2,\text{hf}}^* \simeq 50\,\mu\text{s}$ at $\theta_{zx} = 99°$ where $T_2^{\text{E}} \simeq 90\,\mu\text{s}$ if the limiting noise mechanisms were the same at low and high frequency. The much shorter T_2^* measured in the present device hence support the change of color and/or amplitude of the noise source at low frequency.

Consequently to these two observations, we suspect an additional noise source at low frequency with a different anisotropy, which can be for example hyperfine interaction with surrounding nuclear bath. Although holes should be almost insensitive to this contribution [27], recent work [28] shows the necessity to pay attention to the question.

That being said, we calculated the expected T_2^* in the case of a surrounding nuclear bath interacting with the spin qubit (See theory 2.5.1) and reported it as a dashed black line in Fig. 5.13. T_2^* has been evaluated with the 6 bands $\mathbf{k}\cdot\mathbf{p}$ wave functions computed in Fig. 5.2. For silicon, we use $n_0 = 49.94\ \text{nm}^{-3}$, as well as $\nu = 4.7\%$, $I = 1/2$, and $|A| = 1.67\,\mu\text{eV}$ for ^{29}Si isotopes [28]. This value of $|A|$ was specifically computed for holes with *ab initio* density functional theory [29]. We note that the $T_2^* \approx 1 - 2\,\mu\text{s}$ measured at long t_{meas} is below but fairly close to the

expected hole spin dephasing time due to hyperfine interactions with the naturally present ^{29}Si nuclear spins [7]. This suggests that low-frequency dephasing may be partially due to such hyperfine interactions.

Conclusion

We showed that the anisotropy of the inhomogeneous dephasing time (T_2^*) exhibits almost the same peak as T_2^E when the data are acquired in the non ergodic regime. Nonetheless, the more the qubit experiences very low frequency noise, the more the anisotropy vanishes, suggesting that additional noise sources act on the qubit. We pinpoint that T_2^* saturates around the expected value one should observe if the spin is interacting with a surrounding nuclear bath, opening the question of purification for silicon and germanium hole spin qubit.

5.5 Quality factors

In this section, we discuss the quality factors of the hole spin. We define [19]:

— The inhomogeneous quality factor $Q^* = F_{\text{Rabi}} \times T_2^*$, which is half the number of π rotations that can be achieved within the inhomogeneous dephasing time T_2^*.

— The echo quality factor $Q^{\text{E}} = F_{\text{Rabi}} \times T_2^{\text{E}}$, which is half the number of π rotations that can be achieved within the echo time T_2^{E} shall the manipulations be intertwinned with a Hahn-Echo noise decoupling sequence.

All quantities involved in the different quality factors depend on the magnetic field orientation. In Figure 5.14-a, we plot the Rabi frequency as a function of θ_{zx} at constant Larmor frequency $f_L = 17$ GHz. The spin is driven by microwave bursts on gate G1, with power $P_{\text{MW1}} = 15$ dBm (on top of the MW1 line). The resulting quality factors Q^* and Q^{E} are plotted in Figs. 5.14-b&c. For Q^*, we use the value of $\overline{T}_2^*$ measured at $t_{\text{meas}} = 5.5$ s (see section 5.13). In the present case, the Rabi frequency is minimal around the sweet spot (see 5.14-a). Nonetheless, the quality factors Q^* and Q^{E} do peak near the sweet spot owing to the much improved coherence times. They reach $Q^* = 23$ and $Q^{\text{E}} = 276$, with peak-to-valley ratios of respectively 2.5 and 5.5.

As previously discussed in chapter **??**, with a larger driving power $P_{\text{MW1}} = 20$ dBm, we can achieve Rabi frequencies of at least 5 MHz at the sweet spot, yielding $Q^* \approx 35$ and $Q^{\text{E}} \approx 440$. In particular, we report comparable state of the art values [19] for hole spin qubit echo quality factors : ($Q^{\text{E}} = 200$ [30], $Q^{\text{E}} = 100$: [14]). In principle, the quality factors may be further improved by driving with gate G2 and looking for the sweet spot in the xy plane. As an additional note, we notice that spin control remains efficient at all angles including $\theta_{zx} = 99°$.

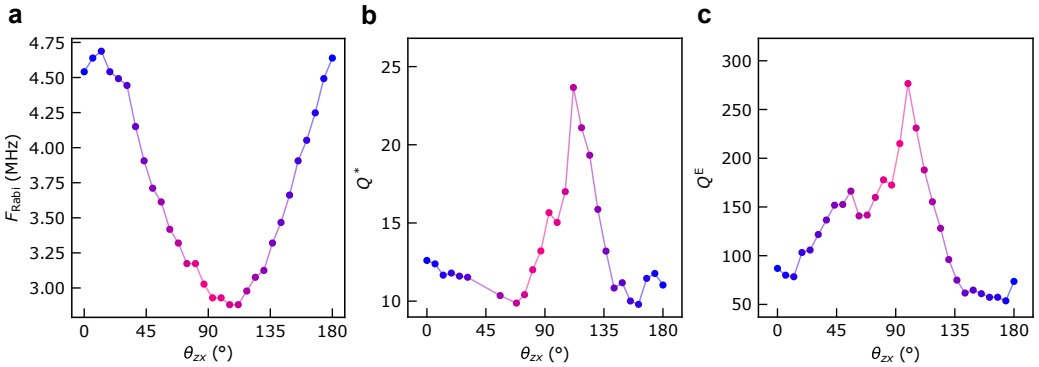

Figure 5.14 – **Rabi frequencies and quality factors.** **(a)** Rabi frequency as a function of magnetic field orientation θ_{zx}. The Larmor frequency $f_L = 17$ GHz is kept constant and the hole spin is manipulated by a microwave burst on gate G1 with power $P_{\mathrm{MW1}} = 15$ dBm on top of the MW1 line. **(b)** Inhomogeneous quality factor Q^* as a function of the magnetic field orientation θ_{zx}. The data are calculated from the Rabi frequencies plotted in (a), and from the values of $\overline{T}_2^*$ measured for $t_{\mathrm{meas}} = 5.5\,\mathrm{s}$ (Fig. 5.13). **(c)** Same as (b) for the echo quality factor Q^{E} (Fig. 5.9).

Conclusion

We report on the first spin qubit with electrical control and single-shot readout based on a single hole in a silicon nanowire device issued from an industrial-grade fabrication line. The hole wave function and corresponding g-factors could be modeled with an unprecedented level of accuracy in these types of devices, denoting a relatively low level of structural and charge disorder.

The hole-spin coherence was found to be limited by a charge noise at high frequencies, with a strong dependence on the magnetic-field orientation that could be faithfully accounted for by the spin-electric susceptibilities. A largely enhanced spin coherence was measured at the sweet-spot angle, far beyond the current state-of-the-art for hole-spin qubits and close to the best figures reported for ^{28}Si electron-spin qubits electrically driven via a micro-magnet. Our study of the inhomogeneous dephasing time revealed a much stronger noise at low frequencies that could be partially ascribed to the expected hyperfine interaction. In this scenario, the possible introduction of isotopically purified silicon devices would lead to significant improvement of hole-spin coherence in the low-frequency range.

Finally, we would like to emphasize that such sweet spots shall be ubiquitous in hole spin qubit devices[10], and that a careful design and choice of operation point can make them pretty robust to disorder. The engineering of sweet spots shall therefore open new opportunities for an efficient realization of multi-qubit or coupled spin-photon systems[31].

References

[1] Christoph Kloeffel, Marko J. Ran či ć, and Daniel Loss. « Direct Rashba spin-orbit interaction in Si and Ge nanowires with different growth directions ». In: *Physical Review B* 97 (23 June 2018), p. 235422. DOI: 10.1103/PhysRevB.97.235422. URL: https://link.aps.org/doi/10.1103/PhysRevB.97.235422.

[2] Vincent P. Michal, Benjamin Venitucci, and Yann-Michel Niquet. « Longitudinal and transverse electric field manipulation of hole spin-orbit qubits in one-dimensional channels ». In: *Physical Review B* 103 (4 Jan. 2021), p. 045305. DOI: 10.1103/PhysRevB.103.045305. URL: https://link.aps.org/doi/10.1103/PhysRevB.103.045305.

[3] Floris A. Zwanenburg et al. « Spin States of the First Four Holes in a Silicon Nanowire Quantum Dot ». In: *Nano Letters* 9.3 (Mar. 2009), pp. 1071–1079. ISSN: 1530-6984. DOI: 10.1021/nl803440s. URL: https://doi.org/10.1021/nl803440s.

[4] N. Ares et al. « Nature of Tunable Hole g Factors in Quantum Dots ». In: *Physical Review Letters* 110 (4 Jan. 2013), p. 046602. DOI: 10.1103/PhysRevLett.110.046602. URL: https://link.aps.org/doi/10.1103/PhysRevLett.110.046602.

[5] A. Bogan et al. « Consequences of Spin-Orbit Coupling at the Single Hole Level: Spin-Flip Tunneling and the Anisotropic g Factor ». In: *Physical Review Letters* 118.16 (2017), pp. 1–5. ISSN: 10797114. DOI: 10.1103/PhysRevLett.118.167701.

[6] Benjamin Venitucci et al. « Electrical manipulation of semiconductor spin qubits within the g-matrix formalism ». In: *Physical Review B* 98.15 (Oct. 2018), p. 155319. DOI: 10.1103/physrevb.98.155319. URL: https://journals.aps.org/prb/abstract/10.1103/PhysRevB.98.155319.

[7] Benoit Voisin et al. « Few-Electron Edge-State Quantum Dots in a Silicon Nanowire Field-Effect Transistor ». In: *Nano Letters* 14.4 (Mar. 2014), pp. 2094–2098. DOI: 10.1021/nl500299h. URL: https://pubs.acs.org/doi/10.1021/nl500299h.

[8] Benjamin Venitucci and Yann-Michel Niquet. « Simple model for electrical hole spin manipulation in semiconductor quantum dots: Impact of dot material and orientation ». In: *Physical Review B* 99 (11 Mar. 2019), p. 115317. DOI: 10.1103/PhysRevB.99.115317. URL: https://link.aps.org/doi/10.1103/PhysRevB.99.115317.

[9] S. D. Liles et al. « Electrical control of the g tensor of the first hole in a silicon MOS quantum dot ». In: *Phys. Rev. B* 104 (23 Dec. 2021), p. 235303. DOI: 10.1103/PhysRevB.104.235303. URL: https://link.aps.org/doi/10.1103/PhysRevB.104.235303.

[10] Stefano Bosco, Bence Hetényi, and Daniel Loss. « Hole Spin Qubits in Si FinFETs With Fully Tunable Spin-Orbit Coupling and Sweet Spots for Charge Noise ». In: *PRX Quantum* 2 (1 Mar. 2021), p. 010348. DOI: 10.1103/PRXQuantum.2.010348. URL: https://link.aps.org/doi/10.1103/PRXQuantum.2.010348.

[11] Ognjen Malkoc, Peter Stano, and Daniel Loss. *Charge-noise induced dephasing in silicon hole-spin qubits*. 2022. arXiv: 2201.06181 [cond-mat.mes-hall].

[12] Zhanning Wang et al. « Optimal operation points for ultrafast, highly coherent Ge hole spin-orbit qubits ». In: *npj Quantum Information* 7.1 (Apr. 2021), p. 54. ISSN: 2056-6387. DOI: 10.1038/s41534-021-00386-2. URL: https://doi.org/10.1038/s41534-021-00386-2.

[13] Jun Yoneda et al. « A quantum-dot spin qubit with coherence limited by charge noise and fidelity higher than 99.9% ». In: *Nature Nanotechnology* 13.2 (2018), pp. 102–106. ISSN: 1748-3395. DOI: 10.1038/s41565-017-0014-x. URL: https://doi.org/10.1038/s41565-017-0014-x.

[14] Leon C. Camenzind et al. « A hole spin qubit in a fin field-effect transistor above 4 kelvin ». In: *Nature Electronics* 5.3 (Mar. 2022), pp. 178–183. ISSN: 2520-1131. DOI: 10.1038/s41928-022-00722-0. URL: https://doi.org/10.1038/s41928-022-00722-0.

[15] Tuomo Tanttu et al. « Controlling Spin-Orbit Interactions in Silicon Quantum Dots Using Magnetic Field Direction ». In: *Physical Review X* 9 (2 May 2019), p. 021028. DOI: 10.1103/PhysRevX.9.021028. URL: https://link.aps.org/doi/10.1103/PhysRevX.9.021028.

[16] F. H. L. Koppens, K. C. Nowack, and L. M. K. Vandersypen. « Spin Echo of a Single Electron Spin in a Quantum Dot ». In: *Physical Review Letters* 100 (23 June 2008), p. 236802. DOI: 10.1103/PhysRevLett.100.236802. URL: https://link.aps.org/doi/10.1103/PhysRevLett.100.236802.

[17] Guido Burkard et al. *Semiconductor Spin Qubits*. 2021. arXiv: 2112.08863 [cond-mat.mes-hall].

[18] Nico W. Hendrickx et al. « A four-qubit germanium quantum processor ». In: *Nature* 591.7851 (Mar. 2021), pp. 580–585. ISSN: 1476-4687. DOI: 10.1038/s41586-021-03332-6. URL: http://dx.doi.org/10.1038/s41586-021-03332-6.

[19] Peter Stano and Daniel Loss. *Review of performance metrics of spin qubits in gated semiconducting nanostructures*. 2021. arXiv: 2107.06485 [cond-mat.mes-hall].

[20] Nico W. Hendrickx et al. « A four-qubit germanium quantum processor ». In: *Nature* 591.7851 (Mar. 2021), pp. 580–585. ISSN: 1476-4687. DOI: 10.1038/s41586-021-03332-6. URL: https://doi.org/10.1038/s41586-021-03332-6.

[21] Elliot J. Connors, JJ Nelson, and John M. Nichol. *Charge-noise spectroscopy of Si/SiGe quantum dots via dynamically-decoupled exchange oscillations*. 2021. arXiv: 2103.02448 [cond-mat.mes-hall].

[22] N. Piot et al. *A single hole spin with enhanced coherence in natural silicon*. 2022. arXiv: 2201.08637 [cond-mat.mes-hall].

[23] Tom Struck et al. « Low-frequency spin qubit energy splitting noise in highly purified 28Si/SiGe ». In: *npj Quantum Information* 6.1 (May 2020), p. 40. ISSN: 2056-6387. DOI: 10.1038/s41534-020-0276-2. URL: https://doi.org/10.1038/s41534-020-0276-2.

[24] O. E. Dial et al. « Charge Noise Spectroscopy Using Coherent Exchange Oscillations in a Singlet-Triplet Qubit ». In: *Physical Review Letters* 110 (14 Apr. 2013), p. 146804. DOI: 10.1103/PhysRevLett.110.146804. URL: https://link.aps.org/doi/10.1103/PhysRevLett.110.146804.

[25] Pascal Cerfontaine et al. « Closed-loop control of a GaAs-based singlet-triplet spin qubit with 99.5% gate fidelity and low leakage ». In: *Nature Communications* 11.1 (Aug. 2020), p. 4144. ISSN: 2041-1723. DOI: 10.1038/s41467-020-17865-3. URL: https://doi.org/10.1038/s41467-020-17865-3.

[26] M. R. Delbecq et al. « Quantum Dephasing in a Gated GaAs Triple Quantum Dot due to Nonergodic Noise ». In: *Physical Review Letters* 116 (4 Jan. 2016), p. 046802. DOI: 10.1103/PhysRevLett.116.046802. URL: https://link.aps.org/doi/10.1103/PhysRevLett.116.046802.

[27] Jan Fischer et al. « Spin decoherence of a heavy hole coupled to nuclear spins in a quantum dot ». In: *Physical Review B* 78 (15 Oct. 2008), p. 155329. DOI: 10.1103/PhysRevB.78.155329. URL: https://link.aps.org/doi/10.1103/PhysRevB.78.155329.

[28] Stefano Bosco and Daniel Loss. « Fully Tunable Hyperfine Interactions of Hole Spin Qubits in Si and Ge Quantum Dots ». In: *Physical Review Letters* 127 (19 Nov. 2021), p. 190501. DOI: 10.1103/PhysRevLett.127.190501. URL: https://link.aps.org/doi/10.1103/PhysRevLett.127.190501.

[29] Pericles Philippopoulos, Stefano Chesi, and W. A. Coish. « First-principles hyperfine tensors for electrons and holes in GaAs and silicon ». In: *Physical Review B* 101 (11 Mar. 2020), p. 115302. DOI: 10.1103/PhysRevB.101.115302. URL: https://link.aps.org/doi/10.1103/PhysRevB.101.115302.

[30] Daniel Jirovec et al. « A singlet-triplet hole spin qubit in planar Ge ». In: *Nature Materials* 20.8 (2021), pp. 1106–1112. ISSN: 14764660. DOI: 10.1038/s41563-021-01022-2. arXiv: 2011.13755. URL: http://dx.doi.org/10.1038/s41563-021-01022-2.

[31] V. P. Michal et al. *Tunable hole spin-photon interaction based on g-matrix modulation*. 2022. DOI: 10.48550/ARXIV.2204.00404. URL: https://arxiv.org/abs/2204.00404.

Chapter 6

Noise characterization

"Study hard what interests you the most in the most undisciplined, irreverent and original manner possible"

Richard Feynman

In all physical system, the ultimate detectability of some weak signal is indubitably limited by noise. By definition, a noise is described as any unwanted signal, which degrades the accuracy of measuring the desired signal. Some types of noise are unavoidable (such as fluctuations in the signal itself such as shot noise) but may be reduced via filtering techniques in frequency (bandwidth narrowing) or time (signal averaging) domain. In the case of external noise sources, analyzing them to determine their origin is the first step before removing them (cancellation or working at sweet spots to reduce the coupling). In this chapter, we explore the noise spectrum over more than 14 decades in frequency using different probing techniques and make a guess on the origin of noises. First section is dedicated to Ramsey interference, to characterize low frequency noise. The next section complement the latter one by evaluating electrical noise recorded via the charge sensor. Third section is based on a special type of RMN spectroscopy sequences (CPMG), sensitive in our case to electrical noise source in the Mega-hertz range. Finally, the exchange of energy between the Qubit and its environment provides hints on ultra-high frequency noise domain.

Contents

6.1 Ramsey interference 149
6.1.1 Free induction decay (FID) 149
6.1.2 Ultra low frequency spectrum 151
6.1.3 Ramsey Single Shot (RSS) 152
6.1.4 RSS auto-correlation 154
6.2 Charge Sensing (CS) 155

6.2.1 Coulomb peak sensitivity 155
6.2.2 Hyperfine ? 157
6.3 Carr–Purcell –Meiboom–Gill (CPMG) 158
6.3.1 CPMG filtering function 158
6.3.2 CPMG measurement 159
6.3.3 CPMG spectrum 160
6.4 Spin life time 161
6.4.1 T_1 measurement protocol 161
6.4.2 Γ_1 versus magnetic field amplitude 162
6.4.3 Γ_1 versus magnetic field orientation 163
6.4.4 TSES versus magnetic field orientation 164
6.4.5 Johnson Nyquist 166
References 172

6.1 Ramsey interference

The frequency of Ramsey oscillations is exactly equal to the detuning in between the Larmor frequency and the microwave excitation [1] [I] which provides a powerful tool to track accurately any change in the Qubit energy. We define the Ramsey spectroscopy as the study of the spectrum of $T_2^*(t)$ which assesses low frequency domain noises. These latter may be, for holes, of different kinds, including charge noise via spin orbit coupling or magnetic noise. Unless it is specifically stated, the magnetic field in this section is oriented along $\vec{x}$ ($\theta_{zx} = 90°$), in such a way that the Larmor frequency is equal to 16.998 GHz.

6.1.1 Free induction decay (FID)

To accurately estimate the noise power spectral density (PSD), we repeatedly measure Ramsey oscillations at a fixed detuning from Larmor frequency (f_{MW1} =)17 Ghz.

As previously stated, the fringes visible in Fig. 6.1 (top) oscillates at frequency Δf (see caption). We measured 3700 Ramsey fringes spread over more than ten hours (t_{tot}). For each realization, we varied the free evolution time τ_{wait} up to 7 μs, and averaged 200 single shot spin measurement to obtain $P_\uparrow$. Finally, to extract $\Delta f(\tau_{\mathrm{lab}})$, we performed a Fourier transformation on each fringe and extracted its fundamental frequency. Corresponding result is displayed in Fig. 6.1 (bottom).

Fig. 6.2 presents the histogram of $\Delta f(\tau_{\mathrm{lab}})$, showing a Gaussian shape. We fit (dashed black curve) the number of counts with the equation :

$$g(f) = \frac{Amp}{\sigma\sqrt{2\pi}}\, e^{-\frac{(f-\mu)^2}{2\sigma^2}} \tag{6.1}$$

Where the best fit yields to a standard deviation ($\sigma_{\Delta f}$) of $196 \pm 2kHz$. Consequently to the Gaussian noise envelope, the noise is completely defined by its spectrum $S_(f)$[2], greatly simplifying the analysis.

I. Equation is : $\Delta f = f_L - f_{\mathrm{MW}}$. For more details see last chapter.

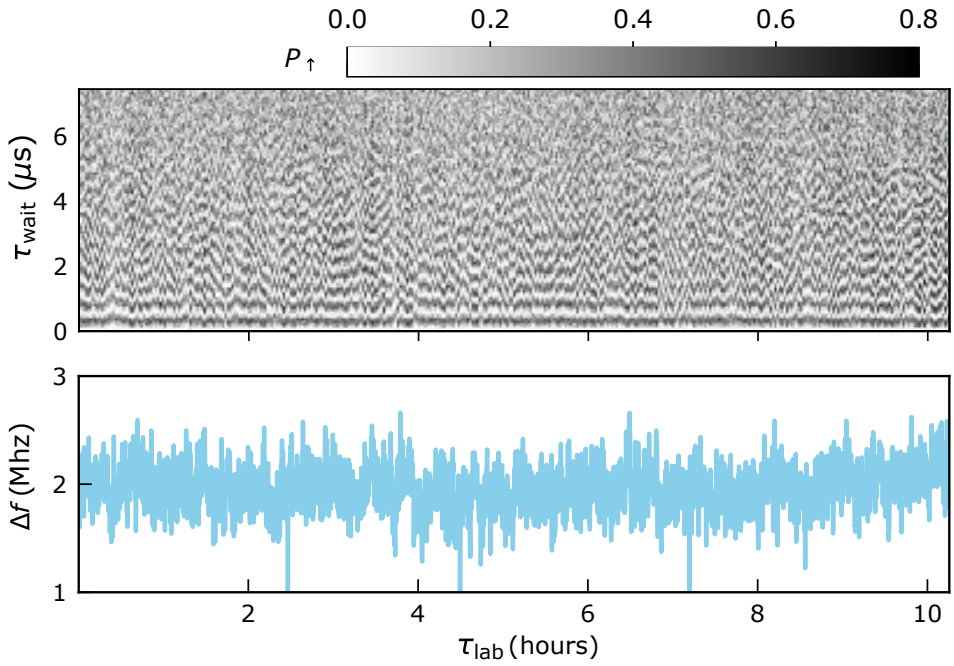

Figure 6.1 – **Free induction decay over night.** (top) Ramsey fringes as a function of τ_{wait} acquired during 10 hours, at $\theta_{zx} = 90°$. Each fringe oscillates at the frequency $\Delta f = f_{\text{MW1}} - f_{\text{L}}$. A single fringe takes roughly 10 s to record. (bottom) Δf, obtained via Fourier transform of the Ramsey fringes, versus laboratory time (τ_{lab}).

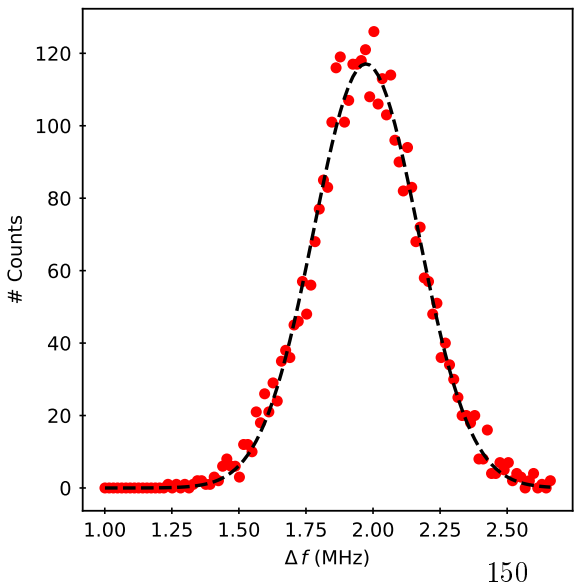

Figure 6.2 – **Histogram of the signal $\Delta f(\tau_{\text{lab}})$.** Histogram of the Larmor frequency shift (points) possesses a Gaussian envelope (black dashed line), with standard deviation inversely proportional to the inhomogeneous dephasing time T_2^* (ergodic regime). The fit yields to $\sigma_{\Delta f} = 196 \pm 2kHz$.

6.1.2 Ultra low frequency spectrum

We used a Fourier transformation on the signal $\Delta f(\tau_{\text{lab}})$ to extract the noise spectrum corresponding to the experiment ($S_L^{FID}(f)$) [3, 4] in Hz^2/Hz (See theory 2.6.1. Index L stands for Larmor fluctuations. We also define $S_\mu^{FID}(f)$ in eV^2/Hz [3, 5, 6, 7], the equivalent noise spectrum in term of chemical potential. The relation between the two PSD, considering uncorrelated noise on gates G1 and G2 is :

$$S_L^{FID}(f) = \sum_i \left(\frac{\partial f_L}{\partial V_{G_i}} * \frac{1}{\alpha_{G_i}} \right)^2 S_{\mu,G_i}^{FID}(f) \tag{6.2}$$

Where α_{G_i} is the lever arm of the gate i on the qubit, and $\partial f_L / \partial V_{G_i}$ is the longitudinal spin electric susceptibility $LSES_{G_i}$ (See definition : 2.5.2). We also previously showed that $S_{\mu,G_1}^{FID} \approx S_{\mu,G_2}^{FID}$. Assuming this relation true for all frequencies, we simplify eq. 6.2 to :

$$S_L^{FID}(f) = S_\mu^{FID}(f) \cdot \sum_i \left(\frac{\partial f_L}{\partial V_{G_i}} * \frac{1}{\alpha_{G_i}} \right)^2 \tag{6.3}$$

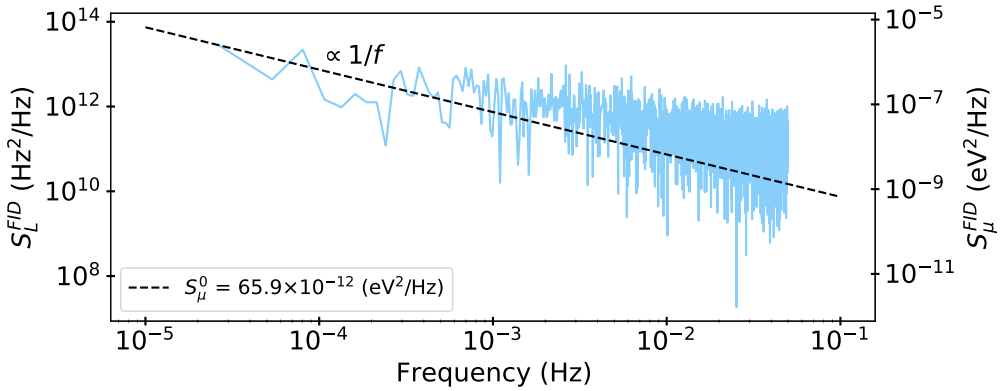

Figure 6.3 – **PSDs from free inductive decay measurement.** PSD extracted at $\theta_{zx} = 90°$, close to the electrical sweet spot. For the conversion we used $\text{LSES}_{\text{G1}} = -0.12\,\text{MHz.mV}^{-1}$ and $\text{LSES}_{\text{G2}} = -2.16\,\text{MHz.mV}^{-1}$. We observe local deviations from 1/f trend. S_μ^0 displayed in the inset correspond to the extrapolated amplitude at 1 Hz.

Where $S_\mu^{FID}(f = 1\,\text{Hz}) = \text{S}_\mu^0$ can be used as a metric to compare noise sources amplitude in the literature. Finally, Fig 6.3 reports the PSD in both units. The global trend shows a $1/f$ signature with local whitening ($[8 * 10^{-2} : 4 * 10^{-3}]$ Hz) also reported in [4].

6.1.3 Ramsey Single Shot (RSS)

In order to probe higher frequency events, we shall increase the measurement speed. The easiest solution would be to reduce the number of cycles necessary to measure a Ramsey oscillations. However, this option would only save a factor of two or three in the best case. The most radical technique is simply to fix a given time τ_{wait} and to measure the signal as singular $P_\uparrow$ events, repeated continuously, thus reducing the measurement time to its minimum. Indeed, in this configuration we obtain $\tau_{\text{meas}} = 210\,\mu$s (full cycle time), allowing to prob frequencies above 1 kHz [8].

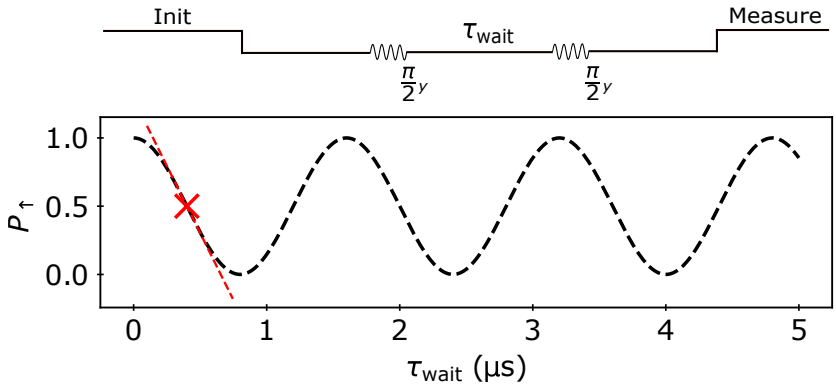

Figure 6.4 – **Simulation of Ramsey oscillations for RSS.** (Black dashed line) Ramsay oscillations with $\Delta f = 1/(4\,\tau_{\text{fix}})$ where $\tau_{\text{fix}} = 400$ ns (red cross) according to eq. 6.4. The measurement is set up in order to access the linear part of the cosine function (red dashed line is a linear development at the red cross).

To record RSS, we fixed the Larmor frequency detuning so that $\Delta_f = 1/(4\,\tau_{\text{fix}})$ corresponding to the configuration in Fig. 6.4. During 7 min, we measured every 210 μs the single shot output of the charge detector ($|\uparrow\rangle$ or $|\downarrow\rangle$) corresponding to almost two million realizations. Each realization is equivalent to $P_\uparrow^{N=1}(t)$, where N represents the number single of shot events used obtain the averaged signal. Fig. 6.5 shows a small part of the total matrix corresponding to the two million realizations. Red elements correspond to a spin $|\uparrow\rangle$ outcome while gray elements are spin $|\downarrow\rangle$.

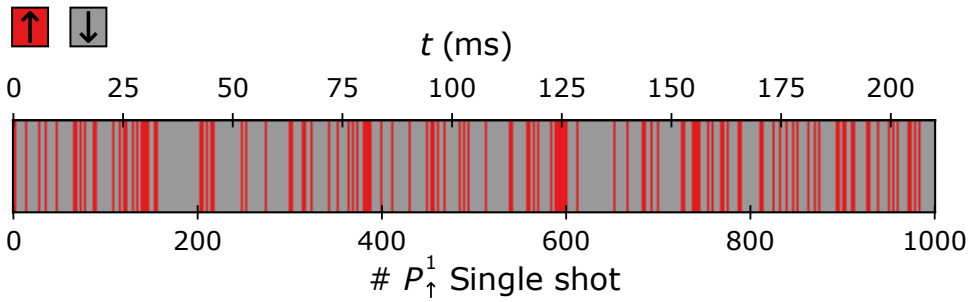

Figure 6.5 – **Blip matrix from RSS measurement.** Each vertical line correspond to a single shot outcome, which is either a spin $|\uparrow\rangle$ (red) or a spin $|\downarrow\rangle$ (grey).

The probability $P_\uparrow^N$, for N sufficiently big [II] (supressing discretization of the signal), is mathematically expressed as :

$$P_\uparrow(t) = \frac{1+\cos(2\pi\Delta f\, t)}{2} \tag{6.4}$$

Assuming that the system experiences small variation of the frequency due to noise, we shall write $f = \Delta f + \delta f$. If the system stays in a linear regime (at $t = \tau_{fix}$), the previous equation simplifies to :

$$P_\uparrow(t=\tau_{\text{fix}}) = \frac{1+\cos(2\pi(\Delta f+\delta f)\tau_{\text{fix}})}{2} = \frac{1+\cos\left(\frac{\pi}{2}+\delta f * \tau_{\text{fix}}\right)}{2} \tag{6.5}$$

A first order Taylor expansion of $P_\uparrow(t=\tau_{\text{fix}})$ gives [III] :

$$P_\uparrow(t=\tau_{\text{fix}}) = \frac{2+\pi}{4} - \pi\,\delta f\,\tau_{\text{fix}} + o(\tau_{\text{fix}}) \tag{6.6}$$

II. Here the error on the state admixture is given by $1/\sqrt{N}$ meaning that $N = 50$ is sufficient.
III. Note that $\cos\left(\frac{\pi}{2}+\theta\right) = -\sin(\theta) = \frac{\pi}{2} - \theta$ around $\theta = 0$.

Represented as the red dashed line in Fig. 6.4. Note that the auto-correlation of signal $P_{\uparrow}^{N=1}(t)$ is different from the auto-correlation of $P_{\uparrow}^{N=100}(t)$ (See theory 2.6.3). But applying the filter describe eq. 2.98 allows to compute $S_L^{RSS}(f)$ [IV].

6.1.4 RSS auto-correlation

We calculated $S_L^{RSS}(f)$ using the auto-correlation of signal $P_{\uparrow}^{N=1}(t)$ (See theory 2.6.3). We selected the length of $P_{\uparrow}^{N=1}(t)$ to be equal to 2^N, with N an integer. We also replaced the first point of the auto-correlated signal ($\delta_t = 0$) which value is huge due to shot noise measurement [V], by it's nearest neighbor (following ref [8]). Finally, taking the Fourier transform of the auto-correlation gives after renormalization spectrum presented in Fig. 6.6. The light gray curve corresponds to the auto-correlation taking into account 2^{18} points while the blue one is an average of 7 curves each containing 2^{15} points. The process is equivalent to a Bartlett post treatment ([9]) where we loose low frequency information in order to reduce the noise at high frequency.

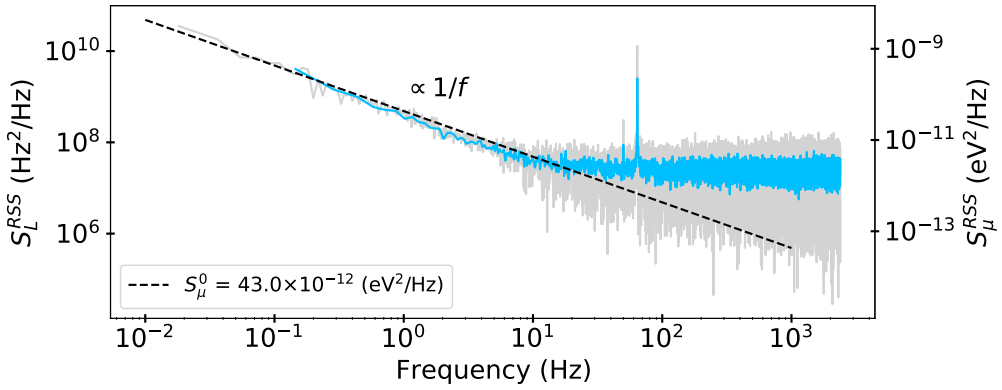

Figure 6.6 – **PSDs from Ramsey single shot measurement.** Spectra show a 1/f trend, where S_μ^0 amplitude is very coherent with previous measurement (Fig. 6.3).

We observed two peaks corresponding to noise at 50 Hz and 64 Hz. The first contribution is due to the alternating voltage frequency in the electricity network, while the second corresponds to the Bluefors pulse tube. Mechanical oscillations on coaxial cables creates electrical oscillations propagating through the line (triboelectricity [10]). Both contributions need to be even more mitigated since they are visible on the qubit's signal. To go further, probing even higher frequency in the

IV. The correction is very little and may be probably neglected. But since FID has been recorded with an average $N = 100$, we correspondingly modified the RSS spectrum.

V. Shot noise is a white noise. Consequently the auto-correlation is huge around 0 and almost zero elsewhere.

spectrum requires to drastically change the experimental method.

6.2 Charge Sensing (CS)

Numerous publications extrapolate the charge noise in the vicinity of the qubit by measuring fluctuations on the nearby charge detector [3, 4, 5, 6, 7]. The main drawback of this experiment is the assumption that the spin qubit experiences exactly the same electrical noise then the charge sensor. Moreover, one has to take care that tunneling noise is not the dominant noise source of the charge sensor [11], or else PSD would be increased.

6.2.1 Coulomb peak sensitivity

We measured the Coulomb peak of the hole island bellow G3 and G4 which is used as a charge detector for qubit experiment. The corresponding result is plotted in Fig. 6.7 as a function of V_{G3}. To extract the conversion factor $\partial\Phi/\partial V_{G3}$, we smoothed the signal with a high order Savgol filter (Savitzky-Golay algorithm), displayed as a black dashed line, and numerically differentiate it.

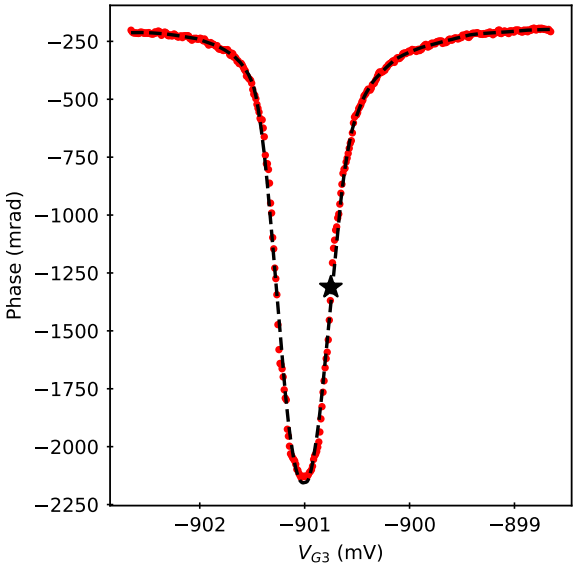

Figure 6.7 – **Coulomb peak used as a charge sensor for the qubit.** (dots) Coulomb peak of the detector near the working point configuration. The black dashed line is a savgol filter of the data in order to numerically derive the function. Black star correspond to the voltage applied on V_{G3} in order to record the temporal trace used to calculate the PSD.

Sitting at the most sensitive part of the signal (Black star), we recorded a time trace $\Phi(t)$ during more than 5 hours, with a sampling frequency of 10 Hz (100 ms). Using a Fourier transform technique (See theory 2.6.1) and assuming no tunneling noise, we calculated via eq. 6.7 the corresponding PSD plotted in Fig. 6.8 (coral

curve, low frequency). We also computed the PSD (red curve, high frequency) corresponding to a similar experiment but with a total time of 60 s and a sampling frequency of 13.732 KHz. Note that for the second curve, data are extracted from a similar device, possessing 8 gates but coming from the same wafer. We show that electrical noise is fairly similar, with a clear peak at 50 Hz.

$$S_{\Phi}^{CS} = \left(\frac{\partial \Phi}{\partial V_{G3}} \frac{1}{\alpha_2}\right)^2 S_{\mu}^{CS} \tag{6.7}$$

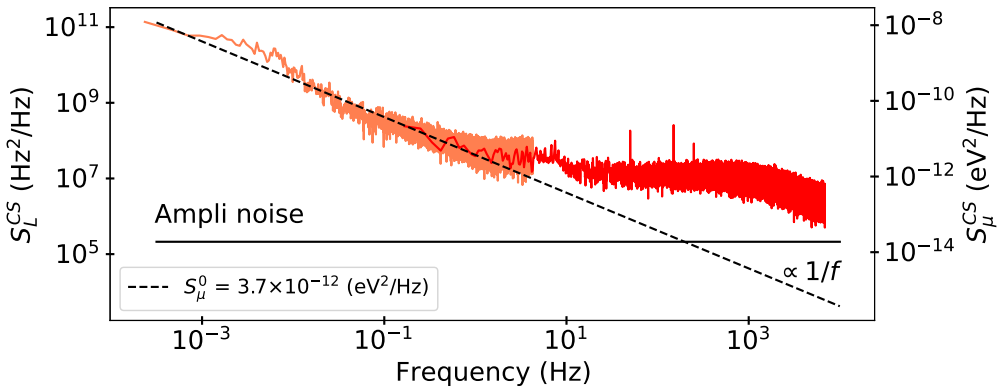

Figure 6.8 – **PSDs from charge sensing measurement.** Spectra show an astonishing continuity depite coming from two different samples. Note that S_{μ}^{0} is one order of magnitude lower than in previous experiment Fig. 6.3. Black line is an estimation of the noise floor due to the 4 K amplifier noise.

We added as a solid black line the estimated noise floor level corresponding to amplifier noise. For simplification, we only considered noise added by the first amplifier (low noise factory) and estimated outside the fridge the voltage fluctuations due to electronic noise. Given the amplification along the line, the corresponding equation is :

$$S_V = 4\,k_B\,T\,R * 10^{\frac{\sum_i amp_i}{10}} \tag{6.8}$$

Where T is the equivalent noise temperature of the amplifier (2.5 K), R is 50 ohm and $\sum_i amp_i$ is the sum of all amplifiers along the reflectometry line.

The spectrum's change of color above 10 Hz does not seem to arise from the amplifier when performing the calculations. To fuel the debate, acquiring time

traces on (black star) and out of Coulomb peak conducts to equivalent amplitude distributions at frequencies above 100 KHz ($\tau_c < 10\mu s$). In this configuration, signal to noise ratio becomes limited by amplifier and not anymore by charge noise in the device. Consequently, we hit the amplifier noise floor around $f = 100$ KHz, which is in good agreement with Fig. 6.8.

6.2.2 Hyperfine ?

So far, we extracted PSDs via the qubit and the charge sensor. On the first hand, the noise acting on the qubit can arise either from electrical noise through SOC or directly from magnetic noise (i.e hyperfine interaction, magnet, etc). On the other hand, the charge sensor is mainly sensitive to any charge displacement in its vicinity. Consequently, in the following we compare the spectra extracted with both techniques.

We draw our attention to the four previous spectra and report them in Fig. 6.9. Strikingly, we observe the same behavior in the frequency range of $\in [10, 1000]$ Hz where spectra saturate. If it was only a limitation from the amplifier itself, the behavior should not appear on qubit experiment. Moreover, there is a clear increase of the gap between both curves going to the lower frequency. As a consequence, we conclude that at low frequency, an additional noise source, which is not electric, acts on the qubit. This experiment supports the analysis done in the previous chapter, in which we detected an additional magnetic noise acting at low frequency when analyzing the peak to valley ratio in Ramsey anisotropy. The analysis strongly supports that hyperfine interaction is not negligeable for hole spin.

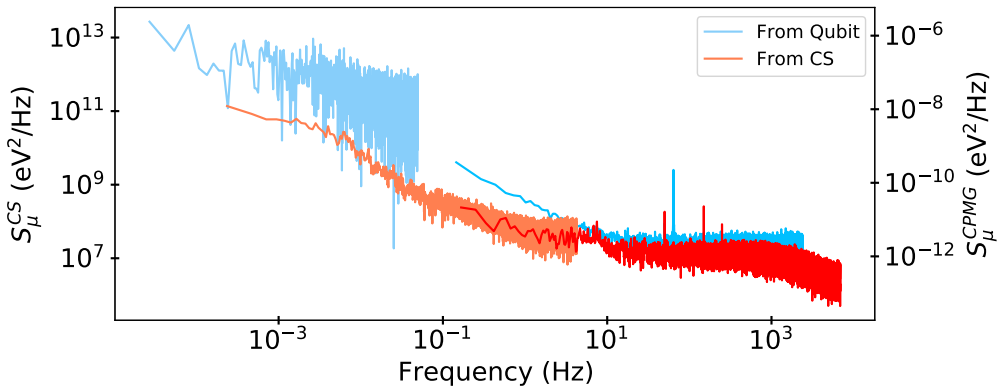

Figure 6.9 – **Summary of the different spectra.** Spectra acquired via the charge sensor (red) and via qubit experiment (blue). The distance between the red and blue curves gradually reduces as the frequency increases, supporting another noise mechanism at low frequency.

Nonetheless, to confirm this hypothesis we propose two main directions for future experiments. First, there is the possibility to detect the Larmor precession of silicon 29 nuclei in the CPMG shape envelope [8, 12, 13]. But, given the gyro-magnetic ratio of silicon nuclei (8.46 MHz/T), the energy selective readout is not suited for the experiment. Indeed, we need to apply high magnetic field to obtain an accurate spin readout. Consequently, the spin precession is too high to be detected by CPMG experiment. The solution here would be to reduce the magnetic field amplitude and use a Pauli spin blockade conversion to read the spin state.

The other solution is to simply get rid of all unwanted nuclear spin by performing isotopic purification of samples and measure on a similar device the spin coherence. Purification is nowadays a consensus in electron spin qubit community, and it will probably be the case for holes soon.

6.3 Carr–Purcell –Meiboom–Gill (CPMG)

6.3.1 CPMG filtering function

To further investigate the hole spin spectrum, we implement Carr–Purcell –Meiboom–Gill (CPMG) sequences, orienting the magnetic field along the x direction ($\theta_{zx} = 90°$). CPMG protocol consists in increasing the number of π pulses canceling faster and faster dephasing mechanisms [4, 6, 8, 14]. CPMG may be seen as a very selective filter [15, 16] at frequencies inversely proportional to the total waiting time [6]. If the number (n) of π pulses is even, and if the experiment is perfectly calibrated, the CPMG filter function may be written as [2] :

$$F(\omega t) = 8\sin^4\left(\frac{\omega t}{4n}\right)\frac{\sin^2\left(\frac{\omega t}{2}\right)}{\cos^2\left(\frac{\omega t}{4n}\right)} \tag{6.9}$$

Where $(\omega t) < 2n$. Giving the very peculiar shape of the filter function plotted in Fig. 6.10, performing CPMG is equivalent to probing the spectrum at very specific frequencies. Increasing the number of pulses, allows to probe even higher and higher frequencies. Note that numerous protocols are available by varying the length of the free evolution time or rotation axis of the pulses. Each of those protocols are related to specific filter functions and are far beyond the scope of this thesis [2], but could be used to go further in the spectrum's study.

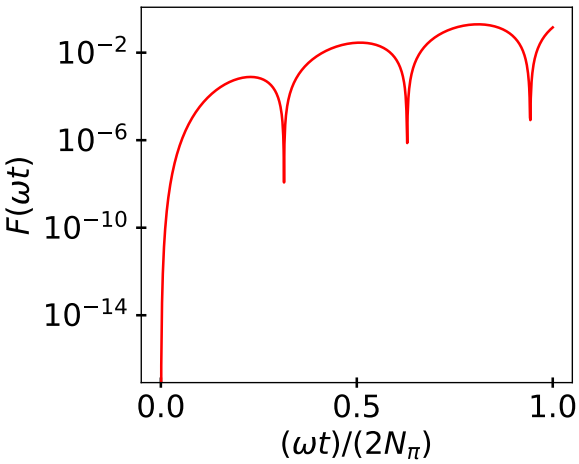

Figure 6.10 – **CPMG filter function.** Filter function for n=10 π pulses equally separated in space time by a free evolution time τ. The total waiting time is denoted as t in the figure for sake of visibility (τ_{wait} in the text). The comb shape of the filter is very efficient to suppress noise contribution on the qubit, especially at very low frequency.

In particular, the spectral weighting function can be approximated with :

$$S_L^{CPMG}\left(\frac{N_\pi}{2\,\tau_{\text{wait}}}\right) = \frac{\ln\left(A_{CPMG}\right)}{2\pi^2\,\tau_{\text{wait}}} \tag{6.10}$$

Where A_{CPMG} is the re-normalized CPMG amplitude.

6.3.2 CPMG measurement

Fig. 6.11-a displays the CPMG echo amplitudes as a function of the total waiting time τ_{wait} for series of $N_\pi = 2^n$ π pulses, where n ranging from 1 to 8. Note that amplitudes are offseted from one another for sake of clarity. To properly extract T_2^{CPMG}, we fit the normalized amplitude with :

$$A_{CPMG} = e^{-(\tau_{\text{wait}}/T_2^{CPMG})^\beta} \tag{6.11}$$

With β is let as a free parameter. The latter exponent is directly related to the power law of the PSD [16, 17]. Here the best fit is given for $\beta = 1.5$ so that $S_L(f) = 1/f^\alpha$ with $\alpha = \beta - 1 = 0.5$, diverging from the classical 1/f noise often measured at high frequency [4, 6].

The CPMG decay times T_2^{CPMG} extracted from Fig. 6.11-a are plotted against N_π in Fig. 6.11-b. As expected, the data points follow a power law $T_2^{\text{CPMG}} \propto N_\pi^\gamma$,

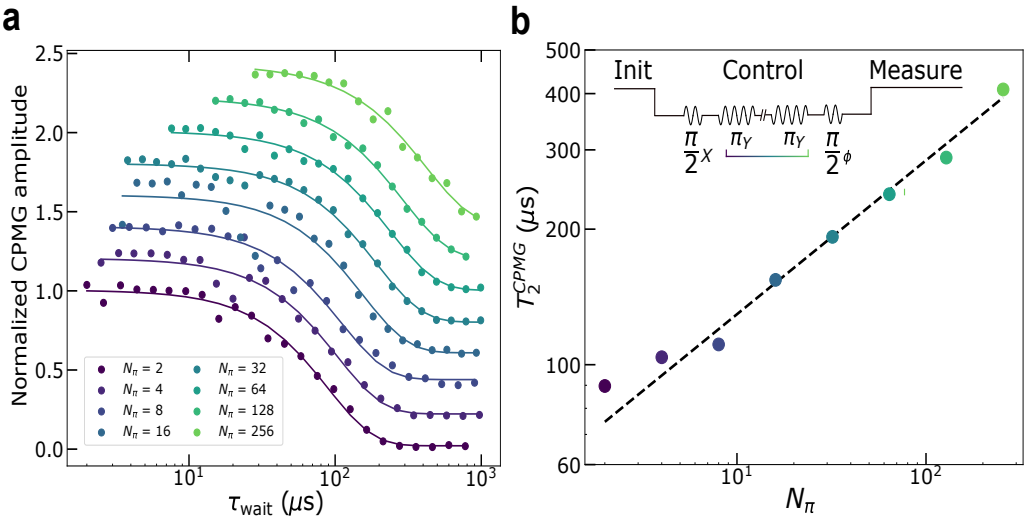

Figure 6.11 – **CPMG protocol. (a)** Normalized CPMG amplitude as a function of free evolution time τ_{wait} for different numbers N_π of π pulses (curves are offset for clarity). The solid lines are fits to the same exponential decay function with $\beta = 1.5$ (see main text). **(b)** Extracted T_2^{CPMG} as a function of N_π. The dashed line is a linear fit with slope $\gamma = 0.34$. The inset sketches the CPMG pulse sequence: N_π equally spaced π_y pulses between two $\pi_x/2$ pulses. As for Hahn-echo experiment, we vary the phase of the last pulse (see 5.3).

where $\gamma = \frac{\alpha}{\alpha+1}$ for a $\propto 1/f^\alpha$ noise spectrum [6]. The best fit value $\gamma = 0.34$ yields once again $\alpha \approx 0.5$. For the largest sequence of 256 π pulses, we find $T_2^{\text{CPMG}} = 0.4\,\text{ms}$, which is the longest coherence ever reported for hole spins [18].

6.3.3 CPMG spectrum

Finally, combining eq. 6.10 with Fig. 6.11 allows to extract the PSD plotted in Fig. 6.12. As expected, the noise spectrum scales with a power law proportional to $1/f^{0.5}$. Compared to previously measured noise spectrum, S_μ^0 is abnormally low. This could be possibly explained by the presence of an inhomogeneous and bounded distribution in frequency of two-level systems in the qubit's vicinity [4, 7, 19]. In this configuration, a cut off frequency (f_c) equal to the higher TLS frequency appears and the charge noise spectrum should quickly collapse (at $f > f_c$) following a $1/f^2$ power law [20]. Given the PSD extracted from the Charge sensor, we estimate the cut-off frequency around 200 KHz.

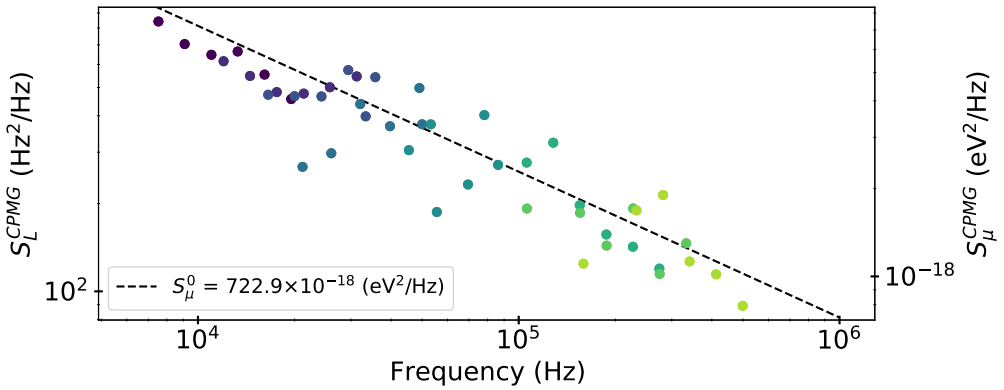

Figure 6.12 – **PSD from CPMG measurement.** The high frequency spectrum (colored dots) is extracted from CPMG measurements with N_π from 2 (dark blue) to 256 (light green). The same color code as Fig. 6.11 has been used. The black dashed line is proportional to $1/f^{0.5}$ (see main text).

6.4 Spin life time

The spin life time (T_1) is a key metric for qubits. The ultra long spin life time measured in silicon and germanium [21, 22, 23, 24] makes spin qubit extremely well positioned outsiders in the worldwide qubit race. Undoubtedly, the largest possible T_1 is desired, setting theoretically the upper limit for spin coherence time but also increasing spin readout fidelity. In addition the study of spin life time offers a way to probe its exchange of energy with the environment.

In the Femi's golden rule, the excitation transition rate may be almost neglected at low temperature so that the spin life time is equal to the de-exitation rate. The process implies an exchange of energy with the environment, implying that the spin decay occurs on account of noise sources at the Larmor frequency (See theory 2.5.2). Consequently, measuring the spin life time as a function of the magnetic field provides both the phenomenological origin of noise and its amplitude at the Larmor frequency.

6.4.1 T_1 measurement protocol

To measure the spin life time, we use a basic two stage (Initialization /Manipulation) protocol. In order not to re-calibrate the polarization pulse, we used a chirping technique [25] to polarize the spin in the $|\uparrow\rangle$ configuration. To do so, we applied a linear frequency modulation in the form of :

$$f(t) = A\cos(2\pi(f_L + \frac{\Delta f}{T}t) * t) \tag{6.12}$$

Where $\Delta f/T$ represents the parameters of the ramp applied for the frequency modulation. The purpose of the chirp pulse is to compensate for Larmor noise in the system by inducing an adiabatic passage from $|\downarrow\rangle$ to $|\uparrow\rangle$ states. The transition probability is in principle given by the Landau–Zener formula.

In the second part of the sequence, we let the spin freely evolve during a time τ_{wait} before measuring the spin up probability ($P_\uparrow$) over 200 cycles. The elementary sequence applied on the qubit is sketched in the inset of Fig. 6.13.

We fit the total $P_\uparrow$ according to the formula $P_\uparrow(t) = Ae(-t/T_1)$ (See theory 2.2.3) and extract the spin life time. A typical T_1 measurement is plotted in Fig. 6.13 at a magnetic field of 771 mT along the x direction, corresponding to a Larmor frequency of 19.065 GHz. We consequently measured a spin life time of $750\mu s$. Note that we were limited at 20 GHz by the microwave source.

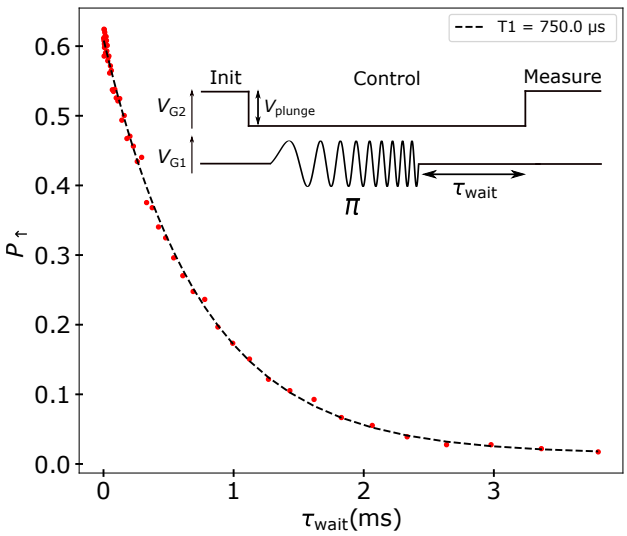

Figure 6.13 – **T1 measurement protocol.** $P_\uparrow$ as a function of τ_{wait}. Red dots exhibits a clear exponential decay with parameter T_1. The dashed black line is a fit to an exponential decay extract the value of 750 μs for the spin life time. Inset sketches the control sequence applied on the qubit for the measurement. After an adiabatic passage pulse (chirp) in Coulomb blockade followed by a free decaying time, the spin polarization is measured.

6.4.2 Γ_1 versus magnetic field amplitude

We reproduced the previous experiment while varying the magnetic field amplitude and report the corresponding data in Fig. 6.14. The lower is the Larmor frequency, the more the Zeeman splitting become comparable to $k_B T$. Consequently, more and more errors occurs at low magnetic field, due to spin readout, explaining the evolution of the error bars in Fig. 6.14. We report a spin decoher-

ence rate Γ_1 with a clear B to the power 3 dependence on all the measurable range, obtained by fitting a linear dependence in log-log scale (slope $p = 3$).

Various field dependence have so far been reported in GaAs, silicon and germanium materials, each corresponding to a singular noise source. Because of the SOC, electric-field fluctuations can lead to spin relaxation. Particularly, at high frequency, phonons (deformations of the lattice) become the dominant processes causing a $T_1 \propto B^7$ (GaAs) due to piezzo-electric properties [26]. In silicon/germanium devices, the piezoelectric effect does not occur, but atoms may move and in-homogeneously deform the crystal lattice. This mechanism occurs in all semiconductors and conduct to $T_1 \propto B^5$ [27].

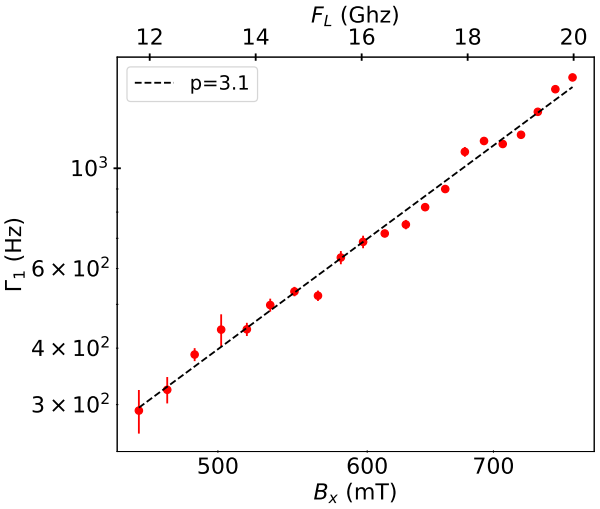

Figure 6.14 – Γ_1 **versus B field in the x direction.** Depolarization Γ_1 rate as a function of B_x field amplitude. Top axis is a conversion to the larmor frequency, using $g_x = 1.84$. An unusual characteristic dependence to a B^3 power low is extracted from the fit (black dashed line).

Theoretically predicted [28, 29, 30, 31], depolarization may also be caused by surrounding electrical noise (Johnson Nyquist) at low magnetic field given a $T_1 \propto B^3$ dependence (See theory 6.4.5), but never demonstrated so far. Nonetheless, the latter mechanism has a hallmark features given by its magnetic field angular dependence. We shall therefore prove its origin by exploring the angular dependence of the spin relaxation rate.

6.4.3 Γ_1 versus magnetic field orientation

We now draw our attention to the dependence of the spin life time with respect to the magnetic field angle θ_{zx} at a fixed Larmor frequency of 16.93 Ghz. Measurements reported in Fig. 6.15 show a cold spot in the x direction, not in agreement with simulation in the previous chapter. We suspect that this discrepancy from the theory is similar to the anomaly reported for $\mathrm{LSES}_{\mathrm{G1}}$. Indeed, those two

quantities are much more sensitive, according to calculations, to the local static disorder in the qubit vicinity.

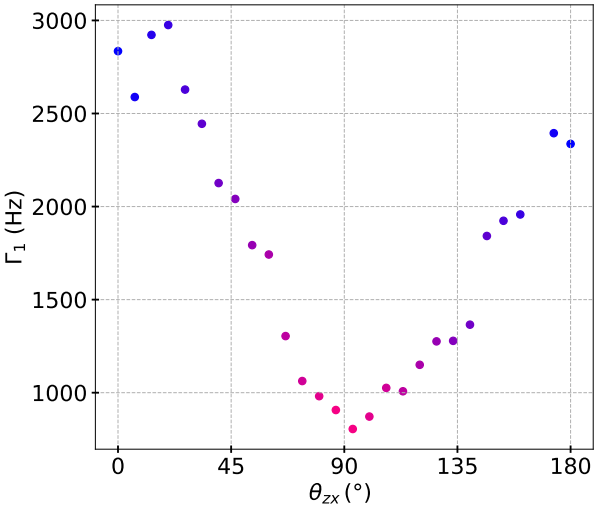

Figure 6.15 – Γ_1 **versus B field orientation.** Depolarization Γ_1 rate as a function of θ_{zx} at $F_L = 16.93\,\text{GHz}$. The anisotropy shows a cold spot in the x direction.

The peak to valley ratio is equal to 3.75, proving a clear anisotropy with the magnetic field orientation. In the case of an electrical noise, we should regain the curve shape in the transversal spin electric susceptibility (TSES) anisotropy (See theory 2.5.2).

6.4.4 TSES versus magnetic field orientation

Similarly to previous chapter experiments, we turn our attention to the spin susceptibility. However, this time, we study its transversal component related to the spin driving.

We define the transversal susceptibility (TSES) with respect to a given gate such that :

$$TSES_{G_i} = \frac{\partial F_{Rabi}}{\partial V_{G_i}} \tag{6.13}$$

Which should be linear with microwave power if not too high. To measure this quantity we first adapt the magnetic field amplitude for each θ_{zx} in order to work at a fixed Larmor frequency of 16.95 GHz. We then record a Rabi chevron with a power of 5 dBm on top of the fridge. From this measure, we precisely extract the

Larmor frequency of the system. Finally, we change the MW power from 0 dBm to 15 dBm in order to access the linear dependence equal to TSES.

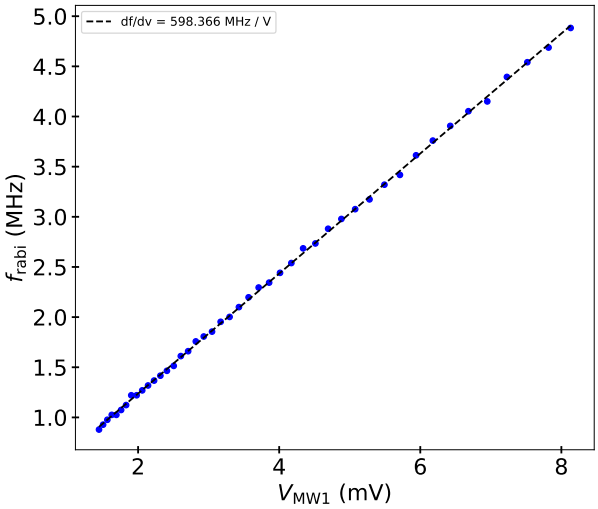

Figure 6.16 – **Rabi frequencies linearity.** Rabi frequency versus estimated microwave amplitude applied on G1. We estimated the total attenuation on the line as the sum of all attenuators plus high frequency attenuation from lines. Back dashed line is a linear fit to the data.

Fig. 6.16 presents at $\theta_{zx} = 0°$ the linear dependence of the Rabi frequency when driving with G1. We did not perform any calibration to know exactly the power really applied on the qubit. As a consequence, we estimated the power by calculating the total attenuation on the line (attenuators and high frequency filtering) and ignoring any standing waves which could drastically change the transmission with the excitation frequency. The black dashed line is a linear fit with a slope equal to TSES_{G1}.

Reproducing the previous experiment for different θ_{zx} when driving with both gates, we obtain the TSES plotted in Fig. 6.17. Strikingly, we observe similarly anisotropy for both gates but with different amplitudes (it was also the case in previous chapter for the LSES).

In particular, for TSES_{G2} we observe two minima close to LSES_{G2} sweet spots. According to Michal et al. [32], we should instead find some reciprocal sweetness when driving the qubit with G2. In other words, when the qubit is tuned to be immune to electrical noise ($\beta_{\parallel} = 0$), it should be a maximum for Rabi frequencies ($\beta_{\perp}$ is maximum). We emphasize on this counter-intuitive phenomenon since no experimental demonstration have been done so far.

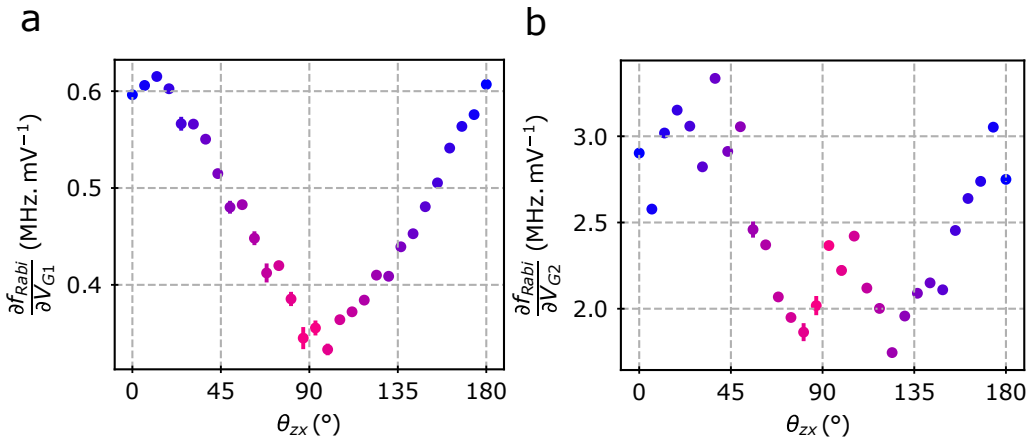

Figure 6.17 – **Transversal spin electric susceptibility.** **(a)** $\mathrm{TSES_{G1}}$ as a function of the magnetic field orientation. Error-bars represents the standard deviation extracted from the linear fit. **(b)** Same as (a) with respect to G2.

6.4.5 Johnson Nyquist

The anisotropies of Fig. 6.14 and Fig. 6.17 seem to be very similar. If we assume that noise at the Larmor frequency is dominated by an electrical contribution, then we would find (See theory 6.4.5) :

$$\Gamma_1 = \sum_i S^{JN}_{V_{Gi}}(\omega_L) \cdot |TSES_{Gi}|^2 \tag{6.14}$$

For sake of simplicity, we assume that the dominant noise source is produced by G1 (anisotropy closer to $\Gamma_1(B)$ shape). We finally obtain Fig 6.18, giving a quasi constant $S^{JN}_{\mu}(\omega_L) = 6.63 \pm 0.51 \cdot 10^{-18}\,\mathrm{eV^2/Hz}$. Note that the calculated value for $S^{JN}_{\mu}(\omega_L)$ highly depends on the real attenuation on the line. Consequently, the real amplitude is hard to estimate without proper calibration of the transmitted power. To improve the experiment, one should record Landau-Zener-Stuckelberg interference pattern under microwave irradiation [33]. Then, one would be able to artificially compensate standing waves that may appear in lines 1&2 by changing the power applied outside the fridge. On top of that, photon assisted tunneling would provide an exact estimation of the excitation at the bottom of each lines [34]. Thus, calibrations would set the spectrum amplitude for Johnson Nyquist noise.

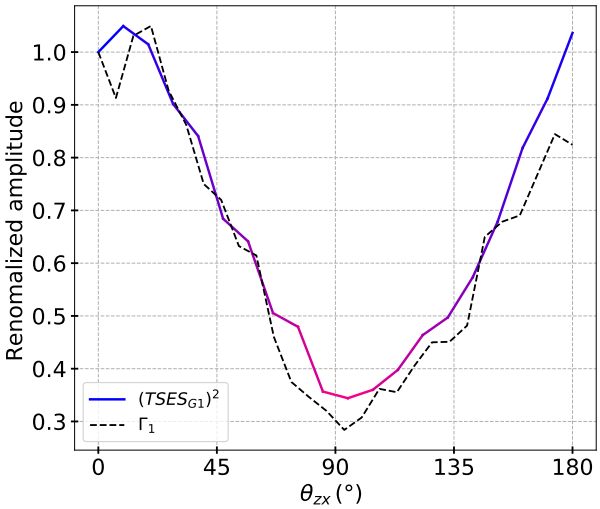

Figure 6.18 – **Anisotropy comparison.** Black dashed line is proportional to Γ_1 from Fig. 6.14 while plain curve is proportional to $(TSES_{G1})^2$ from Fig. 6.17-a. In both case, data have been re-normalized (with respect to the first point) to visually compare the anisotropy.

Essentially, we believe that the lack of attenuation (especially at 1 K) is responsible for a higher electronic temperature on G1 that may possibly explain the low contribution of G2 in the process. In any case, the close matching between both curves in addition to Γ_1 power dependence with B point towards to electrical noise acting on the qubit at high frequency (Johnson Nyquist).

Finally, we converted the T_1 data into a PSD considering only electrical noise on G1 (See theory 6.4.5). Corresponding analysis is plotted as pink dot ($\theta_{zx} = 90°$) in Fig. 6.19. The change of color in the spectrum is given only by the temperature in a simple Johnson Nyquist model. Consequently, we estimate the temperature to be between 22 mK and 150 mK (black dashed line fits).

To go further, we propose supplementary protocols to complete this experiment. A proper calibration of G1 and G2 would set the exact amplitude of the PSD, in order to calculate the couple (R,T) responsible for the observed JN noise. Then, using a variable resistor for the bias-T, one should be able to change the floor noise level giving access to the effective temperature of the emitter. Keep in mind that varying the bias-T resistor will induce deformations in spin manipulation sequences used to measure T_1, that will need to be compensated in the long time domain. To complement, one should vary the temperature and measure $T_1(T)$. These experiences would aim to find the best resistor value to reduce the electrical noise in the system while keeping sufficiently long pulses for spin manipulations. We also exhibit here one of the main limitations of Elzeerman readout. Indeed, The readout stage being very long implies the need of a higher resistance

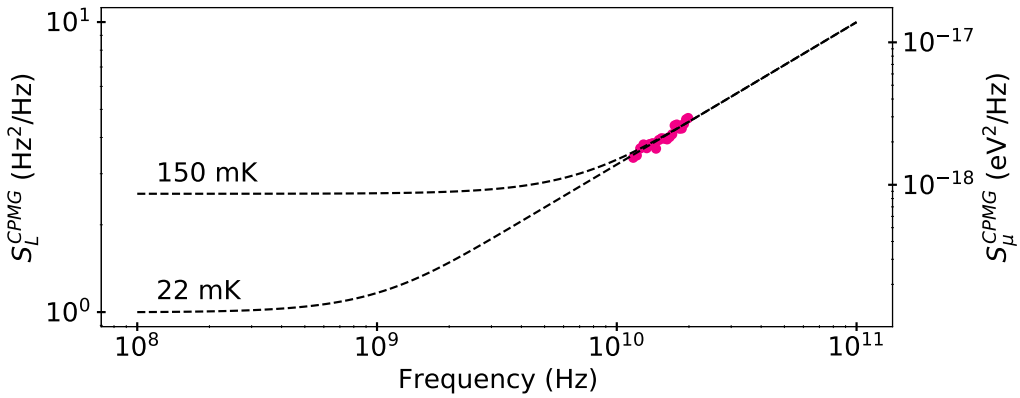

Figure 6.19 – **PSD from T_1 measurement.** (Dots) PSD under the assumption that electrical noise is due to G1. (Black dashed lines) Johnson Nyquist spectrum in the quantum limit for two temperature. 22 mK correspond to the best fit, while 150 mK is the upper limit to keep the fit correct, using $R = 16$ MOhm. The resistor emitting noise has an effective temperature in between those two temperatures.

value. Using a PSB spin to charge conversion should theoretically reduce this problem.

Conclusion

To summarize this chapter, we measured the power spectral density over more than fourteen decades in frequency and observed significant change for noise color, divided into two mechanisms (magnetic and electric). Fig. 6.20 summaries all the spectra measured with different techniques.

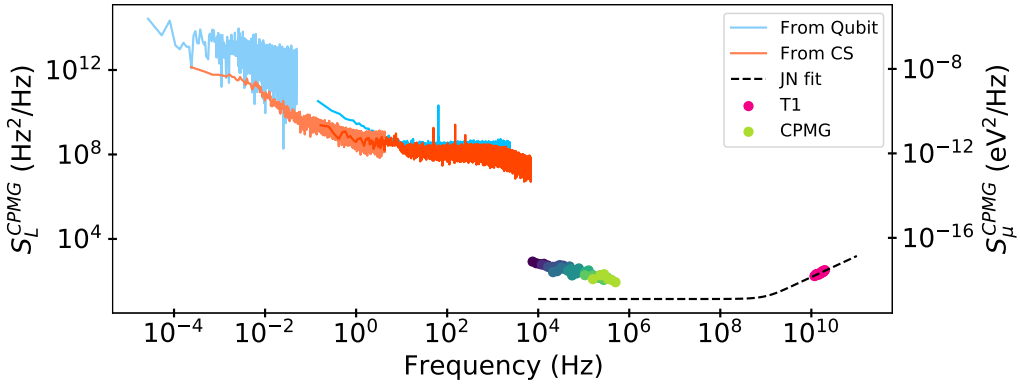

Figure 6.20 – **PSD over 14 decades in frequency.**

From left to right, we obtained a higher PSD with qubit characterization than using the charge sensor. Consequently, we deduced that an additional magnetic noise acts on the single hole spin at very low frequency which slowly vanishes at higher frequency. We measured mainly electrical noise with CPMG technique but with slope diverging from the classical $1/f$ often reported. So far, no convincing explanation is given for this electrical noise whitening . Finally, we reported Johnson Nyquist noise limitation for the spin lifetime, with no signature of phonon at rather high magnetic field. Given the lack of calibration, we could not determine, with a simple model, the resistor interacting with the qubit. Further investigations are required to determine if our bias-T is responsible for the Johnson Nyquist noise and if optimization of printed circuit board components are needed.

References

[1] Norman F. Ramsey. « A Molecular Beam Resonance Method with Separated Oscillating Fields ». In: *Phys. Rev.* 78 (6 June 1950), pp. 695–699. DOI: 10.1103/PhysRev.78.695. URL: https://link.aps.org/doi/10.1103/PhysRev.78.695.

[2] Łukasz Cywi ński et al. « How to enhance dephasing time in superconducting qubits ». In: *Physical Review B* 77 (17 May 2008), p. 174509. DOI: 10.1103/PhysRevB.77.174509. URL: https://link.aps.org/doi/10.1103/PhysRevB.77.174509.

[3] Tom Struck et al. « Low-frequency spin qubit energy splitting noise in highly purified 28Si/SiGe ». In: *npj Quantum Information* 6.1 (May 2020), p. 40. ISSN: 2056-6387. DOI: 10.1038/s41534-020-0276-2. URL: https://doi.org/10.1038/s41534-020-0276-2.

[4] Elliot J. Connors, JJ Nelson, and John M. Nichol. *Charge-noise spectroscopy of Si/SiGe quantum dots via dynamically-decoupled exchange oscillations*. 2021. arXiv: 2103.02448 [cond-mat.mes-hall].

[5] Blake M. Freeman, Joshua S. Schoenfield, and HongWen Jiang. « Comparison of low frequency charge noise in identically patterned Si/SiO2 and Si/SiGe quantum dots ». In: *Applied Physics Letters* 108.25 (2016), p. 253108. DOI: 10.1063/1.4954700. eprint: https://doi.org/10.1063/1.4954700. URL: https://doi.org/10.1063/1.4954700.

[6] Jun Yoneda et al. « A quantum-dot spin qubit with coherence limited by charge noise and fidelity higher than 99.9% ». In: *Nature Nanotechnology* 13.2 (2018), pp. 102–106. ISSN: 1748-3395. DOI: 10.1038/s41565-017-0014-x. URL: https://doi.org/10.1038/s41565-017-0014-x.

[7] L. Petit et al. « Spin Lifetime and Charge Noise in Hot Silicon Quantum Dot Qubits ». In: *Phys. Rev. Lett.* 121 (7 Aug. 2018), p. 076801. DOI: 10.1103/PhysRevLett.121.076801. URL: https://link.aps.org/doi/10.1103/PhysRevLett.121.076801.

[8] Filip K. Malinowski et al. « Spectrum of the Nuclear Environment for GaAs Spin Qubits ». In: *Physical Review Letters* 118.17 (Apr. 2017), p. 177702. DOI: 10.1103/physrevlett.118.177702.

[9] M. S. Bartlett. « Smoothing Periodograms from Time-Series with Continuous Spectra ». In: *Nature* 161.4096 (May 1948), pp. 686–687. ISSN: 1476-4687. DOI: 10.1038/161686a0. URL: https://doi.org/10.1038/161686a0.

[10] Rachpon Kalra et al. « Vibration-induced electrical noise in a cryogen-free dilution refrigerator: Characterization, mitigation, and impact on qubit coherence ». In: *Review of Scientific Instruments* 87.7 (2016), p. 073905. DOI: 10.1063/1.4959153. eprint: https://aip.scitation.org/doi/pdf/10.1063/1.4959153. URL: https://aip.scitation.org/doi/abs/10.1063/1.4959153.

[11] Tobias Wenz et al. « Dopant-controlled single-electron pumping through a metallic island ». In: *Applied Physics Letters* 108.21 (2016), p. 213107. DOI: 10.1063/1.4951679. eprint: https://doi.org/10.1063/1.4951679. URL: https://doi.org/10.1063/1.4951679.

[12] Gary Wolfowicz et al. « 29Si nuclear spins as a resource for donor spin qubits in silicon ». In: *New Journal of Physics* 18.2 (Feb. 2016), p. 023021. DOI: 10.1088/1367-2630/18/2/023021. URL: https://doi.org/10.1088%2F1367-2630%2F18%2F2%2F023021.

[13] K. S. Cujia et al. *Tracking the precession of single nuclear spins by weak measurements*. 2018. DOI: 10.48550/ARXIV.1806.08243. URL: https://arxiv.org/abs/1806.08243.

[14] Nico W. Hendrickx et al. « A four-qubit germanium quantum processor ». In: *Nature* 591.7851 (Mar. 2021), pp. 580–585. ISSN: 1476-4687. DOI: 10.1038/s41586-021-03332-6. URL: https://doi.org/10.1038/s41586-021-03332-6.

[15] G. Ithier et al. « Decoherence in a superconducting quantum bit circuit ». In: *Physical Review B* 72.13 (Oct. 2005), p. 134519. DOI: 10.1103/physrevb.72.134519.

[16] J. Medford et al. « Scaling of Dynamical Decoupling for Spin Qubits ». In: *Physical Review Letters* 108 (8 Feb. 2012), p. 086802. DOI: 10.1103/PhysRevLett.108.086802. URL: https://link.aps.org/doi/10.1103/PhysRevLett.108.086802.

[17] Erika Kawakami et al. « Gate fidelity and coherence of an electron spin in an Si/SiGe quantum dot with micromagnet ». In: *Proceedings of the National Academy of Sciences* 113.42 (Oct. 2016), pp. 11738–11743. DOI: 10.1073/pnas.1603251113.

[18] Peter Stano and Daniel Loss. *Review of performance metrics of spin qubits in gated semiconducting nanostructures*. 2021. arXiv: 2107.06485 [cond-mat.mes-hall].

[19] P. Dutta and P. M. Horn. « Low-frequency fluctuations in solids: $\frac{1}{f}$ noise ». In: *Rev. Mod. Phys.* 53 (3 July 1981), pp. 497–516. DOI: 10.1103/RevModPhys.53.497. URL: https://link.aps.org/doi/10.1103/RevModPhys.53.497.

[20] Utkan Gungordu and J. P. Kestner. « Indications of a soft cutoff frequency in the charge noise of a Si/SiGe quantum dot spin qubit ». In: *Physical Review B* 99.8 (Feb. 2019). DOI: 10.1103/physrevb.99.081301. URL: https://doi.org/10.1103%2Fphysrevb.99.081301.

[21] Andrea Morello et al. « Single-shot readout of an electron spin in silicon ». In: *Nature* 467.7316 (2010), pp. 687–691. ISSN: 1476-4687. DOI: 10.1038/nature09392. URL: https://doi.org/10.1038/nature09392.

[22] C. H. Yang et al. « Spin-valley lifetimes in a silicon quantum dot with tunable valley splitting ». In: *Nature Communications* 4.1 (June 2013), p. 2069. ISSN: 2041-1723. DOI: 10.1038/ncomms3069. URL: https://doi.org/10.1038/ncomms3069.

[23] Thomas F. Watson et al. « Atomically engineered electron spin lifetimes of 30 s in silicon ». In: *Science Advances* 3.3 (2017), e1602811. DOI: 10.1126/sciadv.1602811. eprint: https://www.science.org/doi/pdf/10.1126/sciadv.1602811. URL: https://www.science.org/doi/abs/10.1126/sciadv.1602811.

[24] W. I. L. Lawrie et al. « Spin Relaxation Benchmarks and Individual Qubit Addressability for Holes in Quantum Dots ». In: *Nano Letters* 20.10 (Oct. 2020), pp. 7237–7242. ISSN: 1530-6984. DOI: 10.1021/acs.nanolett.0c02589. URL: https://doi.org/10.1021/acs.nanolett.0c02589.

[25] Mathieu Munsch et al. « Manipulation of the nuclear spin ensemble in a quantum dot with chirped magnetic resonance pulses ». In: *Nature Nanotechnology* 9.9 (Sept. 2014), pp. 671–675. ISSN: 1748-3395. DOI: 10.1038/nnano.2014.175. URL: https://doi.org/10.1038/nnano.2014.175.

[26] R. Hanson et al. « Spins in few-electron quantum dots ». In: *Reviews of Modern Physics* 79.4 (2007), pp. 1217–1265. ISSN: 00346861. DOI: 10.1103/RevModPhys.79.1217. arXiv: 0610433 [cond-mat]. URL: http://scitation.aip.org/getpdf/servlet/GetPDFServlet?filetype=pdf%7B%5C&%7Did=RMPHAT000079000004001217000001%7B%5C&%7Didtype=cvips%7B%5C&%7Dprog=normal.

[27] Leon C Camenzind et al. « Hyperfine-phonon spin relaxation in a single-electron GaAs quantum dot ». In: *Nature communications* 9.1 (Aug. 2018), p. 3454. ISSN: 2041-1723. DOI: 10.1038/s41467-018-05879-x. URL: https://europepmc.org/articles/PMC6110844.

[28] Jonas Bylander et al. « Noise spectroscopy through dynamical decoupling with a superconducting flux qubit ». In: *Nature Physics* 7.7 (July 2011), pp. 565–570. ISSN: 1745-2481. DOI: 10.1038/nphys1994. URL: https://doi.org/10.1038/nphys1994.

[29] Florian Marquardt and Veniamin A. Abalmassov. « Spin relaxation in a quantum dot due to Nyquist noise ». In: *Phys. Rev. B* 71 (16 Apr. 2005), p. 165325. DOI: 10.1103/PhysRevB.71.165325. URL: https://link.aps.org/doi/10.1103/PhysRevB.71.165325.

[30] Pablo San-Jose et al. « Geometrical Spin Dephasing in Quantum Dots ». In: *Phys. Rev. Lett.* 97 (7 Aug. 2006), p. 076803. DOI: 10.1103/PhysRevLett.97.076803. URL: https://link.aps.org/doi/10.1103/PhysRevLett.97.076803.

[31] Peihao Huang and Xuedong Hu. « Electron spin relaxation due to charge noise ». In: *Phys. Rev. B* 89 (19 May 2014), p. 195302. DOI: 10.1103/PhysRevB.89.195302. URL: https://link.aps.org/doi/10.1103/PhysRevB.89.195302.

[32] V. P. Michal et al. *Tunable hole spin-photon interaction based on g-matrix modulation*. 2022. DOI: 10.48550/ARXIV.2204.00404. URL: https://arxiv.org/abs/2204.00404.

[33] E. Dupont-Ferrier et al. « Coherent Coupling of Two Dopants in a Silicon Nanowire Probed by Landau-Zener-Stückelberg Interferometry ». In: *Phys. Rev. Lett.* 110 (13 Mar. 2013), p. 136802. DOI: 10.1103/PhysRevLett.110.136802. URL: https://link.aps.org/doi/10.1103/PhysRevLett.110.136802.

[34] Carola Meyer, Jeroen M. Elzerman, and Leo P. Kouwenhoven. « Photon-Assisted Tunneling in a Carbon Nanotube Quantum Dot ». In: *Nano Letters* 7.2 (Feb. 2007), pp. 295–299. ISSN: 1530-6984. DOI: 10.1021/nl062273j. URL: https://doi.org/10.1021/nl062273j.

Chapter 7

Conclusion

"I think I can safely say that nobody understands quantum mechanics."

Richard Feynman

Contents

7.1 Version Française 174
7.2 English version 176

7.1 Version Française

Depuis plus d'une dizaine d'années maintenant, les bits quantiques de spin dans le silicium ont émergé comme une plateforme prometteuse pour la réalisation de simulateurs quantiques. Pour le moment, aucun dispositif parmi la multitude d'architectures proposée n'a encore prouvé sa supériorité. Pour ne citer que quelques paramètres qui portent à débat, nous évoquerons la particule portant le spin (donneur, électron, trou), les matériaux (Si/Ge hétéro-structures, empilement de grille, l'entretoise) ou encore la géométrie du dispositif. Cette thèse s'est donc inscrite dans l'étude d'un dispositif en particulier : un unique bit quantique de spin porté par un trou dans un nanofil en silicium naturel réalisé à partir de la technologie CMOS, éprouvée industriellement.

Pour la première fois, dans nos dispositifs, nous avons mesuré l'état de spin du premier trou piégé sous une grille. Bien que la lecture dite 'énergie sélective' soit maintenant répandue dans de nombreux laboratoires, de multiples difficultés ont tout de même dû être surmontées. La première était la réalisation d'échantillons, électrostatiquement stables dans le temps et compatibles avec la réflectométrie à haute fréquence. Ce jalon n'est, par exemple, pour le moment pas atteint par les équipes d'IBM sur des structures similaires. Nous avons ensuite été confronté au problème du taux tunnel entre le puits quantique et le réservoir, élément dont le contrôle est crucial. N'ayant pas de véritable levier d'action sur ce paramètre, nous avons dû chercher des points de fonctionnement possible à l'aide d'une routine informatique permettant de scanner l'échantillon. Enfin, une fois ces difficultés surmontées, nous avons optimisé les paramètres du système pour obtenir une lecture de spin dont les performances sont proches des meilleures réalisations à ce jour.

L'un des challenges principaux pour la réalisation de bits quantiques est de comprendre et de pouvoir étendre leur temps de cohérence. De fait, nous avons non seulement étudié la fréquence d'excitation très anisotrope des spins de trou en fonction de l'orientation champ magnétique mais aussi leur temps de décohérence. Nous avons démontré que dans notre cas le temps de cohérence était limité, à haute fréquence, par le bruit de charge environnant. Or étant donné que la direction du vecteur de Larmor dépend de l'orientation du champ magnétique, nous avons mis en évidence l'existence d'un point de fonctionnement pour lequel le système est quasiment insensible, au premier ordre, au bruit de charge. À cet endroit, le temps de cohérence est par conséquent très largement augmenté pour atteindre $88\,\mu s$, ce qui est comparable aux spins d'électrons avec un couplage spin orbite artificiel. À noter toutefois que l'étude se restreint à l'étude du champ magnétique dans un seul plan, alors que des résultats théoriques récents incitent à étudier le temps de cohérence dans toutes les directions de l'espace.

Le dernier chapitre de cette thèse étend l'étude de bruit sur quasiment 14 ordres de grandeur en fréquence. À basse fréquence, le détecteur de charge et le spin

de trou perçoivent des amplitudes et des couleurs de bruits différentes. Nous en avons déduit qu'il existait une seconde source de bruit magnétique, probablement due aux spins nucléaires environnants. Enfin, à très haute fréquence, nous avons enregistré une dépendance des temps de vie avec l'amplitude et la direction du champ magnétique qui vont dans le sens d'un bruit du type Johnson Nyquist. Cette analyse tend à montrer qu'il est important d'optimiser les circuits imprimés placés en amont des bits quantiques de spin en utilisant à la fois des composants de basse impédance et des lignes de contrôle extrêmement bien filtrées.

Enfin, pour la première fois, les résultats théoriques obtenus par nos collaborateurs, corroborent quasiment parfaitement les mesures réalisées. Bien que la rotation du g-facteur dans un champ de contrainte inhomogène soit encore peu comprise et qu'il soit pratiquement impossible de simuler un dispositif réel à cause du grand nombre de défauts localisés aux interfaces Si/SiO2, nous progressons tout de même vers la création d'outils de simulation puissants. A terme, la compréhension poussée de la physique des trous dans le silicium (et par extension le germanium) permettrait de simuler des géométries envisageables et d'en éprouver leurs performances. Il faut garder à l'esprit que l'étude en détail d'un dispositif peut prendre plusieurs semaines voire plusieurs mois à basse température. Bien que l'ensemble des dispositifs utiles pour étudier des bits quantiques soient de plus en plus performants et faciles d'utilisation (dilutions, instrumentations, ...), ils restent extrêmement onéreux et rien ne remplacera une simulation simple et précise. La difficulté résidera alors dans la faisabilité des dispositifs imaginés.

Bien que les résultats obtenus dans ce manuscrit soient très encourageants, il reste un point noir au tableau quant à l'avenir de la technologie CMOS pour la réalisation de bits quantiques : la scalabilité. Présenté comme un avantage compétitif de taille vis-à-vis d'autres technologies, le débat reste tout de même entier. Certes, la technologie industrielle pour la production de transistor classique est extrêmement mature, mais la réalisation de milliards de bits quantiques avec une empreinte spatiale réduite reste tout de même un challenge hors de portée pour le moment. En sus des temps de production qui peuvent être particulièrement long, la réalisation des échantillons présente le désavantage d'être très peu modulable pour plusieurs raisons. D'une part les matériaux doivent être compatibles avec les différentes lignes de productions, et d'autre part les coûts de production et d'innovation sont exorbitants au vu de la complexité des dispositifs. La réalisation de calculateur quantique n'en qu'à ces balbutiements et de nombreux axes de recherche nécessitent encore d'être explorés. Or, à travers la réalisation de dispositifs CMOS, on essaye à tout prix de transposer cette énorme machinerie à un pan de la physique qui requiert encore une grande modularité.

7.2 English version

For more than a decade now, spin qubits in silicon have emerged as a promising platform for the realisation of quantum simulators. For the time being, no device among the multitude of proposed architectures has yet proven its superiority. To mention only a few debatable parameters, we will cite the particle carrying the spin (donor, electron, hole), the materials (Si/Ge heterostructures, gate stacks, spacers) or the geometry of the device. This thesis therefore focused on the study of one device in particular: a single spin quantum bit carried by a hole in a natural silicon nanowire made using industrially proven CMOS technology.

For the first time in our devices, we measured the spin state of the first hole trapped in a quantum dot. Although the so-called 'energy selective' readout is now widespread in many laboratories, several difficulties had to be overcome. The first has been to develop fast charge-sensing schemes based on high frequency reflectometry, by operating multi-gate devices. This has been made possible thanks to the production of high quality p-doped samples by the Leti team, and major improvments in the reflectometry setup on our side. Among others, the use of a low noise cryogenic amplifier, development of novel PCB sample holders, proper filtering and attenuation of DC and RF lines were key in this success. We were then confronted with the problem of the tunnel rate between the quantum dot and the reservoir, an element whose control is crucial. As we had no real control over this parameter, we had to look for possible operating points using a computer routine to search for a proper dot-reservoir transition. Finally, once these difficulties were overcome, we optimized the system to obtain a single shot spin readout whose performance is close to the best achievements to date.

One of the main challenges for the realisation of qubits is to understand and extend their coherence time. To do so, we have not only studied the very anisotropic Larmor frequency of the hole spin as a function of the magnetic field orientation but also their coherence time. We have shown that in our case the coherence time is limited, at high frequency, by the surrounding charge noise. Moreover, in the system, the longitudinal spin electric susceptibility for G1 and G2 is minimal almost at the same magnetic field angle. Consequently, we have demonstrated the existence of an operating sweet point for which the system is almost insensitive, at first order, to charge noise. At this point, the coherence time is consequently greatly increased to $88\,\mu s$, which is comparable to electron spins with an artificial spin-orbit coupling. It should be noted, however, that the study is restricted to a single plane, whereas recent theoretical results suggest that the coherence time should be studied in all directions of space, in order to look for a sweet line (extension of the sweet spot in a plane).

The last chapter of this thesis extends the noise study over almost 14 orders of magnitude in frequency. At low frequencies, the charge sensor and the hole

spin perceive different noise amplitudes and colors. We deduced that there is an additional magnetic noise source, probably due to the surrounding nuclear spins. Finally, at very high frequencies, the magnetic field dependence of the spin lifetime pinpoints to Johnson Nyquist noise. This analysis shows that it is important to optimize the printed circuits placed upstream of the spin qubit by using both low impedance components and extremely well filtered control lines.

Finally, for the first time, the theoretical results obtained by our collaborators almost perfectly corroborate the measurements performed. Although the rotation of g-factor induced by an inhomogeneous stress field is still poorly understood and that it is virtually impossible to simulate a real device because of the large number of defects located at the Si/SiO2 interfaces, we are nevertheless making progress towards the creation of powerful simulation tools. Eventually, a thorough understanding of the physics of holes in silicon (and by extension germanium) would allow us to simulate possible geometries and test their performance. It should be borne in mind that the detailed study of a device can take several weeks or even months at low temperatures. Although all external devices useful for studying qubits are increasingly efficient and easy to use (dilutions, instruments, etc.), they remain extremely expensive and nothing can replace a simple and precise simulation. The difficulty will then lie in the feasibility of the designed devices. Finally, this thesis work makes hole spin qubits candidates just as credible as electrons for quantum computing.

Although the results obtained in this manuscript are very encouraging, there is still a dark spot in the future of CMOS technology for the realisation of qubits : scalability. Theorically presented as a major competitive advantage over available technologies to make qubits, the possibility to scale quantum dots is according to me questionable. So far, the industrial technology for producing classical transistors is extremely mature, but the realization of billions of qubits with a small spatial footprint remains a challenge that is out of reach for the time being. In addition to the production times, which can be particularly long, the production of samples has the disadvantage of being very inflexible for several reasons. On the one hand, the materials must be compatible with the different production lines, and on the other hand, the production and innovation costs are exorbitant given the complexity of the devices. The realization of quantum computers is still in its infancy and many areas of research still need to be explored. However, through the realisation of CMOS devices, we are trying at all costs to transpose this enormous machinery to an area of physics that still requires great modularity.

Epic Story

Within the captivating realm of quantum exploration, this thesis unveils the quest to extend the precious coherence time of a lone spinning hole nestled in the depths of a natural silicon channel while unraveling the secrets that limit its potential. Through a meticulous investigation of spin-orbit coupling, an astonishing breakthrough emerges, bestowing unparalleled control over the properties of the elusive qubit.

By harnessing the power of CMOS technology, an innovative built-in sensor materializes—an harmonious fusion of a vast hole island and a resonating drain reservoir. This visionary integration enables the thorough mapping of the enigmatic spin state onto the charge state using energy-selective readout. Witness the mesmerizing dance of anisotropic Zeeman energy, arising from the intricate interplay between spin and confinement, leading to the discovery of newfound realms of coherence. Through skillful manipulation of magnetic field orientation, the grip of longitudinal susceptibility vanishes, resulting in a remarkable five-fold increase in coherence time.

Finally, the secrets of noise are unraveled, revealing the haunting whispers of magnetic interference from silicon-29 isotopes at lower frequencies, while the electric domain asserts its dominion at higher frequencies. Yet, an enigma persists—phonon-induced spin flips remain shrouded in mystery, eagerly awaiting their revelation. Envisioning a future brimming with quantum possibilities, this innovative work introduces a tunable cornerstone for hole spin qubits, applicable to industrial CMOS technologies, propelling us towards the limitless frontiers of quantum information processing.

cea irig INTERDISCIPLINARY RESEARCH INSTITUTE OF GRENOBLE Pheliqs Quantum Physics & Engineering leti UGA Université Grenoble Alpes